The Pennsylvania State University

The Graduate School

Department of Materials Science and Engineering

MECHANICAL ENERGY HARVESTERS UTILIZING {001} TEXTURED PZT FILMS ON FLEXIBLE METAL FOILS

A Dissertation in

Materials Science and Engineering

by

Hong Goo Yeo

Submitted in Partial Fulfillment

of the Requirements

for the Degree of

Doctor of Philosophy

December 2017

The dissertation of Hong Goo Yeo was reviewed and approved* by the following:

Susan Trolier-McKinstry
Professor of Ceramic Science and Engineering
Dissertation Advisor
Chair of Committee

Clive A. Randall
Professor of Material Science and Engineering

Christopher Rahn
Professor of Mechanical and Nuclear Engineering

Roman Engel-Herbert
Professor of Material Science and Engineering

Suzanne Mohney
Professor of Materials Science and Engineering and Electrical Engineering
Chair, Intercollege Graduate Degree Program in Materials Science and Engineering

* Signatures are on file in the Graduate School

‘

ABSTRACT

This thesis describes the optimization and utilization of piezoelectric $Pb(Zr_xTi_{1-x})O_3$ PZT thin films on flexible metal foils for various types of mechanical piezoelectric energy harvesters. Flexible metal foil substrates with high fracture strength are useful in some microelectromechanical systems (MEMS) applications, including wearable piezoelectric sensors or energy harvesters based on $Pb(Zr,Ti)O_3$ (PZT) thin films. Full utilization of the potential of PZT film on metal foils requires control of the film crystallographic texture to achieve a high figure of merit (FoM) for energy harvesting application. A high level of {001} film orientation enables an increase in the energy harvesting FoM due to the coupling of strong piezoelectricity and low dielectric permittivity.

In this study, {001} oriented PZT thin films were grown by chemical solution deposition (CSD) and *rf*-magnetron sputtering on Ni foil. To overcome the issue with thermodynamic incompatability between the metal substrate and the oxide film during subsequent thermal treatment, pretreated Ni foils were passivated using HfO_2 grown by atomic layer deposition (ALD). Highly {001} oriented PZT films were successfully deposited on Ni foils with (100) oriented $LaNiO_3$ seed layers on HfO_2 buffer layers using either chemical solution deposition or rf sputtering. The (001) oriented PZT thin films achieve an $e_{31,f}$ piezoelectric coefficient of -10 ~ -12 C/m^2 (which is comparable with (100) textured PZT films on silicon substrate) coupled with a low dielectric constant (330 ~ 530 at 1kHz) after hot poling.

Piezoelectric energy harvesters with cantilever type structures consisting of PZT films on Ni foil revealed a strong correlation between the FoM and the harvester output. Both increasing the volume of the piezoelectric element (*e.g.* the film thickness in the 31 mode) as well as

inducing a high FoM via hot poling improve the performance of PZT cantilevers. As a result, it is possible to achieve a power density of 1036 $\mu W/cm^2 \cdot G^2$ with 3 μm thick sputtered PZT film on Ni below 100 Hz.

Extracting energy from low vibration frequencies (<10Hz) is essential for wearable harvesters. Two main types of mechanical energy harvesting devices (*e.g.* resonant and non-resonant harvesters) were investigated. The Piezoelectric Compliant Mechanism (PCM) design proposed by Ma and Rahn was targeted for high efficiency operation at 5 Hz by fostering a uniform strain for its 1st mode shape. In particular, a PCM energy harvester utilizing {001} textured bimorph PZT films on Ni foil provided a large power level of 3.9 $mW/cm^2 \cdot G^2$ and 65% mode shape efficiencies at ~ 6 Hz.

Frequency-up conversion for non-resonant piezoelectric energy harvesters is an excellent strategy to extract electrical energy from human motion for self-powering portable electronics. Three different designs related to magnetic plucking suggested by Xue and Roundy were explored using bimorph PZT films on flexible nickel foils for wrist-worn harvesters (for which the desired device size is less than 16 cm^2). Thick PZT films on Ni foil deposited by high temperature sputtering enable the production of multiple piezoelectric beams with complex designs (e.g., star shaped cantilever beams). Based on analysis of the plucked beam dynamics (simulated by Xue, and Roundy), PZT beams and permanent magnet configuration were selected and demonstrated. The resulting devices successfully convert low frequency vibration sources (i.e. from walking. rotating the wrist, and jogging) to higher frequency vibrations of the PZT beams (100 ~ 200 Hz). Additionally, the devices are able to generate 40~50 μW power during mild activities.

In summary, strongly {001} oriented bimorph PZT films on flexible metal foils are

promising for implementation of high efficiency harvesters with a variety of shapes and dimensions from mm^2 to cm^2.

TABLE OF CONTENTS

LIST OF FIGURES

LIST OF TABLES

ACKNOWLEDGMENTS

My long journey at Penn State has been enriched by many people I have met here and whom I truly appreciate. I would like to thank the people who have supported and helped me so much throughout this period. I believe it would be impossible to complete this fruitful work without the help of all of you.

First and foremost, I would like to offer my sincerest gratitude to my advisor Professor Susan Trolier-McKinstry for her dedication, support and generosity. Her intensity and the compassion she showed to me are much appreciated. Her invaluable guidance and stimulating suggestions have sustained the work and me personally, for which I am truly grateful. I cannot possibly thank her enough for her support and encouragement, particularly during writing.

I also deeply appreciate my committee members, Professors Clive A. Randall, Roman Engel-Herbert and Christopher Rahn for their insight and knowledge throughout my thesis. Their advice and comments have greatly improved to improve the quality of my research.

I would like to thank all of the STM group members that I have spent time with during my Ph D ,for their kindness and their friendly support: Raegan Johnson, Derek Wike, Aaron Welsh, Adarsh Rajaskekar, Charely Yeager, Ryan Keech, Margeaux Wallace, Lizz Michael, Song-Won Ko, Jung-In Yang, Dan Marincel, Lauren Garten, Jon Bock, Sun-Young Lee, Wanlin Zhu, Jason Chan, Lyndsey Denis, Trent Borman, Dixinong Wang, Smitha Shetty Betul Akkopru Akgun, Chris Cheng, Kathleen Coleman, Tianning Liu, Beth Jones, Carl Morandi, and Julian Walker.

I also would like to thank my collaborators Prof Shad Roundy, Tiancheng Xue and Xiaokun Ma for their tremendous help through this work. They were always willing to help me understand the mechanical design of my devices.

I appreciate the help of MCL and MSC cleanroom staff, particularly Nichole Wonderling and Bill Drawl, who gave their time to come to my aid when I faced technical issues with equipment. This work was funded by a National Security Science and Engineering faculty fellowship and the NSF Nano-systems Engineering Research Center (NERC) for Advanced Self-Powered Systems of Integrated Sensors and Technologies (ASSIST).

Lastly, my greatest gratitude goes to my wife Inhee. Without her dedicated love and support I would not have completed this fruitful journey. My daughter, Serena Jiwoo, is the greatest possible reward I could hope for during my Ph D.

Chapter 1.

Statement of Goals and Thesis Organization

1.1 Statement of Purpose

Currently, the development of many future technological devices, including wearable electronics, the Internet of Things (IoT) and self-powered sensors for condition – based maintenance, is heavily constrained by their power supply; their batteries run down and need to be changed regularly. While in principle energy harvesting could solve this problem, in practice, the power levels available have been too low for implementation. This thesis discusses the utilization of piezoelectric materials, specifically $Pb(Zr,Ti)O_3$ PZT thin films on flexible metal foils in the development of various types of mechanical energy harvesters.

Past research on the use of PZT thin films in microelectromechanical devices (MEMS) has shown that while MEMS piezoelectric energy harvesters can be effectively utilized to scavenge energy from some devices, it is ineffective in harvesting energy from the human body; this is due to the extremely low natural frequency of body motion and the intermittent nature of its movement. In an attempt to address this problem, this study focuses on the development of a material designed to have a high energy harvesting figure of merit (FoM) with an advanced mechanical design.

Previous attempts to develop a wearable energy harvester have included experiments involving piezoelectric materials and their processing techniques. For example, researchers explored depositing high figure of merit piezoelectric films onto oxide substrate and transferring the films to a flexible support substrate. However, the Si based etching and lift-off techniques used in these experiments often resulted in chemical and mechanical damage to the film,

hindering the harvesters' performance. A new technique, probing the use of flexible metal foil substrates with high fracture strength has proven successful. These foils are easily shaped by a laser cutter and are highly adaptable. Their flexibility and strong fracture toughness are superior to the stiff passive oxide layer of previous films. Additionally, these foils are cost effective. Therefore, the goal of this thesis is to explore the development of (001) oriented PZT films with flexible metal foil in an advanced harvester design.

Full utilization of the potential of PZT film on metal foils requires control of the films' crystallographic texture to achieve a high figure of merit (FoM) for energy harvesting application. Using the proper deposition method is necessary to overcome the thermodynamic incompatibility between the oxide films and the metal substrates during the crystallization process of the oxide film. Once these PZT films are successfully grown on a flexible foil, they can be used in the piezoelectric components of a wearable energy harvester and will allow the harvesters to operate at low resonance frequency.

Frequency-up conversion design for non-resonant piezoelectric energy harvesters is an excellent strategy to extract energy from human motion. This phenomenon has led to the development of piezoelectric devices of various shapes designed for frequency-up conversion.

1.2 Dissertation Structure

This thesis begins with a discussion of various mechanical energy harvesters, particularly wearable devices, made from high FoM PZT films on flexible Ni foil. An introduction to piezoelectric energy harvesting, including extracting kinetic energy from ambient sources follows. The use of ferroelectric piezoelectric materials to increase the conversion

efficiency of the harvesters is also discussed. Several types of mechanical designs for the harvesters are explored.

Chapter 3 discusses the processing procedures involved in obtaining a preferred orientation in PZT (52/48) films integrated onto Ni substrate by chemical solution deposition. This Chapter also presents variants in the texture of PZT films deposited on Ni foil and discusses their structure, phase and electrical properties. It then compares them with PZT films deposited on Si substrates under the same conditions.

Chapter 4 addresses enhancing the harvesters' performance through changes in the poling condition and/or the thickness of the PZT films. The effects of increasing the total volume of piezoelectric components is investigated through experimentation. Finally, a discussion of resonant harvesters of the same footprint area using PZT films on Ni foil follows.

Body-based energy harvesters require low resonance frequency. A discussion of this is presented in Chapter 5. The chapter discusses research to combine bimorph configuration piezoelectric films on flexible foils with a compliant mechanical design. This design provides improved strain distribution along the piezoelectric material in the energy harvester. The power density of the resultant device compares favorably with other microelectromechanical systems discussed in the literature.

Deposition of highly dense and 001 oriented PZT film by in-situ crystallization rf-sputtering for the development of a variety of wrist-worn energy harvesters utilizing magnet plucking is described in Chapter 6. Additionally, the performance of a different types of wrist worn energy harvester is reported. Key experiments mimic arm movement by using a set-up for pseudo walking on a bench.

Chapter 7 concludes the thesis and provides proposed future work based on preliminary

studies.

Chapter 2

Background and Literature Review

2.1 Background

There are several technologies for energy harvesting that are being extensively studied, including harvesting from ambient light, temperature, temperature gradients, and mechanical motion. As the capabilities of harvesting systems grow, it is becoming increasingly plausible to envision self-powered electronics systems. The need for self-powering can be envisioned readily for the field of structural health monitoring. If thousands of sensor systems are mounted on bridges and buildings to monitor their conditions, then each of those systems will require power. Changing batteries in remote or difficult to access locations requires labor and expense, and can be physically hazardous. For such applications, energy harvesting technique could supply electrical energy to extend the lifetime of the monitoring system.

Each of the technologies for energy harvesting have advantages and disadvantages. Solar cells typically provide the largest power per area in cases where direct sunlight is available as an energy source. Where sunlight is not available, mechanical energy harvesting from sources such as car engines, microwave ovens and human motion offers a viable alternative.[1,2]

2.2 Kinetic Energy Harvesting

2.2.1 Theory of Kinetic Energy Harvesting

Mechanical modeling is used to predict the performance of energy harvesting systems. This is often done using a mass-spring-damper system to describe the harvester system, as shown in Figure 2-1.

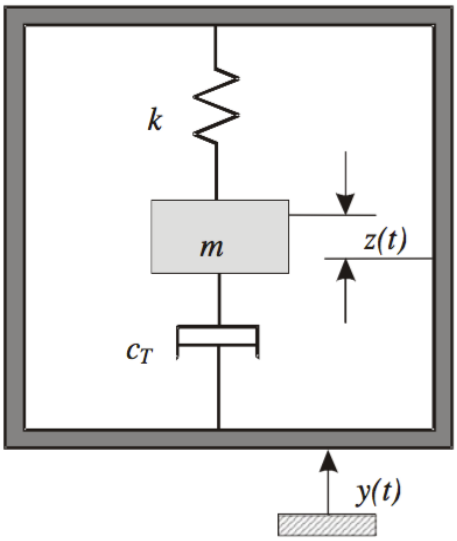

Figure 2-1. Model of a linear mass-spring damper system with mechanical component and inertial frame for a vibration-based generator.[3]

The model of mass-spring system with a linear damper can expressed as

$$m\ddot{z} + c_T\dot{z}(t) + k_s z(t) = -m\ddot{y}(t) \qquad (2.1)$$

where m is a seismic mass and c_T is the combined damping constant ($c_T = c_e + c_m$; c_m is the mechanical damping and c_e is the electrical damping coefficient), k_s is the spring stiffness, *z(t)* is the net displacement of the mass, and $y(t) = Ysin(\omega t)$ is an external sinusoidal vibration of the form within the inertial frame. Y is the amplitude of vibration.

The instantaneous power generated from the resonant system is simply the product of force ($F = -m\ddot{y}(t)$) and velocity ($v = \dot{y}(t) + z(\dot{t})$):[4]

$$p(t) = -m\ddot{y}(t)[\dot{y}(t) + \dot{z}(t)] \qquad (2.2)$$

A complete analytical expression for power can be derived by solving equation 2.1 for $\dot{z}(t)$ and substituting the result into equation 2.2. The standard steady-state solution for the displacement of the mass z(t) yields the following expression:[3,4]

$$z(t) = \frac{\omega^2}{\sqrt{\left(\frac{k}{m}-\omega^2\right)^2+\left(\frac{c_T\omega}{m}\right)^2}} Y sin\,(\omega t - \phi) \quad (2.3)$$

where ω is the frequency of the driving vibrations and phase angle ϕ is expressed as

$$\phi = tan^{-1}\left(\frac{c_T\omega}{k-\omega^2 m}\right) \quad (2.4)$$

Mechanical power is converted to electrical power when damping is present. The electric power generated, $P(t)$ at a single sinusoidal frequency, is given by[3,5,6]

$$P(t) = \frac{m\zeta_t Y^2\left(\frac{\omega}{\omega_n}\right)^3\omega^3}{\left[1-\left(\frac{\omega}{\omega_n}\right)^2\right]^2+\left[2\zeta_t\frac{\omega}{\omega_n}\right]^2} \quad (2.5)$$

where ζ_t is the total damping ratio ($\zeta_t = c_T/2m\omega_n$), ω_n is the natural frequency of the mass spring system. This system can extract maximum energy when the excitation frequency matches the natural frequency of the system (ω_n) given by

$$\omega_n = \sqrt{k_s/m} \quad (2.6)$$

Maximum power occurs when the resonant frequency of the system matches the input frequency, Equation 2.5 can be given the following equations:[3]

$$P(t) = \frac{mY^2\omega_n^3}{4\zeta_t^2} \quad (2.7)$$

$$P(t) = \frac{mA^2}{4\omega_n\zeta_t} \quad (2.8)$$

where A ($A = \omega_n^2 Y$) is the magnitude of the acceleration corresponding to the input vibrations. Based on equation 2.8, the output power is inversely proportional to the natural frequency of the generator when the acceleration is held a constant. Practically the acceleration levels of ambient vibration tend to reduce with increasing frequency. Thus, the design of the generator (related to the generator size and maximum tip displacement) should be appropriate for the input vibration source. Thus, the spectrum of application vibration should be analyzed before designing the generator.[3]

2.2.2 Kinetic Vibration Source in the Ambient

There are numerous environmental sources of kinetic vibration, in a wide range of frequencies, available for energy harvesting. However, not all ambient mechanical sources convert effectively into electrical energy. Table 2-1 lists the maximum acceleration amplitudes and frequencies of several environment vibration sources.[7,8]

Table 2-1. Acceleration amplitude and frequency of ambient vibration sources from commercial devices.[7,8]

Vibration source	**Acceleration (ms^{-2})**	**$Frequency_{peak}$ (Hz)**
Car engine compartment	12	200
Base of 3-axis machine tool	10	70
Blender casing	6.4	121
Clothes dryer	3.5	121
Person tapping their heel	3	1
Car instrument	3	13
Door frame just after door closes	3	125
Small microwave oven	2.5	121
HVAC vents in office building	0.2~1.5	60
Windows next to a busy road	0.7	100
CD on notebook computer	0.6	75
Second story floor of busy office	0.2	100

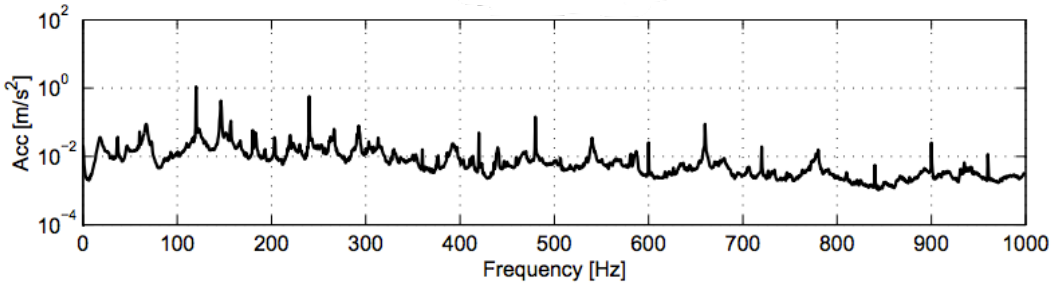

Figure 2-2. Acceleration as a function of frequency for the top of a microwave oven.[9]

Practically, most kinetic mechanical sources emit a low frequency vibration, typically below 200Hz. The energy generated from these sources ranges from micro watt to mW.[4]

It is noted that most vibration sources have small amplitudes and low peak frequencies. Figure 2-2 shows an example of the low vibrational frequency emitted from a microwave oven as studied by du Toit (2005).[9] In this example, the highest acceleration peak is around 120 Hz, a fairly low frequency, with a few higher frequency harmonics. These conditions prevent the effective operation of many piezoelectric energy harvesters.

Recently, interest in wearable devices to monitor human health is increasing. Harvesting energy from the human body for these devices is of particular interest. Most human motion and activity is characterized by large amplitudes of motion at low frequencies less than 10 Hz. These conditions lead to resonating difficulties in micro-scale devices. For example, the acceleration $a(t)$ versus time over a 24-hour period, captured by a tri-axis accelerometer mounted on the arm is plotted in Figure 2-3, where the overall magnitude of the acceleration is given by $a(t) = \sqrt{a_x(t)^2 + a_y(t)^2 + a_z(t)^2}$. This result, coupled with the fact that most human motion is not strongly tonal, may discourage the application of resonant energy harvesters for this purpose.

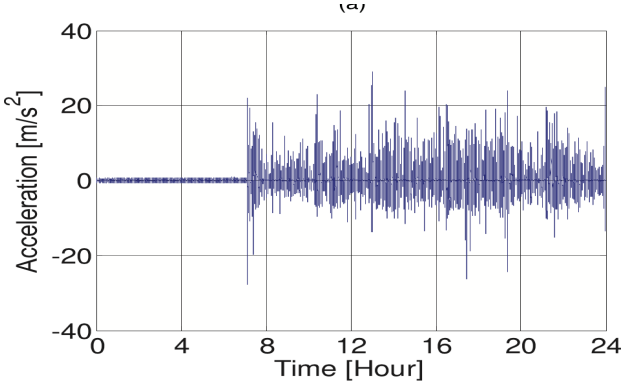

Figure 2-3. Acceleration and time plot evaluated from data using a tri-axis accelerometer with a sensing unit located on the arm for an entire day.[10]

2.1.3 Transducers for Mechanical Energy Harvesting

Three different types of electromechanical traducers are utilized to convert mechanical energy to electrical energy. Schematics of electrostatic (capacitive), electromagnetic (inductive), and piezoelectric harvesters are shown in Figure 2-4.

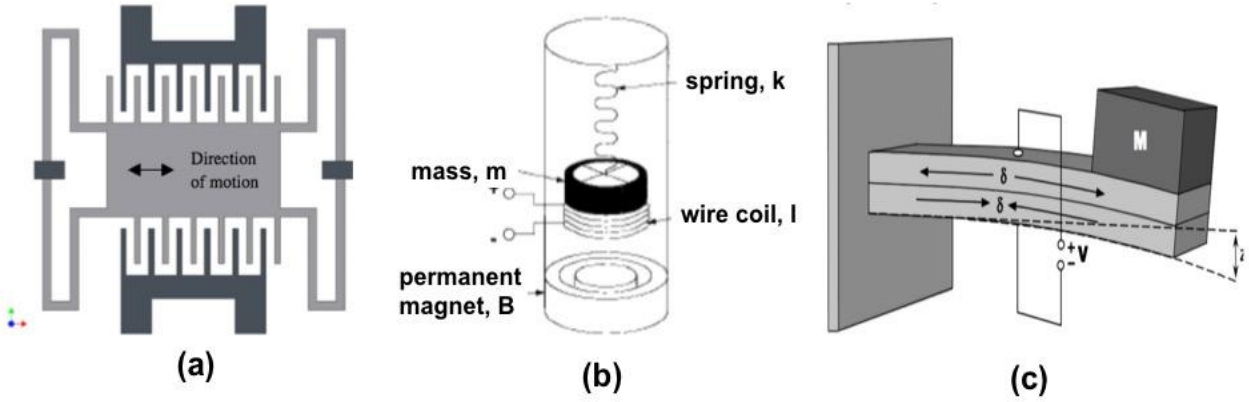

Figure 2-4. Schematic of the three types of electromechanical generators: (a) electrostatic (b) electromagnetic (c) cantilever piezoelectric. Figures from references.[3,7]

The electrostatic generator in Figure 2-4(a) consists of two conductive plates separated by

a capacitor, typically using air as the dielectric. If the distance between plates with constant charge is changed, the voltage is also modulated; this can be used to scavenge energy. Similarly, if the voltage between the plates is held constant, the charge on the electrodes depends on the distance between them.[3] Typically, as shown in Figure 2-4(a), electrostatic generators utilize a comb electrode structure to improve the power density. Also, electrostatic systems require an external voltage source to create the initial voltage or charge. In an electrostatic generator (shown in Figure 2-4(a)), mechanical movement of two oppositely charged electrodes separated by a dielectric provides electrical energy conversion. Fundamentally, the voltage on the plates is express by equation 2.9.

$$V=Q/C \qquad (2.9)$$

where Q is the charge and V is the voltage on the plate. C is the capacitance (C) is given by $C = \varepsilon_0 A/d$, where ε_0 is dielectric constant of free space [8.85×10^{-12} Fm^{-1}], A is the area of the plates in m^2 and d is the distance between the plates in m. It has two operation modes (*e.g.* voltage and charge constrained conversion). For parallel plate structures, when voltage is held constant, the decreasing of d leads to increases in the charge. When the charge is held constant, decreasing the capacitance by increasing d leads to increases in the voltage. According to the principal of an electrostatic generator, it is necessary to charge initial voltage for the conversion process to start. One primary advantage is that the electrostatic converters integrate with electronics and microsystems using MEMS technology more readily than electromagnetic converters do.

Electromagnetic generators typically generate a current in the conductive coil by the relative movement of permanent magnets or a coil, as shown in Figure 2-4(b). The open circuit voltage generated depends on the number of turns in the coil, the length of one coil, the strength of the magnetic field, and the velocity of the relative motion. Table 2-2 presents a comparison of

the power density of a variety of electromagnetic inertial energy harvesters.[11] However, the efficiency of these microscale devices is limited by their low induced voltage (180mV); this is not easily rectified by a diode for electronics, as reported by Amirtharajah et al.[2,12] Another disadvantage of the electromagnetic transducer is that it is hard to integrate with a microsystem with typical output voltage levels. This is due to the limited strength of the magnetic field and the number of turns in the coil for device sizes below 0.5~1cm^3.[2,5] Unlike electrostatic devices, electromagnetic harvesters do not require an external voltage source to extract electricity.

Table 2-2. Comparison of reported electromagnetic energy harvesters.[11]

Author	Volume [cm^3]	Proof mass [g]	Frequency [Hz]	Acceleration [G=9.8m/s^2]	Power density [μW/G^{2}cm^3]
Li[13]	1	0.22	60	2.9	11.9
Ching[14]	1	-	190	8.3	0.07
Williams[15]	0.02	0.0024	4400	39	0.014
El-hami[16]	0.24	0.5	322	10.4	20.3
Ching[17]	1		60	2.9	99
Mizuno[18]	2.1	0.54	700	1.3	0.0001
Lee[19]	7.3	0.14	85	4.4	6
Glynne-Jones[20]	0.84		322	5.4	1.5
Beeby[21]	0.06	0.44	350	0.3	507
Hung[22]	0.04	0.03	100	2	9.86
Perpetuum[23]	131		99	0.1	2685

The third type of mechanical generator is based on a piezoelectric transducer. Piezoelectric materials deform in response to an applied electrical field and produce charge or current in response to a mechanical deformation. The piezoelectric response depends upon the

orientation of the strain, electrical field, and the crystallographic axes. Unlike an electromagnetic generator, a piezoelectric generator provides the needed voltage and current levels for the electrical load circuit.[5,12] Another major advantage is that the piezoelectric films can be used in the microfabrication processes for wafer scale systems with relatively high output voltages.[2] The three families of transducers, along with their advantages and disadvantages, are summarized in Table 2-3. Though mechanical energy harvesting using electromagnetics exhibits high performance with bulk magnets and macro-scale coils in large systems, it is not suitable for integration with MEMS systems.[2,5] Piezoelectric generators show most of the advantages of electromagnetic converters. Additionally, they can be employed in MEMS systems using piezoelectric films. Thus, piezoelectric energy harvesters could be useful for portable electronics.

Table 2-3. Comparison of three types of transducers for vibration energy harvesting.[7]

Mechanism	Advantages	Disadvantages
Piezoelectric	No voltage source required Large voltage generated with simple mechanical structures depends on the film/sample thickness.	Limitation of strain level related to mechanical properties in the piezoelectric materials
Electrostatic	Precise control over the resonance	Separate external voltage source needed
Electromagnetic	No external voltage source needed	Complex design needed for microsystems

2.3 Piezoelectric Vibration Harvesting

2.3.1 Piezoelectricity

Piezoelectricity is the linear coupling between an applied stress and an induced polarization (direct effect), or an applied electric field and an induced strain (converse effect).

Among the 32 crystallographic point groups, 20 of the 21 noncentrosymmetric groups are potentially piezoelectric.[24] Piezoelectricity is symmetry-forbidden in centrosymmetric structures. Figure 2-5(a) illustrates the direct piezoelectric effect, while Figure 2-5(b) shows the converse effect.

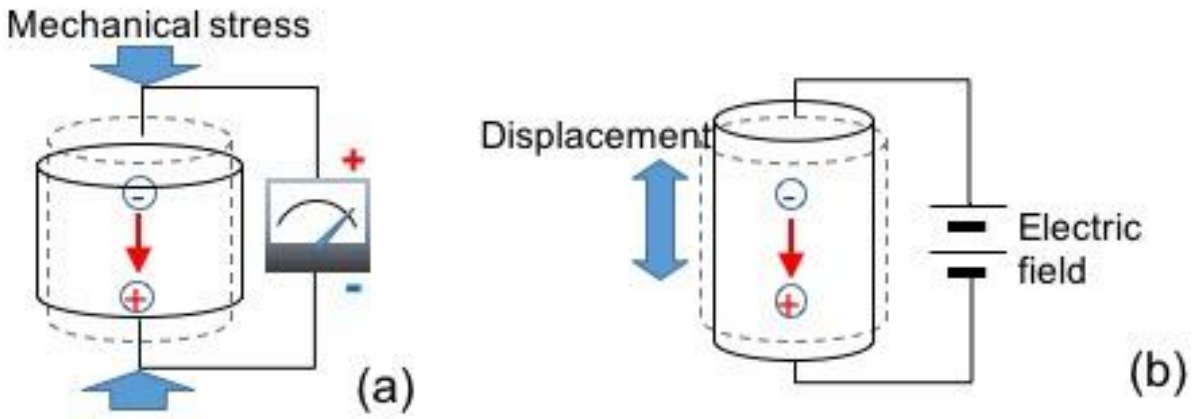

Figure 2-5. (a) Direct piezoelectric effect: a polarization is generated by an applied stress (b) the converse piezoelectric effect: a physical displacement is caused by applied electric field.

For many piezoelectric applications, Pb-containing perovskite piezoelectric (*e.g.* $Pb(Zr,Ti)O_3$ (PZT)) are used because of their high piezoelectric effect, and the ability to reorient the remanent polarization with an applied electric field, unlike wurtzite and quartz.[25] Figure 2-6 shows the ABO_3 crystal perovskite structure in its cubic prototype form (no spontaneous polarization) above the Curie temperature (T_C). Below T_C, the material distorts into a tetragonal or rhombohedral ferroelectric phases (having [001]/[111] polarization directions, respectively) over most of the phase diagram. In the tetragonal perovskite ferroelectrics (*e.g.* $PbTiO_3$), the Ti atom moves close to one of its six oxygen neighbors; this produces a spontaneous polarization directed in one of six possible directions. In rhombohedral perovskite ferroelectrics, the polarization direction favors <111> directions; this shifts the Ti atom close to three adjacent

oxygens. There are 8 possible polarization directions.

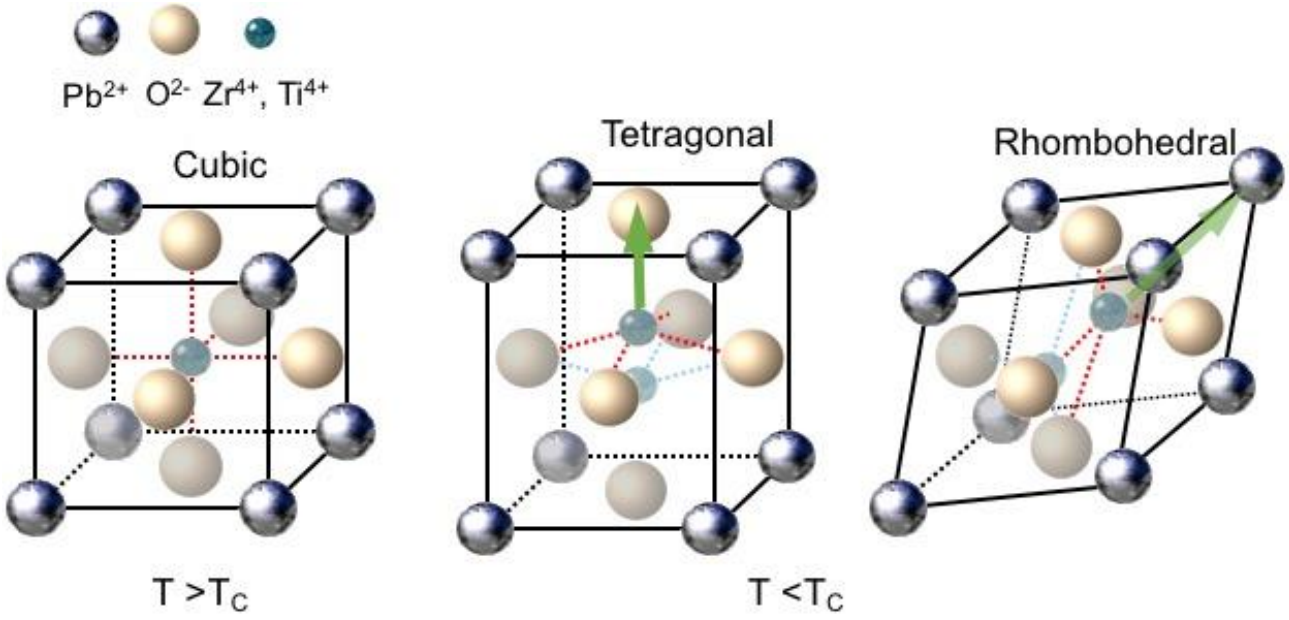

Figure 2-6. Perovskite structure.

2.3.2 Theory of Piezoelectric Vibration Energy Harvesting

Based on the linear inertial model described in section 2-2, the piezoelectric constitutive equations (relating strain (*S*) and electrical displacement (*D*), or stress (*T*) and the electric field (*E*)) can be used to derive the electromechanical coupling coefficient (*k*) and maximum output power (P_{max}). In the constitutive equations *s*, *d* and *ε,* are used for the mechanical compliance, the piezoelectric coefficient, and the dielectric permittivity. These equations are:

$$S_{ij} = d_{ijk}E_k + s^E_{ijkl}T_{kl} \qquad (2.10)$$

$$D_i = \varepsilon^T_{ij}E_j + d_{ijk}T_{jk} \qquad (2.11)$$

(using Einstein notation where *i,j,k,l* can take the values 1,2,3). The efficiency (coupling

coefficient) for a piezoelectric transducer is defined as $k_{ijk}^2 = \frac{d_{ijk}^2}{s\varepsilon}$.

For a linear transducer, when AC power signal is naturally sinusoidal, maximum extracted power (P_{max}) can be expressed

$$P_{max} = \lambda_{max}\omega U_{in} \qquad (2.12)$$

where ω is the circular frequency of driving vibration U_{in} is the input energy and λ_{max} is the maximum transmission coefficient ($\lambda_{max} = \frac{U_{max}}{U_{in}}$). Based on the linear transducer relationship of the output variables *D* and *S* in Figure 2-7, *D*' is the value of the through variable when S is constrained to be zero, and vice versa. When *D* = *D'*/2 and *S*=*S'*/2, the maximum output energy can be expressed by

$$U_{max} = 1/4D'E' \qquad (2\text{-}13)$$

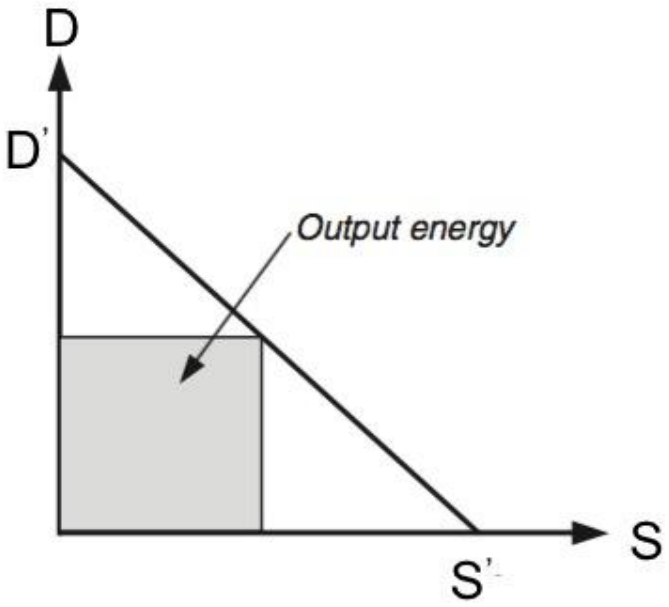

Figure 2-7. Relationship of the output variables *D* and *S* for piezoelectric transducer
If *D* is zero, *E*' is given by equation (2.11)

$$E' = -\frac{d}{\varepsilon}T \tag{2.14}$$

From equations 2.10 and 2.11,

$$\frac{1}{2}D' = dT + \frac{1}{2}\varepsilon E' \tag{2.15}$$

Substituting equation 2.14 into 2.15 into equation 2.13 yields:

$$U_{max} = -\frac{1}{4}\frac{d^2}{\varepsilon}T^2 \tag{2.16}$$

From a standard two-port model of a linear piezoelectric transducer, the maximum transmission coefficient can be expressed by:[26]

$$\lambda_{max} = \frac{d^2}{4s\varepsilon - 2d^2} \tag{2.17}$$

From equation 2.17, the maximum transmission coefficient can be simplified by use of the coupling coefficient ($k^2 = \frac{d^2}{s\varepsilon} = \frac{d^2E}{\varepsilon}$), where E is the elastic (Young's) modulus.

$$\lambda_{max} = \frac{k^2}{4 - 2k^2} \tag{2.18}$$

In the piezoelectric system, the input energy density (u_{in}) is given in terms of the stress (T)

$$u_{in} = (1 - \frac{k^2}{2})\frac{T^2}{E} \tag{2.19}$$

When an AC force of magnitude $|F| = mQA$ is applied to the piezoelectric transducer, the stress in the piezoelectric can be written as $T = |F|/a_p$, where Q is the total quality factor of the resonator and a_p is the cross-sectional area of the piezoelectric element.

$$u_{in} = (1 - \frac{k^2}{2})\frac{(mQA)^2}{Ea_p^2} \tag{2.20}$$

The spring stiffness can be expressed as

$$k_s = \frac{Ea_p}{h} \tag{2.21}$$

where h is the height of the piezoelectric element. Based on equation 2.21, the elastic modulus can be written as $E = \omega_n^2 hm/a_p$. Thus, the input energy ($U_{in} = ha_p u_{in}$) is given by the following expression:

$$U_{in} = (1 - \frac{k^2}{2}) \frac{(QA)^2 m}{\omega_n^2} \quad (2.22)$$

Substituting equation 2.22 and 2.18 into equation 2.12 yields the maximum extracted power from a vibration source using a cantilever structure with a piezoelectric material at resonance (ω_n).[26,27]

$$P_{max} = \frac{k^2 m Q^2 A^2}{4\omega_n} \quad (2.23)$$

Piezoelectric thin films for MEMS scale energy harvesters is governed by the $e_{31,f}$ coefficient for films polarized out of plane with top and bottom planar electrodes. In the case of the 31 mode, the coupling coefficient of piezoelectric films is given by $k_{31}^2 = d_{31}^2 / (s_{11}\varepsilon_{33})$. The $e_{31,f}$ is $d_{31} / (s_{11} + s_{12})$ under the condition of zero strain (but finite stresses) in the plane of the film, while being stress free out-of-the-plane.[28] Thus, output power can be expressed as equation 2.24 including material terms, where v is Poisson's ratio.

$$Power_{max} = \frac{m}{4\omega} (\frac{e_{31,f}^2}{\varepsilon_r \varepsilon_0} \cdot \frac{(1-v)^2}{E}) Q^2 A^2 \quad (2.24)$$

If most of the device volume is occupied by the substrate, the effective mechanical properties of the device are governed by the substrate stiffness.[29] In this case, the output power relies on piezoelectric material properties such as the piezoelectric coefficient and dielectric permittivity. Thus, the figure of merit for energy harvesting in thin film piezoelectric cantilevers is expressed by:[27,30,31]

$$FoM = \frac{e_{31,f}^2}{\varepsilon_r} \quad (2.25)$$

The term $(e_{31,f})^2/\varepsilon_r$ is used to compare the FoM between materials, especially for thin films proposed for MEMS piezoelectric energy harvesters.

Additionally, since the performance of the piezoelectric harvester is governed by the dielectric loss tangent (tanδ). The tanδ of the piezoelectric material should be low for use in energy harvesters. In the off-resonance condition for a 31 mode, the figure of merit (FoM_{off}) for piezoelectric energy harvester can be expressed by the following equation: $FoM_{off} = d_{31} \times g_{31} / tan\delta$ (effective piezoelectric voltage constant, g).[32]

Two main approaches have been widely studied to improve the efficiency of power conversion from mechanical stress/strain to electric field/current: selection of the piezoelectric material and the mechanical design of the harvester.

2.4 Consideration of Piezoelectric Material and Substrate

2.4.1 Materials for Piezoelectric MEMS Harvesting

As was shown in the previous section, the piezoelectric coefficient and dielectric constant are key parameters that influence the performance of piezoelectric energy harvester. Piezoelectric single crystals, ceramics, thick and thin films, and polymers such as poly vinylidene fluoride (PVDF) have all been explored for energy harvesting for piezoelectric energy harvesters.[3,4, 33]

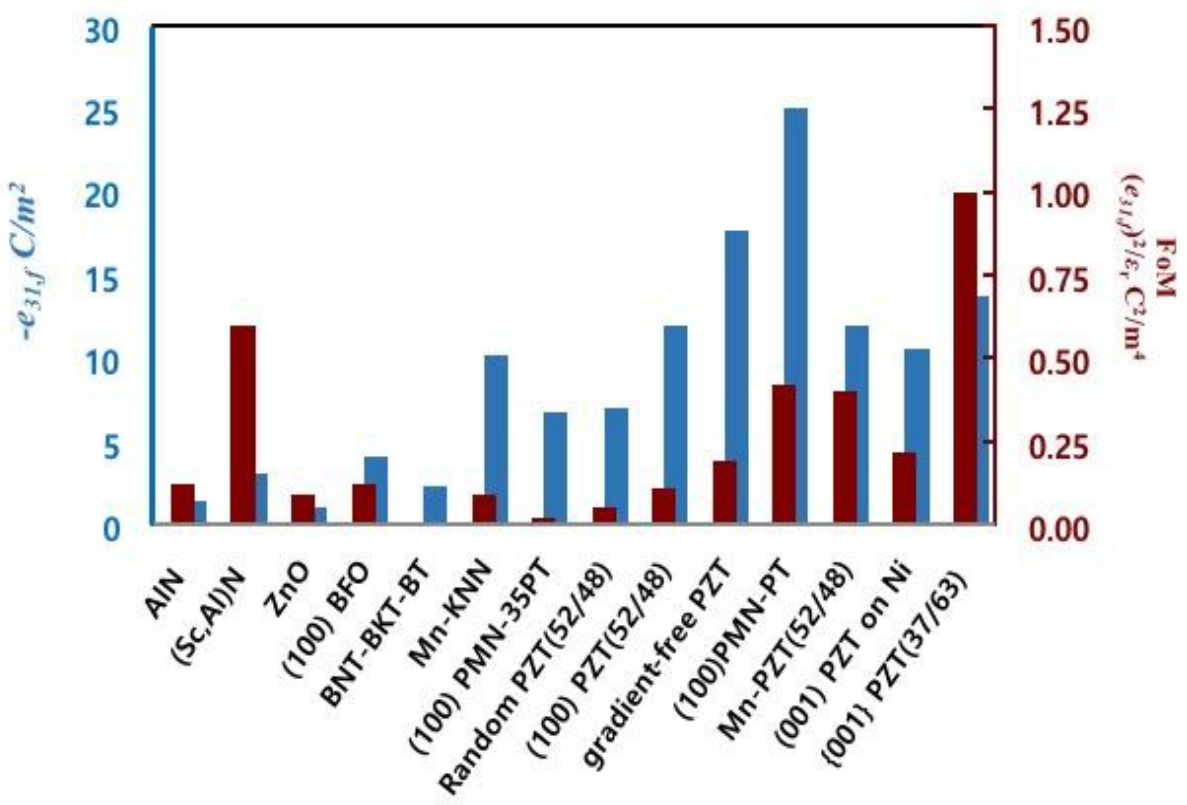

Figure 2-8. Comparison of $e_{31,f}$ and FoM of piezoelectric films for MEMS energy harvesting with different orientations on various substrates.[34~43] [data from: left AlN, $(Sc_{0.41}Al_{0.59})N$ ((Sc,Al)N), ZnO, (100) $BiFeO_3$ on $SrTiO_3$ ((100)BFO), epitaxial $Bi_{0.5}Na_{0.5}TiO_3$-$Bi_{0.5}K_{0.5}TiO_3$-$BaTiO_3$ (BNT-BKT-BT), 0.5 mol% Mn-doped $(K_{0.5}Na_{0.5})NbO_3$ (Mn-KNN), (100) $0.65Pb(Mg_{0.33}Nb_{0.67})$-$0.35PbTiO_3$ ((100)PMN-35PT), random $Pb(Zr_{0.52},Ti_{0.48})O_3$, (Random PZT(52/48)), (100) $Pb(Zr_{0.52},Ti_{0.48})O_3$ on Si ((100)PZT(52/48)), gradient-free (100) $Pb(Zr,Ti)O_3$ on Si (gradient-free PZT), epitaxial (100) $0.67Pb(Mg_{0.33}Nb_{0.67})$-$0.33PbTiO_3$ on $SrRuO_3/SrTiO_3/Si$ ((100) (100)PMN-PT, (001) $Pb(Zr_{0.52},Ti_{0.48})O_3$ on Ni foil ((001) PZT on Ni). Epitaxial (001) $Pb(Zr_{0.52},Ti_{0.48})O_3$ on (100) MgO with 1 mol% Mn (Mn-PZT(PZ/48)), {001} $Pb(Zr_{0.37},Ti_{0.63})O_3$ on CaF_2 substrate ({001} PZT(37/63)))

Figure 2-8 shows a comparison of reported piezoelectric constants and FoM ($(e_{31,f})^2/\varepsilon_r$) for a variety of thin films for 31 mode MEMS energy harvesters.[34,35] Two major groups are apparent (*e.g.* non-ferroelectric: ZnO, AlN; ferroelectric: (K,Na)NbO_3 (KNN), $BiFeO_3$, Pb(Zr,Ti)O_3). Among the nonferroelectric piezoelectric materials, AlN has a large FoM due to low dielectric constant in spite of its modest piezoelectric coefficient.[36,37]

In recent works, Al substitution by Sc enhances of piezoelectric coefficient (e_{33}) by decreasing the stiffness (c_{33}), which leads to increase the longitudinal piezoelectric coefficient ($d_{33,f} = e_{33}/c_{33}$).[38] Akiyama et al. reported that the figure of merit of $Sc_{0.41}Al_{0.59}N$ is 5 times higher than that of undoped AlN, in part, due to the fact that the transverse piezoelectric coefficient ($e_{31,f}$) was also enhanced with decreasing the elastic modulus.[39]

Many researchers have reported improvements in the energy harvesting figure of merit of ferroelectric materials such as PZT, KNN, and $BiFeO_3$ through control of composition (MPB), orientation control (texturing), reducing compositional gradients, doping, control of residual stresses, and introduction of strong levels of imprint.[27,30,31,40,42~46] It has been shown through the research of Jaffe et al. that the Zr/Zr+Ti ratio is a major factor in determining the properties of lead zirconate titantate.[47] The composition of $Pb(Zr_{0.52}Ti_{0.48})O_3$, which corresponds to the MPB, – the nearly temperature independent boundary between rhombohedral and tetragonal phases of PZT, is known to exhibit enhanced dielectric and piezoelectric coefficients. For a given composition, the crystallographic orientation and domain state also influence the magnitude of the remanent polarization and the piezoelectric response. These two factors may be governed by various factors such as the thermal expansion coefficient of the substrates, templating from a seed layer (e.g. $PbTiO_3$), or an orienting bottom oxide (e.g. $LaNiO_3$, $SrRuO_3$) electrode, and optimized nucleation conditions (Pt(111)/Ti/TiO_2).[27,31,42,43,47~50]

Recently, Yeager et al., demonstrated that dependence of FoM on *c*-domain volume fraction (f_{001}) and x=Zr/(Ti+Zr) with tetragonal PZT films grown on CaF_2, MgO, $SrTiO_3$, or Si substrates.[27,43] It was noted that a superior FoM (0.8~1.0 C^2/m^4) was exhibited for *c*-axis PZT films with f_{001}>95%.[42]

Also, reducing the compositional gradient, and increasing the process-induced imprint in the film are critical means to ameliorate the figure of merit for energy harvesting.[30,42,51] As described by Ledermann, the transverse piezoelectric coefficient is significantly influenced by the existence of any gradients in the Zr/Zr+Ti ratio produced in the PZT film during crystallization.[31] Gradient-free (100) textured films on Si exhibited nearly uniform Zr/Zr+Ti ratios (±2.5%) at the MPB with superior $e_{31,f}$ (-17.7 C/m^2) and dielectric constant (1620) as compared to the Zr/Zr+Ti gradient (±12%) PZT film.[42] Another means to enhance the figure of merit is a strong level of imprint. Imprint is a manifestation of the built in internal field, and can be quantified by a shift of the P-E hysteresis loop along the field axis. The internal field tends to increase the remanent polarization, while suppressing the dielectric permittivity. These useful features certainly contribute to an improved figure of merit. Recently, PMN-PT films were reported with an extremely high piezoelectric coefficient, combined with suppressed permittivity caused by the high levels of imprint.[30]

Because mechanical harvesters produce AC current outputs, it is essential to rectify the output. This, in turn, imposes additional constraints. Efficient rectification is possible only when the device generates a voltage that is high enough, but not so high that a buck converter is required. For a MEMS harvester, the first of these conditions is often the most problematic. Decreasing the permittivity is helpful, as the output voltage is inversely proportional to the permittivity.

2.4.2 Effect of Stress Induced by Substrate

The piezoelectric and dielectric responses of mono-domain PZT are anisotropic, and so depend on film orientation and on the electrode type (e.g. interdigitated, parallel plate) related to the possible domain states with respect to the electric field.[52] In particular, the type and level of stress caused by the difference in the thermal expansion coefficients of films and substrate influence the domain orientation.

When a thin-film material is mechanically constrained to a substrate, the total stress present consists of three terms (intrinsic stress, extrinsic stress, and thermal stress) and can be written in the following form:

$$\sigma_{tot}(T) = \sigma_{th} + \sigma_i + \sigma_e \qquad (2.26)$$

Intrinsic stress (σ_i) is determined by deposition parameters.

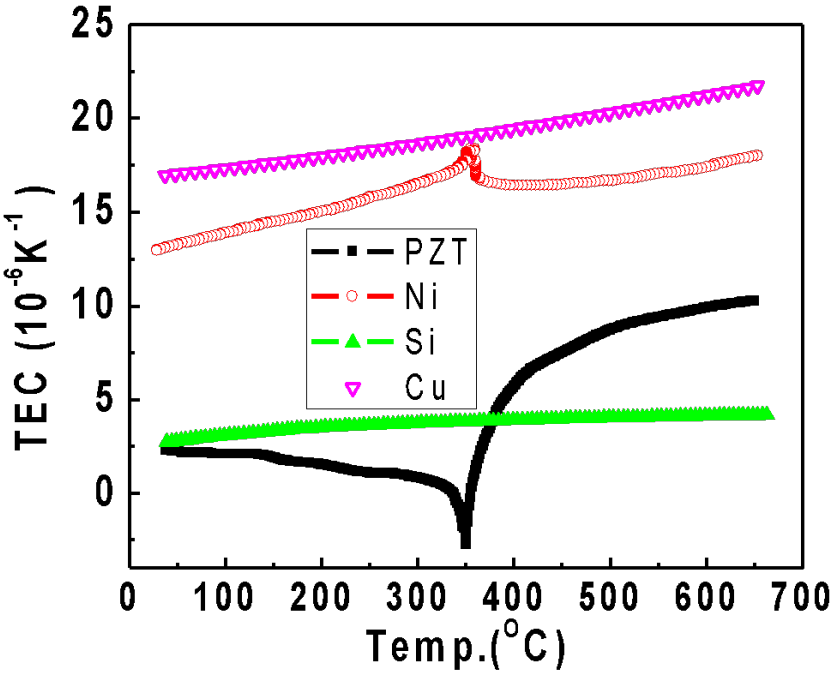

Figure 2-9. Thermal expansion of PZT, Si, Cu, and Ni in the temperature range between crystallization temperature of PZT and room temperature for the residual stress calculation.[53~55]

The extrinsic stress (σ_e) arises from the dimensional changes as the material undergoes either crystallization of the amorphous phase or a phase transition. The most important contribution of film stress in thick films is the thermal stress (σ_{th}) due to the thermal expansion mismatch between substrate and film. Thermal stresses due to cooling from the crystallization temperature (T_{growth}) to room temperature (T_{RT}) can be expressed as:

$$\sigma_{th} = (\alpha_f - \alpha_s)\frac{E_f}{1-v_f}(T_{growth} - T_{RT}) \qquad (2.27)$$

α_f and α_s are the thermal expansion coefficients of the film and substrate. E_f and v_f are the Young's modulus and Poisson's ratio of thin film, respectively.

Especially, the thermal stress/strain generated during cooling from the growth (or crystallization) temperature to the Curie temperature is directly correlated with the volume fractions of *c*- and *a*-domains in a tetragonal film; for a *c*-domain, the spontaneous polarization is aligned *out-of-plane* and for an *a*-domain, the spontaneous polarization is aligned *in-plane*. Below the cubic to tetragonal transition, the volume fraction of *c*- and *a*-domains influence the thermal stress, because partial stress relief occurs at the Curie temperature as favorable domain orientations develop. Figure 2-9 shows the nonlinear thermal expansion coefficient (TEC) of PZT, Si and Ni respectively as a function of temperature; these values were used to calculate the thermal stress and strain in Refs.[52~54] The thermal strain (ξ_{th}) that develops during cooling from T_{growth} to T_C is given by:

$$\xi_{th} = (\alpha_f - \alpha_s)(T_{growth} - T_C) \qquad (2.28)$$

Figure 2-10 illustrates the domain response to different stress types in the film. When the ferroelectric film is under tensile stress, *a*-domain development is preferred to *c*-domain. Conversely, *c*-domain structures are preferred for compressive stress. This phenomenon allows the film-substrate thermal expansion mismatch to govern the domain state at T_C.

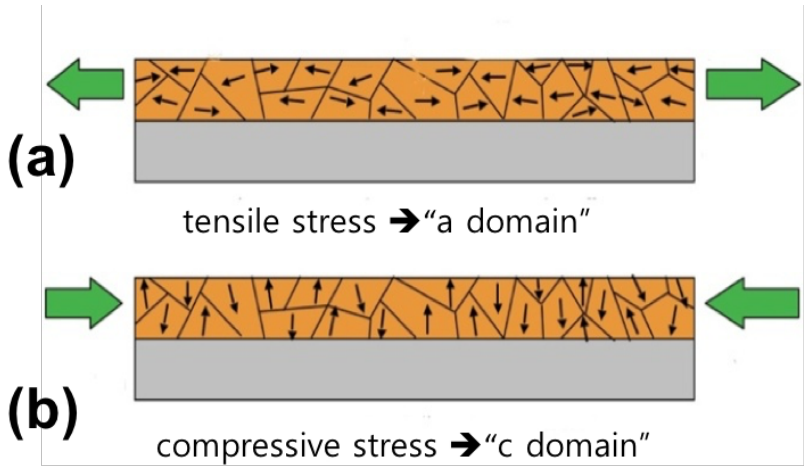

Figure 2-10. Illustration of domain structure in the film under (a) tensile stress (b) compressive stress, in the cases where the stresses are controlled by thermal expansion mismatch.[56]

For example, when the substrate thermal expansion coefficient is larger than that of the PZT film, it causes compressive stress in film and preferred *c*-axis orientation, as shown in Figure 2-10(b). In contrast, substrates with low thermal expansion coefficient, such as Si, induce tensile stresses in the PZT film and preferred *a*-domain states. The resulting domain structure affects the film properties such as dielectric constant and remanent polarization.[27,57~59]

Figure 2-11 shows the dielectric constant of PZT films as a function of calculated thermal strain. Yeager et al. demonstrated experimentally that the dielectric constant of (001) $Pb(Zr_{0.48},Ti_{0.52})O_3$ film (PZT 48/52, blue diamonds) is a function of thermal strain by growing PZT films on three different substrates (*e.g.* silicon, $SrTiO_3$, MgO).[27]

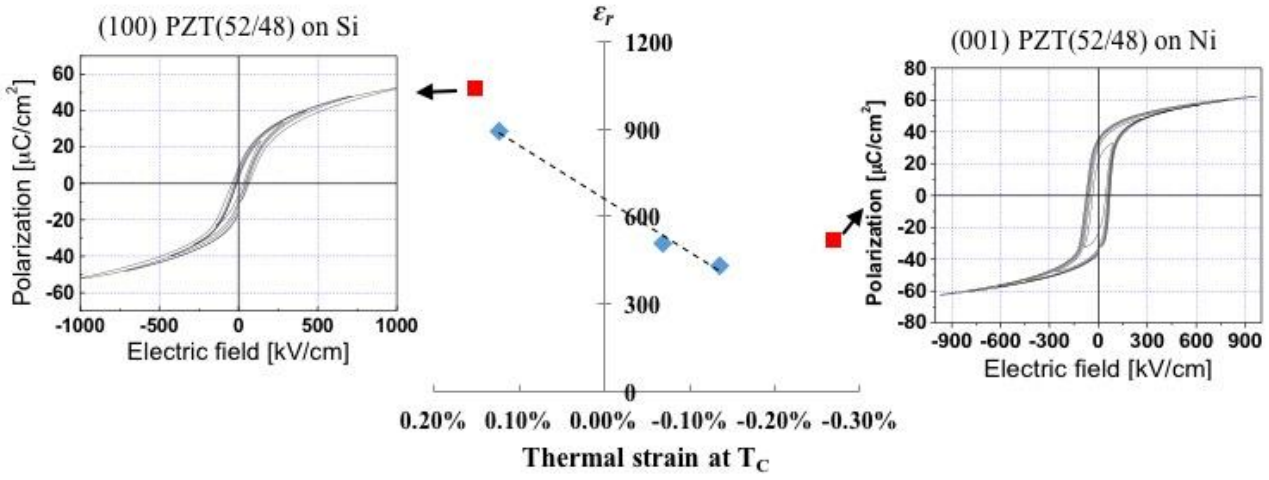

Figure 2-11. Effect of thermal strain on the dielectric constant (blue diamond[27]: PZT 48/52, red cubic[59]: PZT 52/48) and PE hysteresis loops in the PZT 52/48 films.[59]

PZT films under compression (grown using substrates with large thermal expansion coefficients) have lower dielectric constants due to a large volume fraction of *c*-domains. Yeo et al. also confirmed that a lower dielectric constant is obtained in the PZT (52/48) film under compressive stress on Ni substrates.[59] As a result, (001) PZT films on Ni have larger remanent polarizations than those on (100) PZT on Si due to the differences in the volume fraction of *a* and *c*-domains caused by the thermal stress.[59]

2.5 Selection of Design and Configuration of Piezoelectric Harvester

2.5.1 Option of Piezoelectric Configuration

The relative direction of the applied strain/stress from the environment and the electrical polarization plays another important role in the performance of micro-scale vibration energy harvesters using piezoelectric thin films. There are two configuration options, 31 mode and 33 mode, for piezoelectric microdevices.

Figure 2-12 exhibits the relationship between the direction of the applied stress and the poling direction in a PZT layer. In the 31 mode, the film has top and bottom electrodes. In this case, the poling direction, which is typically referred to as the "3" direction, is perpendicular to the direction of in-plane ("1" direction) of the applied strain: On the other hand, for the 33 mode, interdigitated electrodes (IDE) are utilized. In this case, the poling direction and the strain are both in-plane, as shown in Figure 2-12(b).[2,60,61]

For a 31 mode energy harvester with top and bottom electrodes (TBEs) the generated open voltage (V_{OC}) is determined by the thickness of the piezoelectric layer (t_{xx}), the effective piezoelectric constant, $g_{31,f}$ (Vm/N) and the applied stress.[2]

$$V_{OC} = \sigma_x g_{31,f} t_{xx} \qquad (2.29)$$

In the case of the 33 mode, t_{xx} represents the spacing between the interdigitated electrodes.

In general, the longitudinal piezoelectric coefficient $e_{33,f}$ is about 2 times higher than $|e_{31,f}|$.[35] Moreover, the open-circuit voltage can be easily increased by increasing the electrode spacing, and is thus relatively unaffected by the thickness of the piezoelectric layer.

However, there are some disadvantages to the 33 mode. First of all, finite element modeling demonstrates that the piezoelectric material under the electrodes is not active.[60] This means that the electrode width should be minimized, within the constraints imposed by the need for effective poling. Furthermore, the electric field is not uniform through the thickness of the piezoelectric layer.[60,62~64] Thus, design of IDE electrode systems requires optimization of variables such as the electrode and piezoelectric layer dimensions.[64]

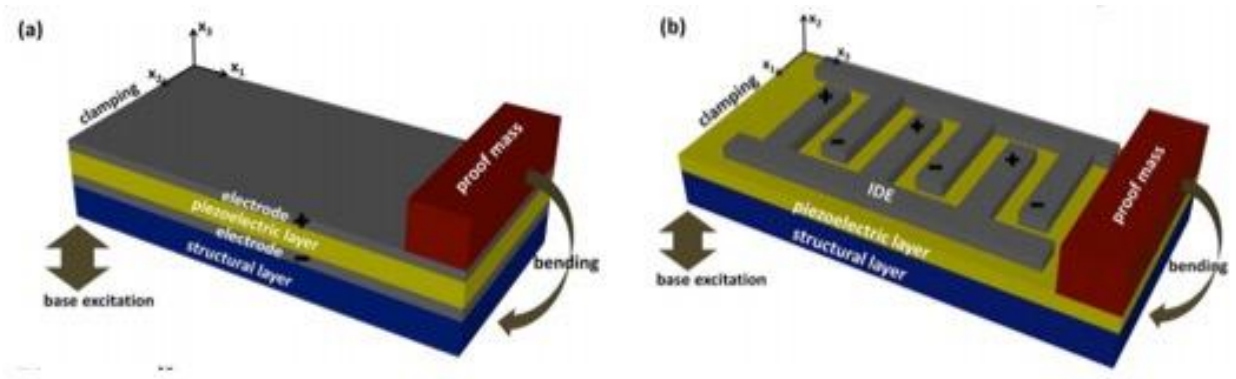

Figure 2-12. Cantilever piezoelectric energy harvesters with proof masses (a) 31 mode device using top and bottom electrodes (TBEs) (b) 33 mode device using interdigitated electrodes (IDE).[64]

In contrast, foe typical excitation levels, the generated voltage of a 31 mode energy harvester is typically too low for simple rectification circuits, when the thickness of the PZT layer is less than 0.5 μm. However, with the use of TBEs, increase PZT thickness produces higher voltages, and yields higher currents than 33 mode devices. Thus, the selection of electrode configuration for energy harvesting should take into account not only anisotropy in the dielectric and piezoelectric properties associated with the domain configuration, but also the film thickness.

2.5.2 Unimorph and Bimorph Structure

Three configurations of piezoelectric energy harvesters are shown in Figure 2-13.[65] In general, they can be prepared with piezoelectrics on one or both sides of the elastic layer for unimorph or bimorph configurations, respectively.

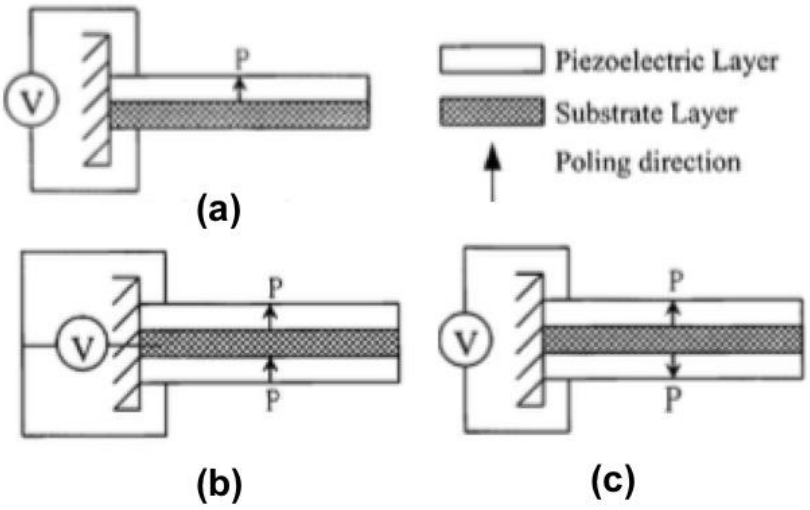

Figure 2-13. (a) Unimorph configuration and (b) bimorph configuration in parallel connection and (c) bimorph configuration in series conection.[65]

Two types of bimorphs can be distinguished based on the electrical connection of the piezoelectric elements: series or parallel connection. During bending, the two PZT layers undergo stresses of the opposite sign (*e.g.* the top layer is in compression whereas the bottom layer is in tension). As a consequence, for the parallel configuration shown in Figure 2-13(b), the two piezoceramic layers should be poled in the same direction. Likewise, Figure 2-13(c) represents the series connection of the bimorph structure with the piezoceramic layers poled in the opposite directions along the thickness. In this case, on bending, the two piezoelectric layers induced the same direction of electric field.[66]

The series connection yields twice the output voltage from the bimorph piezoelectric layer relative to the parallel connection.[67] One of the merits of the bimorph structure is that high power density can be obtained even when the given working area is limited. However, in the arena of MEMS, bimorph structures are hard to achieve by microfabrication processing.[2]

2.5.3 Linear Piezoelectric Energy Harvester

Linear (resonant based) piezoelectric generators are a simple approach for mechanical energy harvesting. These linear piezoelectric harvesters generate maximum power when the frequency of the device matches the ambient frequency, as described in section 2.2. Common configurations are cantilever beams, as bending of the cantilever provides high strain; additional mass can be used to tune the resonant frequency (Figure 2-14).

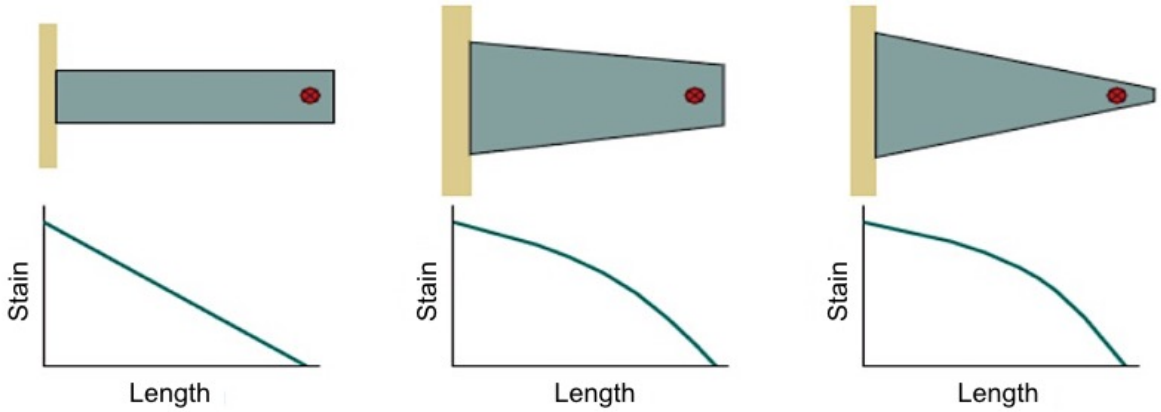

Figure 2-14. Three types of cantilever beams for piezoelectric energy harvesters and strain distribution along the beam.[68]

Rectangular cantilever beams generally suffer from excessively high strains near the clamping point. The strain dramatically decreases in magnitude with distance away from the clamp. On the other hand, trapezoidal beam shapes improve the strain distribution along the length, and so help to prevent overstrain at higher excitation.[69,70] Dhakar et al. proposed a new design using a bimorph piezoelectric cantilever connected to a polymer cantilever to improve the strain distribution along the beam for resonant based energy harvester operated at a low frequency.[71]

2.5.4 Nonlinear Energy Harvesting

In contrast to linear oscillators, which typically have a narrowband response which decays rapidly if excited off their resonance frequency, nonlinear oscillators provide broadband performance. In general, nonlinear energy harvesting uses Duffing (hysteretic resonance), frequency up conversion or bistable oscillator designs using magnetic force and special mechanical structures.

iv) Duffing resonance (nonlinear hysteretic) resonance

Duffing oscillators are characterized by either softening (when the force decreases with the tip deflection) or hardening (when the force increase with the tip deflection) of the system stiffness.[71] Near the resonance frequency, i.e., $\Omega \approx \omega_n$ the result of hardening/softening is a broad resonance peak with three branches: (the large resonant branch, B_r; the nonresonant branch, B_n; and the unstable branch (dashed lines) as shown in Figure 2-15. When δ is negative i.e. softening nonlinearity, the deflection follows the nonresonant branch up to the saddle-node ($s.n$) point as the excitation frequency is increased toward ω_n. Then it shifts up to the resonant branch along the dashed line and follows the upper branch on increasing frequency. On the other hand, when the excitation frequency is decreased toward resonance, the behavior follows the upper branch up to the higher $s.n$ point and then falls down to the lower branch B_n.

For instance, Hajati et al. demonstrated a MEMS piezoelectric bridge Duffing oscillator with a central proof mass. This device achieved a wide bandwidth due to nonlinearites in the stiffness caused by a net stretching with increasing acceleration amplitude.[74] Leland et al. demonstrated that compressive axial stress in the bimorph PZT ceramic beam using a small steel vise for holding and micrometer drive for loading reduces the transverse stiffness, and tuned

resonance frequency.[73]

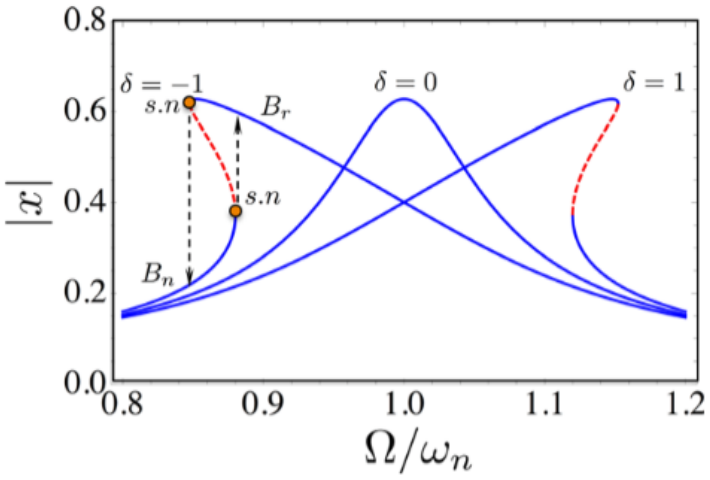

Figure 2-15. Frequency response of an oscillator with stiffness nonlinearity.[72] ($|x|$ is the steady-state amplitude, Ω is the input excitation frequency, ω_n is the resonant frequency of the system and δ is the coefficient of the cubic nonlinearity.

v) Frequency up conversion

Frequency up conversion is a good strategy to excite a high frequency piezoelectric transducer from a low frequency vibration output. In such as device, a large acceleration induced in a low frequency resonator is transferred to a high frequency resonator through a catch-and-release or plucking mechanism. The high frequency output is produced by the piezoelectric elements. The main advantage of this method is that allows more efficient scavenging from low frequency mechanical energy. Pillatsch et al., suggested a rotational piezoelectric beam-plucking energy harvester with a magnet mass in frequency up conversion for wearable applications.[74] The maximum output power of this device was 7 μW during running, though the performance was reported to degrade quickly on operation.[75]

vi) Bistable oscillator

Nonlinear bistable oscillators typically use different permanent magnet configurations to induce a magnetoelastic oscillation in a piezoelectric material with a widened bandwidth of resonance frequency. Bistable behavior occurs when there are two shallow potential wells. For a small stroke per forcing period, the device oscillates within one well. When the force is increased, the oscillator can be excited over the saddle point to oscillate between wells, as depicted in Figure 2-16.[76]

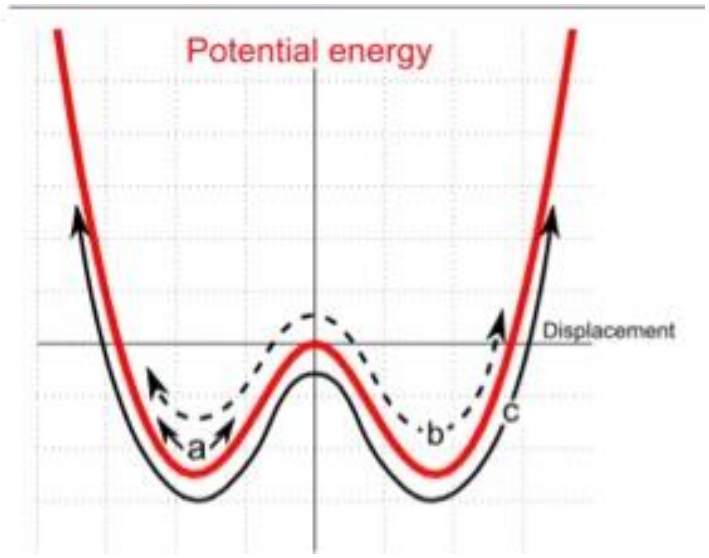

Figure 2-16. Potential as a function of position for a bistable resonator (a) intrawell oscillations, (b) chaotic interwell vibrations and (c) interwell oscillation.[76]

Figure 2-17 shows the concept of a bistable piezoelectric energy harvester with a permanent magnet attached to the tip of the cantilever beam (or on an adjacent platform) designed to induce repulsive or attractive magnetic forces, respectively. Under base excitation, as indicated by the black arrow, a repulsive magnetic force switches the cantilever beam between two stable states at a critical distance (d_r) between beam tip and external magnets in Figure 2-17(a). Figure 2-17(b) shows bistable harvester using attraction force by two separated magnets positioned at two stable

states.

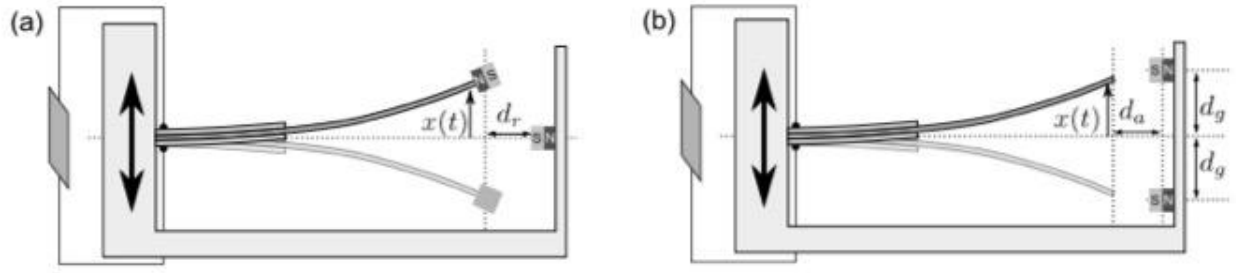

Figure 2-17. (a) Bistable cantilever type of resonator using magnetic repulsion and (b) magnetic attraction.[76]

2.6 Literature Review of Piezoelectric Thin Films on Metal Substrate (Foils)

Many types of MEMS piezoelectric energy harvester are fabricated using Si-based micro-processing. However, Si-based MEMS energy harvesters face mechanical challenges such as weak fracture strength or rigidity. In contrast, base metal substrates, especially foils, are attractive for MEMS piezoelectric harvesters due to their small stiffness and high fracture strength.[77] In this case, the metal foil can be used as the mechanical elastic layer.

Secondly, the large thermal expansion coefficient of metals such as copper, nickel or stainless steel (as compared with that of PZT) produces compressive stress in-plane during cooling down from crystallization temperature to the Curie temperature. As described earlier, compressive stress in the PZT films can be used to reduce the permittivity and enhance the figure of merit for energy harvesting.

Additionally, metal foils are easily cut to shape. However, one challenge in the growth of oxide films such as PZT on metal foils is the thermodynamic incompatibility between the metal substrate and the oxide film. Several reports have been published regarding PZT films coated onto base metal substrates with buffer layers ($LaNiO_3$, Pt) by sputtering or CSD, particularly in

the case where crystallization was conducted at low oxygen partial pressures.[78,79] Other papers have demonstrated PZT film transfer from oxide substrates to flexible metal foil using a laser lift-off process.[80,81]

However, there are limited papers reporting fabrication of highly (001) oriented PZT films on base metal substrates. Such films should show large piezoelectric coefficients and low dielectric permittivities, allowing for better FoM.

2.7 References

[1] S. Priya, "Advances in energy harvesting using low profile piezoelectric transducers," *Journal of Electroceramics* **19** (2007) 165.

[2] S.-G. Kim, S. Priya, and I. Kanno, "Piezoelectric MEMS for energy harvesting," *MRS Bulletin* **37** (2012) 1039.

[3] S. P. Beeby, M. J. Tudor, and N. M. White, "Energy harvesting vibration sources for microsystems applications," *Measurement Science and Technology* **17** (2006) R175.

[4] K. A. Cook-Chennault, N. Thambi and A. M. Sastry, "Powering MEMS portable devices-a review of non-regenerative and regenerative power supply systems with special emphasis on piezoelectric energy harvesting systems," *Smart Materials and Structures* **17**, 4 (2008) 043001.

[5] S. J. Roundy, "Energy scavenging for wireless sensor node with a force on vibration to electricity conversion," *Ph. D thesis* (2003) The University of California, Berkeley.

[6] C. B. Williams, and R. B. Yates, "Analysis of a micro-electric generator for microsystems," *Sensors Actuators A* **52** (1996) 8.

[7] S. Roundy, P. K. Wright, and J. Rabaey, "A study of low level vibrations as a power source for

wireless sensor nodes," *Computer Communications* **26** (2003) 1131.

[8] N. Dutoit, B. Wardle, and S.-G. Kim, "Design considerations for MEMS-scale piezoelectric mechanical vibration energy harvesters," *Integrated Ferroelectrics* **71**, 1 (2005) 121.

[9] N. E. du Toit, "Modeling and design of a MEMS piezoelectric vibration energy harvester," *Ph. D Thesis* Massachusetts Institute of Technology (2005).

[10] J. Yun, S. N. Reynolds, M. S. Reynolds, G. D. Abowed, "Design and performance of an optimal inertial power harvester for human-powered devices," IEEE Transactions on Mobile Computing, **10**, 5 (2011) 669.

[11] P. D. Mitcheson, E. M. Yeatman, G. K. Rao, A. S. Homes, and T. C. Green, "Energy harvesting from human and machine motion for wireless electronic devices," *Proceedings of the IEEE* **96**, 9 (2008) 1457.

[12] R. Amirtharajah, and A. P. Chandrakasan, "Self-powered signal processing using vibration-based power generation," *IEEE Journal of Solid-State Circuits* **33**, 5 (1998) 687.

[13] W. J. Li, T. C. H. Ho, G. M. H. Chan, P. H. W. Leong, H. Y. Wong, "Infrared signal transmission by a laser-micromachined vibration-induced power generator," *Proc. 43rd IEEE Midwest Symp. Circuits Syst. 2000*, vol. 1, 2000-Aug pp. 236.

[14] N. N. H. Ching, G. M. H. Chan, W. J. Li, H. Y. Wong, P. H. W. Leong, "PCB integrated micro-generator for wireless systems," *Proc. Int. Symp. Smart Struct*. 2000-Oct pp 19.

[15] C. B. Williams, S. Shearwood, M. A. Harradine, P. H. Mellor, T. S. Birch, R. B. Yates, "Development of an electromagnetic micro-generator," *Proc. Inst. Elect. Eng. Circuits Devices Syst.*, vol. 148, no. 6, Dec. 2001 pp. 337.

[16] M. El-hami, P. Glynne-Jones, N. M. White, N. Hill, S. Beeby, E. James, A. D. Brown, J. N. Ross, "Design and fabrication of a new vibration-based electromechanical power generator,"

Sensors Actuators A Physical **92**, 1 (2001) 335.

[17] N. N. H. Ching, H. Y. Wong, W. J. Li, P. H. W. Leong, Z. Wen, "A laser-micromachined multi-modal resonating power transducer for wireless sensing systems," *Sensors Actuators A Physical* **97** (2002) 685.

[18] M. Mizuno, D. G. Chetwynd, "Investigation of a resonance microgenerator", *Journal of Micromechanics and Microengineering* **13**, 2 (2003) 209.

[19] J. M. H. Lee, S. C. Yuen, W. J. Li, P. H. W. Leong, "Development of an AA size energy transducer with micro resonators," *Proc. Int. Symp. Circuits Syst.,* vol. 4, 2003-May pp. 876.

[20] P. Glynne-Jones, M. J. Tudor, S. P. Beeby, N. M. White, "An electromagnetic vibration-powered generator for intelligent sensor systems," *Sensors Actuators A Physical* **110** (2004) 344.

[21] S. P. Beeby, M. J. Tudor, R. N. Torah, E. Koukharenko, S. Roberts, T. O'Donnell, S. Roy, "Macro and micro scale electromagnetic kinetic energy harvesting generators," DTIP MEMS MOEMS 2006 Stresa, Italy, Apr. 2006 pp. 6.

[22] W.-S. Huang, K.-E. Tzeng, M.-C. Cheng, R.-S. Huang, "A silicon MEMS micro power generator for wearable micro devices," *Journal of the Chinese Institute of Engineers* **30**, 1 (2007) 133.

[23] Perpetuum Limited, PMG17 datasheet, Jan. 7, 2008. [Online]. Available: http://www.perpetuum.co.uk/resource/PMG17-100_dsheet.pdf.

[24] A. Safari, and E. K. Akdogan, “Crystal chemistry of piezoelectric materials,” in *Piezoelectric and Acoustic Materials for Transducer Applications*. Chapter 3. Springer Science & Business Media (2008) pp 39.

[25] W. Heywang, K. Lubitz, W. Wersing “Piezoelectricity: Evolution and future of a technology,” **114** (2008) Springer Science & Business Media.

[26] S. Roundy, "On the effectiveness of vibration-based energy harvesting," *Journal of Intelligent Material Systems and Structures* **16** (2005) 809.

[27] C. B. Yeager and S. Trolier-McKinstry, "Epitaxial $Pb(Zr_x,Ti_{1-x})O_3$ ($0.3<x<0.63$) films on (100)MgO substrates for energy harvesting applications," *Journal of Applied Physics* **112**, (2012) 074107.

[28] S. Trolier-McKinstry, and P. Muralt, "Thin film piezoelectrics for MEMS," *Journal of Electroceramics* **12** (2004) 7.

[29] P. Muralt, "PZT thin films for microsensors and actuators: Where do we stand?," *Ultrasonics, Ferroelectrics and Frequency Control, IEEE Transactions on* 47, no. 4 (2000) 903.

[30] S. H. Baek, J. Park, D. M. Kim, V. A. Aksyuk, R. R. Das, S. D. Bu, D. A. Felker, J. Lettieri, V. Vaithyanathan, S. S. N. Bharadwaja, N. Bassiri-Gharb, Y. B. Chen, H. P. Sun, C. M. Folkman, H. W. Jang, D. J. Dreft, S. K. Streiffer, R. Ramesh, X. Q. Pan, S. Trolier-McKinstry, D. G. Schlom, M. S. Rzchowski, R. H. Blick, C. B. Eom, "Giant piezoelectricity on Si for hyperactive MEMS," *Science* **334** (2011) 958.

[31] N. Ledermann, P. Muralt, J. Baborowski, S. Gentil, K. Mukati, M. Cantoni, A. Seifert, and N. Setter, "{100}-textured, piezoelectric $Pb(Zrx,Ti_{1-x})O_3$ thin films for MEMS: integration, deposition and properties," *Sensors and Actuators A: Physical* **105**, 2 (2003) 162.

[32] S. Priya, "Criterion for Material Selection in Design of Bulk Piezoelectric Energy Harvesters," IEEE Trans. Ultrason. Ferroelectr. Freq. Control **57**, 12 (2010) 2610.

[33] A. J. Lovinger, "Ferroelectric polymers," *Science* **220** (1983) 1115.

[34] S. Trolier-McKinstry, F. Griggio, C. Yaeger, P. Jousse, D. Zhao, S. S. N. Bharadwaja, T. N. Jackson, S. Jesse, S. V. Kalinin, and K. Wasa, "Designing piezoelectric films for micro electromechanical systems," *IEEE Transactions on Ultrasonics, Ferroelectrics, and Frequency*

Control **58**, 9 (2011) 1782.

[35] C. B. Yeager, "PZT thin films for piezoelectric MEMS mechanical energy harvesting," *Ph. D Thesis,* (2015) The Pennsylvania State University.

[36] I. G. Mina, H. Kim, I. Kim, S. K. Park, K. Choi, T. N. Jackson, R. L. Tutwiler, and S. Trolier-McKinstry, "High frequency piezoelectric MEMS ultrasound transducers," *IEEE Transactions on Ultrasonics, Ferroelectrics, and Frequency Control* **54**, 12 (2007) 2422.

[37] M. Akiyama, K. Umeda, A. Honda, and T. Nagase, "Influence of scandium concentration on power generation figure of merit of scandium aluminum nitride thin films," *Applied Physics Letters* **102**, 2 (2013) 021915.

[38] R. Matloub, M. Hadad, A. Mazzalai, N. Chidambaram, G. Moulard, C. S. Sandu, T. Metzger, and P. Muralt, "Piezoelectric $Al_{1-x}Sc_xN$ thin films: a semiconductor compatible solution for mechanical energy harvesting and sensors," *Applied Physical Letters* **102** (2013) 152903.

[39] M. Akiyama, K. Umeda, A. Honda, & T. Nagase, "Influence of scandium concentration on power generation figure of merit of scandium aluminum nitride thin films," *Applied Physics Letters* **102**, 2 (2013) 021915.

[40] K. Ujimoto, T. Yoshimura, A. Ashida, and N. Fujimura, "Direct piezoelectric properties of (100) and (111) $BiFeO_3$ epitaxial thin films," *Applied Physics Letters* **100**, 10 (2012) 102901.

[41] S. S. Won, J. Lee, V. Venugopal, D.-J. Kim, J. Lee, I. W. Kim, A. I. Kingon, S.-H. Kim, "Lead-free Mn-doped $(K_{0.5},Na_{0.5})NbO_3$ piezoelectric thin films for MEMS-based vibrational energy harvester applications," *Applied Physics Letters* **108**, 23 (2016) 232908.

[42] F. Calame, and P. Muralt, "Growth and properties of gradient free sol-gel lead zirconate titanate thin films," *Applied Physics Letters* **90**, 6 (2007) 062907.

[43] C. B. Yeager, Y. Ehara, N. Oshima, H. Funakubo, and S. Trolier-McKinstry, "Dependence of

$e_{31,f}$ on polar axis texture for tetragonal $Pb(Zr_x,Ti_{1-x})O_3$ thin films," *Journal of Applied Physics* **116**, 10 (2014) 104907.

[44] K. Wasa, T. Matsushima, H. Adachi, I. Kanno, and H. Kotera, "Thin-film piezoelectric materials for a better energy harvesting MEMS," *Journal of Microelectromechanical Systems* **12**, 2 (2012) 451.

[45] I. Kanno, T. Ichida, K. Adachi, H. Kotera, K. Shibata, and T. Mishima, "Power-generation performance of lead-free $(K,Na)NbO_3$ piezoelectric thin-film energy harvesters," *Sensors and Actuators A: Physical* **179** (2012) 132.

[46] B. Jaffe, W. R. Cook, and H. Jaffe, *Piezoelectric Ceramics* (Academic, New York, 1971).

[47] B.A. Tuttle, J.A. Voight, D. C. Goodnow, D. L. Lamppa, T. J. Headley, M. O. Eatough, G. Zender, R. D. Nasby, and S. M. Rodgers, "Highly oriented, chemically prepared Pb (Zr, Ti) O_3 thin films," *Journal of the American Ceramic Society* **76**, 6 (1993) 1537.

[48] P. Muralt, "Ferroelectric thin films for micro-sensors and actuators: a review," *Journal of Micromechanics and Microengineering*, 10, 2 (2000) 136.

[49] C.R. Cho, "Heteroepitaxial growth and switching behaviors of PZT (53/47) films on $LaNiO_3$-deposited $LaAlO_3$ and $SrTiO_3$ substrates," *Materials Science and Engineering: B* **64,** 2 (1999) 113.

[50] S. Yokoyama, Y. Honda, H. Morioka, S. Okamoto, and H. Funakubo, "Dependence of electrical properties of epitaxial $Pb(Zr,Ti)O_3$ thick films on crystal orientation and Zr/(Zr+ Ti) ratio*," Journal of Applied Physics* **98**, 9 (2005) 094106.

[51] Q. Zhang, and R. W. Whatmore, "Sol-gel PZT and Mn-doped PZT thin films for pyroelectric applications," *Journal of Physics D: Applied Physics* **34**, 15 (2001) 2296.

[52] N. Childambaram, A. Mazzalai, D. Balma, and P. Muralt, "Comparison of lead zirconate

titanate thin films for microelectromechanical energy harvester with interdigitated and parallel plate electrodes," *IEEE Transactions on Ultrasonics, Ferroelectrics, and Frequency Control* **60**, 8 (2013) 1564.

[53] W. R. Cook, D. A. Berlincourt, and F. J. Scholz, "Thermal expansion and pyroelectricity in lead titanate zirconate and barium titanate," *Journal of Applied Physics* **34**, 5 (1963) 1392.

[54] Y. Okada, and Y. Tokumaru, "Precise determination of lattice parameter and thermal expansion coefficient of silicon between 300 and 1500 K," *Journal of Applied Physics* **56**, 2 (1984) 314.

[55] T. G. Kollie, "Measurement of the thermal-expansion coefficient of nickel from 300 to 1000 K and determination of the power-law constants near the Curie temperature," *Physical Review B* **16**, 11 (1977) 4872.

[56] M. D. Losego, "The chemical solution deposition of lead zirconate titanate (PZT) thin films directly on copper surfaces," *MS thesis* (2005) North Carolina State University.

[57] G. L. Brennecka, W. Huebner, B. A. Tuttle, P. G. Clem, "Use of stress to produce highly oriented tetragonal lead zirconate titanate (PZT 40/60) thin films and resulting electrical properties," *Journal of the American Ceramic Society* **87**, 8 (2004) 1459.

[58] G. Han, J. Ryu, W-H Yoon, J-J. Choi, B.-D. Hahn, J.-W. Kim, D.-S. Park, C.-W Ahn, S. Priya, and D.-Y. Jeong, "Stress-controlled $Pb(Zr_{0.52}Ti_{0.48})O_3$ thick films by thermal expansion mismatch between substrate and $Pb(Zr_{0.52}Ti_{0.48})O_3$ film," *Journal of Applied Physics* **110** (2011) 124101.

[59] H. G. Yeo, and S. Trolier-McKinstry "{001} Oriented piezoelectric films prepared by chemical solution deposition on Ni foils," *Journal of Applied Physics* **116**, 1 (2014) 014105.

[60] S. B. Kim, H. Park, S. H. Kim, H. C. Wikle, J. H. Park, and D. J. Kim, "Comparison of MEMS

PZT cantilevers based on and modes for vibration energy harvesting," *Journal of Microelectromechanical Systems* **22**, 1 (2013) 26.

[61] S. R. Anton and H. A. Sodano, "A review of power harvesting using piezoelectric materials (2003-2006)," *Smart Materials Structures* **16**, 3 (2007) R1.

[62] M. Kim, S.H. Kim, and S. Hong, (2013). Materials and devices for MEMS piezoelectric energy harvesting. In *Advances in Energy Harvesting Methods* (pp. 417-435). Springer New York.

[63] N. Childambaram, D. Balma, R. Nigon, A. Mazzalai, R. Matloub, C. S. Sandu and P. Muralt "Converse mode piezoelectric coefficient for lead zirconate titanate thin film with interdigitated electrode," *Journal of Micromechanics Microengineering* **25** (2015) 045016.

[64] M. Kim. J. Dugundji, and B. L. Wardle, "Effect of electrode configurations on piezoelectric vibration energy harvesting performance," *Smart Materials and Structures* **24** (105) 045026.

[65] L. Q. Yao, J. G. Zhang, L. Lu, and M. O. Lai "Nonlinear Dynamic Characteristics of Piezoelectric Bending Actuators Under Strong Applied Electric Field," *Journal of Microelectromechanical Systems* **13**, 4 (2004) 645.

[66] A. Erturk, and D. J. Inman, "An experimentally validated bimorph cantilever model for piezoelectric energy harvesting from base excitations," *Smart Materials and Structures* **18** (200) 025009.

[67] A. Safari, E. K. Akdogan, Chapter 20 "Piezoelectric MEMS: Materials and Devices," *Piezoelectric and acoustic materials for transducer applications*. Springer Science & Business Media (2008).

[68] R. Calio, U. B. Rongala, D. Camboni, M. Milazzo, C. Stefanini, G. de Petris, and C. M. Oddo, "Piezoelectric Energy Harvesting Solutions," *Sensor* **14** (2014) 4755.

[69] L. Mateu, F. Moll, “Optimum piezoelectric bending beam structures for energy harvesting using shoe inserts,” *Journal of Intelligent Material Systems and Structures* **16** (2005) 835.

[70] F. Goldschmidtboeing and P. Woias, “Characterization of different beam shapes for piezoelectric energy harvesting,” *Journal of Micromechanics and Microengineering* **18** (2008) 104013.

[71] L. Dhakar, H. Liu, F. E. H. Tay, C. Lee, “A new energy harvester design for high power output at low frequencies,” *Sensors and Actuators A* **199** (2013) 344.

[72] M. F. Daqaq, R. Masana, A. Erturk, D. D. Quinn, "On the role of nonlinearities in vibratory energy harvesting: A critical review and discussion," *Applied Mechanics Reviews* **66** (2014) 040801.

[73] E. S. Leland and P. K. Wright “Resonance tuning of piezoelectric vibration energy scavenging generators using compressive axial preload,” *Smart Materials and Structures* **15** (2006) 1413.

[74] A. Hajati, and S.-G. Kim “Ultra-wide bandwidth piezoelectric energy harvesting,” *Applied Physics Letters* **99**, 8 (2011) 083105.

[75] P. Pillatsch, E. M. Yeatman, A. S. Holmes, “A piezoelectric frequency up-converting energy harvester with rotating proof mass for human body applications,” *Sensors and Actuators A* **206** (2014) 178.

[76] R. L. Harne and K. W. Wang, “A review of the recent research on vibration energy harvesting via bistable systems,” *Smart Materials and Structures* **22** (2013) 023001.

[77] K. Kanda, I. Kanno, H. Kotera, and K. Wasa, "Simple fabrication of metal-based piezoelectric MEMS by direct deposition of $Pb(Zr,Ti)O_3$ thin films on titanium substrates," Journal of Microelectromechanical systems, **18**, 3 (2009) 610.

[78] A. I. Kingon, and S. Srinivasan, “Lead zirconate titanate thin films directly on copper

electrodes for ferroelectric, dielectric and piezoelectric applications," *Nature Materials* **4**, 3 (2005) 233.

[79] M. D. Losego, L. H. Jimison, J. F. Ihlefeld, and J. P. Maria, "Ferroelectric response from lead zirconate titanate thin film prepared directly on low-resistivity copper substrate," *Applied Physics Letters* **86** (2005) 172906.

[80] K. Morimoto, I. Kanno, K. Wasa, and H. Kotera, "High-efficiency piezoelectric energy harvesters of c-axis oriented epitaxial PZT films transferred onto stainless steel cantilever," *Sensors and Actuators A: Physical* **163**, 1 (2010) 428.

[81] E. Suwa, Y. Tsujiura, F. Kurokawa, H. Hida, and I. Kanno, "Fabrication of high-efficiency piezoelectric energy harvesters of epitaxial $Pb(Zr,Ti)O_3$ thin films by laser lift-off," *Energy Harvesting and Systems* **3**, 1 (2016) 61.

Chapter 3

{001} Oriented Piezoelectric Films Prepared by Chemical Solution Deposition on Ni Foils*

3.1 Introduction

Lead zirconate titantate bulk ceramics are widely used as sensors, actuators, and transducers.[1,2] In order to miniaturize component size and decrease operating voltages, PZT thin films are being developed for MEMS on platinized silicon wafers; in many cases, the Si becomes part of the mechanical structure of the device.[3] However, there are some applications for which flexible, high fracture toughness passive elastic layers would be desireable.[4] As one example, in MEMS energy harvesting devices, high density end masses enhance the output power efficiency and reduce the resonance frequency, but can introduce failure mechanisms if the passive layer is brittle.[5] Nevertheless, deposition of PZT films on base metal substrate, because of the thermodynamic incompatibility between PZT and the metal, is a challenge.

Many researchers have reported fabrication of randomly oriented PZT or $(K,Na)NbO_3$-based films on base metal substrates such as stainless steel, Cu, Ni, by using buffer layers ($LaNiO_3$, Pt), annealing in low oxygen partial pressure, or direct sputter deposition.[6,7] In most cases, the reported piezoelectric properties of films on base metal substrates are lower than those reported on silicon or single crystal oxide substrates.[8~11]

To improve on this situation, it is necessary that oriented PZT films, which show better piezoelectric properties than randomly oriented PZT films,[1] be fabricated on base metal

* *The majority of this chapter is reproduced from H. G. Yeo, and S. Trolier-McKinstry (published in the Journal of Applied Physics, 116 (2014) 014105*

substrates. Recently, Shelton et al. reported the integration of strongly oriented PZT film on flexible metal alloy substrates with ion beam-assisted deposition (IBAD) MgO templates.[12] However, global piezoelectric responses such as d_{33} and $e_{31,f}$ have not been reported with highly oriented PZT film on base metal substrate.

In this work, the processing of {001} oriented PZT (52/48) films on Ni foils using {100} $LaNiO_3$ (LNO) as a template layer and an HfO_2 buffer layer to suppress oxidation of the metal foil was investigated. The hypothesis was that the comparatively larger thermal expansion coefficient of Ni, relative to Si, and the small thickness of the foil substrate, would facilitate ferroelastic domain wall motion relative to films on Si.[13] A large population of *out-of-plane* polarization in PZT films should yield larger remanent polarizations and low dielectric permittivities as compared with PZT films on Si, which have a significant fraction of polarization which lies *in-plane*.[13]

3.2 Experimental Procedure

3.2.1 Thin Film Fabrication

25 μm thick Ni foils (99.99%, Alfa Aesar) were first polished with Al_2O_3 powders (3 ~ 0.05 μm) in order to reduce the surface roughness. They were then preannealed for 1 hour at 900 °C under low oxygen partial pressures (~ 10^{-17} atm) using a mixture of gas (H_2/N_2) and N_2 that was bubbled through deionized water to remove any surface oxide.[14] Then, an amorphous HfO_2 buffer layer was grown by atomic layer deposition (ALD, Cambridge Nanotech Savannah 200 ALD System) using tetrakis hafnium ($Hf(NMe_2)_4$) precursors and H_2O at 200 °C for 300 cycles (1.01 Å/pulse). This acted as a passivant for the Ni substrate.

Following this, a $LaNiO_3$ film was deposited to serve as an orienting perovskite seed

layer. For the deposition, a 0.2M $LaNiO_3$ precursor solution based on 2-methoxyethanol (2MOE) (Aldrich, 99.9%) was prepared by mixing lanthanum (III) nitrate hexahydrate (Aldrich 99.99%) and nickel (II) acetate tetrahydrate (Aldrich 99.998%). The solution was refluxed for 3 hr at 110 °C. After the solution was prepared, it was spin coated onto the HfO_2 – passivated substrate at 3000 rpm, dried (150 °C for 2min) and pyrolyzed (400 °C for 2min). Layers were then crystallized by rapid thermal annealing (RTA) at 700 °C in air to produce (100) oriented $LaNiO_3$ films. This process was repeated 5 times to reach a bottom electrode thickness of 100 nm.

A 0.4M $Pb(Zr_{0.52}Ti_{0.48})O_3$ (PZT (52/48)) sol-gel solution, with 10 mol% excess PbO to compensate for the loss of lead during crystallization was prepared as described elsewhere.[15] The solution was spin coated at 1500 rpm for 40 sec on $LaNiO_3/HfO_2/Ni$ or $LaNiO_3/HfO_2/SiO_2/Si$ substrates. After spin coating, they were dried at 225 °C for 60 second and pyrolyzed at 400 °C for 60 sec in air on a hotplate. The PZT layers were then crystallized by rapid thermal annealing (RTA) at 700 °C for 60 sec in air. This procedure was repeated to reach a PZT film thickness of around 1μm. After all of the PZT layers crystallized, a PbO capping was used to convert surface lead-deficient phases to the perovskite.[16]

3.2.2 Analysis of Thin Film

X-ray diffraction (XRD, PANalytical X'pert) was used to assess the crystallinity, phase purity, and the degree of orientation of the films. Field emission scanning electron microscopy (FE-SEM, Leo 1530) was utilized to assess the existence of pores and small amounts of pyrochlore phases, which cannot be detected by XRD. For electrical characterization of the films, dc magnetron sputtered (Kurt J. Lesker) Pt top electrodes (100nm in thickness) were patterned by a lift-off process. After heat treatment at 500 °C in air to improve the top

electrode/film interface, the low field dielectric constant (ε_r) as a function of frequency was characterized using an LCR meter (HP4284A) with a 30 mV oscillating signal. Polarization hysteresis loops were measured using a Radiant Technologies Precision LC ferroelectrics tester. All electrical measurement were conducted by using the Pt top electrode, with the bottom Ni foil grounded after scratching the oxide layers to reach the nickel. Prior to measuring the transverse piezoelectric coefficient $e_{31,f}$ by a wafer flexure method, the PZT films were poled at three times the coercive field for 15 min at 150 °C.[17]

3.3 Results and discussion

3.3.1 Characteristics of Crystallinity and Microstructure

Figure 3-1 shows the XRD patterns of LNO and PZT films on Ni or Si substrates. For all of the Ni treatments investigated, the $LaNiO_3$ is strongly {100} oriented. It is clear that 30nm ALD HfO_2 layers are effective as buffer layers to minimize oxygen diffusion to the Ni foil during annealing of the $LaNiO_3$ in air, as no NiO is apparent for the case of a foil which had been both polished and pre-annealed. It is also apparent that the quality of the oriented LNO films depends on the original Ni surface condition. Decreased roughness and suppressed oxidation of the Ni surface are correlated with increased intensity for the *h00* $LaNiO_3$ reflections.

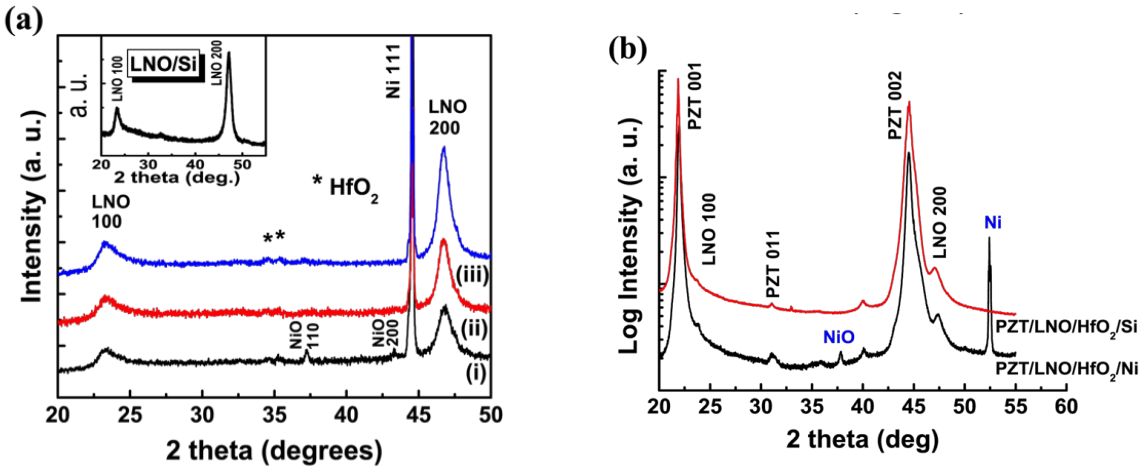

Figure 3-1. (a). XRD θ-2θ scan of crystallized $LaNiO_3$ films on various pre-processed Ni foils (i) polished (ii) pre-annealed in low PO_2 (iii) combination of polished and pre-annealed in low PO_2 (Inset: XRD $LaNiO_3$ film deposited on oxidized Si substrate) (b) PZT (52/48) film on $LaNiO_3/HfO_2/Ni$ and $LaNiO_3/HfO_2/Si$ substrates.

For comparison, the inset in Figure 3-1 (a) shows the XRD pattern of a strongly (100) oriented LNO film on a $HfO_2/SiO_2/Si$ substrate. The integrated intensities of (200) LNO peak, which were fitted with a Lorentz function, increase after pre-treatments of the Ni foil, implying an improved crystalline texture. This was correlated with a decrease in the full-width-at-half-maximum (FWHM) of the (200) LNO rocking curves, as shown in Table I. These results confirm that strongly textured LNO film can be achieved by reducing the surface roughness and suppressing the oxidation of the Ni foils.

The oriented LNO films were used to template the orientation of the PZT film, as previously reported.[18,19] PZT films on both the $LNO/HfO_2/Ni$ and $LNO/HfO_2/SiO_2/Si$ substrates showed no pyrochlore peaks, as is observed in Figure 3-1 (b). Based on the intensity of the PZT film peaks in Figure 3-1 (b), the Lotgering factor (f) was calculated. It was found that strongly {001} oriented PZT ($f = 0.99$) could be achieved on {100}-textured LNO films on either Ni or Si substrates.[20]

Table 3-1. FWHM and integrated intensities of $LaNiO_3$ films on Si and Ni foils on with various pretreatments.

Film	FWHM (degrees)	Integrated Intensity (counts)
(200) LNO on Si	3.5	42505
(200) LNO on polished Ni	8.5	1827
(200) LNO on pre-annealed Ni	6.9	2165
(200) LNO on polished + pre-annealed Ni	6.0	3283

Films on Ni show a higher intensity for 00*l* peaks than *h*00 peaks. The reverse is true for films on Si, as shown in Figure 3-2 (a), (b). These results are consistent with a higher degree of c-axis orientation for the tetragonal component of the films on Ni. The FWHM of the rocking curve for the PZT $\{200\}_{pc}$ reflections on Si and Ni were about 2.7° and 4.1° respectively, as shown in Figure 3-2 (a), (b), where the subscript pc denotes the pseudocubic unit cell. Thus, the PZT film on Si has better alignment than the PZT on Ni. It is expected that the orientation for both films is affected by the quality of the seed layer and the roughness of the surface.

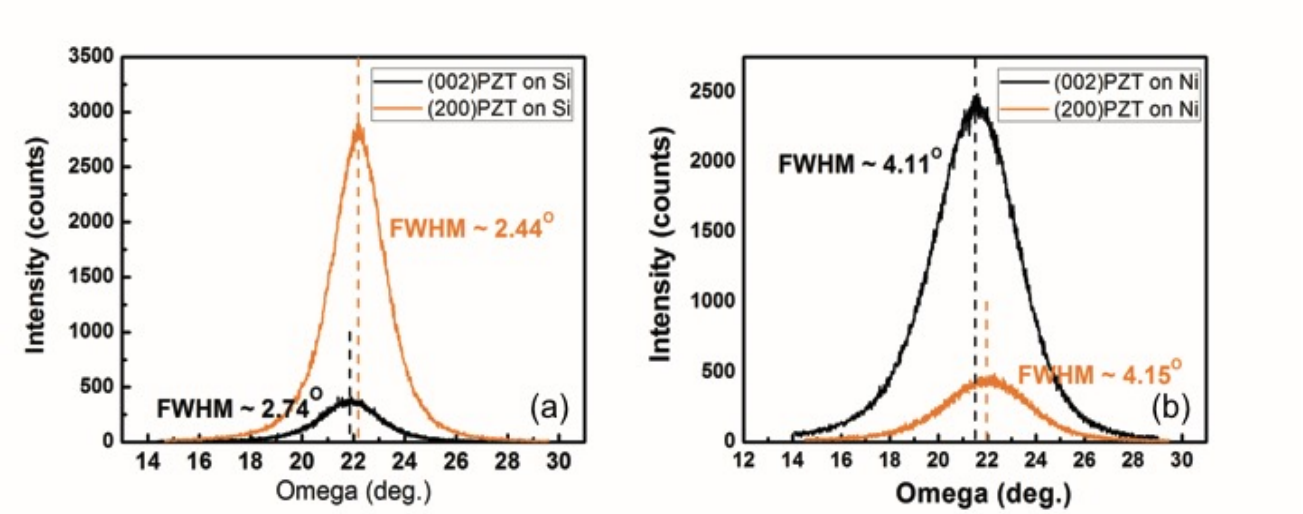

Figure 3-2. Comparison of omega-rocking curve at (002) and (200) peaks of PZT on (a) Si and (b) Ni.

Surface and cross section microstructure images of PZT films on Ni are shown in Figure 3-3 (a), (b). A small amount of surface pyrochlore phase can be seen primarily at the PZT grain boundaries after crystallization. This could be removed using the PbO cover coat method described by Tani and Payne.[16] The cross-sectional FE-SEM image of a PZT/LNO/HfO_2/Ni stack, as shown in Figure 3-3 (b), reveals a columnar PZT microstructure with little porosity; there is no evidence of cracks or delamination. The PZT film on the LNO/HfO_2/SiO_2/Si substrate exhibited similar grain size, columnar growth and density (not shown).

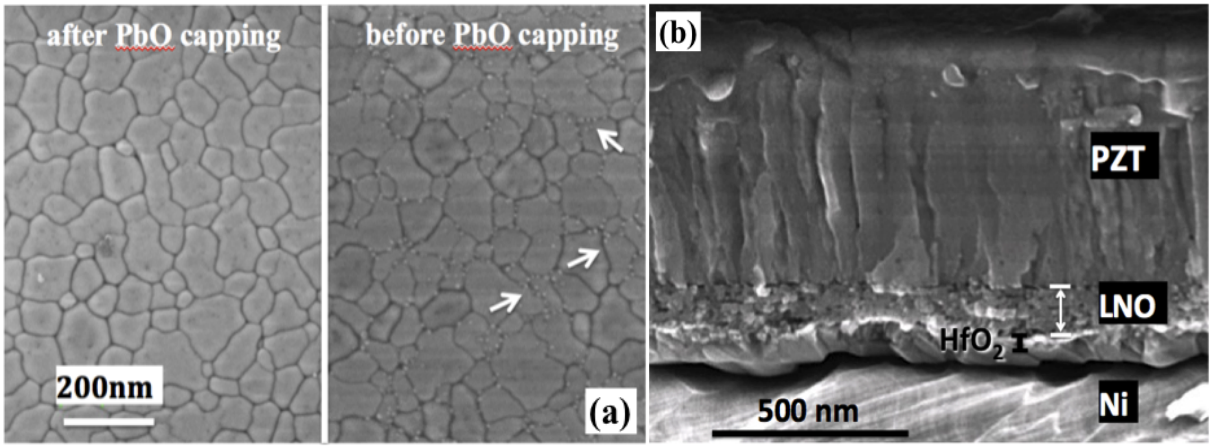

Figure 3-3. (a) Surface FE-SEM image of PZT/LNO/HfO_2/Ni before and after a PbO-precursor cover coat (b) cross-sections of PZT films deposited on LNO (100nm)/HfO_2 (30nm) /Ni foil after the cover coat.

3.3.2 Electrical Properties

Figure 3-4 illustrates the dielectric properties as a function of frequency in the range between 100 Hz and 10 kHz at room temperature for PZT grown on LNO/HfO_2/Ni and LNO/HfO_2/SiO_2/Si substrates. Dielectric loss tangents of less than 5% at 1 kHz are observed in both films before polarization – electric field (P-E) measurements. The dielectric constant of

PZT on Ni (~780) is much lower than that of PZT on silicon substrate (~1120) at 1 kHz. This difference in the dielectric constant was attributed to a higher volume fraction of *c*-domains, which have a lower permittivity than *a*-domains, on the Ni substrate.[21] Fundamentally, the population of *c* and *a* domains in relaxed films is governed, at least in large part, by the thermal expansion coefficient mismatch between the film and the substrate.[13,22] The average thermal expansion coefficient (α) of the Ni substrate ($\alpha = 17.7 \times 10^{-6}$/K) is larger than that of the PZT film ($\alpha = 9.1 \times 10^{-6}$/K) from the crystallization temperature to the Curie temperature, which should favor the *c*-domain state.[9,23,24] On the other hand, the lower average of thermal expansion coefficient of Si ($\alpha = 4.2 \times 10^{-6}$/K) leads to a higher fraction of *a*-domains in response to the tensile stress present on cooling the PZT films through its Curie temperature.[25,26]

Additionally, the dielectric properties were measured before and after P-E measurements, as shown in Figure 3-4 (a) and (b). A 30% decrease of ε_r was observed for the PZT films on Ni substrate, which was accompanied by a reduction in the dielectric loss after the polarization-electric field measurement. In contrast, little change in the dielectric properties is observed following P-E measurements for PZT on Si. It is suggested that the permittivity changes for the PZT film on Ni arise from ferroelastic domain switching from *a* to *c* domains. The compressive stress induced by large thermal expansion of Ni substrate, coupled with the small substrate thickness (which enables stress relief by bending) is believed to encourage the dipole moment to align out-of-plane with 90° domain wall motion under applied field.[9] The permittivity recovered to its original higher value if the film was heated above the Curie temperature.

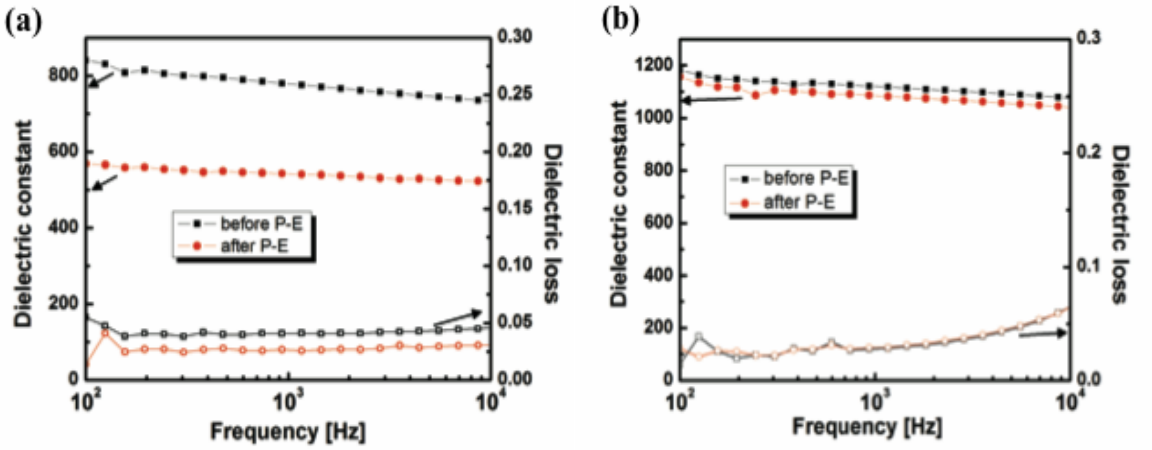

Figure 3-4. Dielectric constant and loss as a function of frequency for PZT grown on $LaNiO_3/HfO_2$ buffered (a) Ni and on (b) Si substrate before and after high-electric field ferroelectric measurement.

In contrast to the behavior of the films on Ni, the unchanged dielectric constant of PZT film on Si substrate after P-E measurement indicates that the ferroelastic domain switching is remarkably difficult even at strong electric fields.[27] In many ferroelectric films on Si, relatively low levels of non-180° domain wall motion are observed compared to ceramics of the same composition. This is typically attributed to the smaller grain size and clamping from the substrate.[28]

The dielectric response of ferroelectric films reflects not only the intrinsic permittivity, representing the average response of single domains with the same orientation distribution, but also extrinsic contributions arising from domain wall and phase boundary motion.[28] To obtain information on domain wall motion in PZT film on different substrate at sub-switching fields, the Raleigh Law was used:

$$\varepsilon = \varepsilon_{init} + \alpha_{irr} E_{ac} \qquad (3\text{-}1)$$

where ε is the dielectric constant, ε_{init} and α_{irr} are the reversible and irreversible Rayleigh constants, respectively, and E_{ac} is the ac electrical driving field. Figure 3-5 shows the Rayleigh response of the PZT films before and after P-E measurements. It is observed that for (100) oriented PZT films on Si, the reversible and irreversible Rayleigh constants at 1kHz are nearly unchanged by P-E measurement (See Figure 3-5). This is consistent with the observation above that little ferroelastic switching occurs in PZT film on Si.

In contrast, comparatively large values of the irreversible Rayleigh parameter are shown in unpoled (001) oriented PZT films on Ni. Furthermore, both the reversible and irreversible Rayleigh constants decrease after P-E measurements. Both of these would be consistent with either more or more mobile domain walls prior to high field exposure, and a significant change in the domain state during the P-E measurement. In particular, it is likely that the decreased Rayleigh constants after P-E measurements are a result of a change in the population of domain walls. It is important to note that there was no evidence for local dielectric breakdown events being responsible for the decreased permittivities. It is not clear at present whether the larger degree of ferroelastic switching in films on Ni is due to reduced substrate clamping associated with the smaller substrate thickness or to the compressive stress associated with the large thermal expansion of Ni substrate.

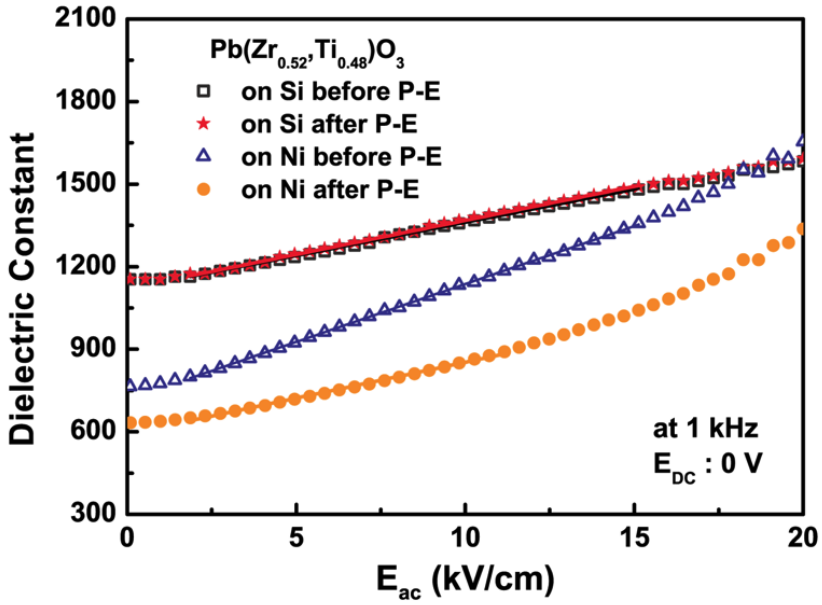

Figure 3-5. The nonlinear behavior of the dielectric constant as a function of ac electric field in PZT films on Si or Ni substrates before and after polarization-electric field measurement.

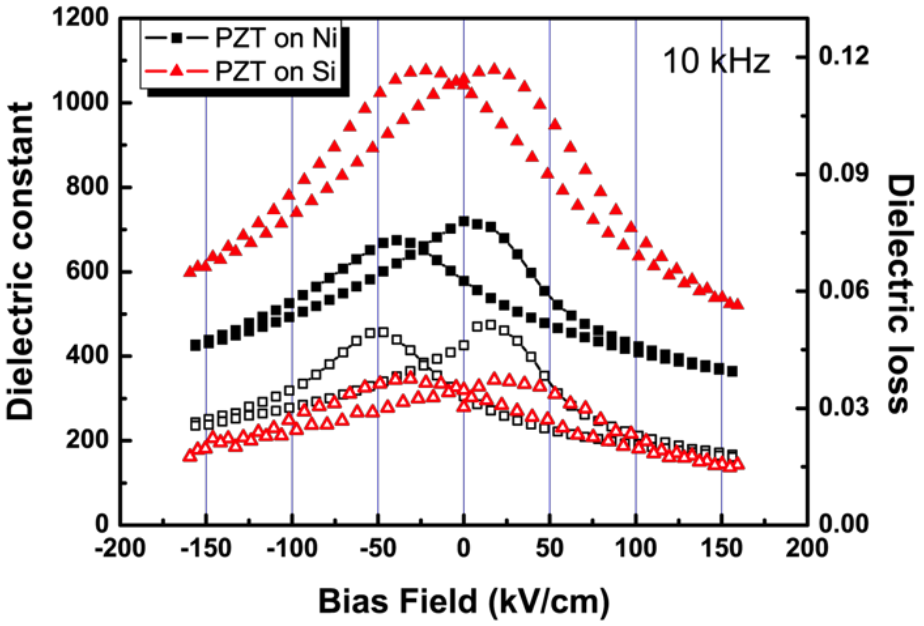

Figure 3-6. The dielectric properties versus DC electric bias for PZT/LNO/HfO_2/Ni and PZT/LNO/HfO_2/Si.

It is also notable that the amount of imprint in the films is too small to account for all of the observed differences in permittivities. This is apparent in a comparison of the dc field dependence of the permittivities for films on Ni and Si, as shown in Figure 3-6. The PZT deposited on LNO/HfO_2/Ni clearly has a more asymmetric butterfly curve compared to those of PZT on Si. However, even at bias fields of several times the coercive field, the data for the films on the two types of substrates do not converge.

In Figure 3-7, the (001) oriented PZT films on nickel shows square and well-saturated hysteresis loops with remanent polarization ~36 μC/cm^2 and a coercive field ~ 73 kV/cm. In contrast, the films on silicon have more rounded and slanted hysteresis characteristic with P_r ~ 17 μC/cm^2 and E_c ~ 72 kV/cm at 100 Hz. This difference is attributed to differences in the relative volume fraction of *a* and *c* domains. The films on Ni, because they have a more compressive stress state that the films on Si, favor the *c*-domain state, and hence have a larger remanent polarizations.

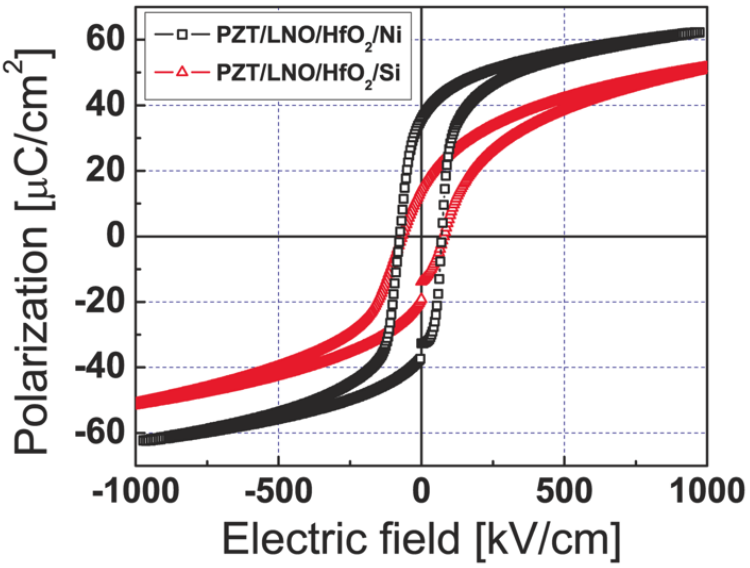

Figure 3-7. Polarization-electric field hysteresis loops of {001} oriented PZT(52/48) film on Ni and silicon substrates respectively.

The transverse piezoelectric constant $|e_{31,f}|$ of PZT(52/48) film on metal substrate are 10.6 ± 0.8 C/m^2 after poling at three times the coercive field for 15 min at 150 °C. The value is comparable to (100) oriented PZT films deposited on silicon substrates,[29] and higher than previous reports for PZT films on metal foils. The higher values shown here are believed to be a result of the high degree of orientation (f = 0.99).

3.4 Conclusions

In summary, strongly {001} oriented PZT films were deposited on Ni foils by chemical solution. HfO_2 buffer layers (30nm) capped with {100}-textured LNO films lead to strongly {001} oriented PZT (f = 0.99) on Ni foils. {001} PZT/LNO/HfO_2/Ni films exhibited ε_r of 530 following P-E measurement with tanδ of 2.7% at 1 kHz, E_c of 73 kV/cm and P_r of 35.8 μC/cm^2. In addition, large piezoelectric constant ($|e_{31,f}|$ ~ 10.6 C/m^2) were shown. The combination of high piezoelectric response and low dielectric constant suggest the use of these films for energy harvesters with low resonance frequency and improved fracture toughness compared to Si substrates.

3.5 References

[1] S. Trolier-McKinstry and P. Muralt, "Thin films piezoelectric for MEMS," *Journal of Electroceramics* **12**, 1 (2004) 7.

[2] C.-B. Eom and S. Trolier-McKinstry, "Thin-film piezoelectric MEMS," *MRS Bulletin* **37**, 11 (2012) 1007.

[3] P. Muralt, "PZT thin films for microsensors and actuators: Where do we stand?," *IEEE*

Transactions Ultrasonics Ferroelectrics Frequency Control **47**, 4 (2005) 903.

[4] S. Trolier-McKinstry, F. Griggio, C. Yeager, P. Jousse, D. Zhao, S. S. N. Bharadwaja, T. N. Jackson, S. Jesse, S. V. Kalinin, and K. Wasa, "Designing piezoelectric films for micro electromechanical systems," *IEEE Transactions Ultrasonics Ferroelectrics Frequency Control* **58**, 9 (2011) 1782.

[5] K. Morimoto, I. Kanno, K. Wasa, H. Kotera, "High-efficiency piezoelectric energy harvesters of c-axis-oriented epitaxial PZT films transferred onto stainless steel cantilevers," *Sensors and Actuators A* **163** (2010) 428.

[6] C. Kügeler , R. Rosezin , T. Schneller , U. Böttger , and R. Waser, "Large area piezoelectric actuators using metal foil substrates with $Pb(Zr_x,Ti_{1-x})O_3$ thin films," *Integrated Ferroelectrics* **100** (2008) 254.

[7] S. Glinsek, S.-H. Kim and A. I. Kingon, "Piezoelectric thin films on flexible substrates with enhanced functional properties," 16th US-Japan Seminar on Dielectric and Piezoelectric Materials (2013) D9.

[8] T. Suzuki, I. Kanno, "Characterization of Pb $(Zr,Ti)O_3$ thin films deposited on stainless steel substrates by RF-magnetron sputtering for MEMS applications," *Sensors and Actuators A* **125** (2006) 382.

[9] B. Ma, S. Liu, S. Tong, M. Narayanan, and U. Balachandran, "Enhanced dielectric properties of $Pb_{0.92}La_{0.08}Zr_{0.52}Ti_{0.48}O_3$ films with compressive stress," *Journal of Applied Physics* **112** (2012) 114117.

[10] T. Kim, J. N. Hanson, A. Gruverman, A. I. Kingon, and S. K. Streiffer, "Ferroelectric behavior in nominally relaxor lead lanthanum zirconate titanate thin films prepared by chemical solution deposition on copper foil," *Applied Physics Letters* **88**, 26 (2006) 262907.

[11] J.-R. Cheng, W. Zhu, N. Li, and L. E. Cross, "Electrical properties of sol-gel-derived $Pb(Zr_{0.52}Ti_{0.48})O_3$ thin films on a $PbTiO_3$-coated stainless steel substrate," *Applied Physics Letters* **81**, 25 (2002) 4805.

[12] C. T. Shelton, and B. J. Gibbons, "Epitaxial Pb $(Zr,Ti)O_3$ Thin films on flexible substrates," *Journal of the American Ceramic Society* **94**, 10 (2011) 3223.

[13] G. L. Brennecka, W. Huebner, B. A. Tuttle, and P. G. Clem, "Use of stress to produce highly oriented tetragonal lead zirconate titanate (PZT 40/60) thin films and resulting electrical properties," *Journal of the American Ceramic Society* **87**, 8 (2004) 1459.

[14] H. Nagata, S. W. Ko, E. Hong, C. A. Randall, P. Pinceloup, D. Skamser, M. Randall, A. Tajuddin, and S. Trolier-McKinstry, "Microcontact printed $BaTiO_3$ and $LaNiO_3$ thin films for capacitors," *Journal of the American Ceramic Society* **89**, 9 (2006) 2816.

[15] R. A. Wolf and S. Trolier-McKinstry, "Temperature dependence of the piezoelectric response in lead zirconate titanate films," *Journal of Applied Physics* **95**, 3 (2004) 1397.

[16] T. Tani, and D. A. Payne, "Lead Oxide Coatings on Sol–Gel-Derived Lead Lanthanum Zirconium Titanate Thin Layers for Enhanced Crystallization into the Perovskite Structure," *Journal of the American Ceramic Society* **77** (1994) 1242.

[17] R. Wilke, P. Moses, P. Jousse, C. Yeager, and S. Trolier-McKinstry, "Wafer mapping of the transverse piezoelectric coefficient, $e_{31,f}$, using the wafer flexure technique with sputter deposited Pt strain gauges," *Sensors and Actuators A* **173**, 1 (2012) 152.

[18] G. S. Wang, D. Rémiens, C. Soyer, E. Dogheche, E. Cattan, "The effect of $LaNiO_3$ bottom electrode thickness on ferroelectric and dielectric properties of (100) oriented $PbZr_{0.53}Ti_{0.47}O_3$ films," *Journal of Crystal Growth* **284**, 1 (2005) 184.

[19] C. R. Cho, "Heteroepitaxial growth and switching behaviors of PZT (53/47) films on $LaNiO_3$-

deposited $LaAlO_3$ and $SrTiO_3$ substrates," *Materials Science and Engineering B* **64** (1999) 113.

[20] F. K. Lotgering, "Topotactical reactions with ferrimagnetic oxides having hexagonal crystal structures—I," *Journal of Inorganic and Nuclear Chemistry* **9**, 2 (1959) 113.

[21] M. J. Haun, Z. Q. Zhuang, E. Furman, S. J. Jang, and L. E. Cross, "Thermodynamic theory of the lead zirconate-titanate solid solution system, part I: phenomenology," *Ferroelectrics* **99** (1989) 63.

[22] C. B. Yeager, and S. Trolier-McKinstry, "Epitaxial Pb $(Zr_x,Ti_{1-x})O_3$ $(0.30\leq x\leq 0.63)$ films on (100) MgO substrates for energy harvesting applications," *Journal of Applied Physics* **112**, 7 (2012) 074107.

[23] W. R. Cook, Jr., D. A. Berlincourt, and F. J. Scholz, "Thermal expansion and pyroelectricity in lead titanate zirconate and barium titanate," *Journal of Applied Physics* **34** (1963) 1392.

[24] T. G. Kollie, "Measurement of the thermal-expansion coefficient of nickel from 300 to 1000 K and determination of the power-law constants near the Curie temperature," *Physical Review B* **16**, 11 (1977) 4872.

[25] Y. Okada, and Y. Tokumaru, "Precise determination of lattice parameter and thermal expansion coefficient of silicon between 300 and 1500 K," *Journal of Applied Physics* **56** (1984) 314.

[26] R. J. Ong, D. A. Payne, and N. R. Sottos, "Processing effects for integrated PZT: residual stress, thickness, and dielectric properties," *Journal of American Ceramic Society* **88**, 10 (2005) 2839.

[27] F. Xu, S. Trolier-McKinstry, W. Ren, B. Xu, Z.-L. Xie and K. J. Hemker, "Domain wall motion and its contribution to the dielectric and piezoelectric properties of lead zirconate titanate films," *Journal of Applied Physics* **89**, 2 (2001) 1336.

[28] N. Bassiri-Gharb, I. Fujii, E. Hong, S. Trolier-McKinstry, D. V. Taylor and D. Damjanovic, "Domain wall contributions to the properties of piezoelectric thin films," *Journal of Electroceramics* **19**, 1 (2007) 49.

[29] N. Ledermann, P. Muralt, J. Baborowski, S. Gentil, K. Mukati, M. Cantoni, A. Seifert, and N. Setter, "{100}-textured, piezoelectric $Pb(Zr_x,Ti_{1-x})O_3$ thin films for MEMS: integration, deposition and properties," *Sensors and Actuators A* **105**, 2 (2003) 162**.**

Chapter 4

Cantilever Piezoelectric Energy Harvesters Utilizing the Poling Conditions and Various Thickness of PZT on Ni Foils

4.1 Introduction

Solar, thermal and mechanical environmental sources contain available energy to harness for the operation of electronics. Energy harvesting technologies which generate electrical power from mechanical vibration or movement for low-power electronic devices (*e.g.* for wireless sensor networks or consumable electronics) are of especial interest. In principle, mechanical harvesting provides a potential solution to minimize the replacement of batteries for emplaced sensors in remote areas.[1] Lead zirconate titanate (PZT) thin films, which have a high piezoelectric response, are good candidates for piezoelectric microelectromechanical (MEMS) energy harvesters used in scavenging energy from continuous mechanical vibrations. Numerous reports have focused on improving the power density of energy harvesters through advanced device structures, improved circuits for energy extraction, and increased piezoelectric properties.[2~7] To enhance the efficiency of energy transformation from mechanical to electrical energy, it is crucial to optimize the material properties. Improvements in the materials used in piezoelectric energy harvesters (PEH) include the control of composition (MPB), orientation control (texturing),[8] ameliorating processing-induced defects (*e.g.* preparation of gradient free films),[9] doping,[10] control of the stress state,[7] and development of strong levels of imprint.

The maximum extractable electric power for a cantilever structure (Figure 4-1) operating in the 31 mode (*e.g.* a piezoelectric layer with top and bottom electrodes, poled out of the plane of the film) is generated at the resonance frequency. The power can be expressed by [11~13]

$$Power_{max} = \frac{m}{4\omega}\left(\frac{e_{31,f}^2}{\varepsilon_r \varepsilon_0} \cdot \frac{(1-\nu)^2}{E}\right) Q^2 A^2 \qquad (4.1)$$

where m is the mass of the proof mass, ω is the natural frequency, v_b and Y_b are Poisson's ratio and Young's modulus of the passive layer for thin film piezoelectric, $e_{31,f}$ is the piezoelectric coefficient, ε_0 and ε_r are the permittivity of free space and relative permittivity, respectively, Q is the total quality factor of the resonating device, and A is the acceleration level. Of these parameters, the transverse coefficient ($e_{31,f}$) and the relative permittivity (ε_r) of the piezoelectric can be modified to increase an energy harvester's figure of merit (FoM), defined as $(e_{31,f})^2/\varepsilon_r$. Therefore, $e_{31,f}$ and ε_r are the crucial parameters to enhance the output power of piezoelectric energy harvesting MEMS. However, there are few reports that directly demonstrate a link between the figure of merit and the performance of piezoelectric energy harvester for devices of the same size and resonance frequency.[14]

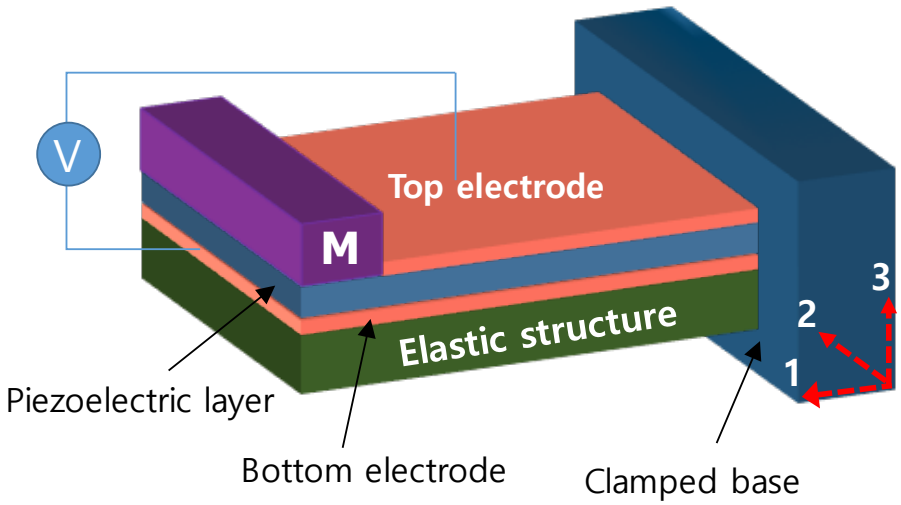

Figure 4-1. Illustration of cantilever structure with elastic layer and proof mass (M) for a piezoelectric energy harvester operating in the 31 mode.

In general, the process of poling, where a high DC electric field is applied to the film along the desired direction, is essential to improve the piezoelectric response by alignment of ferroelectric domains in the direction of the applied field.[15] Additionally, the dielectric constant depends on the poled domain state; this is important in controlling the FoM of the energy harvester.[16]

Thus, the first goal of this chapter is to prove the link between the output power of the harvester and the figure of merit; this was done by the use of poling conditions to affect the degree of domain alignment. The second goal of this chapter is to demonstrate an increase in the extracted voltage for a fixed vibrational input via an increase in the piezoelectric film thickness. For a 31 mode energy harvester, the open circuit voltage V by:[12,17]

$$V = -\frac{e_{31,f}}{\varepsilon_0 \varepsilon_r}(1 - v_s)^2 \frac{3h_s t_p (l_s + l_m)}{l_s^2 (4l_s + 3l_m)} \delta_s \qquad (4.2)$$

where t_p, l_s, l_m are the thickness of the PZT thin film, the length of the beam and tip mass, δ_s is cantilever displacement at the boundary between the beam and tip mass, and v_s is Poisson's ratio of the substrate. Thus, a 31 mode device will generate higher open-circuit voltages when the thickness of the PZT film is increased, provided that the dimensions are fixed (i.e. $V_{OC} \propto t_p$) and the strain is the same. However, it is important to note that the properties of films are rarely constant as a function of thickness.[18~20] In particular, the thick films of interest for mechanical energy harvesting are more susceptible to cracking at high strain levels.[21,22] Such cracking can reduce the $e_{31,f}$ coefficient to zero. Thus, it is important to assess the maximum in the harvester performance as a function of the film thickness.

In this study, highly {001} oriented PZT films with high energy harvesting figures of merit (See chapter 3) were coated on flexible nickel metal foils. Ni foil can deform plastically, and so is less susceptible to brittle mechanical failure compared substrates such as Si. In order to

assess the importance of PZT film thickness and porosity on the energy harvesting figure of merit and the extracted energy from a vibrational input, piezoelectric MEMS energy harvesters were prepared as rectangular cantilevers 7 mm×5.5 mm ~ 0.385 cm^2 with 0.4 g proof mass; thus, all devices had approximately the same resonance frequency.

4.2. Process of Integrating Devices and Measurement

4.2.1 Fabrication of Piezoelectric Energy Harvesters

{001} oriented undoped and Mn doped PZT thin films were coated on (100)$LaNiO_3$//HfO_2//Ni foil by *rf*-magnetron sputtering (using a Kurt J. Lesker CMS-18 tool) or CSD. Prior to growing the piezoelectric layer, a $LaNiO_3$ seed layer and a HfO_2 passivation layer were deposited on 25 μm thick Ni foils (Aldrich Aesar 99.99%) following polishing and pre-annealing as described elsewhere.[16][15] In brief, atomic layer deposition (ALD, Cambridge Nanotech Savannah 200 ALD System) was used to deposit a 30 nm thick layer of amorphous HfO_2. (100) oriented $LaNiO_3$ (LNO) was deposited by chemical solution deposition using a 0.2 M $LaNiO_3$ precursor solution based on 2-methoxyethanol (2MOE). Use of these two layers allowed PZT layers to be deposited and crystallized under the same conditions employed to grow PZT films on platinum-coated Si substrates.

Two different approaches were used to grow the PZT films: chemical solution deposition and *rf* magnetron sputtering. 1% Mn doped $Pb(Zr_{0.52}Ti_{0.48})O_3$ films were prepared by CSD using 0.4 M 1% Mn doped PZT solution with 10 mol% excess PbO on $LaNiO_3$//HfO_2//Ni; further details are described in previous work.[16] After all of the PZT layers were crystallized, PbO solution was spin coated and crystallized to convert a small amount of lead-deficient phases on the surface to phase- pure perovskite PZT phase.

In a second approach, RF-magnetron sputtering with *ex situ* post annealing was used to grow PZT films with thicknesses between 1 and 3 μm on (100)LNO//HfO_2//Ni foil using 8% PbO excess PZT(53/47) target under the conditions shown in Table 1. For *rf* sputtering at room temperature, *ex-situ* crystallization by RTA was used to crystallize the amorphous PZT layer. Each 0.5 μm layer of PZT was deposited and post annealed to achieve (001) orientation by controlling nucleation sites at the bottom interface; these layers were stacked until the desired thickness of PZT was achieved as described elsewhere.[4] It was found that crystallization was required approximately every 0.5 μm in order to retain orientation for the whole film thickness.

X-ray diffraction (XRD, PANalytical X'pert) was used to determine the crystallinity, phase purity, and the orientation of the films. The existence of pores and second phases was assessed through field emission scanning electron microscopy (FE-SEM, Leo 1530, and Merlin) of both cross-sections and the film surface. The electrical properties of all PZT samples were measured using small Pt top electrodes (diameter 200 μm ~ 400 μm). An LCR meter was used for measurement of the dielectric constant and loss as a function of frequency (100 Hz ~ 1 MHz) at low electric field (30mV). Polarization as a function of electric field was assessed using a Radiant Technologies Precision Multiferroics tester.

For the fabrication of the piezoelectric energy harvester, 100 nm thick Pt top electrodes (2 mm × 6 mm) were deposited on the PZT film by dc magnetron sputtering (Kurt J. Lesker) and patterned using a lift-off process. Additionally, the adhesion strength between the top electrode and the PZT film was enhanced by heat treatment at 500 °C in air. The PZT-coated Ni foils were cut by scissors for fixed-free cantilever beams; most piezoelectric MEMS energy harvesters on silicon substrates require a complex etching process. The PZT beam was 7 mm in width, which is a little larger than the electrode size, to avoid the propagation of cutting-induced cracks into

the active area (See FESEM images in Figures 4-2). The beams were 5.5 mm in length to provide an area to attach the proof mass.

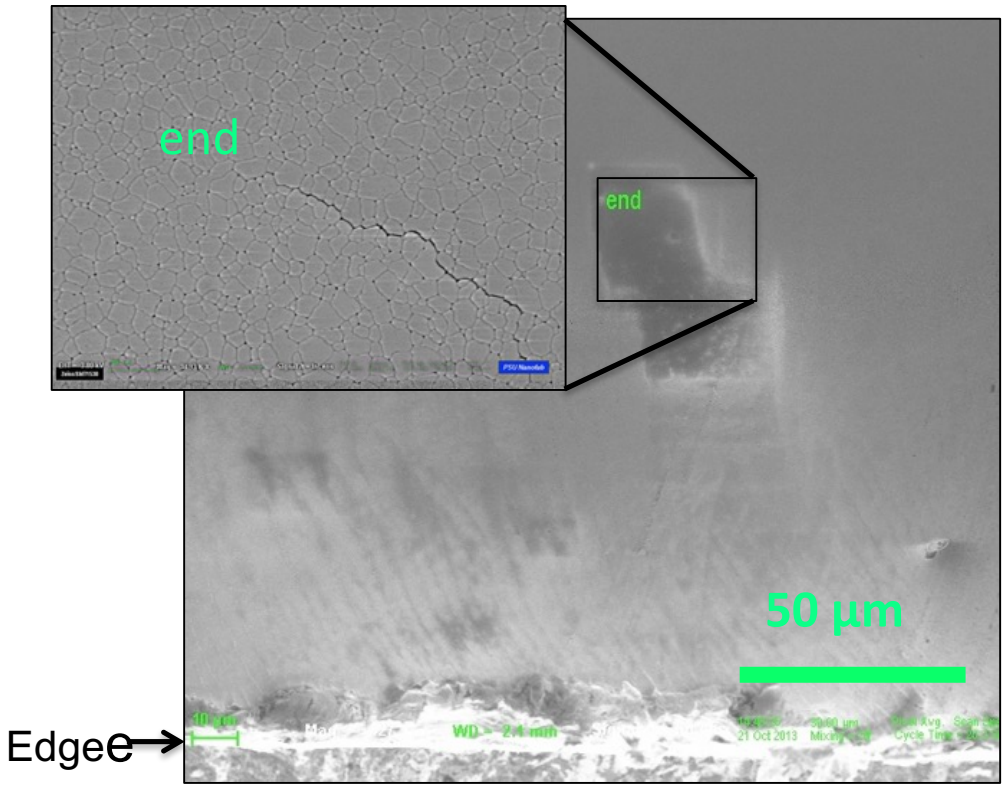

Figure 4-2. FESEM surface images of PZT films with cracks near the edge cut by scissors.

The PZT beams were poled under various conditions (*e.g.* unpoled, poled at 3 times the coercive field (E_c) at room temperature or poled at $3E_c$ at 150 ^oC) to determine the relationship between the transverse piezoelectric coefficient $e_{31,f}$ and the electrical output power from a unimorph PZT beam. The bottom electrode was exposed by scratching the PZT films using a razor blade. A positive voltage was applied to the bottom electrode for poling. After attaching a brass proof mass (~0.4g) to the end of the beam, the base of the beam was bonded to a rigid plastic fixture frame. This allowed the harvester to be handled easily and mounted on a shaker

with a magnet.

4.2.2 Experimental Setup for Testing of Harvesters

Figure 4-3 provides a schematic illustration of the experimental setup for measuring the performance of the vibrational energy harvester. The harvester is shown connected to the external load resistance. A shaker table (F3, Wilcoxon) was used as a vibration source. The sinusoidal excitation frequency and base excitation level was controlled using a lock-in-amplifier (SRS830, Stanford Research Systems).

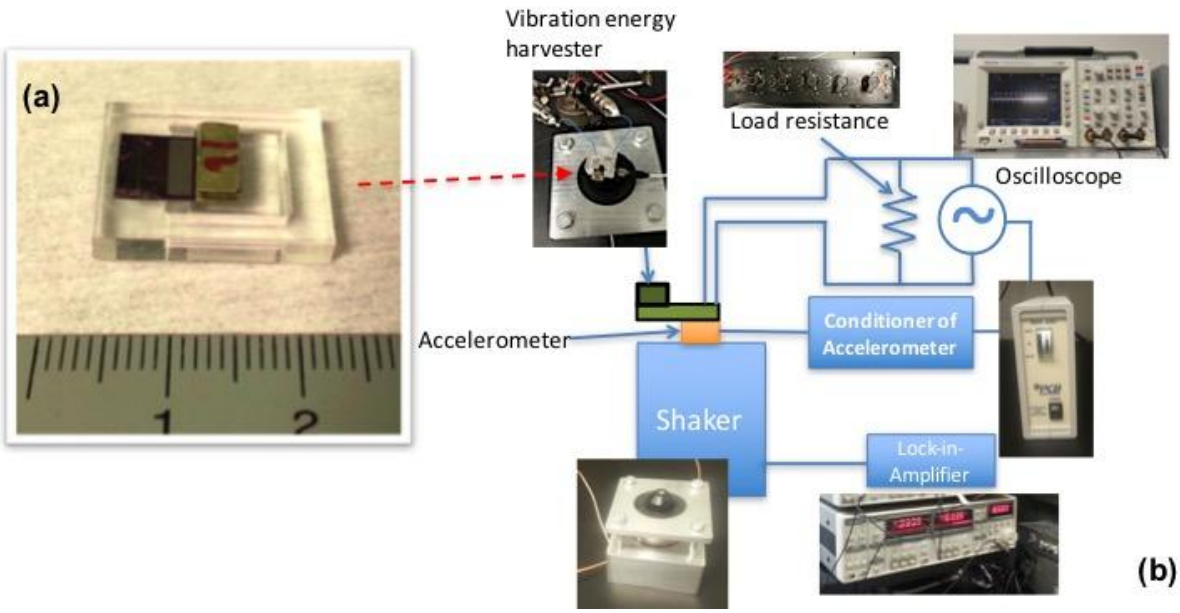

Figure 4-3. (a) Top view photograph of a piezoelectric energy harvester utilizing PZT films on Ni foil with a resonance frequency of 63~72 Hz. (b) Experimental setup for measurement of the output performance of the piezoelectric energy harvester.

An accelerometer (352C65, PCB Piezotronics) was mounted to the spindle of the shaker to detect the vibration frequency and acceleration level. A magnet, placed on the accelerometer, was utilized to hold the harvesters to the accelerometer. A resistor box connected to the harvester

was used to alter the load resistance to determine the optimum value showing maximum output power. During vibration of the shaker, the mechanical input (operating frequency and excitation level) and the output voltage developed by the harvester were monitored on an oscilloscope (TDS3054C, Tekrtronix). The output power was calculated from $P=V^2/R$. Data were taken at multiple frequencies to assess the resonance frequency and the optimal load resistance.

4.3. Characteristics of Thin Films and Devices

4.3.1. PZT Crystallinity and Microstructure

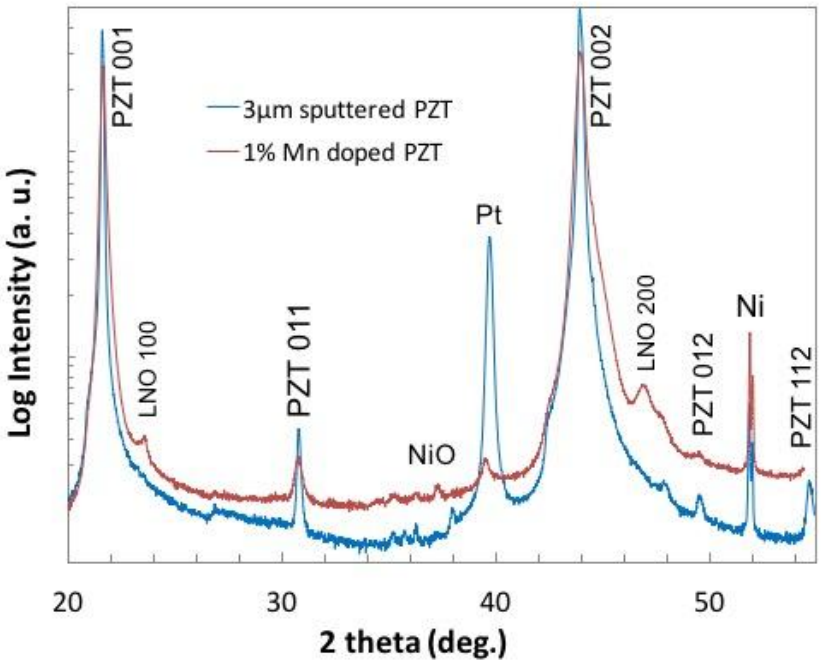

Figure 4-4. XRD θ-2θ scan of crystallized PZT (52/48) film grown by sputtering and CSD (Mn-doped sample) on $LaNiO_3/HfO_2/Ni$.

Figure 4-4 exhibits the XRD pattern of strongly {001} oriented PZT films on $LNO/HfO_2/Ni$ prepared either by CSD or sputtering with *ex-situ* crystallization. Consistent with the work presented in Chapter 3, strongly {001} oriented PZT films were achieved on Ni foils

without a pyrochlore phase by both techniques. In the case of sputtered PZT films, the multilayer stacking with post annealing every 0.5 μm thick layer works well to control the nucleation sites and grow the desired orientation. $LaNiO_3$ serves as an orienting perovskite seed layer.[4] The crystallinity of the Mn doped PZT film by CSD shows the same results as undoped PZT films on Ni foil.[16]

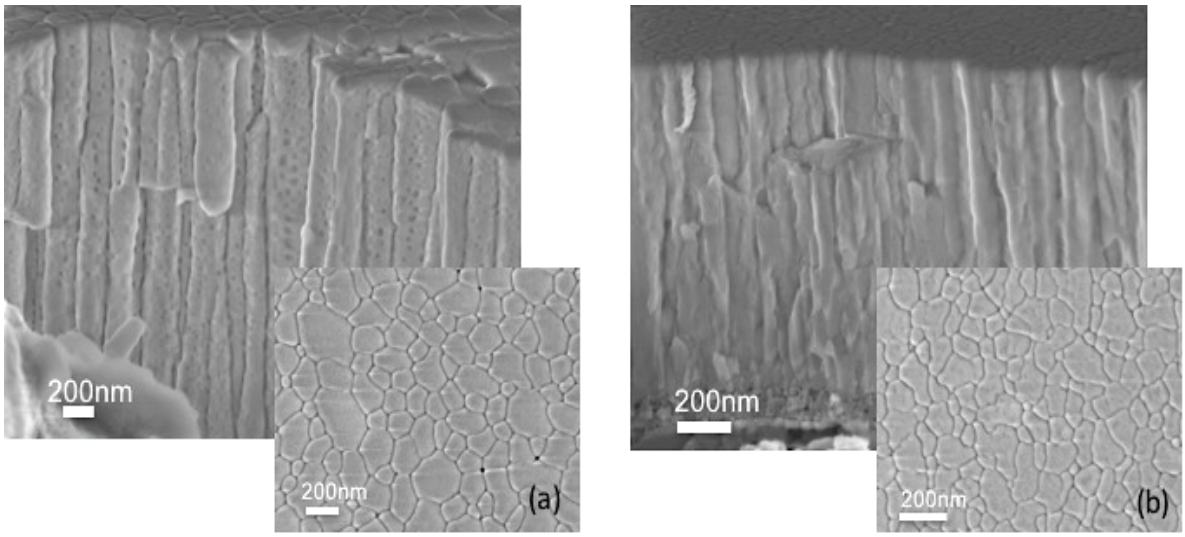

Figure 4-5. Comparison of surface FE-SEM image of PZT/LNO/HfO_2/Ni cross-sections of PZT films deposited by (a) sputtering and (b) CSD.

Figure 4-5 (a), (b) show surface and cross section microstructures of the sputtered PZT and sol-gel PZT films. There is no evidence of pyrochlore phase on PZT films grown by either method. In the case of sputtered PZT film, a columnar PZT structure with nanoporosity is plainly shown in Figure 5(a). These pores influence the ferroelectric and piezoelectric properties.[23] On the other hand, the 1% Mn doped PZT (52/48) CSD films have dense and columnar grains.[16]

Figures 4-6 and 4-7 show the P-E hysteresis loops and dielectric properties of various thickness PZT films grown by either sputtering or CSD. With 200 μm diameter Pt electrodes, all

of the 100Hz, polarization-electric field hysteresis loops display well-saturated, square hysteresis loops with large remanent polarization (P_r ~ 40 μC/cm^2).[4,17] There is no significant difference between the various specimens as shown in Figure 4-6.

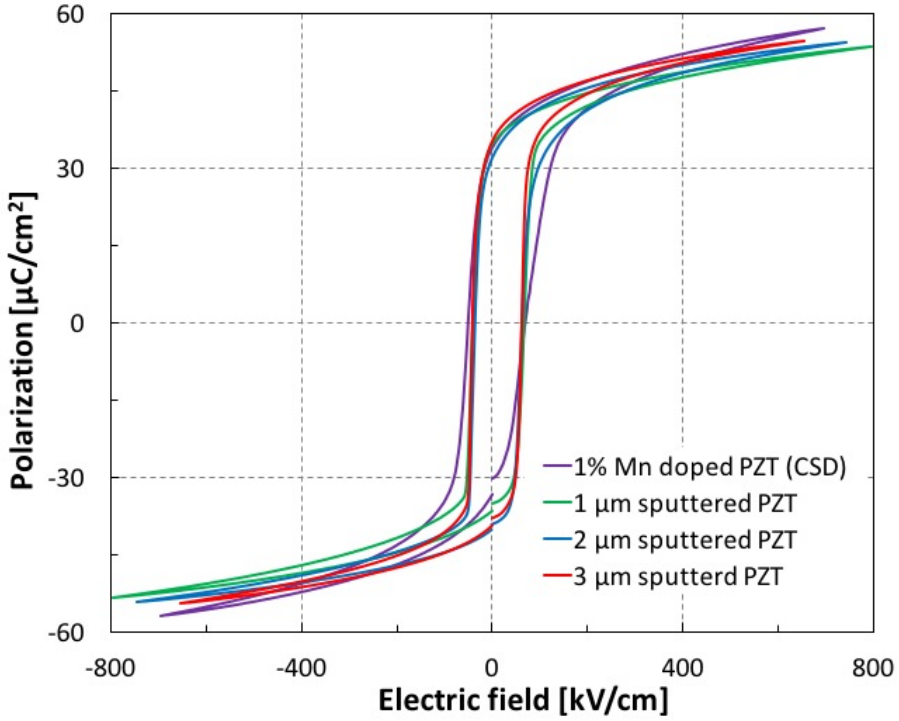

Figure 4-6. P-E hysteresis loops of 1~3 μm thick sputtered PZT films and 1%Mn doped sol-gel PZT film on Ni foils.

To confirm the material figure of merit for piezoelectric energy harvesters, measurements of the piezoelectric $e_{31,f}$ coefficient and the dielectric constant (ε_r) are essential to directly compare with the power generation from a unimorph cantilever made from the same piece of PZT film. The dielectric properties measured at a 30 mV oscillation level for all samples after P-E measurement with high electric field (~800kV/cm) are shown in Figure 4-7. Dielectric constants for the sputtered undoped PZT films and Mn doped PZT film by CSD were 390 and

500 respectively with a loss tangent of 3% at 10 kHz. The comparatively low relative permittivities are a result of a large *c*-domain population caused by a combination of the crystallographic orientation and compressive stress in the PZT film on cooling.[17] Furthermore, the ε_r of sputtered PZT films are lower than that of Mn doped PZT film by CSD. This is a consequence of the porosity in the sputtered films.

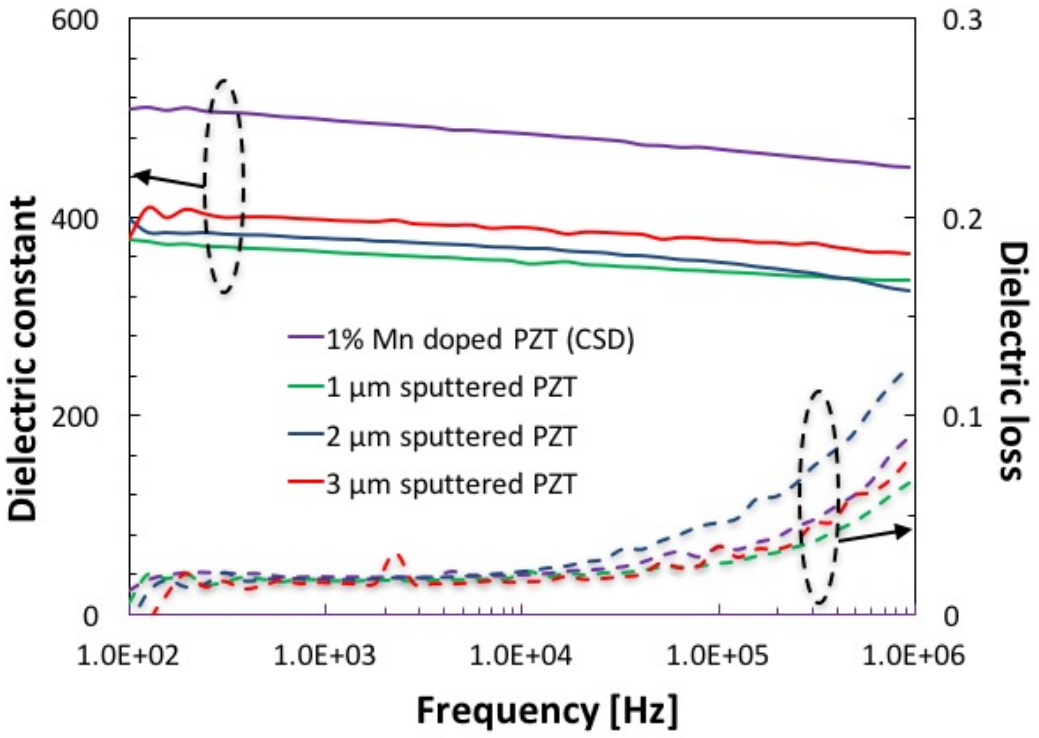

Figure 4-7. Dielectric constant and loss of 1 ~ 3 μm thick sputtered PZT films and 1%Mn doped sol-gel (1 μm) PZT film on Ni foils respectively.

In general, the poling conditions influence how well the dipoles are oriented in the allowable direction closest to the direction of applied field, and how stable the net polarization is after removing the applied field.[15] The stability of oriented dipoles is impacted by the build-up of an internal bias field after poling. It is well known that PZT ceramics undergo extensive 180°

and non-180° domain switching on poling. PZT films are at least partially mechanically clamped by the substrate and so tend to demonstrate limited ferroelastic reorientation.[23]

The $e_{31,f}$ of various samples were determined by the wafer flexure method.[24] To measure the piezoelectric response of PZT films, the sputtered PZT films were poled at 3 times the coercive field for 10 min at room temperature (RT), while Mn doped PZT films by CSD were measured either unpoled, poled at RT, or hot poled at 150°C. Figure 4-8 exhibits the results of $e_{31,f}$ obtained from different thicknesses of sputtered PZT films and various poling conditions of sol-gel Mn doped PZT film.

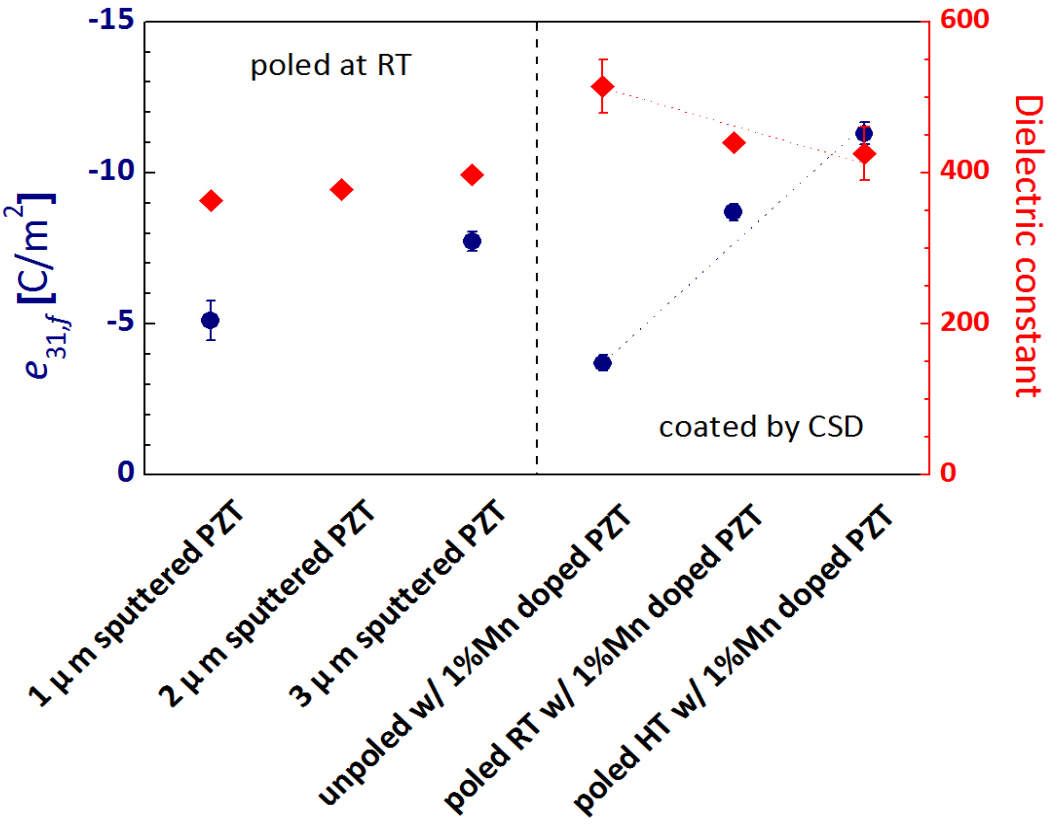

Figure 4-8. Transverse piezoelectric coefficient and dielectric constant as a function of thickness, and poling condition [blue circle ($e_{31,f}$), red diamond (dielectric constant)].

For the 1% Mn doped sol-gel PZT films on Ni foil, the dependence of the piezoelectric transverse coefficient on the poling process was assessed. Figure 4-8 shows that hot poled films have higher $e_{31,f}$ than either unpoled films or those poled at room temperature. It is believed that the elevated temperatures enhanced the dipole alignment and the stabilization of the domain structure.[15] The higher $e_{31,f}$ produced by hot poling improves the efficiency of piezoelectric energy harvesters.[14]

4.3.2 Performance of Harvester Dependence on Thickness of Film

To demonstrate the use of PZT films with strong out-of-plane polarization in a vibrational energy harvesting system, 31 mode cantilever beams were fabricated using strongly {001} textured 1~3 μm thick sputtered and 1μm thick sol-gel Mn doped PZT films on Ni foils. Figure 4-3(a) shows a fabricated energy harvesting device with a 0.4g brass proof mass. The top electrode area is 0.122 cm^2. The active area of the fabricated energy harvester, including the proof mass, is around 0.385 cm^2. The resonance frequency of each device was found by sweeping the input frequency for the shaker, and detecting the open circuit voltage on an oscilloscope. At the resonance frequency, the device was excited at an acceleration level of 1.0 G (G=9.8 m/s^2). The maximum voltages ($V_{max}=V_{pk-pk}/2$) of 1 μm and 3μm sputtered PZT film were measured to determine the optimum load resistance for maximum power transfer ($P_{max}=V_{max}^2/R$) as shown in Figure 4-9(a). The maximized output power of 1 μm and 3 μm thick sputtered PZT films on Ni foil was generated at the optimal load resistance of 50 kΩ and 100 kΩ respectively. At the optimal load resistance, the maximum output power depends on frequency as shown in Figure 4-9(b).

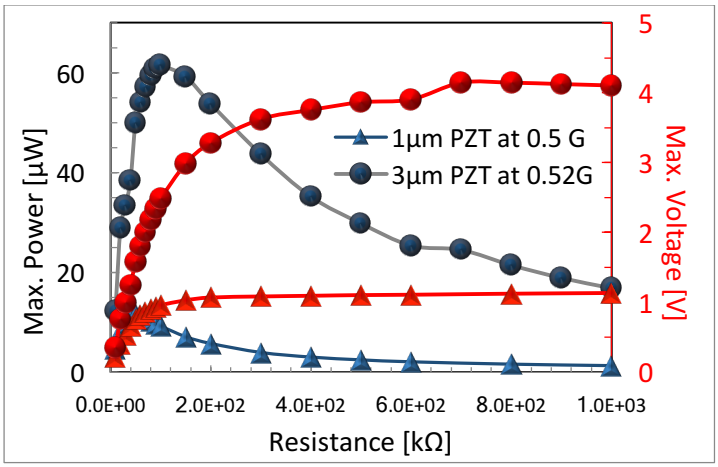

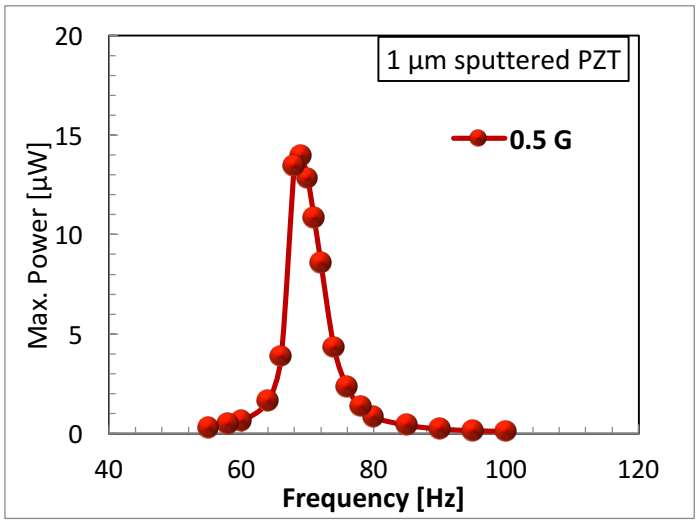

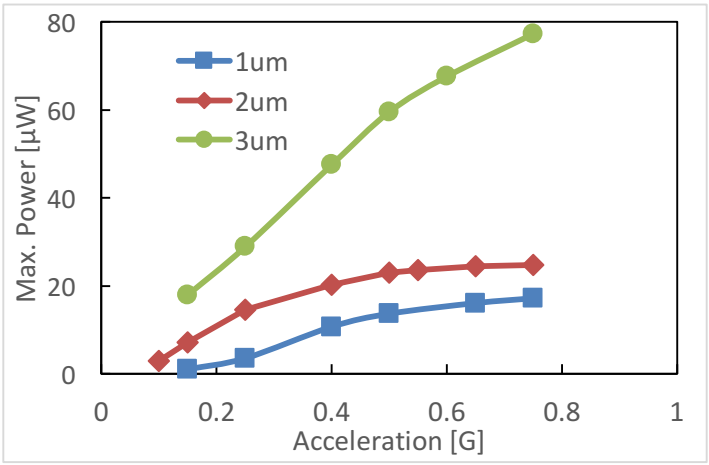

Figure 4-9. Maximum output power as a function of (a) external load resistance, (b) frequency at 0.5 G, and (c) acceleration level with optimum load resistance of piezoelectric energy harvester using 1~3 μm thick (001) oriented sputtered PZT films on Ni foil (25 μm) measured at resonance. Variations in dimensions produced small differences in frequencies for the samples.

The sample with 1 μm thick sputtered PZT film has a resonance frequency of 69 Hz. Most of the devices prepared in this work have similar resonance frequencies (around 65 Hz) with slight deviations mainly caused by small differences of dimension. The variation is small enough to enable direct comparison.

The mechanical quality factor (Q) and mechanical damping ratio (ζ) also have strong roles in controlling the achievable output power. In this work, Q was defined using the half power method as: $Q = f_r/(f_b - f_a)$ where f_r is the resonance frequency and the bandwidth at the half-maximum amplitude (FWHM) is $f_b - f_a$.[25,26]

High Q-factors of a device indicate high power sensitivity as function of frequency; *i.e.* a narrow frequency bandwidth leads to a tremendous drop of the output power if the input vibration frequency deviates from the resonance frequency of device. On the other hand, a lower Q-factor with a broad frequency bandwidth is suitable to increasing scavenged energy from a wide spectrum of environmental vibration.[27] The mechanical quality factor of all samples was around 13.9±1.3. The mechanical damping ratio ($\zeta = (f_b - f_a)/2f_r$) was 3.6% in Figure 4-9 (b). The Q value is lower than the previous reported Q values of (233) PZT on Si, (85) transferred PZT to stainless steel PZT, and (30) KNN on metal foil.[25,27,28]

Figure 4-9 (c) exhibits the maximum output power as a function of acceleration level for samples with 1~3 μm thick sputtered PZT films. Overall, the output power increases rapidly with acceleration level below 0.5 G acceleration and then rises more slowly. Ideally, the output power is proportional to the square of the acceleration level (A) per equation (4.1). However, an increase of air damping and nonlinear elastic compliance at large stresses (large acceleration levels) can provide lower power densities as a function of acceleration level (Figure. 4-10).[27,29]

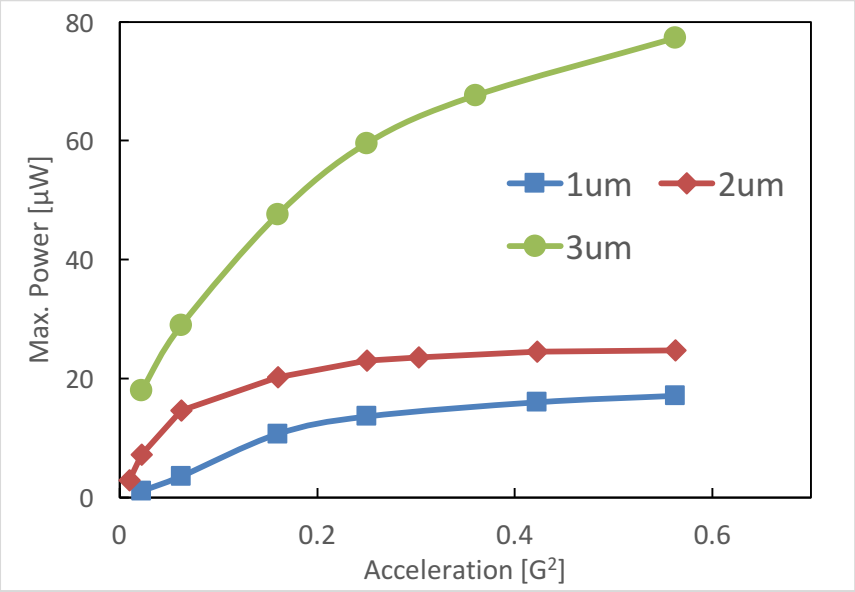

Figure 4-10. Maximum output power as a function acceleration level with optimum load resistance of piezoelectric energy harvester using 1~3 μm thick (001) oriented sputtered PZT films on Ni foil (25 μm) measured at resonance.

4.3.3 Performance of Harvester Dependence on Poling Condition

As mentioned earlier, improvement of FoM of piezoelectric materials depends on the poling condition such as electric field, time and temperature. Thus, the poling efficiency strongly impacts the output of the piezoelectric harvester.[14]

Using Mn doped sol-gel PZT films on Ni foil, the output voltage was measured for different poling conditions. Figure 4-11 exhibits the output voltage and generated power as a function of external load resistance for samples that are unpoled, poled at room temperature (RT) and poled at 150 °C (high temperature (HT)). For the same acceleration level (0.5 G) and frequency, it is observed that the hot poling process improves the extracted power compared with the performance of either unpoled or RT poled samples, due to more efficient domain alignment.[14]

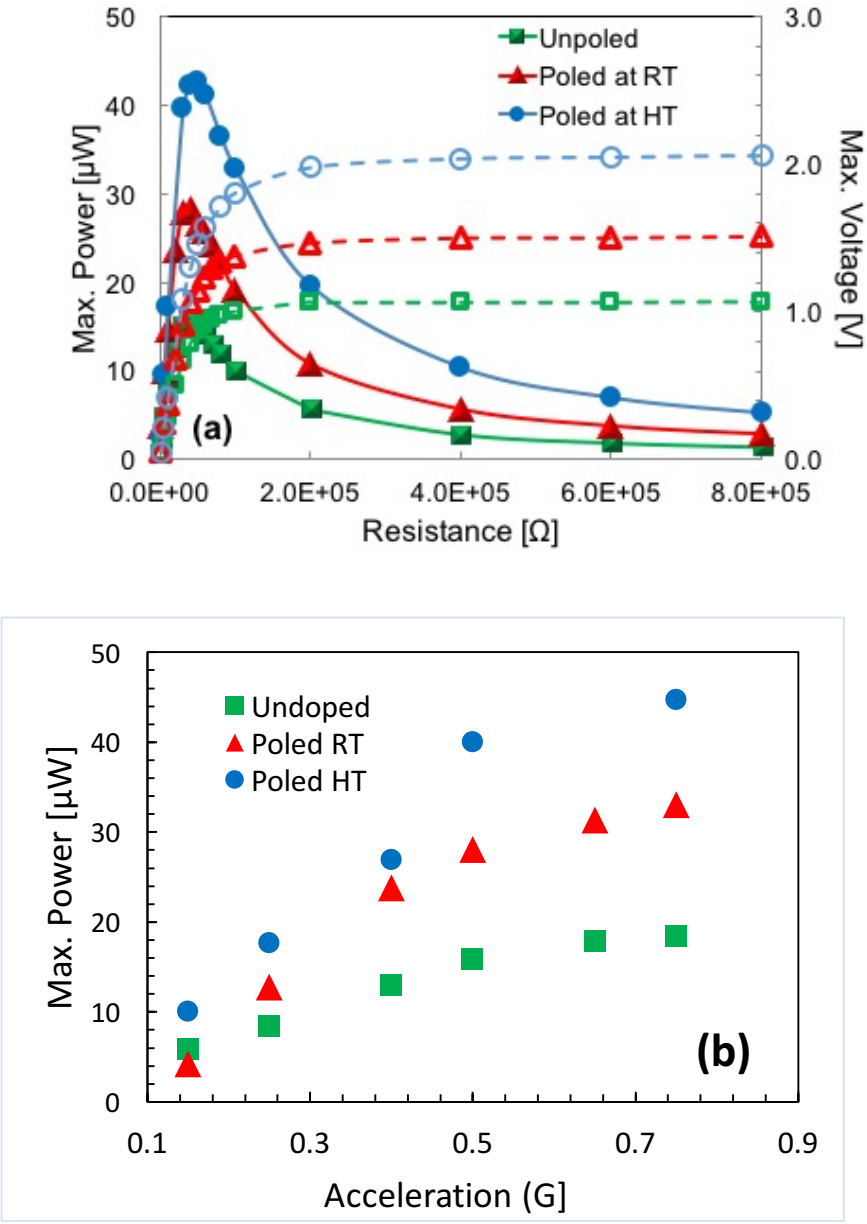

Figure 4-11. Maximum output (bold) power as a function of (a) external load resistance at 0.5 G and (b) acceleration level at optimum load resistance of piezoelectric energy harvester using 1 μm thick 1%Mn doped sol-gel PZT films on Ni foil at resonance.

The optimum load resistance of unpoled and RT poled samples was about 40 kΩ. On the

other hand, the optimum load resistance was 50 kΩ after hot poling treatment. This is because the electrical load resistance matching depends on the capacitance of the device.[25] Hot poling reduced the dielectric constant of the PZT film due to significant preferential *c*-domain alignment.

Figure 4-11(b) shows the output power of a harvester as a function of acceleration amplitude using 1 mol% Mn doped sol-gel PZT films under different poling conditions. Overall, the hot poling process delivers better output performance than either unpoled or room temperature poled samples as shown in Figure 4-11(b). Thus, enhanced piezoelectric response contribute and reduction of permittivity from the poling improve the generated power from the cantilever harvester.[14] Similar trends were observed using sputtered PZT films on Ni foil in Figure 4-9(c). For both deposition methods, at increased acceleration level, the power does not rise as fast as predicted, presumably due to the enhancement of mechanical damping.[28]

Table 1 shows the relationship between piezoelectric, dielectric properties and output performance of PZT films on Ni foil based on the results of this work. 3 μm thick sputtered films on Ni foil shows better output performance compared with thinner PZT films, even if they have similar piezoelectric and electrical properties. Thus, there is an incentive to grow thicker films for harvesting. The result is consistent with the simulation developed by Xue and Roundy in terms of relation between average power and the ratio of piezoelectric films (t_{PZT}) to total beam thickness (t_{total}).[30] The simulation based on Erturk and Inman's distributed bimorph beam model under base excitation demonstrates that the average power is significantly increased by increasing the ratio of thickness (t_{PZT}/t_{total}) from 0 to 0.4.[31]

Table 4-1. Summary of the performance of sputtered and sol-gel PZT films on Ni foils.

Thickness of PZT film	Poling condition	FoM	Res. Freq. @ 0.5 G [1G ≈ 9.8 m/s^2]	Max. Voltage [mV]	Optimal Load Resistance [kΩ]	Max. Power [μW]
1 μm (Sputtered)		**0.071**	69	760	50	**12**
2 μm (Sputtered)	3× E_C at R.T		62	1190	70	**23**
3 μm (Sputtered)		**0.15**	72	2440	100	**60**
1%Mn doping PZT 1μm (CSD)	No poling	**0.026**	63	790	40	**15.6**
	Poling at RT	**0.17**	63	1065	40	**28**
	Poling at 150ºC	**0.33**	63	1460	50	**42.6**

4.4 Conclusions

In summary, piezoelectric energy harvesters using oriented PZT films grown either by sputtering or CSD were successfully fabricated with similar dimensions to determine the relationship between output power performance, PZT thickness, and piezoelectric response. It was found that the volume of the PZT layer strongly depended upon the power output of the devices under the same conditions. All devices operated around 65 Hz. Piezoelectric energy harvesters with 3 μm thick sputtered PZT film on Ni resulted in an average power density of 1036 μW/cm^2·G^2. An enhanced power density of the harvester (582 μW/cm^2·G^2) was achieved using an elevated temperature poling process, with 1% Mn doped sol-gel PZT films on Ni foil, relative to room temperature poling. This result promises the extraction of energy from ambient vibration with high power density for use in devices consuming energy in microwatt ranges.

4.5 References

[1] C. R. Bowen, H. A. Kim, P. M. Weaver, and S. Dunn "Piezoelectric and ferroelectric materials and structures for energy harvesting applications," *Energy & Environmental Science* **7**, 1 (2014) 25.

[2] S.-G. Kim, S. Priya, and I. Kanno, "Piezoelectric MEMS for energy harvesting" *MRS Bulletin* **37** (2012) 1039.

[3] A. Hajati and S. G. Kim, "Ultra-wide bandwidth piezoelectric energy harvesting," *Applied Physics Letters* **99**, 8 (2011) 083105.

[4] H. G. Yeo, X. Ma, C. Rahn, and S. Trolier-McKinstry, "Efficient piezoelectric energy harvesters utilizing (001) textured bimorph PZT films on flexible metal foils," *Advanced Functional Materials* **26**, 32 (2016) 5940.

[5] L. Dhakar, H. Liu, F.E.H. Tay, C. Lee, "A new energy harvester design for high power output at low frequencies," *Sensors and Actuators A* **199** (2013) 344.

[6] S. Roundy and P. K. Wright "A piezoelectric vibration based generator for wireless electronics," *Smart Materials and Structures* **13**, 5 (2004) 1131.

[7] C. B. Yeager and S. Trolier-McKinstry, "Epitaxial $Pb(Zr_x,Ti_{1-x})O_3$ ($0.30 \leq x \leq 0.63$) films on (100)MgO substrates for energy harvesting applications," *Journal of Applied Physics* **112**, 7 (2012) 074107.

[8] N. Lederman, P. Muralt, J. Baborowski, S. Gentil, K. Mukati, M. Cantoni, A. Seifert, and N. Setter, "{100}-Textured, Piezoelectric Pb(Zr, Ti)O_3 thin films for MEMS: Integration, deposition and properties," *Sensors and Actuators A* **105**, 2 (2003) 162.

[9] F. Calame, and P. Muralt, "Growth and properties of gradient free sol-gel lead zirconate titanate thin films," *Applied Physics Letters* **90**, 6 (2007) 062907.

[10] K. Wasa, T. Matsushima, H. Adachi, I. Kanno, and H. Kotera, "Thin-film piezoelectric materials for a better energy harvesting MEMS," *Journal of Microelectromechanical Systems* **12**, 2 (2012) 451.

[11] S. Roundy, "On the effectiveness of vibration-based energy harvesting," *Journal of Intelligent Material Systems and Structures* **16**, 10 (2005) 809.

[12] T. M. Kamel, R. Elfrink, M. Renaud, D. Hohfeld, M. Goedbloed, C. deNooijer, M. Jambunathan, and R. von Schaijk, "Modeling and characterization of MEMS-based piezoelectric harvesting devices," *Journal of Micromechanics and Microengineering* **20**, 10 (2010) 105023.

[13] M. A. Dubois, and P. Muralt, "Measurement of the effective transverse piezoelectric coefficient $e_{31,f}$ of AlN and Pb $(Zr_x,Ti_{1-x})O_3$ thin films," *Sensors and Actuators A* **77**, 2 (1999) 106.

[14] E. M. A. Fuentes-Fernandez, B. E. Gnade, M. A. Quevedo-Lopez, P. Shah, and H. N. Alshareef, "The effect of poling conditions on the performance of piezoelectric energy harvesters fabricated by wet chemistry," *Journal of Materials Chemistry A* **3**, 18 (2015) 9837.

[15] A. L. Kholkin, D. V. Taylor and N. Setter, "Poling effect on the piezoelectric properties of lead zirconate titanate thin films," *Applications of Ferroelectrics, ISAF 98, Proceeding of the Eleventh IEEE International Symposium on*, Montreux, Switzerland (1998) 69

[16] H.G. Yeo, S. Trolier-McKinstry, "{001} Oriented piezoelectric films prepared by chemical solution deposition on Ni foils," *Journal of Applied Physics* **116**, 1 (2014) 014105.

[17] Y. Tsujiura, E. Suwa F. Kurokawa, H. Hida and I. Kanno, "Modeling of metal-based piezoelectric MEMS energy harvesters," *Micro-NanoMechatronics and Human Science* (MHS), 2013 International Symposium on. IEEE, 2013.

[18] J. F. Shepard, Jr., F. Chu, I. Kanno, and S. Trolier-McKinstry "Characterization and aging

response of the d31 piezoelectric coefficient of lead zirconate titanate thin films," *Journal of Applied Physics* **85**, 9 (1999) 6711.

[19] P. Bintachitt, "Local origin of macroscopic properties and patterning in $PbZr_{1-x}Ti_xO_3$ films," Doctoral dissertation, THE PENNSYLVANIA STATE UNIVERSITY (2009).

[20] H. Daniel Chen, K. R. Udayakumar, Christopher J. Gaskey, and L. Eric Cross, Jonathan J. Bernstein and Lance C. Niles, "Fabrication and Electrical Properties of Lead Zirconate Titanate Thick Films," *Journal of the American Ceramic Society* **79**, 8 (1996) 2189.

[21] C. S. Park, J. W. Lee, G. T. Park, H. E. Kim, and J. J. Choi, "Microstructural evolution and piezoelectric properties of thick Pb $(Zr,Ti)O_3$ films deposited by multi-sputtering method: Part I. Microstructural evolution," *Journal of Materials Research* **22**, 05 (2007) 1367.

[22] G. A. Schneider, "Influence of electric field and mechanical stresses on the fracture of ferroelectrics," *Annual Review of Materials Research* **37**, 1 (2007) 491.

[23] S. Trolier-McKinstry and P. Muralt "Thin films piezoelectric for MEMS," *Journal of Electroceramics* **12**, (2004) 7.

[24] R. Wilke, P. Moses, P. Jousse, C. Yeager, and S. Trolier-McKinstry, "Wafer mapping of the transverse piezoelectric coefficient, $e_{31,f}$, using the wafer flexure technique with sputter deposited Pt strain gauges," *Sensors and Actuators A* **173**, 1(2012) 152.

[25] T. Shiraishi, N. Kaneko, M. Kurosawa, H. Uchida, Y. Suzuki, T. Kobayashi, and H. Funakubo, "Vibration-energy-harvesting properties of hydrothermally synthesized $(K,Na)NbO_3$ films deposited on flexible metal foil substrates," *Japanese Journal of Applied Physics* **54** (2015) 10ND06.

[26] B. Crowell, "Vibrations and Waves," *Light and Matter* online text series, **Ch.2** (2006).

[27] D. Shen, J.-H. Park, J. Ajitsaria, S.-Y. Choe, H. C. Wikel III and D.-J. Kim, "The design,

fabrication and evaluation of a MEMS PZT cantilever with an integrated Si proof mass for vibration energy harvesting," *Journal of Micromechanics and Microengineering* **18** (2008) 055017.

[28] K. Morimoto, I. Kanno, K. Wasa, and H. Kotera, "High-efficiency piezoelectric energy harvesters of c-axis-oriented epitaxial PZT films transferred onto stainless steel cantilevers," *Sensors and Actuators A* **163** (2010) 428.

[29] Y. Tsujiura, E. Suwa, F. Kurokawa, H. Hida, K. Suenaga, K. Shibata, and I. Kanno, "Lead-Free Piezoelectric MEMS Energy Harvesters of (K,Na)NbO_3 Thin Films on Stainless Steel Cantilevers," *Japanese Journal of Applied Physics* **52** (2013) 09KD13.

[30] unpublished data from Tiancheng Xue and Shad Roundy, the University of Utah

[31] A. Erturk, and D. J. Inman, "An experimentally validated bimorph cantilever model for piezoelectric energy harvesting from excitations," *Smart Materials and Structures* **18**, 2 (2009) 025009.

Chapter 5

Efficient Piezoelectric Energy Harvesters Utilizing (001) Textured Bimorph PZT Films on Flexible Metal Foils*

5.1 Introduction

There are numerous applications where it would be desirable to track system responses over time, ranging from wearable sensor devices for health and fitness, to emplaced wireless sensors for infrastructure and building monitoring. In most cases, such devices require periodic recharging or replacement of batteries. However, with the on-going introduction of low power electronics, opportunities are being opened to replace batteries with solar, thermal and mechanical harvesters. Piezoelectric energy harvesters can extract energy from human activities such as walking, breathing, and typing, or from motion of walls, air ducting, or bridges without limitations on the location and time of use (*e.g.* indoors or at night).[1,2] However, mechanical energy harvesting is faced by challenges such as weak base excitations with low natural frequency (< 10 Hz)[3,4] and fragile structures that are susceptible to shock. To overcome these challenges, the piezoelectric energy harvester should have high efficiency, be flexible, and have a low resonance frequency with wide bandwidth. Numerous methods to improve the output power density and reduced resonance frequency have been explored, including advanced mechanical design,[5] maximizing intrinsic piezoelectric materials properties[6,7] and using a flexible passive layer.[8,9]

---

* *The majority of this chapter is reproduced from H. G. Yeo, X. Ma, C. Rahn "Efficient Piezoelectric Energy Harvesters Utilizing (001) Textured Bimorph PZT Films on Flexible Metal Foils." Advanced Functional Materials 26, 32 (2016) 5940.*

In the last decade, microelectromechanical (MEMS) energy harvesters based on piezoelectric materials such as AlN and $Pb(Zr,Ti)O_3$ (PZT) have been studied for use in harvesting energy from small amplitude mechanical vibration.[10~12] Improving the piezoelectric material for a piezoelectric energy harvester (PEH) can be pursued via an energy harvesting figure of merit. The maximum extractable electric power generated at the resonance frequency of a $e_{31,f}$ mode cantilever structure is [13,14]

$$Power_{max} = \frac{1}{4}\left(\frac{e_{31,f}^2}{\varepsilon_r \varepsilon_0} \cdot \frac{m}{Y}\right)\frac{a^2}{\omega} \qquad (5.\ 1)$$

where m = mass, ω = angular frequency, Y = Young's modulus, ε_0 = vacuum permittivity, and a is the acceleration. The in-plane piezoelectric coefficient ($e_{31,f}$) and the relative permittivity (ε_r) control the energy harvesting figure of merit (FoM) = $(e_{31,f})^2/\varepsilon_r$ when the mechanical energy is stored in the passive layer. The orientation of the PZT grains strongly influences the figure of merit.[7,15] In particular, strongly (001) oriented PZT films, which have a significant fraction of the ferroelectric polarization directed out-of-plane, have large FoM.[16]

From the standpoint of improving the toughness and reliability of the piezoelectric energy harvester, a metal foil is preferable compared to Si, the typical substrate for MEMS.[17] Moreover, thin metal foils enable low resonance frequencies without etching, and are easily machined. Morimoto et al.[8] reported a cantilever piezoelectric energy harvester using epitaxial PZT thin films transferred onto stainless steel that shows output power of 5.3 μW at 5.0 m/s^2 and 126 Hz without a proof mass. In much the same way, $(Na_{0.5}K_{0.5})NbO_3$ (NKN) piezoelectric thin films coated on Ni-based metal foils were investigated for vibration energy harvesters.[18] Another benefit of using metal substrates for PEH is that copper and nickel have larger thermal expansion coefficients than many perovskite films. This produces compressive stresses in the tetragonal PZT film on cooling, increasing the volume fraction of the out-of-plane polarization direction.[19]

Thus, high compressive stresses in {001} PZT films give rise to an improved FoM for energy harvesting.[7,19, 20,21]

Typical PEH designs use a fixed-free cantilever beam configuration with or without a proof mass. While fixed-free cantilevers undergo larger strains compared to bridges, for the same input force, the strain distribution along the piezoelectric beam is not uniform.[22] Thus, it would be preferable to improve the efficiency of the 1st mode shape to maximize power by uniformly straining PZT films while preventing overstrain near the clamping points. Ma et al.[23] proposed a piezoelectric compliant mechanism (PCM) design for PEH that leads to a much more uniform strain distribution. Simulations for the compliant mechanical design suggested that this configuration can reach 100% mode shape efficiency by curving the beam into a perfect parabola, compared to 24% efficiency for a cantilever beam.[23] PZT films on metal foils are well suited for this design. To achieve a high efficiency piezoelectric energy harvester operated at a low resonance frequency and acceleration level, this study focuses on using bimorph textured PZT films on Ni foil in a PCM harvester. The PZT films have stress-tailored domain structures that provide efficient electromechanical conversion with high FoM. Bimorph piezoelectric energy harvesters using piezoelectric ceramics are well known but there is little literature on implementing this idea in films.[24] Indeed, the deposition of PZT films in a bimorph structure on a released structure on a Si substrate is very difficult using typical microfabrication processes.[2,25]

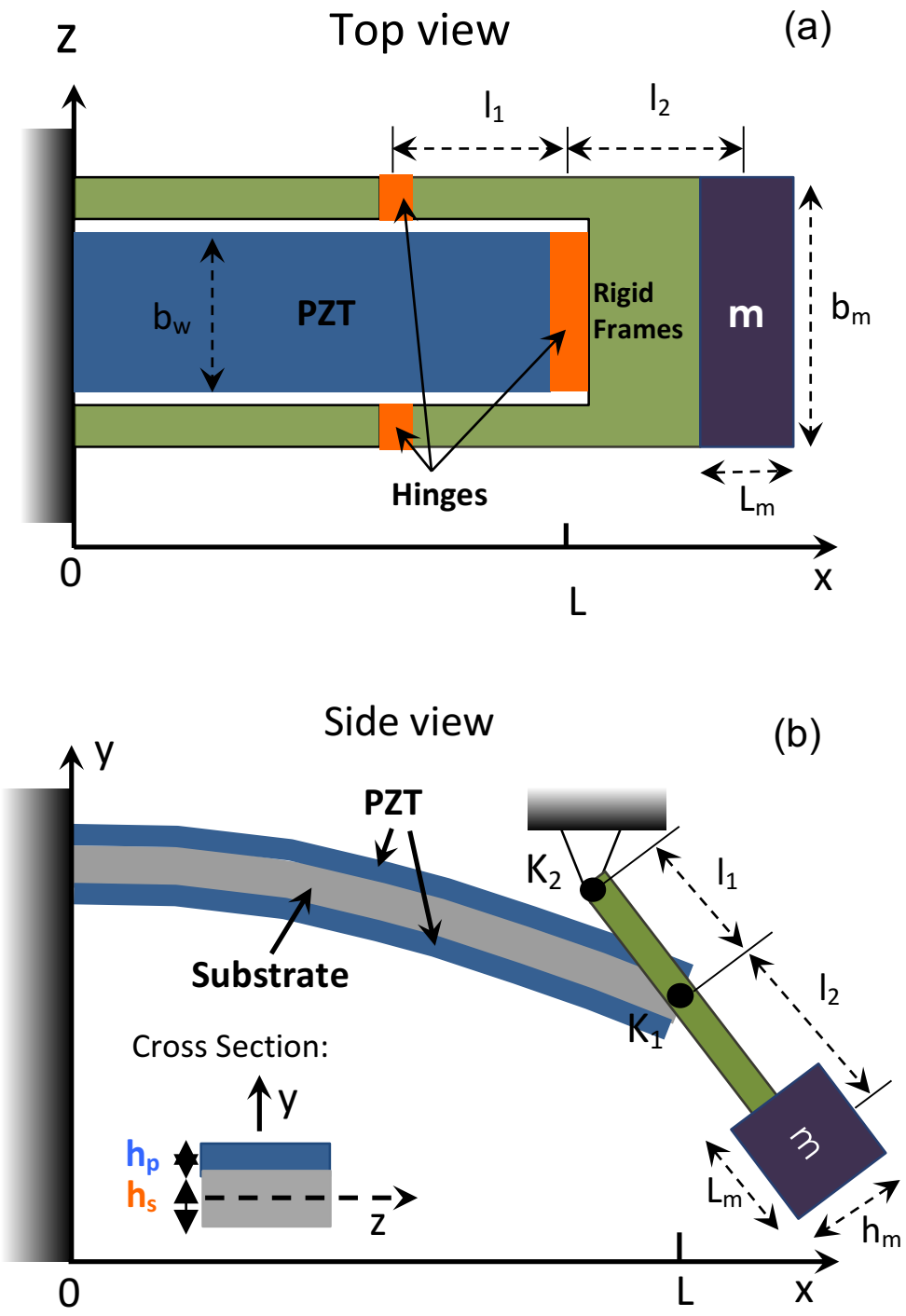

Figure 5-1. Schematic (a) top and (b) side views of PCM

A PCM energy harvester consists of three parts, as shown schematically in Figure 5-1. First, the bimorph PZT beam electroded on the major surfaces converts mechanical energy to

electrical energy. A two part rigid frame is employed; the U-shaped frame elements are connected to the compliant hinges which ideally have zero stiffness, to make a single structure. A third compliant hinge, with a torsional spring stiffness K_1, connects the PZT beam to the rigid frame on the side with the proof mass. In the design of the PCM, the shape of the deflected PZT beam length can be adjusted by the values of the spring constant K_1 and equivalent mass as described elsewhere.[23] In this work, a, PCM device was fabricated from {001} oriented PZT films on Ni foils, epoxy plates for the rigid frame and 75 μm thick polyethylene terephthalate (PET) films with low stiffness for the compliant hinges. The output power of the fabricated PCM device was evaluated as a function of resonance frequency, acceleration level and load resistance. Additionally, the displacement distribution along the PZT beam was characterized.[23]

5.2 Experimental Procedure

5.2.1 Fabrication of the Buffer and Seed Layers on Ni Foil

For fabrication of bimorph PZT beams, an amorphous HfO_2 passivation layer was coated on both sides of the Ni simultaneously, by propping the Ni foil at an angle to the sample stage using glass spacers; atomic layer deposition was utilized at 200 °C for 300 cycles (0.95 Å/pulse). 0.2M $LaNiO_3$ chemical solutions based on a 2-methoxyethanol (2MOE) solvent were spin-coated on one side of the Ni foil at a time and pyrolyzed on a hot plate in air. Each $LaNiO_3$ layer was crystallized by RTA at 700 °C in air; these processes were repeated 5 times to fabricate a 100nm thick (100) oriented LNO layer. The other side was coated with $LaNiO_3$ following exactly the same procedure.

Table 5-1. RF magnetron sputtering parameters for PZT films.

Target	PZT (52/48) + 10% excess PbO+1% Mn
Substrate	$LaNiO_3/HfO_2/Ni/HfO_2/ LaNiO_3$
RF Power	88 Watts
Chamber Pressure	4 mTorr
Gas	Ar only
Substrate Temperature	Room Temp.
Time	12500 sec for ~0.5 μm
Crystallization temperature	650°C in O_2 atmosphere

PZT layers for the bimorph were fabricated by rf magnetron sputtering using a 10% Pb excess and 1% Mn doped $Pb(Zr_{0.52}Ti_{0.48})O_3$ target under the conditions shown in Table 5-1. The 10% Pb excess compensated for lead content due to PbO volatility during sputtering and crystallization.[26] Mn doping provided a lower dielectric permittivity following poling than could be achieved in undoped PZT as a result of an internal bias; this increased the FoM of the energy harvester.[7] To achieve (001) preferred orientation in PZT films by room temperature sputtering, it is necessary to control nucleation and growth during crystallization.

Ideally, heterogeneous nucleation sites on (100) oriented LNO enables preferred (001) oriented PZT films.[19,27,28] However, if random surface nucleation occurs during RTA crystallization, the PZT orientation tends to be random.[28] In practice, it was found that when amorphous PZT films thicker than 0.5 μm were crystallized, surface nucleation was observed before completion of the growth of columnar grains from interface nucleation sites.[29] Thus, in order to maintain orientation, 0.5 μm thick PZT layers were sputtered at room temperature and post-annealed by RTA iteratively in order to reach the desired thickness (~ 3 μm).

Each 0.5 μm PZT layer was grown on alternative sides of the Ni. This procedure helped

keep the samples flat during crystallization and suppress large transverse curvature after crystallization due to thermal expansion mismatch between PZT films and Ni foil (*e.g.* the average thermal expansion coefficient of Ni is 17.7×10^{-6}/K and that of PZT 9.1×10^{-6}/K).[30,31] Figure A-1 (in the first appendix) shows pictures of typical unimorph and bimorph PZT films on Ni foil. The bimorph beams are seen to be much flatter due to balancing of the stresses on both sides of the metal.

5.2.2 Pt Top Electrode Coating and Poling

Pt top electrodes (20 mm by 10mm) were coated on both sides of the PZT film via rf-sputtering (Kurt J. Lesker) and were patterned by a lift-off process. Alignment between the two electrodes was accomplished using a contact printer (Karl Suss MA/BA6). The dimensions of the PZT beam were made a little larger than the electrode size to avoid shorting from thermal or mechanical damages at the edge of beam induced by cutting the foil either with a laser or with scissors. It was found that cracks from the edge extended < 200 μm into the beam. Finally, large-scale flexible bimorph {001} oriented PZT beams (dimension of 21.5 mm by 11.5 mm) were fabricated. The Ni substrate that served as the middle electrode was exposed by scratching the oxide layers with a razor blade. A resurrection treatment as described by Johnson-Wilke et al.[32] was used to remove or reduce any conducting pathways on these large area electrodes. The upper and lower PZT layers were then poled in opposite directions[33,34] using a high DC bias ($3\times E_c$, or 47V) for 10 min at 150 °C. For poling, the bottom electrode (Ni substrate) was held at a positive voltage and the two Pt top electrodes were grounded. The opposing polarization directions between the two layers leads to an increase in the output voltage in series connection.[35]

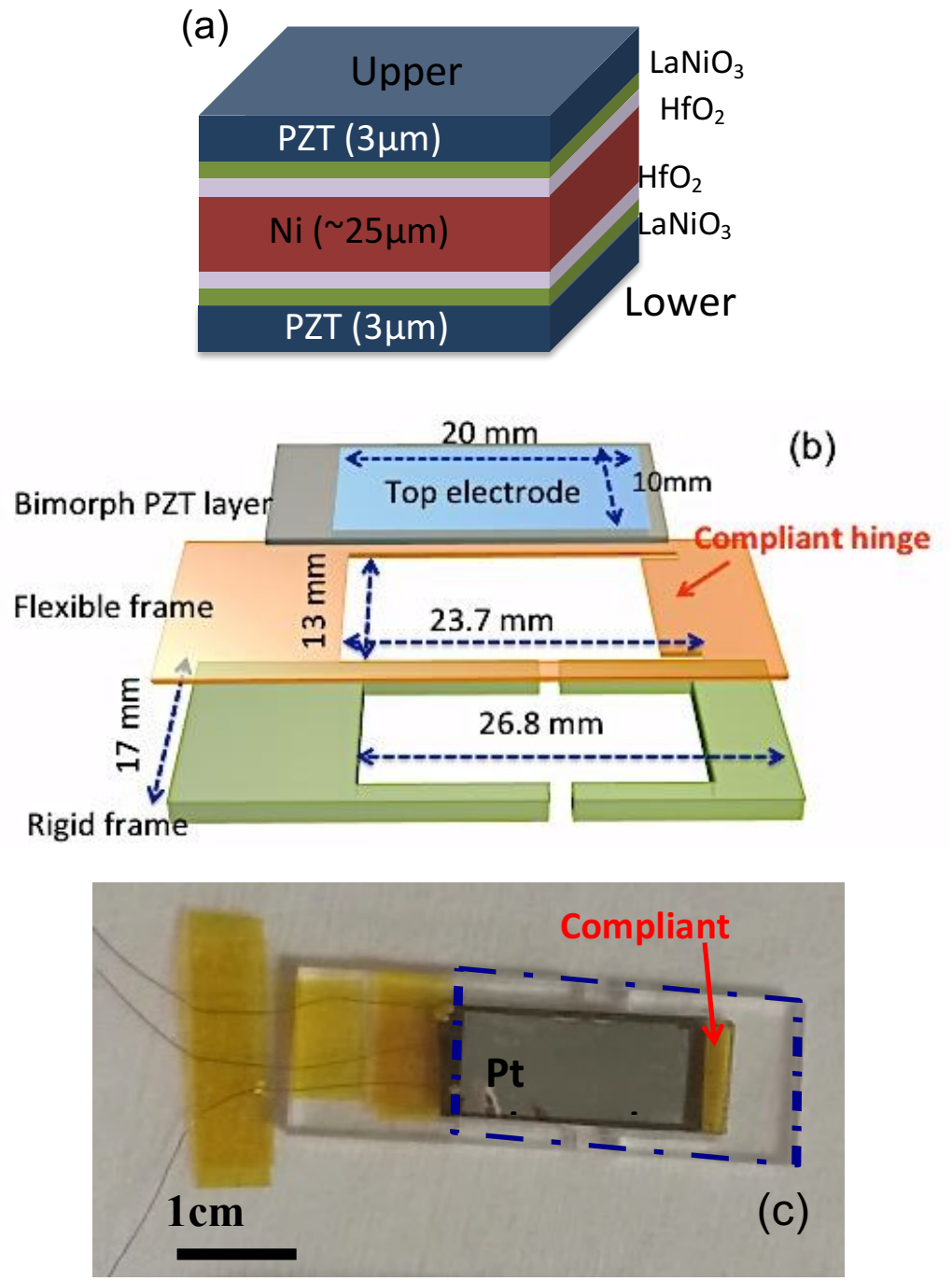

Figure 5-2. (a) Schematic of bimorph PZT film stacks with $LaNiO_3$ and HfO_2 layers on Ni. (b) Schematic illustration of each part; bimorph PZT beam with top electrode, flexible, and rigid frame with dimensions. (c) Prototype PCM device integrated with bimorph PZT film, PET hinge and acrylic plates.

5.2.3 Assembly

Table A-1 (Appendix A) shows parameters for each part of the PCM with material properties of the bimorph PZT film and Ni substrate. Following optimization of parameters from the PCM model, rigid frames were laser cut (Universal CO_2 laser) from 3 mm thick epoxy plate. The compliant hinges were made from 75 μm thick PET with the addition of Kapton tape layers to reach the optimum stiffness K_1. Finally, parts were combined by super glue (Cyanoacrylate). To connect the large-area bimorph PZT beam to the center hinge, 1.5 mm of the beam was not covered with a Pt electrode in Figure 5-2b. A 3 mm distance separated the two rigid frames; ideally this should have zero stiffness (K_2). A photograph of the assembled device is given in Figure 5-2c. The active area of the fabricated energy harvester is around 5.2 cm^2 (blue box in Figure 5-2c). The device was designed for 4.95 Hz resonance frequency; details on the modeling approach are provided elsewhere.[23]

5.3 Results and Discussion

5.3.1. Characteristics of Crystallinity

Figure 5-3 shows the X-ray diffraction (XRD) patterns of upper and lower PZT films on Ni. Strongly {001} textured PZT films on both side of Ni foils were achieved without second phase, as was earlier reported for chemical solution deposited PZT thin films on Ni foils.[19]

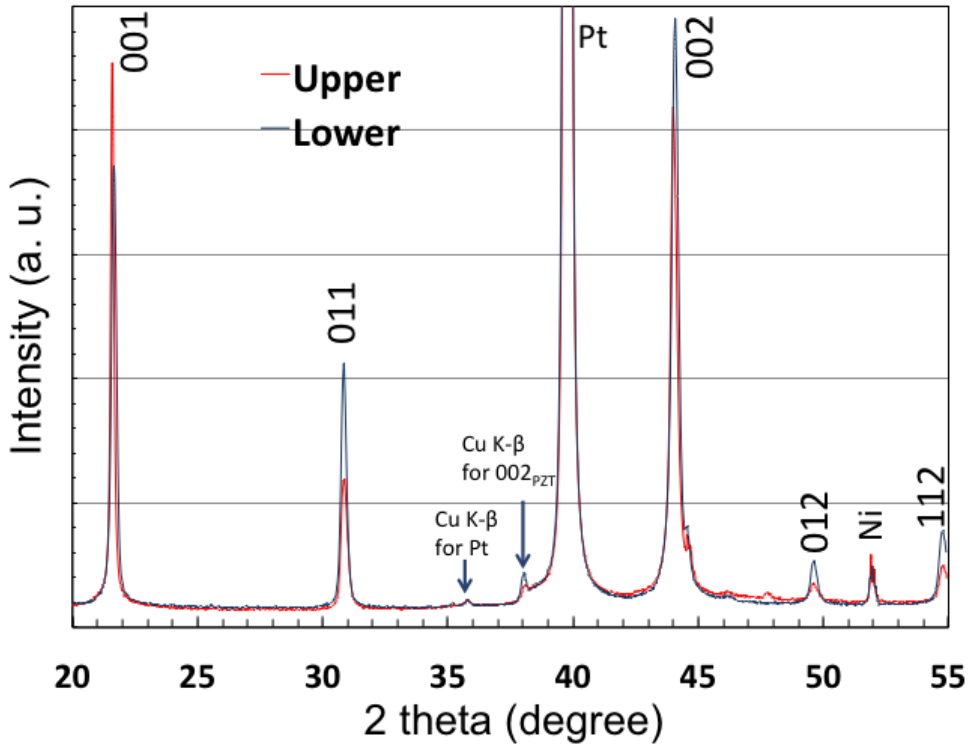

Figure 5-3. X-ray diffraction (XRD) scan of crystallized upper and lower 1%Mn doped PZT(52/48) films respectively by sputtering on $LaNiO_3/HfO_2/Ni/HfO_2/LaNiO_3$ substrate (PANalytical X'pert).

$LaNiO_3$ serves as an orienting perovskite seed layer. The PZT orientation is affected by the quality of the seed layer and the roughness of the surface.[19,29] Microstructure images of both PZT layers utilizing field emission scanning electron microscopy (FE-SEM, Leo 1530) are shown in Figure A-4; both layers show 150~250 nm columnar perovskite grains with pores at the grain boundaries. Some granular grains, which are expected to be randomly oriented are also seen in Figure 5b. No pyrochlore phases were observed (Figure A-4c).

Based on the crystallinity of both PZT films, low dielectric constants ($\varepsilon_r \sim 210$) and large remanent polarizations ~ 40 $\mu C/cm^2$ were observed for both PZT layers in Figure A-5 (Appendix). The low dielectric constant is caused by a large *c*-domain population and pores[19,35] and enhances the FoM of the PEH. This is the first report of deposition of high figure of merit

bimorph PZT films on metal foil for piezoelectric energy harvester.

5.3.2 Performance of Piezoelectric Compliant Mechanism Energy Harvester

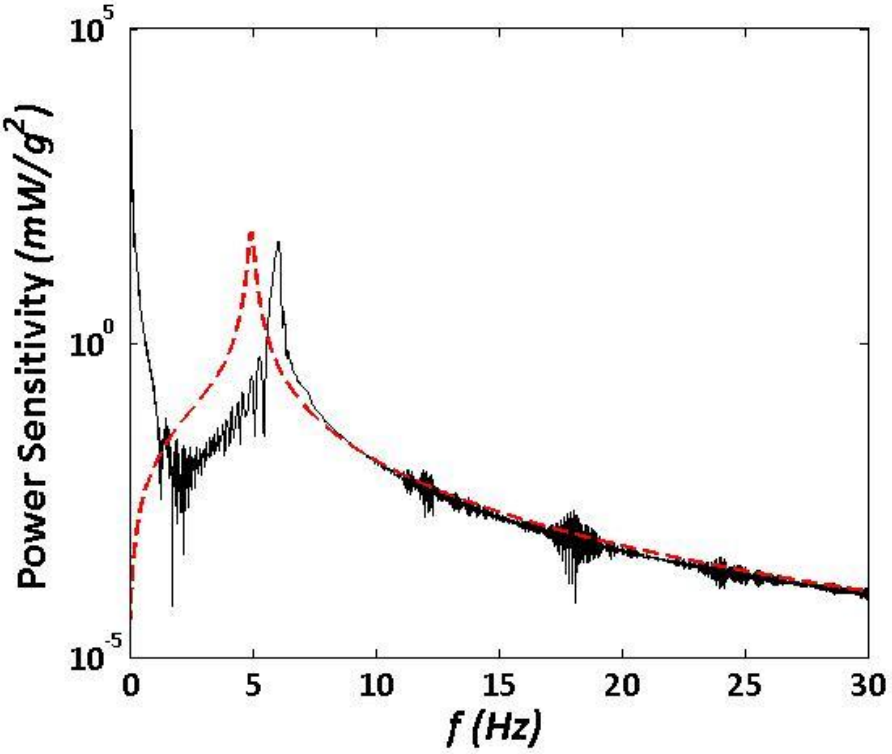

Figure 5-4. Dynamic power sensitivity as a function of frequency for PCM device (black line) and theory (red line) at a load resistance of 330 kΩ.

The performance of the PCM energy harvester was characterized using a laser Doppler vibrometer (OFV-534 Compact Sensor head, Polytec), an electrodynamic shaker and LabVIEW data acquisition system (Figure A-2a, A-2b).[23] The PCM was mounted hanging vertically to a shaker table as shown in Figure A-2 in Appendix A. To measure the performance of the PCM device, the top electrode of the upper and lower PZT layers were wired in series and connected to a resistor box to tune the load resistivity. The sinusoidal excitation base excitation was swept from 0 Hz to 30 Hz in order to understand the dynamic behavior, including the resonance frequency, the mechanical quality factor (Q) and damping ratio (ζ). A video showing device

operation under resonant excitation is shown in Appendix A Video A-1.

Figure 5-4 shows the theoretical and experimental power sensitivity as a function of frequency. The measured first resonance frequency was ~ 6.3 Hz, in reasonable agreement with the theoretical model. It is noted that although the model presumes zero stiffness for the hinges, the finite stiffness of the PET film leads to some deviation between the measured and modeled resonance frequencies. The mechanical quality factor calculated using the half power method: $Q = f_r/(f_b - f_a)$ (where f_r is resonance frequency and $f_b - f_a$ is the bandwidth at the half-maximum amplitude) was 24.5.[25] The mechanical damping ratio, $\zeta = (f_b - f_a)/2f_r$, was 2.07%.

Figure 5-5a shows the voltage and power of the PCM device as function of the external load resistance (R) connected in parallel with the device for steady-state excitation at 6.3 Hz. The maximum voltages ($V_{max} = V_{pk\text{-}pk}/2$) were measured as a function of load resistance to determine the optimum load resistance for maximum power transfer ($P_{max} = V_{max}^2/R$). The modeled optimal load resistance (R_{opt}) was 239.6 kΩ at 0.045 g [g = 9.8 m/s^2] for series connection of the PZT elements. The experimental results gave an optimal load resistance around 330 kΩ; at this point the generated power reached a maximum of 113 μW and a peak-to-peak voltage of 12.2 V (red dot and line) for series connection at an acceleration level of 0.08 g. Figure 5-5b shows the generated electric maximum power of PCM device versus acceleration. The experimental output power increases with increasing base excitation for amplitudes above 0.05 g.

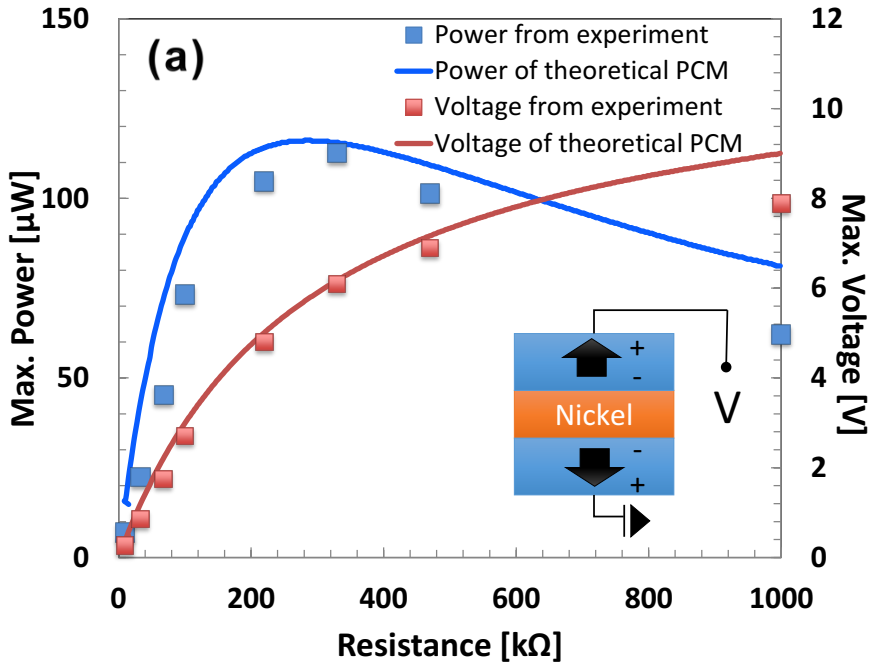
(a)
Power from experiment
Power of theoretical PCM
Voltage from experiment
Voltage of theoretical PCM
Nickel
V
Max. Power [μW]
Max. Voltage [V]
Resistance [kΩ]
150
100
50
0
12
10
8
6
4
2
0
0
200
400
600
800
1000

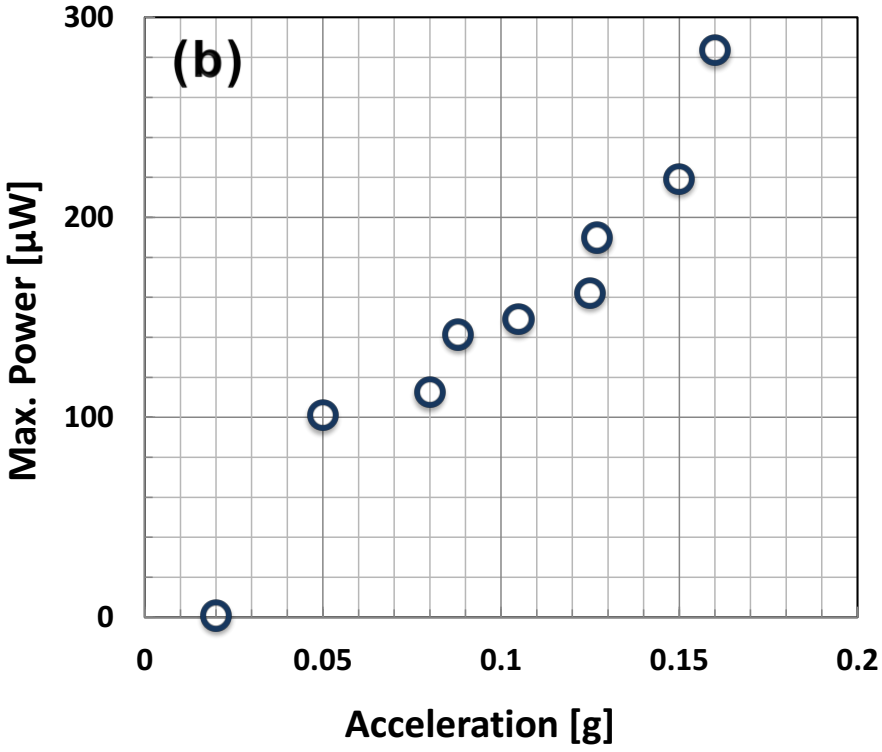
(b)
Max. Power [μW]
Acceleration [g]
300
200
100
0
0
0.05
0.1
0.15
0.2

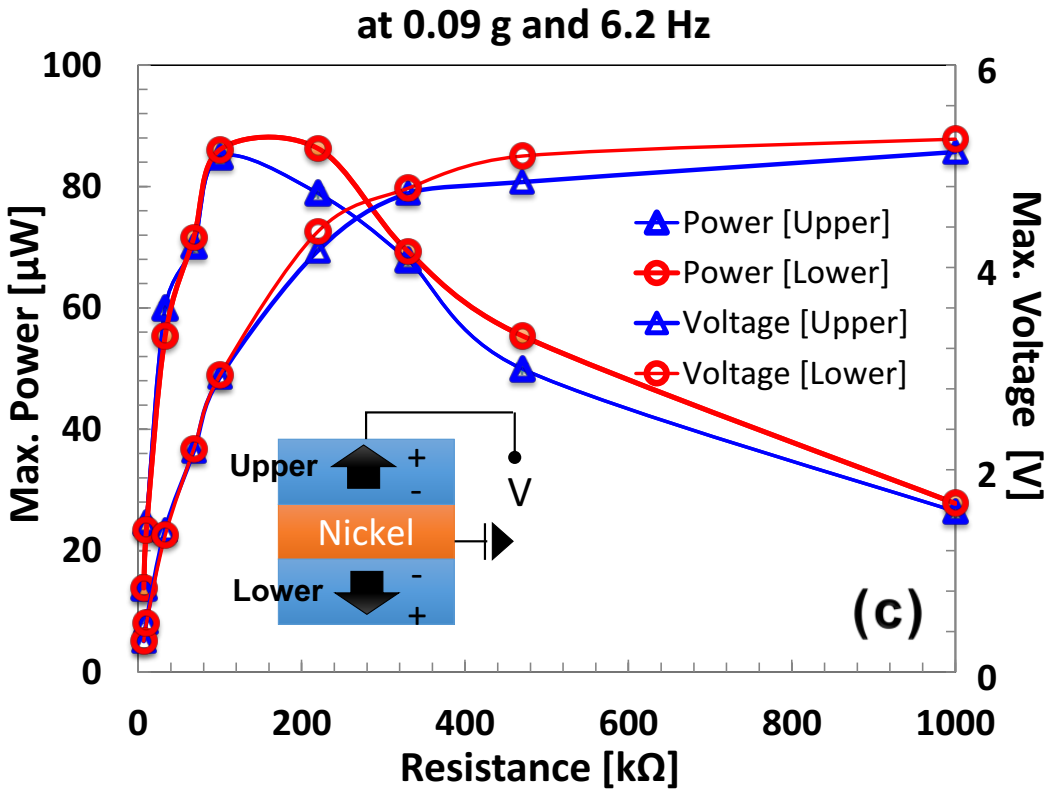

Figure 5-5. (a) Maximum output voltage (red) and power (blue) as a function of external load resistance for PCM device (dots) and theory (lines). [Insert: series poling configuration for bimorph PZT layers. Arrows represent poling direction through the PZT] (b) Maximum output power versus acceleration amplitude. (c) Maximum output voltage and power for upper (blue triangle) and lower (red circle) PZT layers respectively as a function of external load resistance

On the other hand, the generated power significantly dropped under 0.05 g. It is believed that the drop-off at low excitations is due to finite local curvature in the PZT-coated beam. As a result, a finite input force is required to excite the full length of the PZT beam.

Even though PZT films were coated on both sides of the Ni foil to compensate for stresses associated with thermal expansion mismatch during cooling, it is challenging to fabricate perfectly flat PZT beams without partial buckling. This local curvature also degrades the resonant mode shape at higher acceleration levels. It is also possible that the damping ratio

increases.

The output voltages of the upper and lower PZT beams at an excitation level of 0.09 g are shown in Figure 5-5c. Under 0.09 g acceleration, the maximum output power generated from the upper and lower beams was around 85 μW at load resistances of 100 and 220 kΩ, respectively (See Figure 5-5c). In principle, the output voltage could be scaled up when both layers are connected in series. However, the measured power output from both PZT layers (P_{max} = 141 μW) falls below the sum of the powers from the individual PZT layers. It is believed that small differences in thickness, dielectric permittivity, and/or the volume of c-domains of the two PZT layers resulted in mismatched optimum load resistances, decreasing the output power slightly.[35]

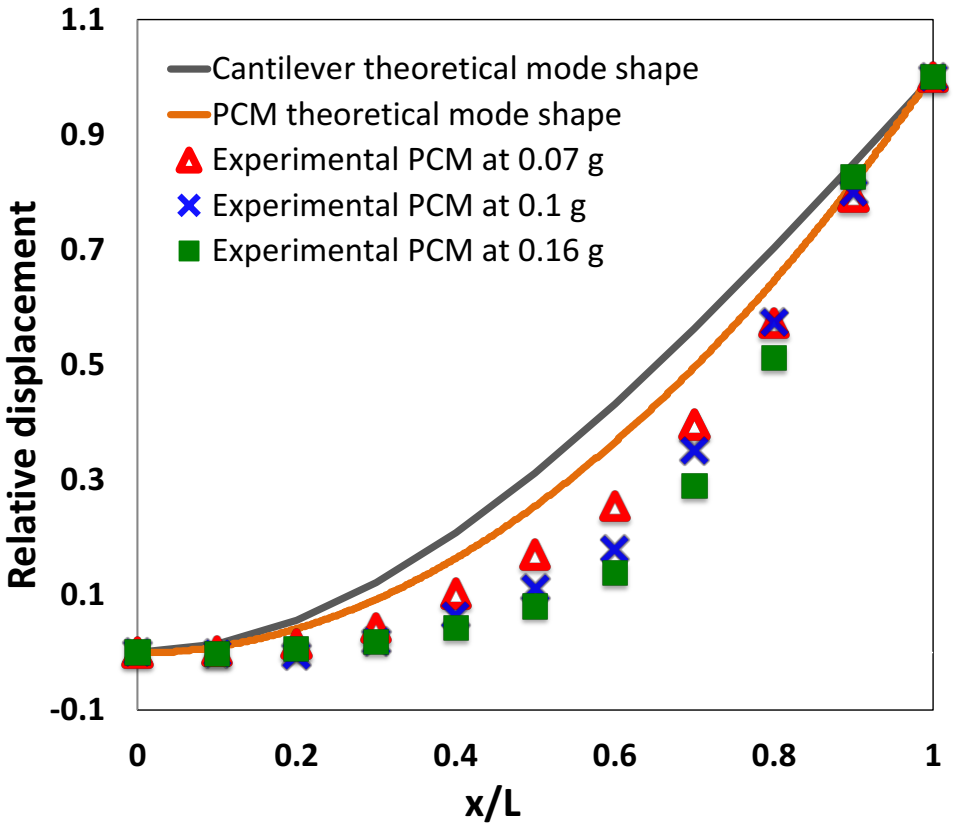

Figure 5-6. Normalized 1st mode shape along the relative distance of experimental PCM device at various excitation amplitudes, theory (orange) and proof mass cantilever theory (grey).

As designed, the first mode shape of the PCM is close to parabolic, enabling a uniform strain distribution along the beam direction. In Figure 5-6, the experimental 1st mode shapes measured by various excitation levels are plotted along with the theoretical first mode shape of the PCM and a proof mass cantilever energy harvester. The displacement of the PCM device at each point along the beam from the clamped point to the tip of PZT beam was measured using a laser vibrometer. Flexible reflective tape was fixed to the PZT beam in order to detect the signals. It can be seen that the first mode shape of the PCM at low acceleration levels is relatively close to a parabola, although significant deviation is observed for higher acceleration levels. The origin of the non-uniform strain distribution of PCM device was also explored. Figure A-3 shows the displacement responses along the PZT beam length. We observed a linear/symmetric response to a sinusoidal input vibration as expected from a theoretical model having no initial asymmetrical deformation near the clamped end of the beam (x = 0.1); this is shown in Figure A-3a. However, 30 – 60% along the beam length, strongly nonlinear displacements were observed at 0.07 g. This was attributed to some initial beam curvature as marked by the green box in Figure A-3b (Appendix A). Also, the bending response to resonance excitation is shown in the Appendix A Video A-1.

Table A-2 shows the output power and power density (in $\mu W/cm^2 \cdot g^2$, where g is the acceleration) of PCM device at various acceleration levels compared with the modeled output at 0.05 g. The output power increased with the acceleration over the whole measured range, reaching a maximum power of 284 μW at 0.16 g. The power density decreased with increased acceleration level, due to degradation of the uniformity of strain distribution. For a maximum strain of 0.1% corresponding to the acceleration level of 0.1 g in the PZT, the maximum power of 149 μW from PCM device shows 65% mode shape efficiency compared to theoretical

estimates. This is much higher than the efficiency of normal cantilever with a proof mass.[23] It is anticipated that up to 100% mode shape efficiency could be achieved as initial curvature along PZT beam is eliminated with clamping at the end of the PZT beam.

5.3.3 Comparison of Piezoelectric Energy Harvester Performance

A comparison of the power density of various reported piezoelectric energy harvesters is shown in Table 5-2. For the 3 μm thick bimorph PZT film on Ni foil, under 0.05 g acceleration, the root mean square (RMS) power of the device is 51 μW at ~ 6 Hz. This significantly outperforms all of the MEMS devices using piezoelectric films. This is the first report that demonstrates both a low resonance frequency and high power density respectively in a small structure. Furthermore, normalized to the resonance frequency, the power density exceeds all other reports, including the average of the two branches reported by Leadenham et al. for a strongly nonlinear harvester.[43] It is noted that the PCM devices using textured bimorph PZT beams demonstrate excellent power density (~3.9 mW/cm^2g^2) at 6 Hz relative to other reports due to the combination of advanced design and the excellent characteristic of bimorph PZT film with high figure of merit on Ni foil.

Table 5-2. Comparison of recently reported resonant based piezoelectric energy harvesters.

Reference	Active material, Mode	Device area [cm^2]	Acceleration [g]	Frequency [Hz]	$Power_{rms}$ [μW]	Power density [$\mu W/cm^2 \cdot g^2$]	Power density/f_r [$\mu W/Hz \cdot cm^2 \cdot g^2$]
Shen[36]	PZT film sol-gel, d_{31}	0.0256	2	462.5	2.15	21	0.05
Morimoto[8]	(001) PZT on Stainless steel, d_{31}	0.925	0.5	126	5.3	22.9	0.18
Kim[37]	Cymbal type w/ High-g PZT ceramic	6.6	9.4	100	19500	33.4	0.334
Kim[18]	NKN on Ni-rich foil, d_{31}	0.1	0.5	128	1.75	70	0.546
Andosca[38]	Sputtered AlN d_{31}	0.653	1	58	64	98	1.69
Durou[39]	Bulk PZT-5H thin-bonded, d_{31}	0.894	0.2	76	13.9	388.7	5.11
Zawada[40]	PZT thick film, d_{31}	0.75	0.102	205	3.78	481	2.35
Aktakka[41]	Bonded & Thinned Bulk-PZT5A d_{31}	0.49	0.1	167	2.74	559.2	3.35
Ricart[42]	5.6 μm AlN, d_{31}	3.38	0.18	155	165	1507	9.72
Leadenham[43]	M-shaped beam w/ four piezoelectric patches	55.88	0.06		2610 [a]	12974	895
					14 [b]	70	4.83
Ma[23]	Compliant design using PVDF, d_{31}	5.2	0.01	5.13	0.062	119.2	23.2
PSU compliant	3 + 3 μm bimorph PZT film on Ni, d_{31}	**5.2**	**0.05**	**6**	**50**	**3887**	**617**

[a] high-energy branch (up frequency sweep), [b] low-energy branch (down frequency sweep)

5.4 Conclusions

In conclusion, a piezoelectric compliant mechanism mechanical energy harvester providing comparatively uniform strain along the beam length was successfully fabricated using bimorph PZT films on flexible Ni foils. The (001) textured 3 μm thick PZT films coated on both sides of Ni foil (PZT/$LaNiO_3$/HfO_2/Ni/HfO_2/$LaNiO_3$/PZT) were obtained by rf-sputtering with post annealing under controlling nucleation sites and growth. The bimorph PZT beam exhibits approximately twice the power output of a unimorph PZT layer and avoids large transverse curvature along the beam produced by thermal expansion mismatch. A 6 Hz PCM device utilizing a 2cm×1cm PZT beam generated a maximum voltage and power of 7 V and 149 μW respectively at 0.1% strain limit at 0.1 g acceleration level. Large power densities (3.9 mW/cm^2g^2) and higher mode shape efficiencies (65%) relative to available reports on piezoelectric energy harvesters were shown.

5.5 References

[1] S. Priya, "Advances in energy harvesting using low profile piezoelectric transducers," *Journal of Electroceramics* **19** (2007) 165.

[2] S.-G. Kim, S. Priya, and I. Kanno, "Piezoelectric MEMS for energy harvesting," *MRS Bulletin* **37** (2012) 1039.

[3] P.D. Mitcheson, E.M. Yeatman, G.K. Rao, A.S. Holmes, and T.C. Green, "Energy harvesting from human and machine motion for wireless electronic devices," *Proceeding of the IEEE,* **96** (2008) 1457.

[4] T. Starner, and J.A. Paradiso, "Human-generated power for mobile electronics," *Low-Power Electronics Design* (Eds: C. Piguet), CRC Press, Boca Raton, FL, USA (2004) Ch. 1.

[5] L. Dhakar, H. Liu, F.E.H. Tay, C. Lee, "A new energy harvester design for high power output at low frequencies," *Sensors and Actuators A* **199** (2013) 344.

[6] T. Harigai, H. Adachi, and E. Fuuii, "Vibration energy harvesting using highly (001)-oriented Pb(Zr,Ti)O_3 thin film," *Journal of Applied Physics* **107** (2010) 096101.

[7] C. B. Yeager and S. Trolier-McKinstry, "Epitaxial Pb (Zr_x,Ti_{1-x})O_3 ($0.30 \leq x \leq 0.63$) films on (100) MgO substrates for energy harvesting applications," *Journal of Applied Physics* **112** (2012) 074107.

[8] K. Morimoto, I. Kanno, K. Wasa, and H. Kotera, "High-efficiency piezoelectric energy harvesters of c-axis-oriented epitaxial PZT films transferred onto stainless steel cantilevers," *Sensors and Actuators A* **163** (2010) 428.

[9] K-I. Park, J. H. Son, G-T. Hwang, C. K. Jeong, J. Ryu, M. Koo, I. Choi, S. H. Lee, M. Byun, Z. L. Wang, and K. J. Lee, "Highly-efficient, flexible piezoelectric PZT thin film nanogenerator on plastic substrates," *Advanced Materials.* **26** (2014) 2514.

[10] S. Trolier-McKinstry, F. Griggio, C. Yaeger, P. Jousse, D. Zhao, S. S. N. Bharadwaja, T. N. Jackson, S. Jesse, S. V. Kalinin, and K. Wasa, "Designing piezoelectric films for micro electromechanical systems," *IEEE Transactions on Ultrasonics, Ferroelectrics, and Frequency Control* **58**, 9 (2011) 1782.

[11] N. S. Hudak and G G. Amatucci, "Small-scale energy harvesting through thermoelectric, vibration, and radiofrequency power conversion," *Journal of Applied Physics* **103** (2008) 101301.

[12] S.R. Anton, H.A. Sodano, "A review of power harvesting using piezoelectric materials (2003–

2006)," *Smart Materials and Structures* **16** (2007) R1.

[13] C. B. Yeager, "PZT thin films for piezoelectric MEMS mechanical energy harvesting," *Ph. D Thesis,* (2015) The Pennsylvania State University.

[14] S. Roundy, "On the effectiveness of vibration-based energy harvesting," *Journal of Intelligent Material Systems and Structures* **16**, 10 (2005) 809.

[15] F. Calame, and P. Muralt, "Growth and properties of gradient free sol-gel lead zirconate titanate thin films," *Applied Physics Letters* **90**, 6 (2007) 062907.

[16] G. L. Brennecka, W. Huebner, B. A. Tuttle, P. G. Clem, "Use of stress to produce highly oriented tetragonal lead zirconate titanate (PZT 40/60) thin films and resulting electrical properties," *Journal of the American Ceramic Society* **87**, 8 (2004) 1459.

[17] S.-C. Lin, and W.-J. Wu, "Fabrication of PZT MEMS energy harvester based on silicon and stainless-steel substrates utilizing an aerosol deposition method," *Journal of Micromechanics and Microengineering* **23** (2013) 125028.

[18] S.-H Kim, H. Seo, S. Glinsek, Y. Kim and A I. Kingon, "Lead-free piezoelectric thin film-based energy harvesters for self-powered implantable medical devices," in 16th US-Japan Seminar on Dielectric and Piezoelectric Materials (2013), D13.

[19] H. G. Yeo, S. Trolier-McKinstry, "{001} Oriented piezoelectric films prepared by chemical solution deposition on Ni foils," *Journal of Applied Physics* **116** (2014) 014105.

[20] B. A. Tuttle, J.A. Voight, D. C. Goodnow, D. L. Lamppa, T. J. Headley, M. O. Eatough, G. Zender, R. D. Nasby, and S. M. Rodgers, "Highly oriented, chemically prepared $Pb(Zr,Ti)O_3$ thin films," *Journal of the American Ceramic Society* **76**, 6 (1993) 1537.

[21] K. Wasa, T. Matsushima, H. Adachi, I. Kanno, and H. Kotera, "Thin-film piezoelectric materials for a better energy harvesting MEMS," *Journal of Microelectromechanical Systems* **12**,

2 (2012) 451.

[22] R. Caliò, U. B. Rongala, D. Camboni, M. Milazzo, C. Stefanini, G.D. Petris, and C.M. Oddo, "Piezoelectric Energy harvesting Solutions," *Sensor* **14** (2014) 4755.

[23] X. Ma, A. Wilson, C.D. Rahn, and S. Trolier-McKinstry, "Efficient Energy Harvesting Using Piezoelectric Compliant Mechanisms: Theory and Experiment," *Journal of Vibration and Acoustics* **138** (2016) 021005.

[24] C. L. Kuo, S. C. Lin, and W. J. Wu, "Fabrication and characteristic of piezoelectric bimorph MEMS generators based on stainless steel substrate for vibration generator," 25nd International Conference on Adaptive Structures and Technologies The Hague, The Netherlands (2014) 019.

[25] J.-I. Inoue, K. Kanda, T. Fujita, and K. Maenaka, "Thin-film piezoelectric bimorph actuators with increased thickness using double Pb [Zr,Ti]O_3 layers," *Journal of Micromechanics and Microengineering* **25** (2015) 055001.

[26] S.-M. Ha, D.-H. Kim, H-H. Park, and T.-S. Kim, "Crystallization and ferroelectric behavior of sputter deposited PZT using a target containing excess Pb and O contents," *Thin Solid Films* **525** (1999) 355.

[27] H. Suzuki, Y. Miwa, T. Naoe, H. Miyaraki, T. Ota, M. Fuji, and M. Takahashi, "Orientation control and electrical properties of PZT/LNO capacitor through chemical solution deposition," *Journal of the European Ceramic Society* **26** (2006) 1953.

[28] T. Kobayashi, M. Ichiki, J. Tsaur, and R. Maeda, "Effect of multi-coating process on the orientation and microstructure of lead zirconate titanate (PZT) thin films derived by chemical solution deposition," *Thin Solid Films* **489** (2005) 74.

[29] R. W. Schwartz, J. A. Voigt, B. A. Tuttle, D. A. Payne, T. L. Reichert, and R. S. DaSalla, "Comments on the effects of solution precursor characteristics and thermal processing conditions

on the crystallization behavior of sol-gel derived lead zirconate titanate thin films," *Journal of Materials Research* **12** (1997) 444.

[30] W. R. Cook, Jr., D.A. Berlincourt, and F.J. Scholz, "Thermal expansion and pyroelectricity in lead titanate zirconate and barium titanate," *Journal of Applied Physics* **34** (1963) 1392.

[31] T. G. Kolie, "Measurement of the thermal-expansion coefficient of nickel from 300 to 1000 K and determination of the power-law constants near the Curie temperature," *Physical Review B* **16**, 11 (1977) 4872.

[32] R.L. Johnson-Wilke, R.H. Wilke, V. Cotroneo, W.N. Davis, P.B. Reid, D.A. Schwartz, and S. Trolier-McKinstry, "Improving yield of PZT piezoelectric devices on glass substrates," Proc. SPIE 8503 (2012) 85030A.

[33] A. Erturk and D. J. Inman, "An experimentally validated bimorph cantilever model for piezoelectric energy harvesting from base excitations," *Smart Materials and Structures* **18** (2009) 025009.

[34] A. Erturk and D. J. Inman, *Piezoelectric Energy Harvesting*, John Wiley & Sons, United Kingdom (2011).

[35] R. Xu, A. Lei, C. Dahl-Petersen, K. Hansen, M. Guizzetti, K. Birkelund, E.V. Thomsen, and O. Hansen, "Screen printed PZT/PZT thick film bimorph MEMS cantilever device for vibration energy harvesting," *Sensors and Actuators A* **188** (2012) 383.

[36] D. Shen, J.-H. Park, J. Ajitsaria, S.-Y. Choe, H. C. Wikle, and D.-J. Kim, "The design, fabrication and evaluation of a MEMS PZT cantilever with an integrated Si proof mass for vibration energy harvesting," *Journal of Micromechanics and Microengineering* **18** (2008) 055017.

[37] H. W. Kim, A. Batra, S. Priya, K. Uchino. D. Markley, R.E. Newnham, and H.F. Hofmann,

"Energy harvesting using a piezoelectric "cymbal" transducer in dynamic environment," *Japanese Journal of Applied Physics* **43** (2004) 6178.

[38] R. Andosca, T. McDonald, V. Genova, S. Rosenberg, J. Keating, C. Benedixen, and J. Wu, "Experimental and theoretical studies on MEMS piezoelectric vibrational energy harvesters with mass loading," *Sensors and Actuators A* **178** (2012) 76.

[39] H. Durou, G. A. Ardilla-Rodriguez, A. Ramond, X. Dollat, C. Rossi, D. Esteve, "Micromachined bulk PZT piezoelectric vibration harvester to improve effectiveness over low amplitude and low frequency vibrations," PowerMEMS 2010, Leuven, Belgium, (2010) 27.

[40] T. Zawada, K. Hansen, R. Lou-Moeller, E. Ringgaard, T. Pedersen, E. V. Thomsen, "High-performance piezoelectric thick film based energy harvesting micro-generators for MEMS," *Procedia Engineering* **5** (2010) 1164.

[41] E. E. Aktakka, R. L. Peterson, and K. Najafi, "Thinned-PZT on SOI process and design optimization for piezoelectric inertial energy harvesting," 16th Int. Conf. on Solid-State Sensors, Actuators, and Microsystems, Transducers, Beijing, China (2011) 1649.

[42] T. Ricart, P-P. Lassagne, S. Boisseau, G. Despesse, A. Lefevre, C. Billard, S. Fanget and E. Defay, "Macro energy harvester based on aluminium nitride thin films," IEEE International Ultrasonics Symposium, (2011) 1928.

[43] S. Leadenham, A. Erturk, "Nonlinear M-shaped broadband piezoelectric energy harvester for very low base accelerations: primary and secondary resonances," *Smart Materials and Structures* **24** (2015) 055021.

Chapter 6

{001} Oriented Bimorph PZT Films on Ni Foil by High Temperature Sputtering

6.1 Introduction

Energy harvesting has recently attracted attention for wireless sensor nodes and wearable electronics in combination with low power consumption electronic devices. Thus, considerable research efforts are directed towards self-powering devices to eliminate the need to change or manually recharge batteries. Mechanical energy harvesters using piezoelectric materials such as lead zirconate titanate ($Pb(Zr_xTi_{1-x})O_3$, or PZT) are promising for energy scavenging from environmental vibration, including human motion.[1]

Several approaches have been explored in attempts to enhance the output power of mechanical harvesting systems. Two main strategies are commonly considered: exploitation of advanced mechanical design and improvement of the piezoelectric material itself. In terms of the piezoelectric material, high transverse piezoelectric responses ($e_{31,f}$) and low dielectric constants (ε_r) are essential to achieve a high figure of merit (FoM = $e_{31,f}^2/\varepsilon_r$) for piezoelectric energy harvesting.[2,3] The energy harvesting FoM is mainly governed by the orientation and domain state of the ferroelectric, due to the anisotropy in the dielectric constant and piezoelectric response. This is particularly apparent in polycrystalline, lead-based, ferroelectric perovskite films.[2,4] For instance, (001) oriented PZT films develop a large fraction of *c*-domains and exhibit low dielectric permittivity and large FoM relative to (100) PZT. In contrast, (100) PZT films develop a large fraction of *a*-domains, which results in a large dielectric permittivity and lower FoM.[2,5] Yeager et al. reported that the FoM in tetragonal PZT films is a sensitive function of the *c*-

domain fraction.[6]

There are a variety of approaches for preparing high figure of merit films by controlling the orientation. Chemical solution deposition, pulsed laser ablation, metal-organic chemical vapor deposition and sputtering are utilized to grow polycrystalline and epitaxial PZT thin films for piezoelectric energy harvesters.[7~15]

Chemical solution deposition (CSD) is a well-established deposition method for preparation of PZT films and has a lower set-up cost relative to other thin film preparation methods.[8] Also, chemical solution deposition has been extensively explored to control preferred orientation by manipulating the grain nucleation and growth behavior with textured seed layers such as $PbTiO_3$.[3,16]

Rf-sputtering is another deposition technique that has been intensively investigated for the deposition of PZT films with uniform film thickness and composition over a large area.[9] There are two sputter deposition approaches used to achieve perovskite PZT films. The first method involves depositing the desired thickness of PZT while the substrate is maintained at the crystallization temperature. The second method involves the deposition of PZT layers onto a substrate at room temperature, with post-deposition annealing to promote crystallization of each layer. The process is repeated until the desired film thickness is reached.

Metal organic chemical vapor deposition (MOCVD) is another promising deposition technique that allows for excellent control of stoichiometry and compositional modification. The technique uses liquid-reagents, under carefully controlled deposition conditions to obtain high quality PZT films.[7,10]

PZT can also be deposited using a pulsed laser deposition (PLD) technique, which has the advantage of being a simple deposition process that can be readily adapted to various forms

of targets such as a powder, sintered ceramic, or single crystal.[7,14,15] However, the main limitation of the technique is that is can typically produce only a small area of uniformly deposited film. The various deposition techniques for PZT films used in energy harvester devices are summarized in Table 6-1.

Table 6-1. Comparison of methods for deposition of PZT films.[7~15]

	Advantages	Challenges
Chemical solution deposition (CSD)	Easy to control orientation of PZT film, dense	Needs multiple spin coating and thermal process steps to build thickness
Pulsed-laser deposition (PLD)	Easy to control orientation and composition	Limited deposited area
Metal-organic chemical vapor deposition (MOCVD)	High growth rate, good film uniformity, composition control	Often requires hazardous reagents, stoichiometry changes (especially of minor amounts of dopant) are challenging
RF magnetron sputtering	Uniformity of film thickness and composition over a large area, easy to control orientation	Hard to control Pb content in the film due to the high volatility of Pb

Most reported MEMS piezoelectric energy harvesters utilize polycrystalline or epitaxial PZT films grown on various substrates (*e.g*. Si, MgO, sapphire and stainless steel) by the sol-gel route or *rf*-sputtering.[2,8,9,11,17] Recently, Yeo *et al.* demonstrated the growth of a high FoM (001) oriented PZT film on flexible Ni foils by CSD and *rf*-magnetron sputtering with post annealing.[18,19] The films showed an enhanced mechanical durability and flexibility, highly desirable for resonant based piezoelectric energy harvester devices. A device using 3 μm thick bimorph PZT film on Ni foil exhibited an excellent energy output performance.

Achieving a high power density ($\mu W/G^2 \cdot cm^2$) from a film is critical for the efficiency of an energy harvesting device. One promising strategy for achieving this in the 31 mode for films with a high FoM is to focus on increasing the layer thickness to several micrometers while maintaining a high degree of preferred orientation and high density without cracking.[1] There are

previous reports demonstrating the deposition of PZT films with a thickness greater than 3 μm by polyvinylpyrrolidone (PVP)-modified or carboxylic acids-based sol-gel routes. However, it is difficult to prepare dense, thick films by these routes.[20~22] The challenge remains to prepare high density PZT films with a high FoM and a thickness greater than 3 μm without cracks and pores.

Figure 6-1 shows an example of micro-cracking in thick PZT films prepared by *rf*-magnetron sputtering on a room temperature substrates followed by post-deposition annealing. The 4 μm thick PZT film was achieved by deposition of eight 0.5 μm thick layers; each layer was crystallized before the next layer was deposited (Figure 6-1 (b)). The choice of 0.5 μm thick layers was made to enable to control film orientation and prevent cracking when thicker amorphous films are converted to crystalline films with post annealing.[23]

These sputtered PZT films with post-annealing crystallization also exhibit porosity. It is believed that the porosity forms as a result of PbO volatilization at high temperatures during the crystallization process. Porosity can be seen in Figure 6-1 (b).[23,24]

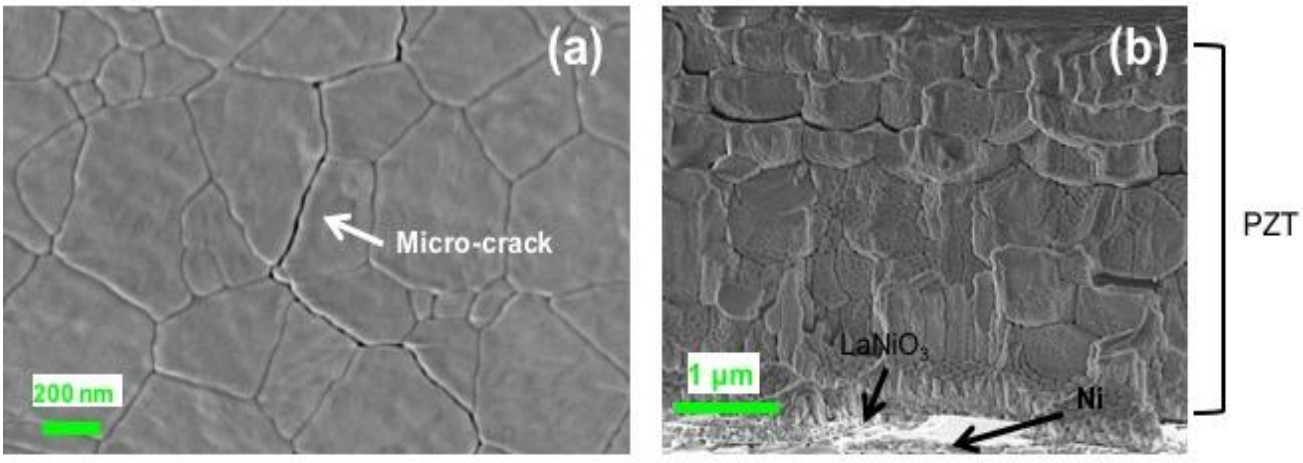

Figure 6-1. (a) Surface and (b) cross-sectional images of 4 μm thick PZT films on Ni foil by *rf*-magnetron sputtering at room temperature, with post-deposition crystallization.

While no microcracks were observed in 3 μm thick PZT films deposited in six 0.5 μm steps,[19] when the film thickness was increased to 4 μm, cracking is apparent. Due to the formation of microcracks in films grown to total thickness of 4 μm and greater, it is necessary to look for an alternative deposition technique for the growth of > 5 μm thick PZT films with high density and the desired orientation. Fuji et al., reported 4~5 μm thick Nb-doped PZT films coated on a stainless steel substrate by high temperature *rf*-magnetron sputtering, for MEMS applications.[25] The high temperature allows for in situ crystallization during the sputtering process. Based on their results, sputtering the PZT film with in-situ crystallization produces a dense PZT film with greater than 3 μm thickness without cracking. In particular, this technique can be applied to the deposition of oriented PZT films on both side of a Ni foil substrate to produce a bimorph structure. A bimorph structure is particularly advantageous for energy harvesting applications because it generates an output voltage approximately double that of a unimorph structure, without increasing the total area of the film. To grow a phase-pure perovskite PZT film by high temperature sputtering, various parameters, such as the amount of excess Pb in the PZT target, the oxygen and Ar pressure, and the substrate temperature, should be optimized.[26~29] In general, the PbO concentration in the films strongly depends on the energy of bombardment at the surface of the film.

This chapter describes optimization of a process for the growth of thicker (i.e. > 3 μm) crack-free films by in-situ crystallization during *rf* magnetron sputtering, for piezoelectric energy harvesters.

6.2 Experimental Procedure

First, optimization of the high temperature sputtering conditions was undertaken by sputtering PZT onto platinized silicon wafers (Nova Electronic Materials, Flower Mound, TX) with and without a randomly oriented PZT seed layer; the seed layers were prepared by sputtering at room temperature with post-deposition annealing (The deposition conditions are described in Table B-1). A PZT (52/48) ceramic target (manufacturer: Kurt J. Lesker) with 10% excess PbO was used. The growth of approximately 2 μm thick PZT was carried out in an atmosphere of either Ar gas or an Ar/O_2 mixture, at a chamber pressure of 8 mTorr, a power of 90 W for 59994 seconds. The substrate and holder were heated by a high temperature infrared (IR) lamp placed behind the holder. For a given heat input through IR radiation, holder/substrate's equilibrium temperature is influenced by its reflection, absorption, and transmission in the IR region. Figure 6-2 exhibits a schematic of a substrate loaded into the chamber for high temperature sputtered PZT film. In the sputter system, the substrate set temperature strongly depends on the type of holders (e.g. old and new holder) used for this work. Schematics of these holders are shown in Figure 6-3.

When using the old type of holder, shown in Figure 6-3(a), the substrate was mounted using bolts to tighten the edge of the sample. Especially for substrates such as metal foil, this method of mounting produced poor contact between the substrate and the holder. The new substrate holder was fabricated from a circular Hastelloy metal plate, with windows cut in it where the samples were placed in Figure 6-3(b). Rectangular pieces of Hastelloy were used as weights to hold the samples in place during the deposition process. This was found to improve the thermal contact.

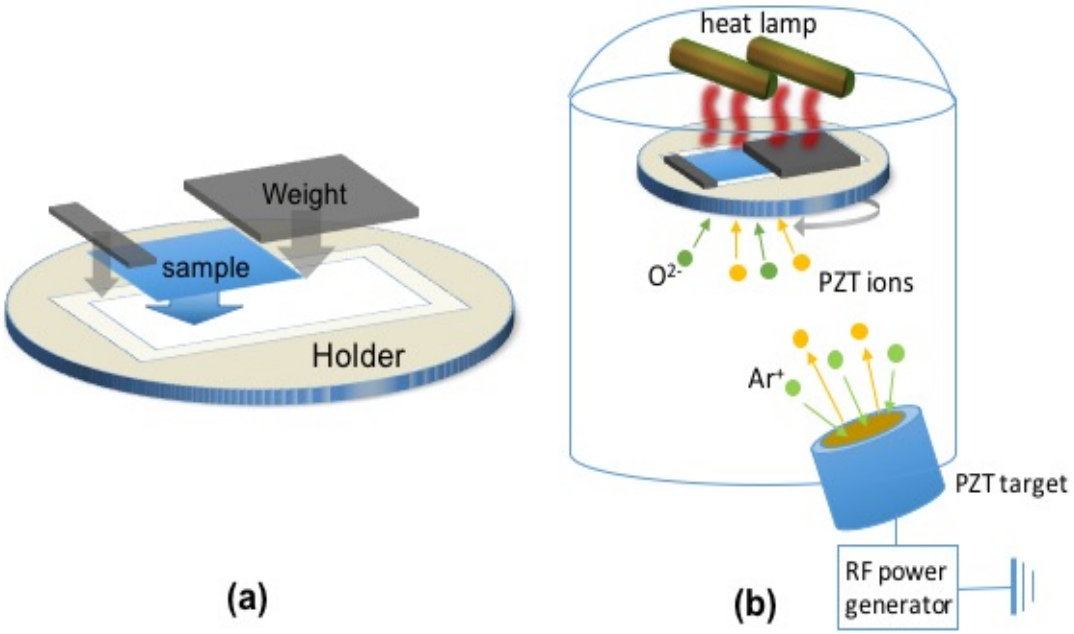

Figure 6-2. (a) Schematic illustration of new substrate holder, weights and sample. (b) Schematic view of high temperature *rf*-sputtering system.

The type of holder should, in principle, affect only the substrate set temperature. It was found that the old substrate holder acted as a thermal obstacle for heating the substrate from the IR heat source. Thus, it was necessary to increase the set temperature for in-situ crystallization of sputtered films in order to compensate for the large thermal loss through the Hastelloy metal holder, which acted as a radiative heat source. In contrast, much lower setting temperatures (approximately 180 ºC lower) could be used with the new holder due to improved heat transfer from IR radiation (shown in Figure 6-3(d)).

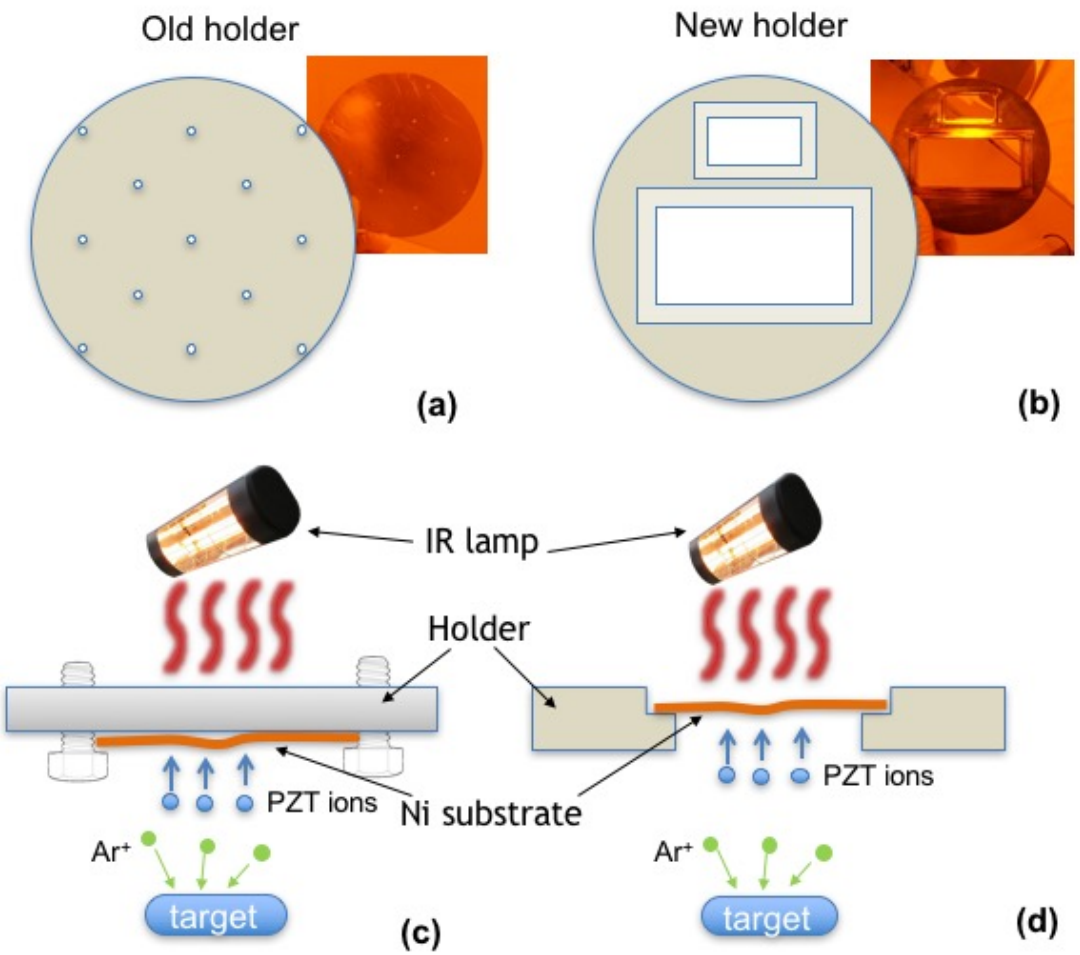

Figure 6-3. Schematic top down view of (a) an old type substrate holder and (b) a new substrate holder. [Insert pictures: photograph of holders]. The cross section view of the high temperature sputtering system with substrate mounted onto (c) old and (d) new substrate holders.

Although the new substrate holder is limited to a certain substrate shape, it is suitable to transfer thermal energy efficiently from the heat source (IR lamp) to the substrate, while maintaining a uniform thermal distribution as shown in Figure 6-3 (d).

Table 6-2. High substrate temperature sputtering conditions for *in-situ* crystallization of PZT films.

Parameter	Sputtering condition
Target	PZT (52/48) + 10% PbO excess
Substrate	Pt/Si, PZT(seed layer)/Pt/Si or PZT/LNO/Ni
Distance between target and substrate	6 inch
RF power	88 Watts (Power density: 2.0 W/cm^2)
Chamber Pressure	8 mTorr
Gas	Ar+3% mixture of (10% O_2+ 90% Ar)
Deposition rate	0.11 μm/hr
Setting Temperature of Substrate	530 ~ 585 °C w/ New holder, > 680 °C w/ Old holder (dwell time prior to deposition: 100 min)

For fabrication of bimorph blanket PZT films on Ni foils by high temperature sputtering, the Ni substrate requires the same preparation steps as those described in Chapters 3 and 5, in order to achieve preferred orientation with limited oxidation. Ni foils were first prepared by polishing, then HfO_2 was deposited as a buffer layer, followed by deposition of (100) textured $LaNiO_3$ as a template layer (see Chapters 3 and 5 for details).[18] The parameters used for high temperature *rf* magnetron sputtering (Kurt J. Lesker) including the target composition, chamber pressure, gas composition, power and temperature are listed in Table 6-2.

X-ray diffraction (Panalytical X'pert Pro MPD) was utilized to study the phase purity and orientation of the sputtered PZT films. Microstructural characteristics such as the grain size, grain boundary grooving and porosity were assessed using field emission scanning electron microscopy (FESEM, Leo 1530). Lift-off patterning was used to define circular Pt top electrodes with diameters of 100 μm ~ 200 μm. The top electrodes were 100 nm Pt layers grown at room

temperature using a dc magnetron sputtering tool (CMS-18 Sputter system, Kurt J. Lesker). To enhance adhesion between the top electrode and the film, samples were annealed at 500 °C for 1 min using RTA. To assess the ferroelectric and dielectric properties, a Radiant Technologies Precision LC ferroelectric tester (Radiant Technology, Inc.) and an impedance analyzer (HP 4294A, Hewlett-Packard) were used.

6.3 Results and Discussion

For *in-situ* crystallization during sputtering, excessive evaporation or re-sputtering of Pb from the growing film leads to formation of Pb-deficient pyrochlore phases.[30] Thus, it is important to control the Pb content to achieve the desired stoichiometry. In practice, this can be done via the optimization of parameters such as the amount of Pb excess in the target and the chamber pressure. High chamber pressure can suppress resputtering of Pb atoms from the oxide layer, but the increased gas scattering in the plasma at higher pressures decreases the deposition rate during sputtering.[31,32]

First of all, it is essential to understand Pb content in film as a function of chamber pressure before exploring the relationship between temperature and Pb content. For instance, in the case of using a 5% Pb excess PZT target, the Pb-deficient pyrochlore phase was found below ~5 mTorr chamber pressure for sputtering at room temperature with ex-situ crystallization. Films sputtered at pressure 5 mTorr have small amounts of surface pyrochlore phase (confirmed by microstructure images in Figure B-4), which could be removed using a PbO capping layer.[37,38] Phase pure perovskite films were achieved at 6 mTorr. As the pressure is decreased, the amount pyrochlore phase increased and the amount of Pb-deficient pyrochlore phases could not be completely converted to the perovskite phase using the PbO capping (*e.g.* sample #4 shown in

Figure B-6). While the data in Figure 6-4 are qualitative (given that the substrate setting temperature does not indicate the surface temperature and the limited amount of data points to fix the boundaries), it is clear that the chamber pressure during deposition strongly influence the phase by controlling the lead content in the as-grown films.[23]

On the other hand, targets with higher Pb contents (10% Pb excess PZT52/48) enable growth of the perovskite phase at lower chamber pressures than that of the 5% Pb excess PZT52/48 target. For this reason, using a target with excess Pb effectively compensates for the loss of PbO and suppresses the formation of Pb-deficient pyrochlore phases without reducing the deposition rate.

Substrate temperature is also an important parameter that strongly influences the phase composition and crystalline properties of the PZT film.[33~35] Based on a series of experiments with the parameters of the sputtering system shown in Table B-2 and Figure B-2, it was found that an increase of the sputtering gas pressure is required for sputtering at elevated substrate temperatures, to compensate for the rapid temperature-induced increase in the evaporation of Pb from the grown films.[34, 36,37] The schematic processing diagram can be illustrated with the results of XRD patterns and microstructure images of sputtered PZT films after post annealing (detailed data are shown in Figure B-3~14) depending on the chamber pressures and the setting substrate temperature with the old substrate holder.

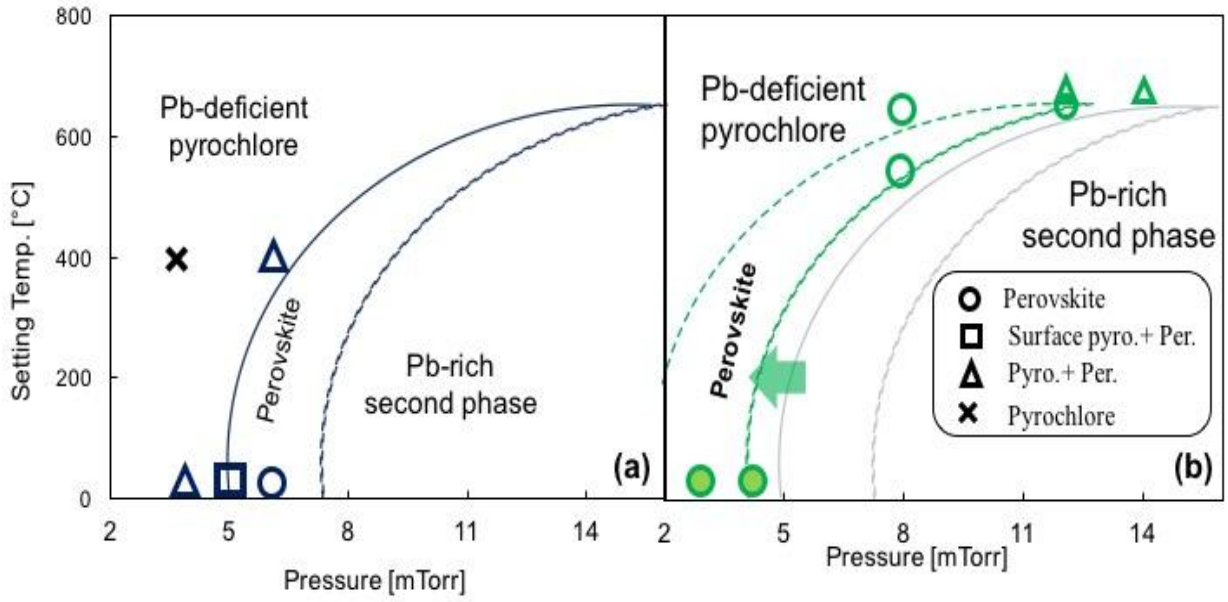

Figure 6-4. Schematic diagram of phase formation in PZT films sputtered (following a post-growth heat treatment step: crystallization at 650 °C for 1min in O_2 by RTA) as a function of Ar sputtering pressure and substrate set temperature. Data were acquired with the old sample holder using (a) 5% Pb excess target and (b) 10% Pb excess target. [Filled circles indicate PZT films sputtered on LNO/HfO_2/SiO_2/Si substrate]. Lines are drawn to guide the eye.

The perovskite single-phase zone is moved to lower pressure when the substrate temperature increases. For instance, sputtering at 6 mTorr and room temperature (~20 °C) with ex-situ crystallization was suitable for forming phase pure perovskite PZT films. In contrast, when PZT films were sputtered at a setting substrate temperature of 400 °C and 6 mTorr , a pyrochlore phase was found, which cannot be converted perovskite by annealing at 650 °C in RTA.

This suggests that the Pb content in the growing film could be decreased due to resputtering of PbO as the substrate temperature is increased during deposition.[31,33,39,40] In particular, the volatility of Pb from the film is likely to dramatically increase above ~500 °C.[41,42]

It has previously been reported that for growth of textured phase-pure perovskite PZT,

stringent control of the nucleation and growth process is required.[43] Generally this is done with a textured seed layer such as $PbTiO_3$ or $LaNiO_3$ to promote heterogeneous nucleation.[15] For *in situ* crystallization during sputtering at elevated substrate temperatures, a (001) oriented PZT seed layer was found to facilitate nucleation of the perovskite structure.

In this work, randomly oriented PZT(52/48) seed layers were prepared by sputtering onto a $Pt/TiO_x/SiO_2/Si$ substrate at room temperature with a subsequent annealing step for optimization of high temperature sputtering (An XRD pattern of the seed PZT layer is shown in Figure B-1).

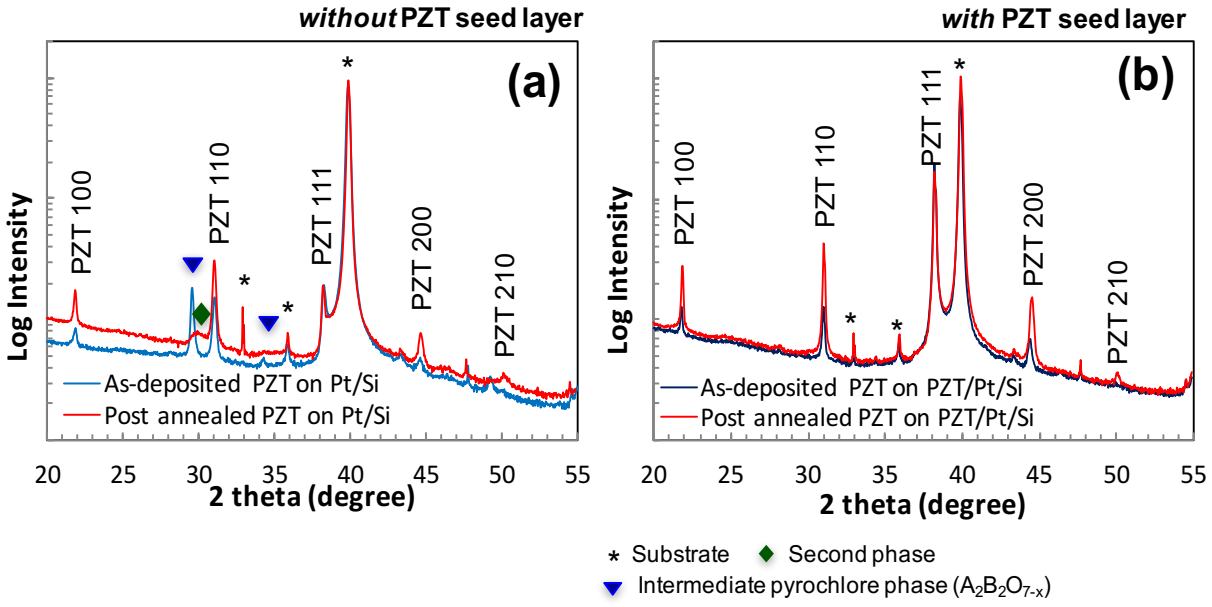

Figure 6-5. XRD pattern of (a) as deposited and post-annealed PZT films without seed layer (b) as-deposited and post-annealed PZT films with seed layer on platinized silicon substrate. Each deposition was for 15000 seconds to produce a PZT thickness of 0.5 μm.

First, PZT films were grown at an 8 mTorr chamber pressure with 3% gas mixture (90% [Ar]: 10% [O_2]) and 97% Ar gas flow at elevated temperature (setting temperature of 680 °C

with the old substrate holder) for 15000 seconds using a platinized silicon wafer with and without a randomly oriented PZT seed layer. Figure 6-5 shows XRD patterns of the high temperature sputtered PZT films. In the absence of a PZT seed layer, intermediate pyrochlore phase was found in the an as-grown PZT layer, which suggests that the actual temperature of the substrate is too low to allow for fully crystallized PZT films. This phase predominately did not convert to the pure perovskite phase after post deposition annealing (650 °C for 1min in O_2 atmosphere).

On the other hand, as-deposited single phase PZT films were achieved on the PZT seed layer, as shown in Figure 6-5(b). The observed random orientation of the PZT phase is a consequence of the random orientation of the seed layer.[15,44] No phase transformation appeared after post annealing, which suggests that the sputtered film was fully crystallized during sputtering. Thus, the presence of the seeding layer leads to improved perovskite formation of the sputtered PZT films.[45] Comparing the high temperature sputtered PZT films on Pt/Si substrate with and without the seed layers (in Figure 6-5(a)), it is clear that the PZT seed layer reduces the energy barrier for nucleation of the perovskite phase of PZT, enabling growth of well-crystallized films without second phases.[43,45]

Figure 6-6 shows the dielectric properties as a function of frequency, as well as the P-E hysteresis behavior for as-deposited and post annealed 0.5 μm thick PZT films on a (0.5 μm) PZT seeded $Pt/TiO_x/SiO_2/Si$ substrate. The dielectric constant of the as deposited PZT film is around 1100, which is comparable to randomly oriented PZT (52/48) films synthesized by other methods.[7] The dielectric constant of post annealed PZT films is slightly reduced (~1000) as is the dielectric loss, which dropped from 0.024 to 0.015 at 1 kHz. Ferroelectric hysteresis loops of as-deposited random PZT films have a remanent polarization of 20 $\mu C/cm^2$ and a coercive field of

~55 kV/cm. Thus, the electrical properties of the high temperature sputtered PZT films are comparable to those previous reported for other randomly oriented PZT films.[18,31]

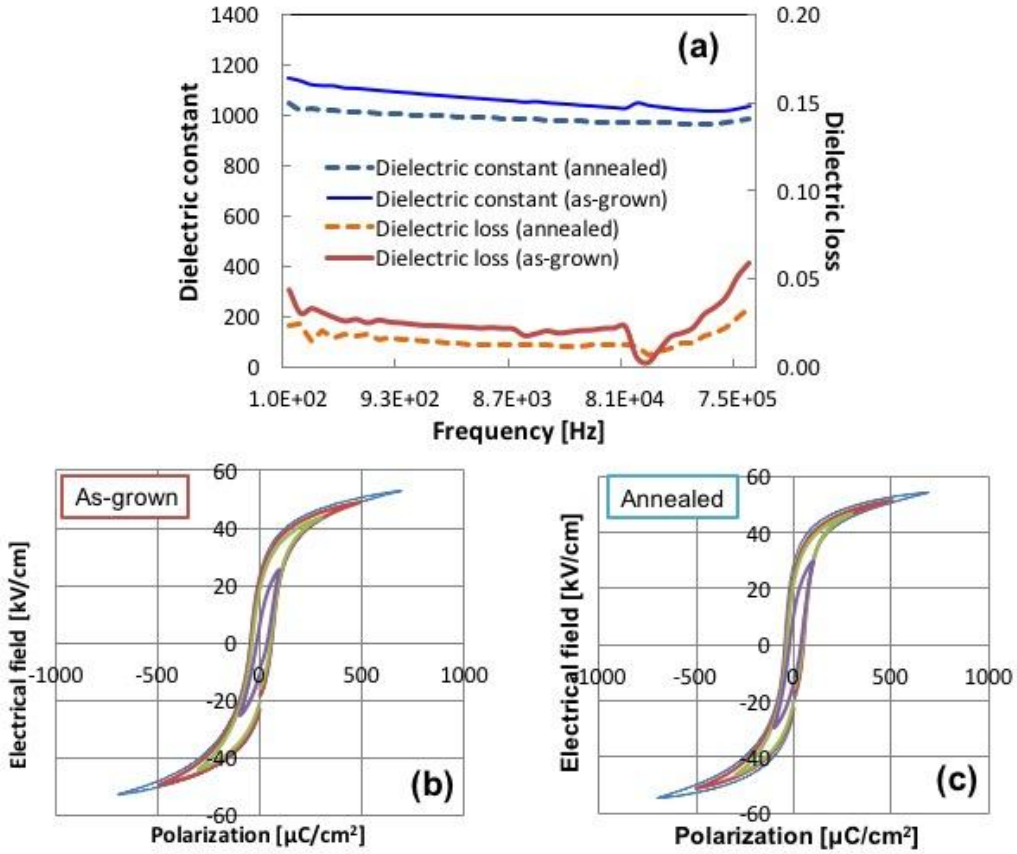

Figure 6-6. Dielectric constant and loss as a function of frequency. Polarization versus field (P-E) loops at 100 Hz of (b) as-grown and (c) post annealed PZT film coated by high temperature sputtering using a setting temperature of 680 °C for 15000 seconds (old sample holder).

As indicated by a peak at approximately 29°, in the XRD pattern (Figure 6-6 (a)), when the sputtering time was increased to 45000 s to achieve a thicker PZT film under the same sputtering conditions, an intermediate pyrochlore phase is observed in as-grown 1.4 μm thick PZT films on a seeded PZT substrate. However, in this case, the pyrochlore phase can be converted to the perovskite phase by post deposition annealing.

Microstructure images of the as-grown films, as well as post annealed films indicate that

both the grain shape and porosity change with the different processing conditions (Figure 6-6 (b)~(e)). It was observed that grains in the samples that were post annealed to remove the pyrochlore phase exhibited round shapes. There was little grain growth (grain size of as-grown film: 111±45 nm, and post annealed film: 138±51 nm by intercept method), but there were some pores that developed (red areas) during the post annealing step (Figure 6-6 (d) and (e)).[46]

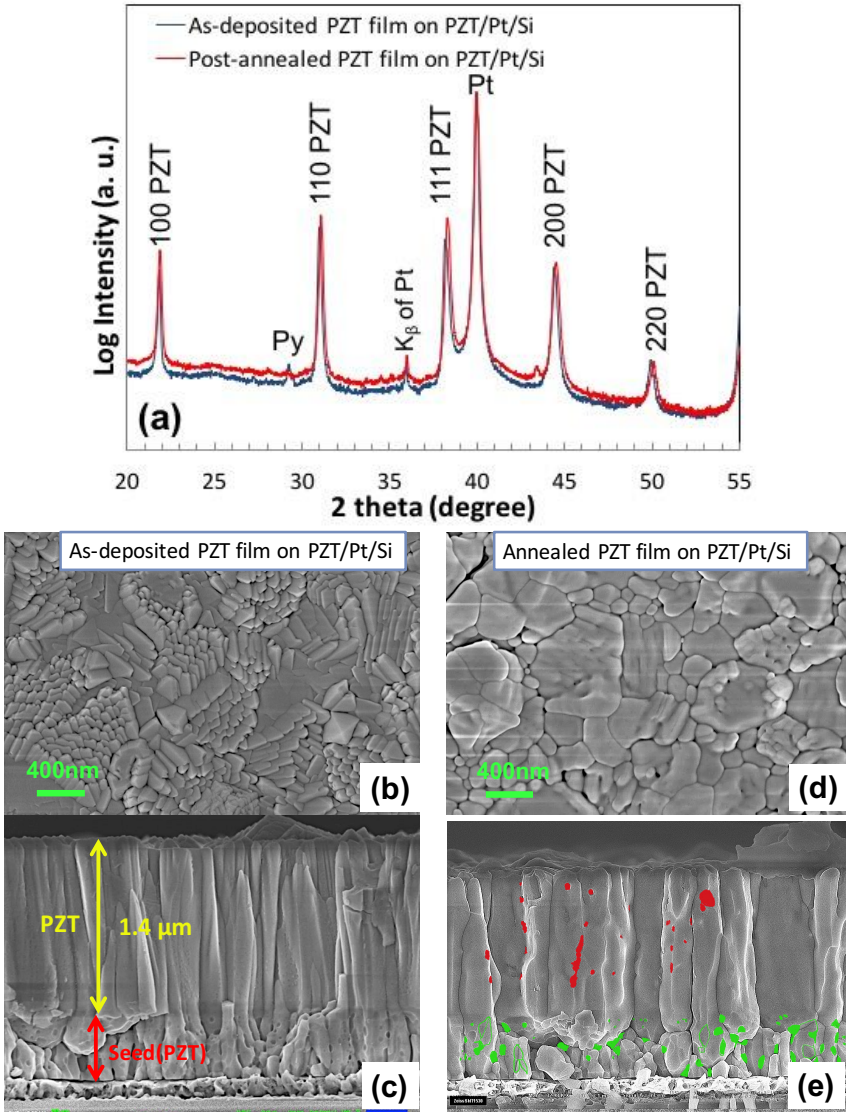

Figure 6-7. (a) XRD patterns of the sputtered PZT film on PZT/Pt/Si substrate at 680 °C setting temperature for 45000 seconds without and with post-annealing. [The symbols Py indicates pyrochlore phase]. FESEM micrographs of as sputtered films: (b) surface image, and (c) cross section image. (d) Surface and (e) cross sectional micrograph of post annealed films.

It is believed that Pb-rich intermediate pyrochlore phases near grain boundaries transform to PZT phase during post-annealing. The transformation can cause the development of pores (red areas) at the grain boundary due to evaporation of PbO.[23,46,47,48,49]

By sputtering at high temperatures, the density of the PZT film (pores marked in red) was improved compared to the room temperature sputtered seed layers (where pores are marked in green), as shown in Figure 6-6 (c) and (e). Both films show a columnar structure.

Practically, it is hard to control the temperature of substrate surface, because it strongly depends on the type of substrate holder, substrate, and thickness of sputtered films. For instance, a 700 °C setting temperature yielded fully crystallized 1.8 μm PZT films on a 0.5 μm PZT/Pt/TiO_x/SiO_2/Si substrate (confirmed by XRD pattern in Figure B-16), however, intermediate pyrochlore peaks are apparent for a 1.8 μm sputtered PZT films on 2.0 μm PZT/Pt/TiO_x/SiO_2/Si or a 2 μm PZT/ 100nm LNO/30 nm HfO_2/ 25 μm Ni foil (total thickness of PZT~ 3.8 μm). It was found that the relative intensity of the pyrochlore peak for the PZT on Ni foil was higher than that of the PZT film grown on PZT seeded silicon substrate (shown in Figure B-16).

The stoichiometry of target, especially deviation of lead content in the target, influence the ideal substrate temperature window during the sputtering to achieve fully crystallized PZT films. Therefore, a calibration study with each new target is necessary to determine the optimal setting substrate temperature. However, practically, the calibration study for new target was not always performed to settle the optimal substrate temperature window through a series of experiments with consideration of other variables (*e.g.* deposition time and substrate). Because targets were replaced after approximately every 25 μm deposited as a consequence of low deposition rate with the small target area (3”).

Furthermore, from the standpoint of phase uniformity on large substrates, the old sample holder did not provide uniform heat to the Ni foil, because the foil could not be tightly mounted without space between the substrate and holder (as described in Figure 6-3(c)). On the other hand, the new type of substrate holder with the window improved the temperature uniformity for the Ni foil since it removes the thermal obstacle between the heat source and the sample.

Figure B-17 and B-18 show the crystallinity of sputtered PZT films at different spots on the Ni foil with old and new holders, respectively. The new substrate holder provides superior uniformity. Moreover, fully crystallized sputtered PZT films (< 1 μm) were achieved on a PZT seeded Pt-coated silicon substrate at a 500 °C setting temperature with the new holder, which is approximately 180 °C lower than that with the old type holder under the same conditions in Figure B-19(a). Although there is still some intermediate pyrochlore phase, strongly oriented PZT perovskite phases peaks are visible in the sputtered film on Ni substrate at 500 °C in Figure B-19(b).

Subsequently, fully crystallized, high density thick PZT films (> 1.8 μm) were obtained on Si (550 μm) and Ni foils (25 μm) for substrate setting temperatures above 530 °C with the new holder in Figure B-18. The film growth required 16 hours 45 minutes at a chamber pressure of 8 mTorr Ar with 0.3% oxygen ratio using a 10% Pb excess PZT (52/48) target and a PZT seed layer.

The optimized conditions for in-situ crystallization sputtering with PZT seeded substrates were adopted for the deposition of thick PZT films (>5 μm) on Ni foil for piezoelectric energy harvesters. To build up a thick film (> 5 μm), 1.8 μm thick PZT layers were sputtered 3 times. Based on previous experimental results, three layers were sputtered under the same condition listed in Table B-3 in sequence. These conditions provide fully crystallized perovskite phase in

first and second sputtered PZT layer without post annealing. Some intermediate pyrochlore phase was detected in the third PZT layer on 3.6 μm PZT grown on Ni foil (25 μm) as shown in Figure B-20. On the other hand, it was found that third 1.8 μm layer of PZT grown on 3.6 μm PZT/ 100nm LNO/30 nm HfO_2/ 50 μm Ni foil at setting temperature of 550 ºC was well-crystallized without diffraction peaks attributed to pyrochlore as shown in Figure B-20. These results suggested that a higher substrate setting temperature will allow for complete perovskite formation of thicker PZT films during sputtering. Therefore, the substrate temperature set point was progressively increased with each successive sputtered PZT layer.

Following these optimization experiments, a PZT film was sputtered on Ni foil with (001) oriented PZT seed layer and (100) textured $LaNiO_3$ template layer at elevated temperature (above 550 °C). A (001) oriented PZT film is desired for obtaining high figure of merit for the piezoelectric energy harvester.[2,17,18,19] (100) oriented $LaNiO_3$ grown on a HfO_2 capped Ni substrate plays the role of template layer for (001) orientation of PZT seeded films, as shown both in Figure 6-8 (b) and previous chapters. The crystallized PZT seed layer (~ 70 nm thick) was prepared by CSD with 0.15 mole of 10 % Pb excess PZT (52/48) Mitsubishi solution based 1-butanol solvent. Figure 6-8 (c) shows the surface microstructure of the dense PZT seed layer without any visible surface pyrochlore phase, and with a similar grain size and shape as was observed in previous work.[18] A larger scale optical image shows reasonable thickness uniformity across the foil. The XRD pattern of the as-deposited PZT layer shows well oriented (00*l*) perovskite peaks, without any indication of intermediate pyrochlore phase, as shown in Figure 6-8(b). Thus, for the deposition conditions described in Table 6-2, (001) oriented PZT (52/48) thin films can be grown on a textured seed layers ((001) oriented PZT layer by CSD) using in-situ crystallization by sputtering at an elevated substrate temperature (>550 °C) with new substrate

holder.

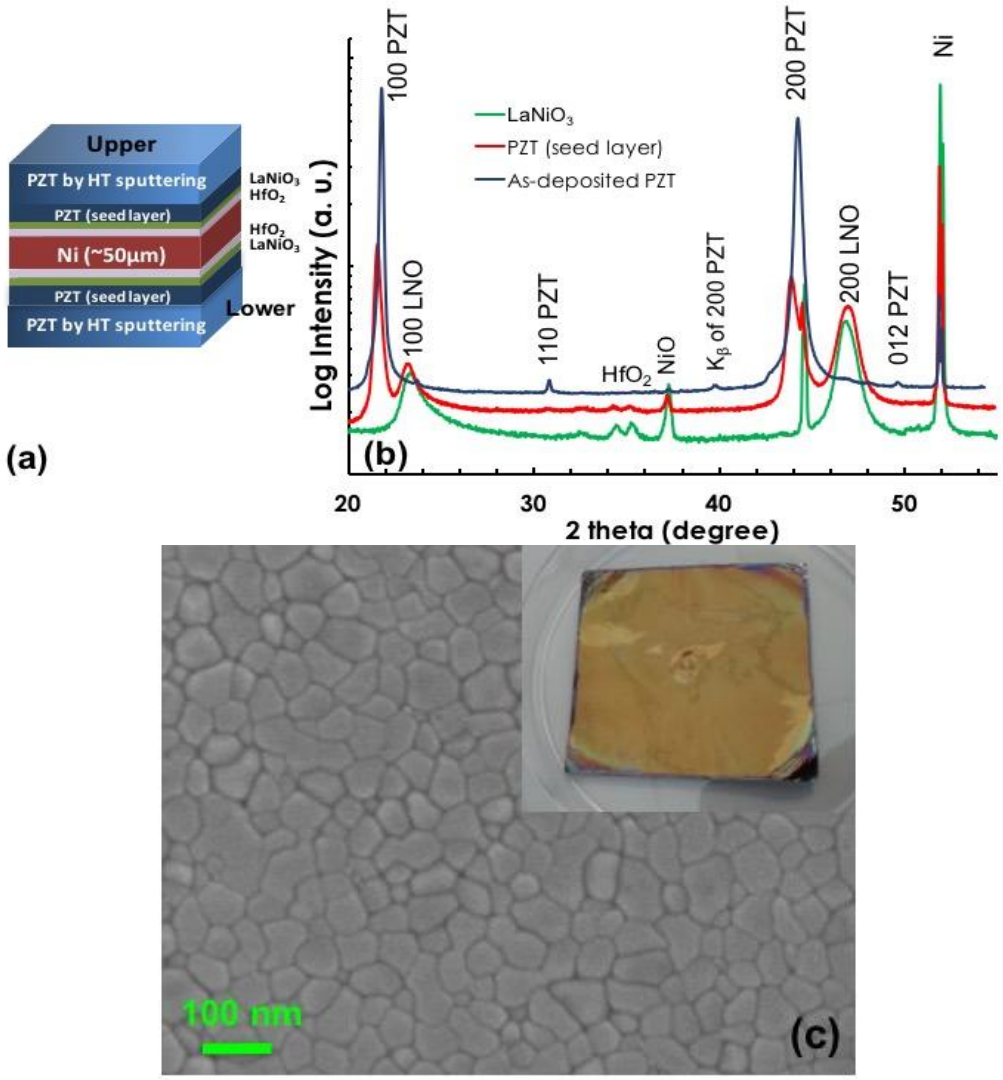

Figure 6-8 (a) Schematic cross-section of as-grown PZT, PZT seed layer, $LaNiO_3$ template, and HfO_2 passivated Ni foil bimorph. (b) XRD $\theta - 2\theta$ scan of high temperature (550 °C) sputtered PZT, seed layer (PZT) and $LaNiO_3$ (c) Surface FESEM images and (insert: optical picture: sample size is 5cm by 5cm square) of PZT seed layer by CSD.

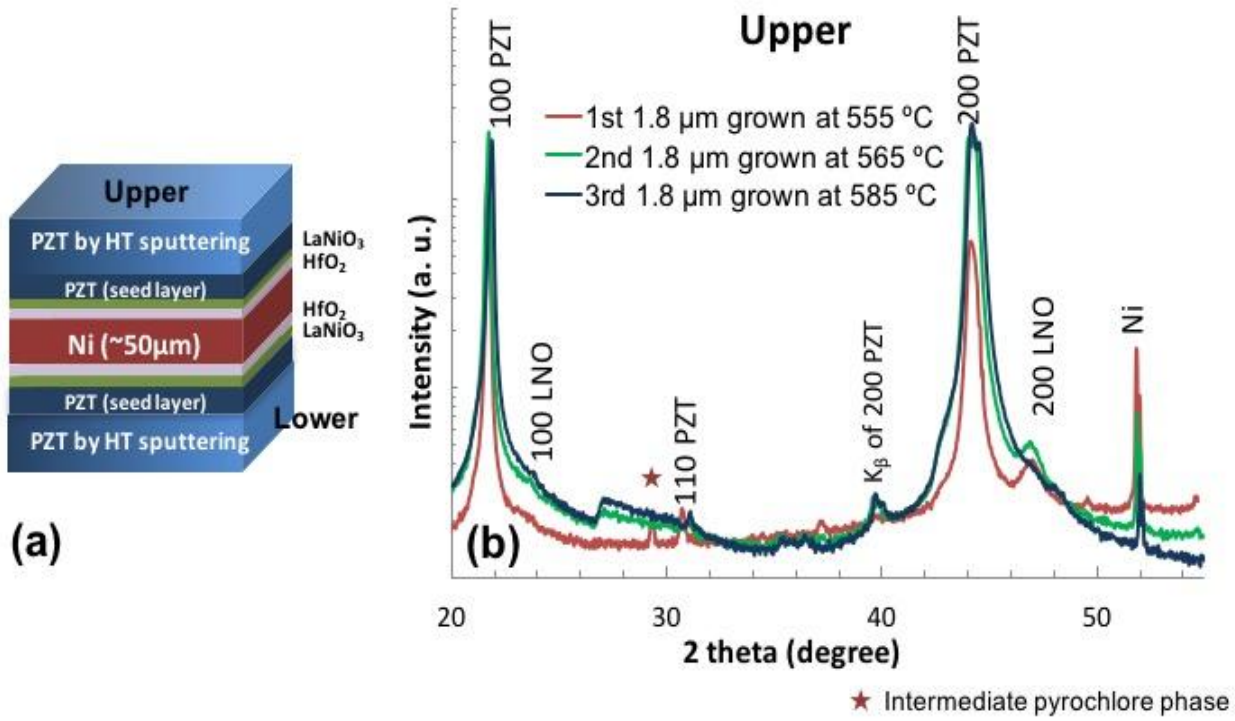

Figure 6-9. (a) Schematic of cross-section of bimorph PZT structure and (b) XRD patterns taken from each 1.8 µm thick PZT layer sputtered at various substrate setting temperatures.

The crystallinity of each layer in Figure 6-9(a) was assessed by XRD patterns taken after each successive PZT layer was grown. The XRD exhibits strongly (001) oriented perovskite peaks for each as-deposited PZT layer as shown in Figure 6-9(b). Although the first layer shows a small amount of intermediate pyrochlore phase (marked with a star) it was completely converted to the perovskite phase by post-deposition annealing in an RTA for 1 min at 650 °C. The deposition of the 5.4 µm thick PZT layer was achieved in three 1.8 µm steps.

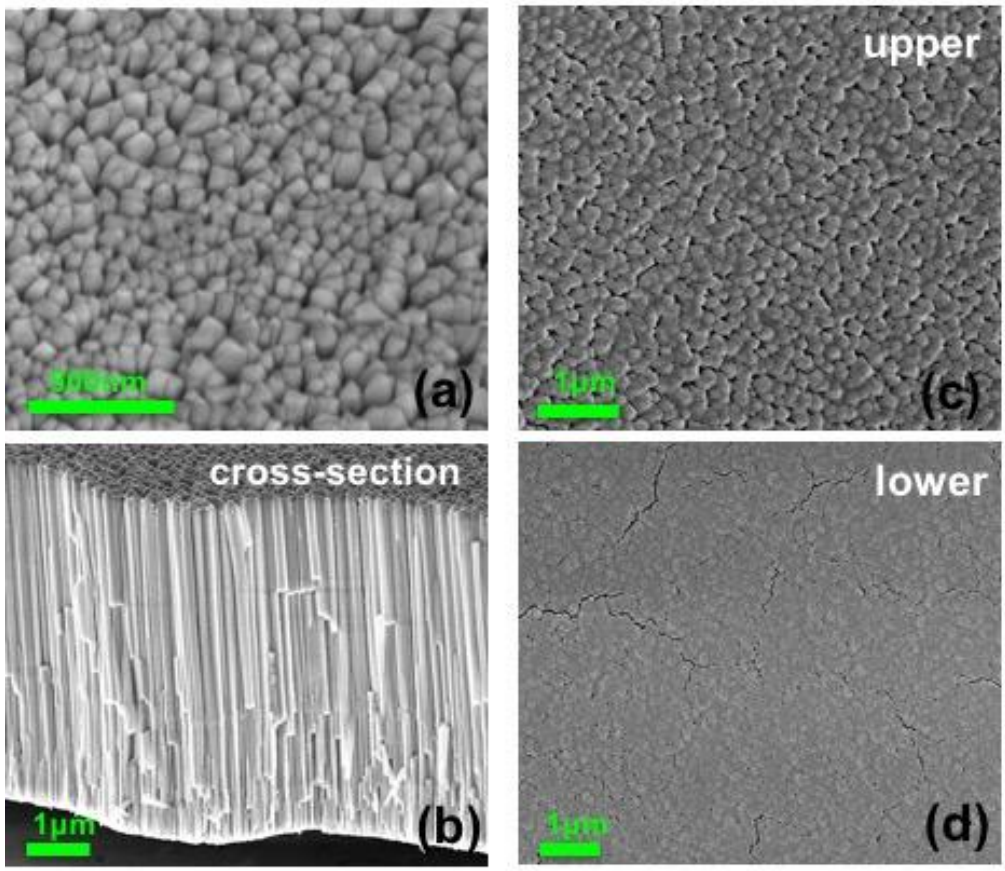

Figure 6-10. (a) Surface and (b) cross sectional FESEM images of 5.4 μm layers of PZT sputtered with in-situ crystallization. Top down microstructure images of (c) upper and (d) lower films after PZT layer capping by CSD.

Improved crystallization was observed as the substrate temperature was increased for the growth of each additional PZT layer. By following the same procedure, the reverse (back) side of the Ni foils was also deposited alternately three times with 1.8 μm thick sputtered PZT layer to reach a 5.4 μm thick PZT layer. A columnar structure with 50 to 90 nm of pyramid shaped grains were observed in the surface microstructure and cross section images in Figure 6-10(a) and (b) respectively. These pyramidal columnar grains and grooved grain boundaries produce a rough surface topography. The rough surface could cause electric field concentration, especially at grooved grain boundaries, which can lead to electrical breakdown.[50] To reduce the surface

roughness, one CSD PZT capping layer was grown on both sides of the as-deposited sputtered PZT layers as shown in Figure 6-10(c) and (d).

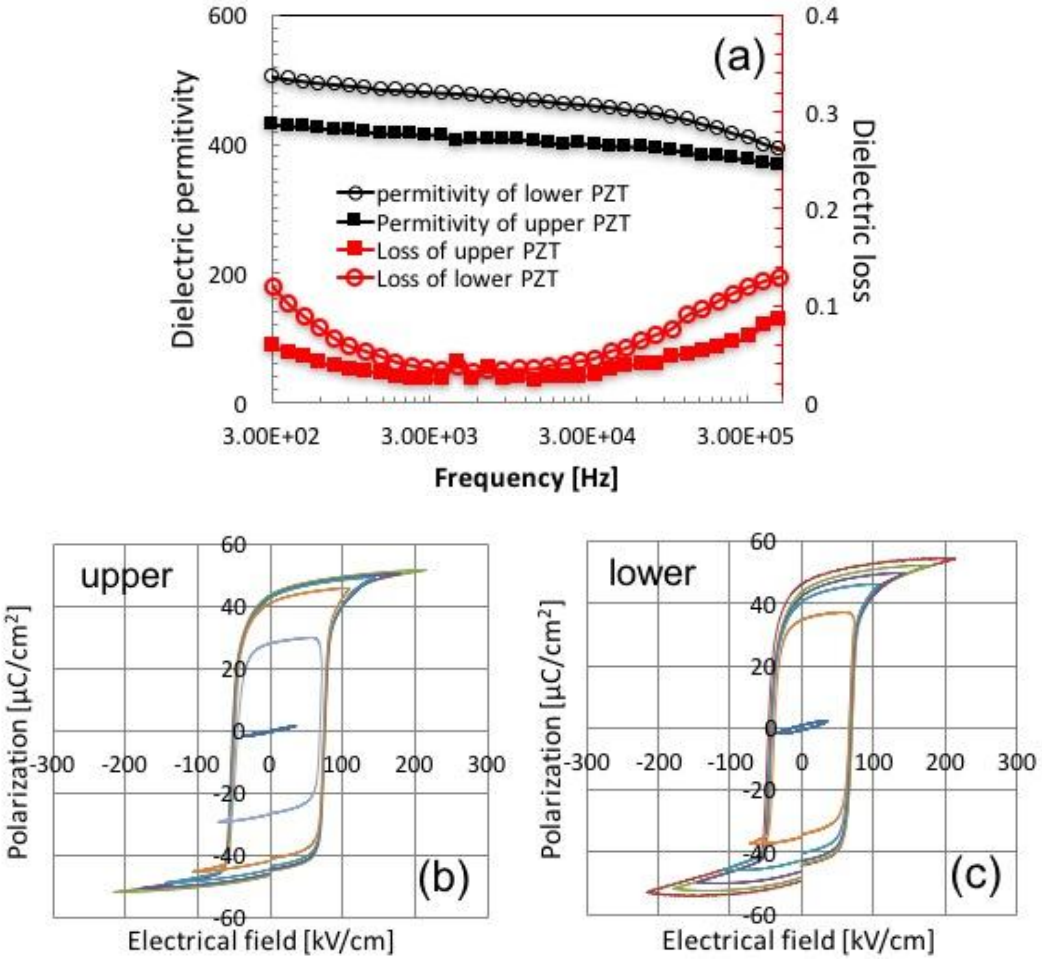

Figure 6-11. Electrical property measurements for both PZT layers on Ni foil grown by high temperature sputtering. (a) Dielectric constant and loss tangent of upper and lower PZT layer. Polarization-electric field hysteresis of (b) upper and (c) lower PZT layer.

The dielectric constant and loss of the upper and lower PZT films prepared by high temperature sputtering were measured by an LCR meter at 30 mV AC voltage signal from300 ~ 300 kHz. Dielectric constants (ε_r) of 410 and 470 with low losses of 0.03 and 0.035 were observed for the upper and lower PZT layers respectively at 10 kHz, as shown in Figure 6-12(a).

The P-E hysteresis loops of both PZT layers have square shapes with large remanent polarizations (Figure 6-11(b) and (c)). Low dielectric constants and large remanent polarizations, which are characteristic of (001) oriented PZT films with large *c*-domain populations, were observed for both PZT layers.[17,18] Thus, (001) strongly oriented thick bimorph PZT films on Ni foil by in-situ crystallization sputtering show significant promise for enhancement of the FoM of the piezoelectric energy harvester.[2] The method for producing 5.4 μm thick bimorph structure of the PZT films on Ni foil can be applied to produce a wide range of shapes for diverse types of piezoelectric energy harvesters.

6.4 Conclusions on High Temperature Sputtering

An overview was given on the growth of {001} oriented PZT films on Ni substrate using in situ crystallization *rf* magnetron sputtering. The Pb content of as-grown PZT film is strongly dependent on the substrate temperature and chamber pressure. To compensate for evaporation of Pb atoms at higher substrate temperatures, a higher chamber pressure is required. Also, a PZT seed layer is essential for obtaining pure perovskite phase by high temperature sputtering under the conditions described in Table 6-2.

This study exhibits successfully grown dense PZT films on flexible Ni foil by high temperature sputtering. Furthermore, strongly {001} oriented PZT film have been obtained on both sides of Ni substrates up to a thickness of 5.4 μm. Well-saturated square shaped P-E hysteresis loops and low dielectric constant (ε_r ~ 450 at 10Hz) suggest that the sputtered PZT films have a large fraction of *c*-domains aligned along out-of-plane. This produces a high figure of merit for energy harvesters.

6.5 References

[1] S.-G. Kim, S. Priya, and I. Kanno, “Piezoelectric MEMS for energy harvesting,” *MRS Bulletin*, **37**, 11 (2012) 1039.

[2] C. B. Yeager and S. Trolier-McKinstry, “Epitaxial $Pb(Zr_x,Ti_{1-x})O_3$ ($0.3<x<0.63$) Film on (100) MgO Substrate for Energy Harvesting Applications,” *Journal of Applied Physics*, **112**, 7 (2012) 074107.

[3] F. Calame, P. Muralt, "Growth and properties of gradient free sol-gel lead zirconate titanate thin films," Applied Physics Letters **90**, 6 (2007) 2907.

[4] S. Trolier-McKinstry, F. Griggio, C. Yeager, P. Jousse, D. Zhao, S. S. N. Bharadwaja, T. N. Jackson, S. Jesse, S. V. Kalinin, and K. Wasa, “Designing piezoelectric films for micro electromechanical system,” *Ultrasonics, Ferroelectrics and Frequency Control, IEEE Transactions*, **58**, 9 (2011) 1782.

[5] B. A. Tuttle, J. A. Voigt, T. J. Garino, D. C. Goodnow, R. W. Schwartz, D. L. Lammpa, and M. O. Eatough, “Chemically prepared Pb $(Zr,Ti)O_3$ thin films: the effects of orientation and stress,” Applications of Ferroelectrics, ISAF'92., *Proceedings of the Eighth IEEE International Symposium on. IEEE*, (1992) 344.

[6] C. B. Yeager, Y. Ehara, N. Oshima, H. Funakubo, and S. Trolier-McKinstry, “Dependence of $e_{31,f}$ on polar axis texture for tetragonal $Pb(Zr_x,Ti_{1-x})O_3$ thin films,” *Journal of Applied Physics*, **116**, 10 (2014) 104907.

[7] N. Izyumskay, Y. –I. Alivov, S.-J. Cho, H. Morkoc, H. Lee and Y.-S. Kang, “Processing, structure, properties, and applications of PZT thin films,” *Critical Reviews in Solid State and Materials Sciences*, **32** (2007) 111.

[8] J. C. Park, D. H. Lee, J. Y. Park, Y. S. Chang, and Y. P. Lee, "High performance piezoelectric

MEMS energy harvester based on d_{33} mode of PZT thin film on buffer-layer with $PbTiO_3$ inter-layer," *TRANSDUCERS 2009-2009 International Solid-State Sensors, Actuators and Microsystems Conference. IEEE*, (2009) 517.

[9] Y. Qi, N. T. Jafferis, K. Lyons Jr, C. M. Lee, H. Ahmad, and M. C. McAlpine, "Piezoelectric ribbons printed onto rubber for flexible energy conversion," *Nano letters*, **10**, 2 (2010). 524.

[10] Z. Song, J. Gao, X. Zhu, L. Wang, X. Fu, C. Lin, "Effects of excess Pb on structural and electrical properties of $Pb(Zr_{0.48}Ti_{0.52})O_3$ thin films using MOD process," *Journal of Materials Science*, **36** (2001) 4285.

[11] K. Morimoto, I. Kanno, K. Wasa, and H. Kotera, "High-efficiency piezoelectric energy harvesters of c-axis-oriented epitaxial PZT films transferred onto stainless steel cantilevers," *Sensors and Actuators A: Physical*, **163**, 1 (2010) 428.

[12] M. de Keijser, J. F. M. Cillessen, R. B. F. Janssen, A. E. M. De Veirmn, and D. M. de Leeuw, "Structural and electrical characterization of heteroepitaxial lead zirconate titanate thin films," *Journal of Applied Physics*, **79**, 1 (1996) 393.

[13] K. Sreenivas, M. Sayer, and P. Garrett, "Properties of D. C. magnetron-sputtered lead zirconate titanate thin films," *Thin Solid Films*, **172** (1989) 251.

[14] S. S. N. Bharadwaja, F. Griggio, J. Kulik, and S. Trolier-McKinstry, "Highly textured laser annealed Pb $(Zr_{0.52}Ti_{0.48})O_3$ thin films," *Applied Physics Letters*, **99**, 4 (2011) 042903.

[15] A. Rajashekhar, A. Fox, S. S. N. Bharadwaja, and Susan Trolier-McKinstry, "In situ laser annealing during growth of $Pb(Zr_{0.52}Ti_{0.48})O_3$ thin films," *Applied Physics Letters*, 103 (2013) 032908.

[16] N. Bassiri-Gharb, B. Yaser, and B. Ashley, "Chemical solution growth of ferroelectric oxide thin films and nanostructures," *Chemical Society Reviews*, **43**, 7 (2014) 2125.

[17] K. Wasa, T. Matsushima, H. Adachi, I. Kanno, and H. Kotera, "Thin-film piezoelectric materials for a better energy harvesting MEMS," *Journal of Microelectromechanical Systems*, **21**, 2 (2012) 451.

[18] H. G. Yeo, and S. Trolier-McKinstry "{001} Oriented piezoelectric films prepared by chemical solution deposition on Ni foils," *Journal of Applied Physics*, **116**, 1 (2014) 014105.

[19] H. G. Yeo, X. Ma, C. Rahn, and S. Trolier-McKinstry, "Efficient piezoelectric energy harvesters utilizing (001) textured bimorph PZT films on flexible metal foils," *Advanced Functional Materials*, **26** (2016) 5940.

[20] G.-T. Park, C.-S. Park, J.-J. Choi, J.-W. Lee and H.-E. Kim, "Effects of thickness on piezoelectric properties of highly oriented lead zirconate titanate films," *Journal of American Ceramic Society*, **89**, 7 (2006) 2314.

[21] Q. Zhao, D. Su, M. Cao, G. He, J. Di, J. Yuan, and D. Wang, "Thickness-dependent electrical properties of sol–gel derived $Pb(Zr_{0.52}Ti_{0.48})O_3$ thick films using $PbTiO_3$ buffer layers," *Journal of Materials Science: Materials in Electronics*, **24**, 9 (2013) 3521.

[22] H. D. Chen, K. R. Udayakumar, C. J. Gaskey, L. E. Cross, J. J. Bernstein, and L. C. Niles, "Fabrication and electrical properties of lead zirconate titanate thick films," *Journal of the American Ceramic Society*, **79**, 8 (1996) 2189.

[23] M. Wallace "Performance of PZT based MEMS devices with integrated ZnO electronics," Ph.D. thesis in Materials Science and Engineering, *The Pennsylvania State University* 2016.

[24] G. R. Fox, S. B. Krupanidhi, K. L. More, and L. Allard, "Composition/structure/property relations of multi-ion-beam reactive sputtered lead lanthanum titanate thin films: Part I. Composition and structure analysis," *Journal of Material Research*, **7**, 11 (1992) 3039.

[25] T. Fujii, Y. Hishinuma, T. Mita, and T. Naono, "Characterization of Nb-doped $Pb(Zr,Ti)O_3$

films deposited on stainless steel and silicon substrates by RF-magnetron sputtering for MEMS applications," *Sensors and Actuators A* **163** (2010) 220.

[26] O. Blanco, J. Heiras, J. M. Siqueiros, E. Martinez, and A. G. Castellanos-Guzman, "PZT films grown by RF sputtering at high oxygen pressure," *Journal of Materials Science Letters*, **22** (2003) 449.

[27] G. Velu and D. Remiens, "In situ deposition of sputtered PZT films: Control of the growth temperature by the sputtered lead flux," *Vacuum*, **56**, 3 (2000) 199.

[28] K. Komaki, T. Kamada, S. Hayashi, M. Kitagawa, R. Takayama, and T. Hirao, "Preparation of pyroelectric $Pb_{1-x}La_xTi_{1-x/4}O_3$ thin films from ceramic target by RF magnetron sputtering," *Japanese Journal of Applied Physics*, **33**, 3B (1994) L443.

[29] S.-M. Ha, D.-H. Kim, H.-H. Park, and T.-S. Kim "Crystallization and ferroelectric behavior of sputter deposited PZT using a target containing excess Pb and O contents," *Thin Solid Films*, **355** (1999) 525.

[30] R. N. Castellano, "Ion beam deposition of ferroelectric thin films sputtered from multicomponent targets," *Journal of Vacuum Science & Technology*, **17**, 2 (1980) 629.

[31] S. B. Krupanidhi, N. Maffei, M. Sayer, and K. El-Assal, "RF planar magnetron sputtering and characterization of ferroelectric $Pb(Zr,Ti)O_3$ films," *Journal of Applied Physics*, **54**, 11 (1983) 6601.

[32] U. Poppe, "Herstellung von oxidschichten mit physikalischen methoden: Sputtern, reaktives aufdampfen, laserablation." *Elektrokeramische Materialien* **26** (1995) 1.

[33] G. Velu, D. Remiens, "In situ deposition of sputtered PZT films: control of the growth temperature by the sputtered lead flux," *Vacuum*, **56** (2000) 1999.

[34] B. Vilquin, R. Bouregba, G. Poullain, H. Murray, E. Dogheche, and D. Remiens,

Crystallographic and optical properties of epitaxial $Pb(Zr_{0.6}Ti_{0.4})O_3$ thin films grown on $LaAlO_3$ substrates, *Journal of Applied Physics*, **94**, 8 (2003) 5167.

[35] K. Suu, A. Osawa, N. Tani, M. Ishikawa, K. Nakamura, T. Ozawa, K. Sameshima, A. Kamisawa, and H. Takasu, "Preparation of $(Pb,La)(Zr,Ti)O_3$ ferroelectric films by RF sputtering on large substrate," *Japanese Journal of Applied Physics*, **35**, 9S (1996) 4967.

[36] M. Kratzer, L. Castaldi, B. Heinez, R. Mamazza, D. Kaden, H.-J. Quenzer and B. Wagner, "In-situ large scale deposition of PZT films by RF magnetron sputtering." 2011 International Symposium on Applications of Ferroelectrics (ISAF/PFM) and 2011 International Symposium on Piezoresponse Force Microscopy and Nanoscale Phenomena in Polar Materials. IEEE, (2011) pp1.

[37] G.L. Brennecka, and B. A. Tuttle, "Fabrication of ultrathin film capacitors by chemical solution deposition," *J. Mater. Res.* **22**, (2007) 2868]

[38]T. Tani and D. A. Payne, "Lead-oxide coatings on sol gel-derived lead lanthanum zirconium titanate thin-layers for enhanced crystallization into the perovskite structure," *J. Am. Ceram. Soc.* **64** (1981) 517.

[39] A. Pignolet, R. A. Roy, J. P. Doyle, and J. J. Cuomo, "Model of lead loss in $Pb(Mg_xNb_{1-x})O_z$ ion beam sputtered thin films," *J. Vac. Sci. Technol. A* **12**, 5 (1994) 2840.

[40] K. Yamakawa, O. Arisumi, K. Okuwada, K. Tsutsumi, and T. Katata, (1998). "Development of stable PZT sputtering process using ex-situ crystallization and PZT/Pt interface control technique," In Applications of Ferroelectrics, 1998. ISAF 98. Proceedings of the Eleventh IEEE International Symposium on (pp. 159-162). IEEE.]

[41] E. Sato, Y. Huang, M. Kosc, A. Bell, and N. Setter, "Lead loss, preferred orientation, and the dielectric properties of sol-gel prepared lead titanate thin films," *Applied Physics Letters*, 65, 21

(1994) 2678.

[42] R. H. T. Wilke, R. L. Johnson-Wilke, V. Cotroneo, W. N. Davis, P. B. Reid, D. A. Schwartz, and S. Trolier-McKinstry, "Sputter deposition of PZT piezoelectric films on thin glass substrates for adjustable x-ray optics," *Applied Optics*, **52**, 14 (2013) 3412.

[43] P. Muralt, "Texture control and seeded nucleation of nanosize structures of ferroelectric thin films," *Journal of Applied Physics*, **100**, 5 (2006) 51605.

[44] A. Bose, M. Sreemany, and S. Bysakh, "Crystallization trend in STO-seeded sputtered PZT thin films: Effects of seed layer thickness and post-annealing temperature," *Vacuum*, **107** (2014) 10.

[45] C. K. Kwok, and S. B. Desu, "Low temperature perovskite formation of lead zirconate titanate thin films by a seeding process," *Journal of Materials Research*, **8**, 2, (1993) 339.

[46] G. R. Fox, S. B. Krupanidhi, K. L. More, and L. Allard, "Composition/structure/property relations of multi-ion-beam reactive sputtered lead lanthanum titanate thin films: Part II. Textured microstructure development," *Journal of Material Research*, **8**, 9 (1992) 2191.

[47] J. A. Voigt, B. A. Tuttle, T. J. Headley, and L. Lamppa, "The pyrochlore-to-perovskite transformation in solution-derived lead zirconate titanate thin films," *MRS Proceedings*, **361** (1995) 395.

[48] A. Croteau, S. Matsubara, Y. Miyasaka, and N. Shohata, (1987). Ferroelectric Pb $(Zr,Ti)O_3$ thin films prepared by metal target sputtering," *Japanese Journal of Applied Physics,* **26(S2)**, 18.

[49] A. H. Carim, B. A. Tuttle, D. H. Doughty, and S. L. Martinez, "Microstructure of solution-processed lead zirconate titanate (PZT) thin films," *Journal of the American Ceramic Society*, **74**, 6 (1991) 1455.

[50] M. M. Samantaray, A. Gurav, E. C. Dickey, C. A. Randall, "Electrode defects in multilayer capacitors part i: modeling the effect of electrode roughness and porosity on electric field enhancement and leakage current," *Journal of the American Ceramic Society* **95**, 1 (2012) 257.

Chapter 7

Non-resonant Piezoelectric Energy Harvesters Utilizing High Temperature Sputtered PZT films

7.1 Introduction

For a vibrational energy harvester, the resonance frequency of the harvester should match the source vibration frequency in order to generate maximum output performance. However, conventional resonant piezoelectric energy harvesters (PEH) are not appropriate to extract electrical energy from human motion due to aperiodic excitation with components over a broad range of frequencies and various directions of acceleration.[1~3]

Recently many reports have proposed alternative design strategies to overcome these limitation and challenges. One strategy for ultra-low-frequency vibration is to convert the low frequency vibration caused by mechanical source to a higher frequency vibration of the piezoelectric material via repulsive/attractive magnetic coupling and mechanical plucking (frequency up-conversion design).[4,5] Fan et al. developed a beam-roller PEH source which couples very low frequency sway excitation to a conventional cantilever PZT beam (brass substrate and a piezoelectric patch) with an embedded magnet.[6] Pillatsch et al. proposed a frequency up design with a permanent magnet and a 130 μm thick piezoelectric layer on a 110 μm thick carbon fiber center shim. The rotational harvester utilizes the rotation of an eccentric proof mass to produce plucking of the piezoelectric beam by coupling between a pair of permanent magnets when these magnets are close each other.[6] In those energy harvesters, the PZT beam should be long (19.5mm) due to the use of a stiff PZT bulk ceramic that leads to poor free oscillation and low powers.[5] Thus, PZT films on flexible metal foil for frequency up-converting harvesters could be beneficial in terms of large deflection at limited beam size.

The goal of this research is to develop and fabricate an optimized non-resonant PEH for a wrist worn harvester. The wrist is one good location on the body to wear a device, such as watch, without adverse feelings. For wrist-worn non-resonant piezoelectric energy harvesters, three different magnetic plucking configurations were proposed by collaborators Shad Roundy and Tiancheng Xue using strongly (001) oriented bimorph PZT films on Ni foil for the piezoelectric beams. Those designs arose from optimization of the rotor dynamics, magnetic interactions and piezoelectric beam model.

In terms of the piezoelectric element, the ability to undergo and survive large strains (which requires a highly flexible and mechanically tough piezoelectric) and a large volume of piezoelectric material with high figure of merit improve the performance of the harvesters. As highly textured PZT films on flexible Ni foil satisfy these requirements, they were applied in these designs for non-resonant piezoelectric energy harvesters.

7.1.1 Generation I (Gen-I, Star Shaped Design)

Gen-I is based on a frequency up-conversion mechanism using multiple magnetically plucked thin-film piezoelectric beams with an out-of-plane deflection mode.[5,7,8] This configuration is shown in Figure 7-1 (a) for the rotational designs.

The beam is deflected by the indirect repulsive force between one fixed magnet (on the end of the beam) and one moving magnet (embedded in the rotor). The deflection is perpendicular to the plane of magnet motion in the out-of-plane plucking configuration. Figure 7-1 (b) illustrates a schematic model of a prototype harvester consisting of a star shaped six rectangular beam array with permanent magnets (NdFeB, Grade N42 (Chinese standard), mass = 0.06g) attached to the end of each beam and to the eccentric rotor. The gap between magnets is 1

mm with 0.5 mm offset in the z direction. The star shaped piezoelectric element allows the use of multiple beams fabricated on a single substrate. Therefore, assembly is comparatively simple for multiple beams in the device. In addition, it can be easily miniaturized using MEMS technology.[8] In this configuration, the PZT beams are fixed at the center point, while the rotor is freely moving, and can be excited into motion by human activity. As is characteristic of cantilever beams, this device concentrates the strain at the root of the cantilever (unlike the compliant design mechanism discussed in Chapter 5). It means that the beams can suffer over strain near the clamping points during large oscillations.

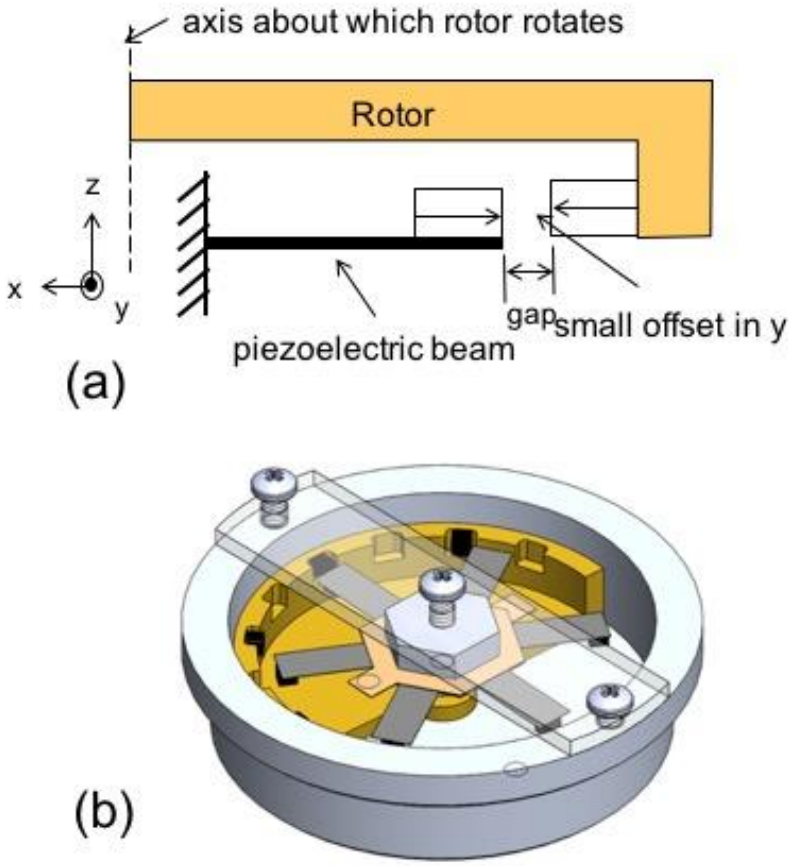

Figure 7-1. (a) Magnet configuration showing coupling between the magnets on the eccentric rotor with the magnets glued to the piezoelectric beams. (b) Illustration of Gen I device with six star shaped PZT beams. [Drawn by Tiancheng Xue]

The model has a large space where no piezoelectric material is utilized. Thus, it is necessary to improve space utilization for wrist-worn harvesters, to increase the energy output without increasing the device size.

7.1.2 Generation II (Gen-II, Clamped-Clamped Design)

Gen-II used fixed-fixed rectangular beams to improve area utilization (i.e. so that there is a higher volume of piezoelectric to be utilized). In this design, six piezoelectric beams (four on the front side and two on the back) are feasible to assemble for a wrist-worn non-resonant energy harvester, as illustrated in Figure 7-2.

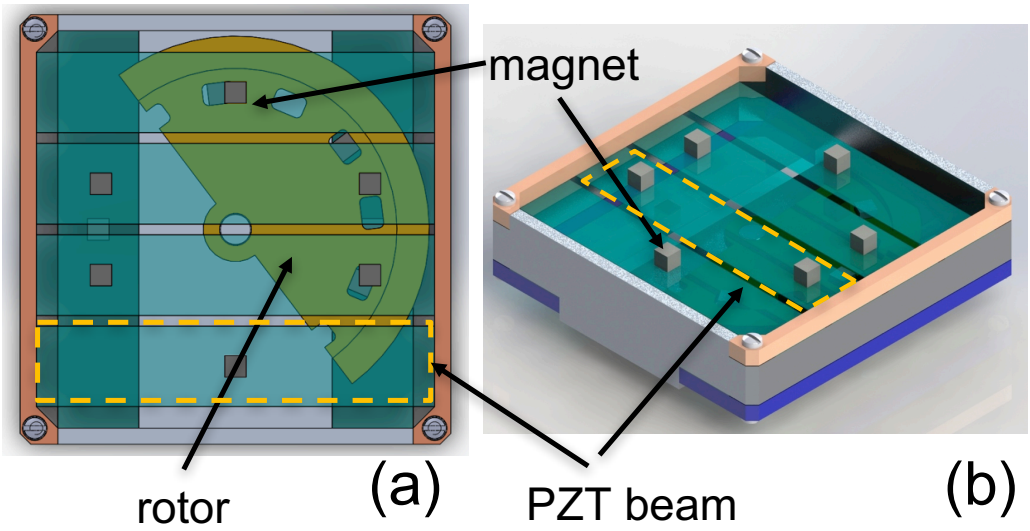

Figure 7-2. Schematic (a) top down view and (b) angled view of the Gen II harvester design. [Drawn by Tiancheng Xue]

Ideally, the simplest plucking geometry for the rectangular beams would be the direct repulsive force caused by coupling of magnets placed on the middle of the beams and on the rotor. The direct repulsive configuration provides the largest transverse force of out-of-plane plucking configurations for a given gap between magnets.[9] In this device, the clamped-clamped beams operate in two strain modes: a stretching mode and bending strain mode. The bending

strain is not uniform; it varies along the cross-section and length of the beam as shown in Figure 7-3 (a). In contrast, the stretching strain mode always applied tensile strain for both upward and downward motion, as seen in Figure 7-3 (b).[9]

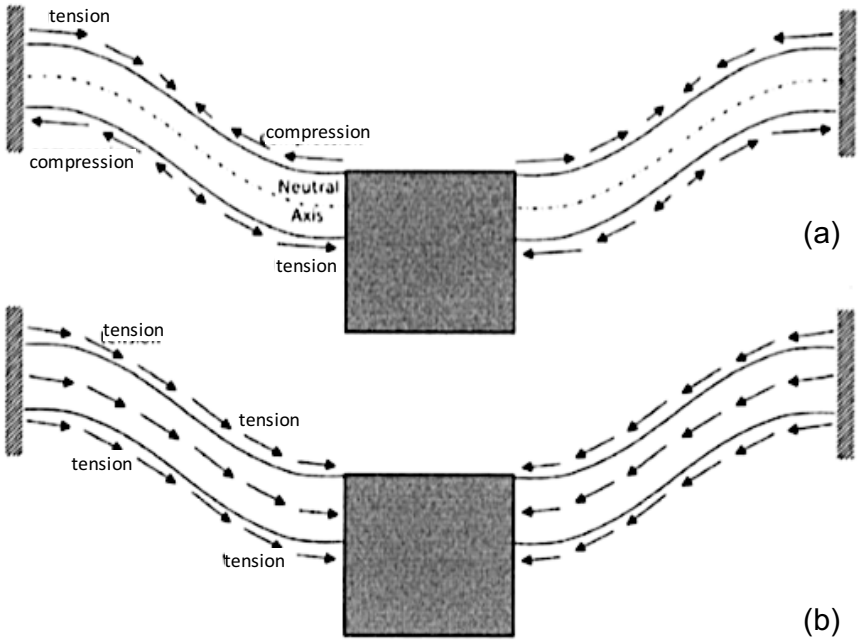

Figure 7-3. Strain distribution in clamped-clamped structures: (a) Bending vs. (b) stretching. (Figure from reference 9).

The relative contributions of the two strain modes strongly depends on the amplitude of the oscillations. Bending-dominated behavior occurs for small deflection of the proof mass (i.e. when the deflection is smaller than beam thickness).[9] The clamped-clamped beam is more likely to be dominated by the stretching mode at large deflections (*i.e*. when the deflection is larger than the beam thickness) and the strain is uniform throughout the thickness in the majority of the beam.[9] In principle, a direct repulsive magnet configuration producing large deflection can give a

tensile stretching strain, which is a key feature in this design.[9,10]

Unlike the clamped-free cantilever beams used in Gen-I, clamped-clamped beams undergo nonlinear stiffness corresponding to hardening due to the stretching of the beam.[11] The nonlinearity of the stiffness becomes dominant at large vibrational amplitude, with an associated widening of the resonance peak due to Duffing stiffening.[9] For large deflections using the direct repulsive configuration, a larger gap between opposing magnets is indispensable to avoid being stuck together in a side by side orientation (called the pull-in effect).[8] Moreover, large gaps between magnets restricts the magnetic coupling and complicates achieving higher strain in the beam.

7.1.3 Generation III (Gen-III, Flower Petal Design)

The Gen-III model for a rotational harvester was designed with six trapezoidal shaped cantilever beam with attached permanent magnets; each beam is excited based on out-of-plane magnetic plucking as shown in Figure 7-1(a). 1 mm tip displacement in the out-of-plane direction produces an average strain of ~0.03% on the surface. This can be induced by 0.05 N of transverse force using 2 mm^3 size of NdFeB magnets as predicted by finite element analysis (FEA) on one trapezoidal beam (modeling by T. Xue in the S. Roundy group at the University of Utah). Through this simulation, it was predicted that the out-of-plane indirect repulsive magnet configuration should have a 1 mm gap and 1.2 mm out-of-plane offset between the magnet on the rotor and the one at the end of beam in order to apply 0.05 N of transverse force. (tip displacement 1mm, average strain on surface :0.0282%)

A trapezoidal shaped beam also improves the strain distribution applied to the piezoelectric, relative to a rectangular cantilever beam.[12] This design also utilized large area top

electrodes to maximize efficiency. Unlike other designs, heavier tungsten weights were used to enhance inertial motion of the eccentric rotor to overcome repulsive magnetic coupling force.

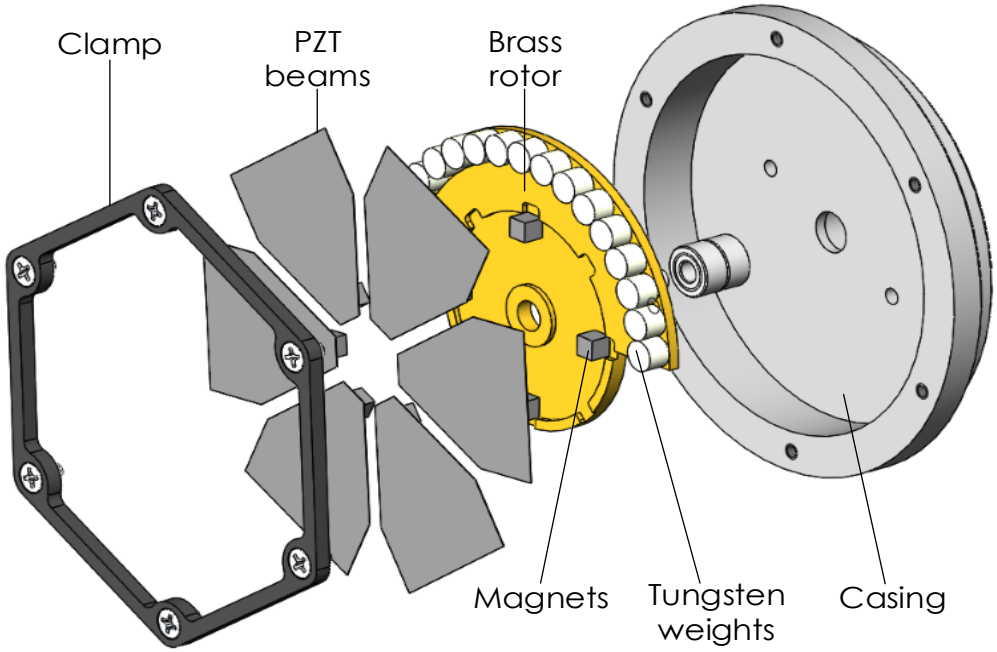

Figure 7-4. Illustration of PZT beams, rotor, magnets with other parts for flower petal designed device (Gen III). [Drawn by Tiancheng Xue]

7.2 Experimental Procedure

7.2.1 Fabrication of Gen-I

For the Gen-I wrist-worn PEH, six cantilever PZT beams, which are the electromechanical transducer of the device, are required. Complex star shapes with six rectangular beams were prepared from {001} textured bimorph PZT films on Ni foils (5 cm×5 cm×25 μm). The PZT films on Ni were grown by *rf*-magnetron sputtering with post annealing to achieve 3 μm thickness on both sides, in the same manner as described in Chapter 4.[13]

The complex star shape configuration shown in Figure 7-5(a) was cut by the laser ablation tool, which uses a short pulse duration laser (pico-second) at a wavelength of 355 nm

and small laser spot (20 μm~40 μm) (355nm Q-switched ultraviolet laser source, Laser Innovative Solutions L4IS). A small center hole was required for assembly of the device. Figure 7-6(a) shows a photo of the laser-cut star shaped beams from the PZT/Ni/PZT bimorphs.

After cutting, Pt top electrodes were patterned by lithography, as shown in Figure 7-6 (b). In order to spin-coat the 3012 photoresist, the star shaped device was attached to a glass carrier plate as shown in Figure 7-6 (b). The photoresist was exposed to a UV light intensity of 8 mW/cm^2 for 10 sec using a Karl Suss MA/BA6 contact aligner. After developing the photoresist with CD-26 for 2 min, as shown in Figure 7-6 (c), the surface of the PZT film was cleaned using with an oxygen plasma ash (M4L Plasma System, Metroline) for 4 mins at a power of 400 W, a chamber pressure of 1000 mTorr, and a 500 and 50 sccm gas mixture of O_2 and He, respectively.

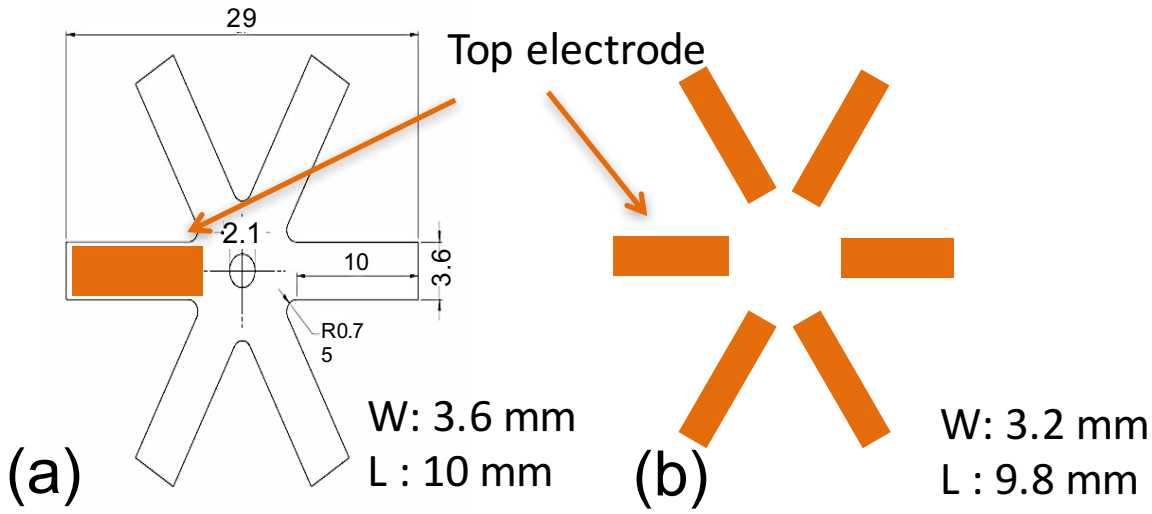

Figure 7-5. (a) Piezoelectric beam configuration (width 3.6 mm and length of 10 mm). (b) Top electrode configuration (6 rectangular electrodes with a width of 3.2 mm and a length of 9.8 mm, arranged at 60° angles with respect to each other) patterned by lithography.

The first side was then coated with a 100 nm thick Pt top electrode using dc-magnetron sputtering (CMS-18 Sputter System, Kurt J. Lesker) as shown in Figure 7-6 (d). The same

process was followed for the second side of the device, using a backside alignment process. To avoid electrical short circuits, the dimension of the top electrode pattern was intentionally smaller than the device dimension for each cantilever beam. It was found that the thermally damaged area was <70 μm from edge; this is smaller than the damaged area produced by mechanical cutting using scissors in Figure 7-7.

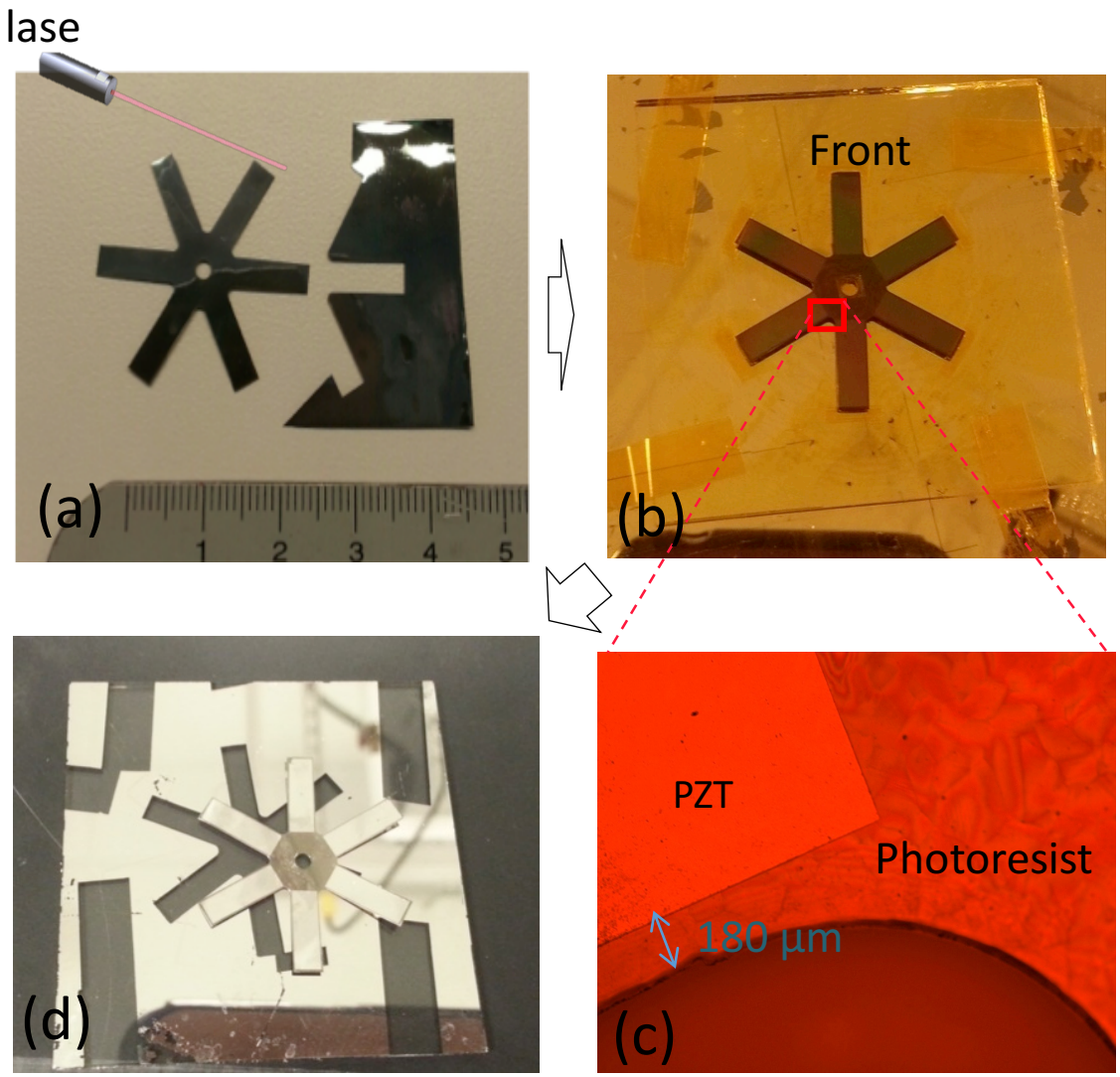

Figure 7-6. Photos showing (a) laser cutting, (b), (c) lift off and (d) Pt top electrode coating for star-shaped PZT beams.

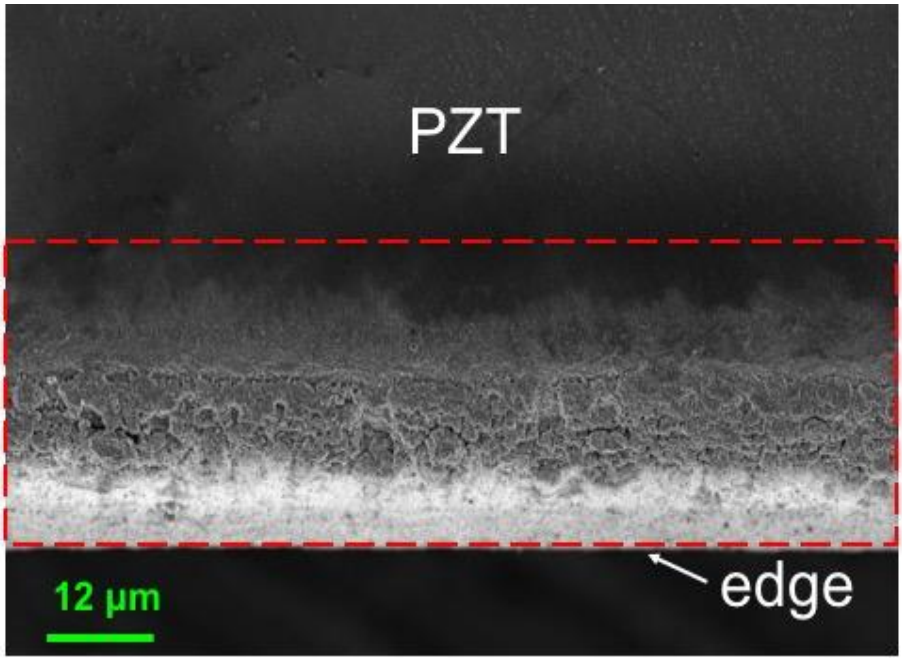

Figure 7-7. FESEM surface image of PZT film with thermal and mechanical damage caused by laser cutting near edge.

One of the challenges with the complex beam design is that it is hard to make the connections from the top electrode to the circuit board. In this work, a copper printed flex circuit (prepared by A. R. Tellado from the group of T. N. Jackson) was used to connect the zero-insertion force (ZIF) connector on the printed circuit board (PCB) to the six piezoelectric beams. Figure 7-8(a) shows the six copper wires and pads printed on a flexible circuit cut by a laser engraver (Universal CO_2 laser) and attached to the Pt top electrodes by silver epoxy (Epo-tek H31) to give electrical contact and enough mechanical support following curing at 125 °C for 30min.

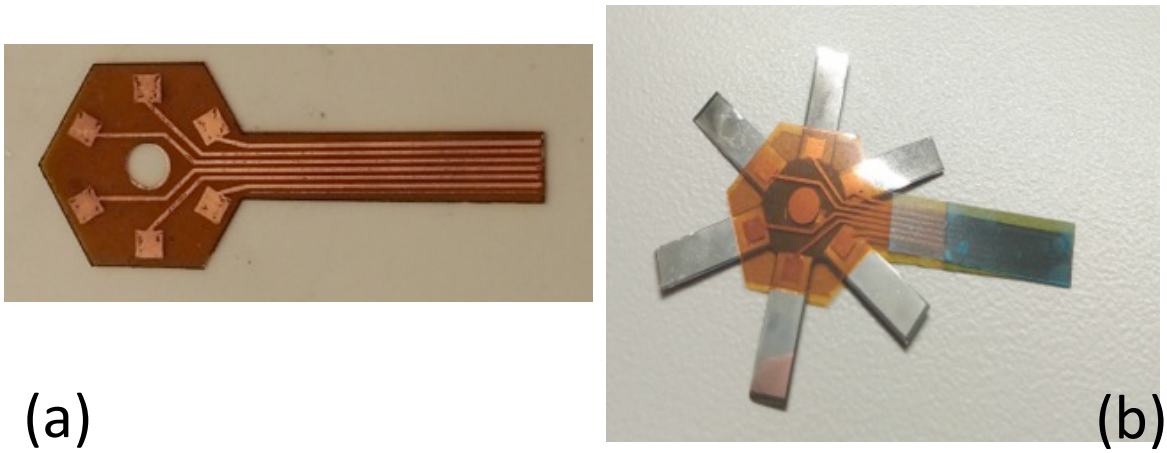

Figure 7-8. (a) A copper flexible circuit (flexible wiring traces), (b) flex circuit bonded to one side of star shaped PZT beams.

After the two flex circuit cables were attached, one to each side of the PZT beams, a contact to the bottom electrode (Ni substrate) was required to pole the two PZT layers in opposite directions for operation in series.[14]

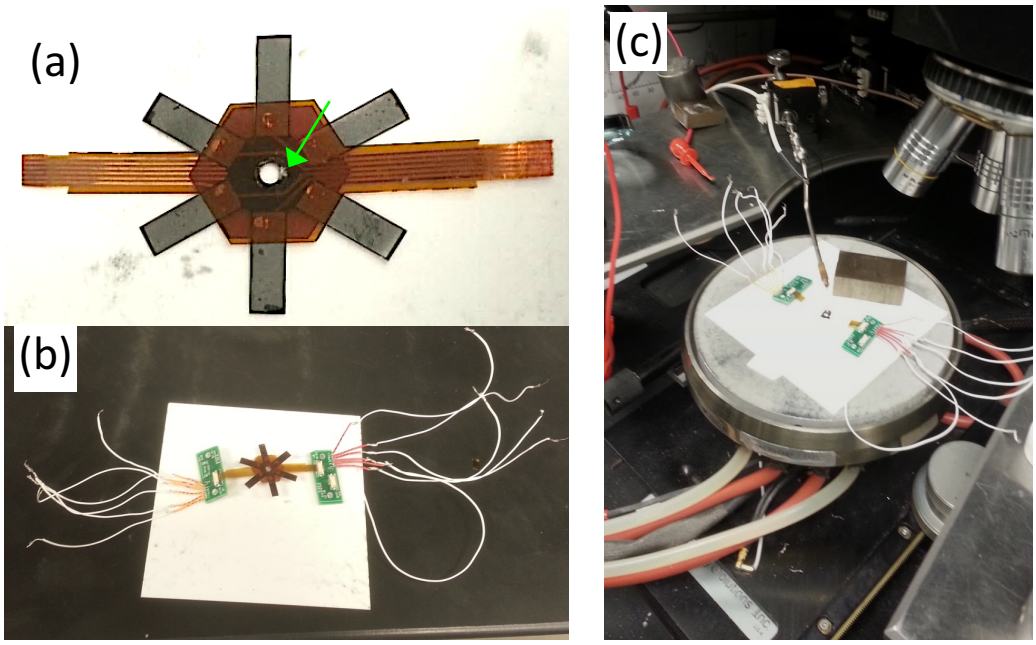

Figure 7-9. (a) Photo images of two flexible cables bonded to star-shaped PZT beams (the green arrow indicates the spot where the bottom electrode was accessed). (b) Photo of ZIF connection with the flexible cables and (c) set-up for poling.

As shown in Figure 7-9 (a), near the center hole, in an area that was not covered by the flex circuit cable, the Ni substrate was exposed by scratching the PZT film using a razor blade; this allowed the bottom electrode to be probed during hot poling (green arrow). Figure 7-9 (b) shows the flex cable connected to the ZIF connector in order to pole all six beams simultaneously at high temperature.

For 31 mode operation with a series connection, six bimorph PZT beams were poled to align the polarization direction of the two layers in opposite directions under high electric field ($2\times E_c \approx 29$ V) at 150 °C for 10 min. (i.e. during poling the middle electrode (Ni substrate) was grounded and a voltage was applied to the top and bottom electrodes) The yield was around 50% of the electrodes for the 1st prototype. It is believed that some of the shorts arose when the Pt electrode partially undercoated to the backside of the beam, creating an electrical pathway to the Ni substrate.

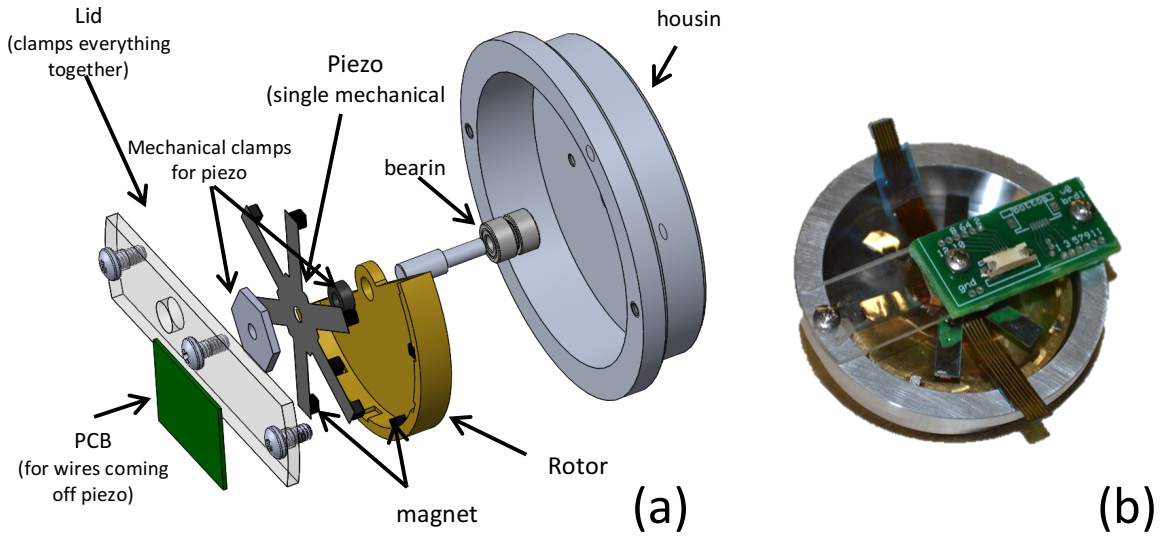

Figure 7-10. (a) Schematic exploded view with all parts and (b) optical images of assembled Gen-I prototype. [figure provided by Tiancheng Xue]

After the permanent magnets were glued at the end of each beam, the device was assembled with a brass rotor 16 mm in radius, two ZIP connectors printed on PCB and the 45 mm diameter casing as shown in Figure 7-10.

7.2.2 Fabrication of Gen-II and -III

In terms of the piezoelectric material, it is worthwhile to prepare thicker (>3 μm) PZT films for fabrication of Gen-II and -III devices in order to enhance the power density. As described in chapter 4, the output performance of the energy harvester increases with the volume of piezoelectric material, given the same quality of material, and similar strain levels. For the two later generation devices, 5.5 μm thick (001) textured bimorph PZT films on Ni foil were obtained using high temperature sputtering as described in section 6.

The design of Gen-II gives tensile stretching strain, which is the dominant mode at large deflections, with a small portion of bending strain especially near the central area as described earlier. Based on this, the electrode configuration for clamped-clamped piezoelectric beam was sized presuming that the stretching terms would dominate. Figure 7-11 illustrates two separated electrodes covering the clamped-clamped beam except in a region near the proof mass. This avoids complications from spatially varying strains associated with the bending mode.

Figure 7-11 shows the procedure to prepare the Gen-II non-resonant energy harvester. The main difference compared to Gen-I was that clamped – clamped PZT beams were used. For the first prototype of Gen-II, 4 rectangular PZT beams (37 mm×7.5 mm×35 μm) were prepared with 5 cm by 5 cm continuous sputtered PZT films on Ni foil (25 μm). The intent of the design was to maximize the utilization of the piezoelectric area relative to the total area of the device (40 mm×40 mm×10mm). The fabrication steps for the Gen-II device are similar to those of the

Gen-I, excepting for the machining of the PZT beam. Simple rectangular structures can be cut by scissors after coating Pt top electrodes on both PZT layers shown in Figure 7-12(b). Accidently, the PZT layer and top electrodes of one released beam was damaged by the scissors.

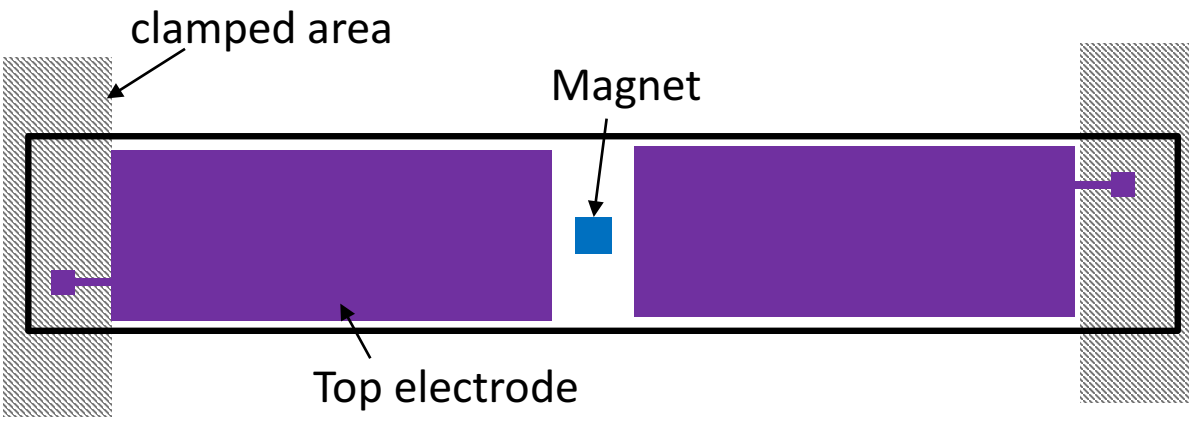

Figure 7-11. Schematic electrode configuration of clamped-clamped beam (purple). The blue area is where the magnet is placed.

Figure 7-12(d) shows a picture of one of the PZT beams with two separate top electrodes and the bottom electrode (Ni substrate) connected to wires using silver paste (Leitsiber 200 Silver paint, TED PELLA) and Kapton tape. Both PZT layers should be poled in the same direction and connected in series, given that the models suggest that the clamped-clamped straight rectangular beam is more likely to be stretched rather than bent during large amplitude oscillation.[9] Large area electrodes face the risk of the breakdown during poling. Despite applying the resurrection technique to improve yield, 6 of 12 electrodes (46 mm^2 of size) within 3 clamped-clamped beams were electrically shorted during high temperature (150 °C) poling.[15]

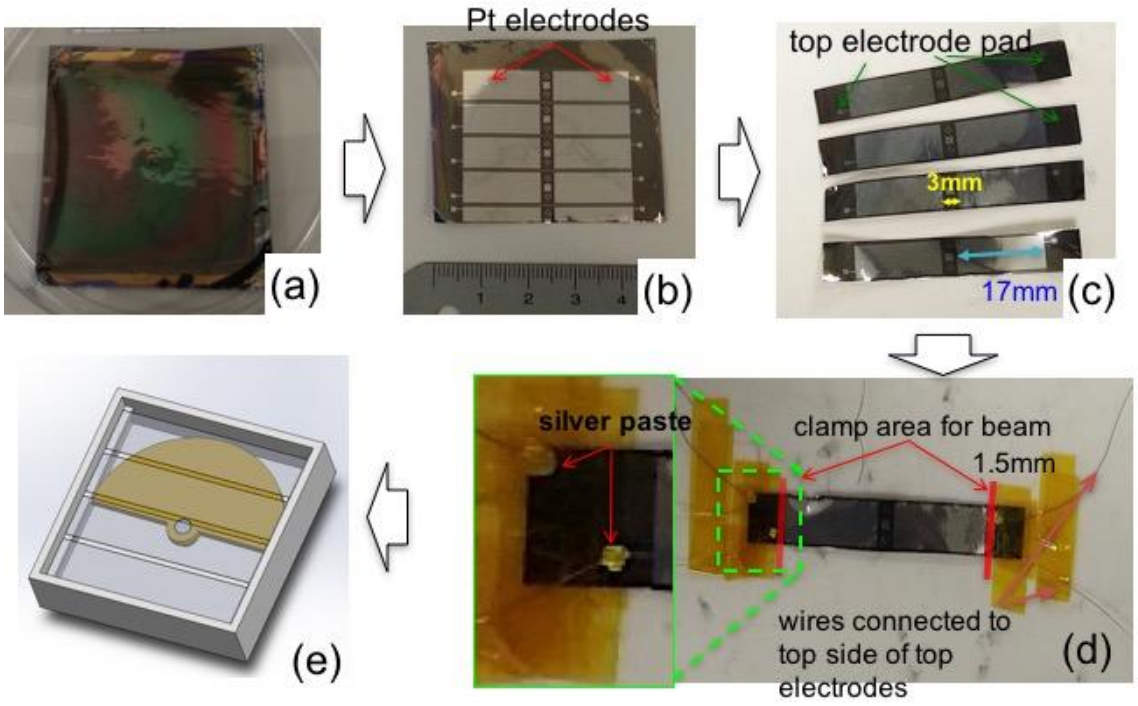

Figure 7-12. Photos of (a) continuous bimorph PZT films on Ni foil (25 μm), (b) Pt top electrodes patterned by lift-off and (c) Four clamped-clamped PZT beams released by scissors. (d) Electrodes are bonded with wires by silver paste and Kapton tapes. (e) Gen II model of clamped clamped piezoelectric harvesters designed by Tiancheng Xue of the University of Utah.

The clamped-clamped beams with one proof mass at the center of beam were placed on the sides of the device (i.e. the prototype did not contain the two beams with two magnets located near the center), as illustrated in Figure 7-2. Figure 7-13 exhibits an assembled Gen-II prototype device being worn on a wrist. This prototype was used to compare experimental data with the analytical model.

Unlike the top electrode pads in the Gen-I design, where electrical contact to the electrodes was made near the star center in a limited space (~5.6 mm^2) in Gen-I device, for the Gen-II design, the top electrode pads were placed out of the frame, which facilitates hand-wiring.

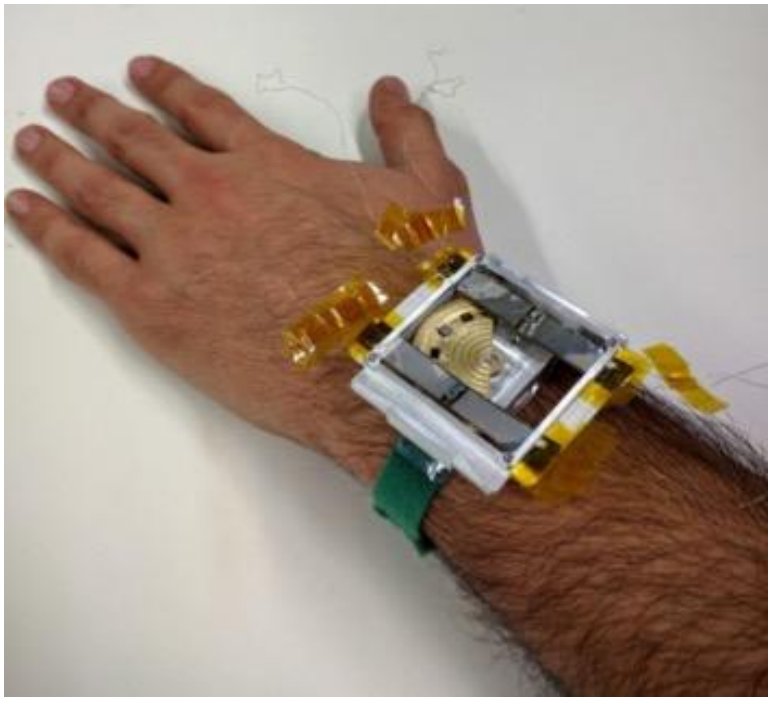

Figure 7-13. Photograph of first prototype of a Gen-II device with two bimorph PZT beams. [figure from Tiancheng Xue]

The Gen-III device utilized a flower petal design with six fixed-free trapezoidal PZT beams (Figure 7-14). These devices used continuous (001) textured bimorph PZT films on Ni foil (50 μm) prepared by high temperature sputtering under the conditions described in Chapter 6. The fabrication procedure of Gen-III is essentially identical to that for Gen-II.

As shown in Figure 7-14, the mask layout consists of 6 individual 1.54 cm^2 (active area) trapezoidal beams prepared from a 5 cm by 5cm continuous PZT(5.5 μm)/Ni(50 μm)/PZT(5.5 μm) bimorph. The top electrode (red area) was designed to be a littler smaller than the actual beam area to avoid extended damage near the edge induced by cutting (with a 150 μm gap). The electrode pads were designed to make the connection over the clamped area where the beams were extended beyond that actual working area for each beam. This gives easy access for wiring with silver paste and Kapton tape. While wire-bonding in principle provides precise probing, it is

difficult to applied to a flexible Ni foil, so a manual approach was applied instead.

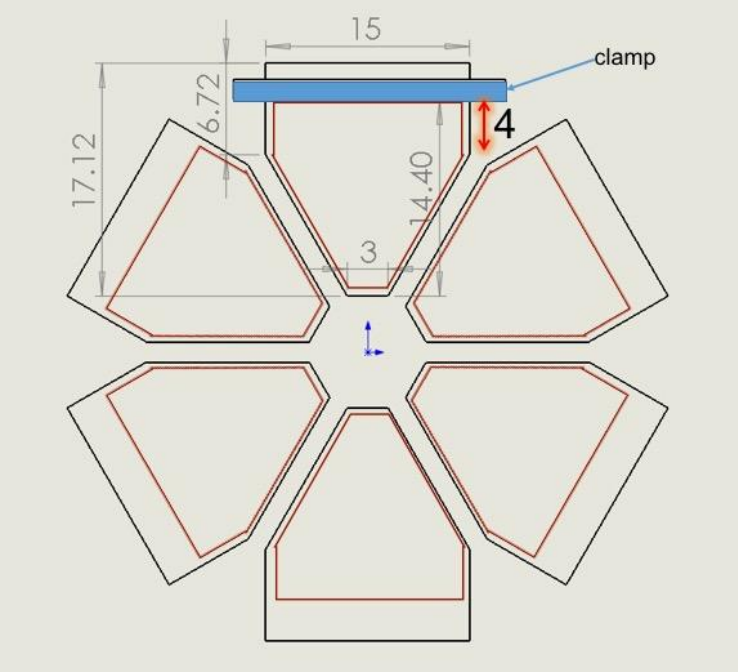

Figure 7-14. Flower petal design configuration. (red line: active area covered by Pt top electrodes, black line: beam dimension, unit [mm])

Following lift-off processing for the top electrode, both 100 nm thick Pt top electrodes were deposited using dc-magnetron sputtering at room temperature. The electrical properties of both PZT layers were measured with a 400 μm diameter circle electrode placed on an area of the sample where it is not covered by the top trapezoidal electrode as shown in Figure 7-15(b). After cutting to shape with scissors, two wires for top electrodes and one wire for bottom electrode were connected using silver paste and Kapton tape as was done for the Gen-II device (see Figure 7-15(c)). The bottom electrode is only essential to pole the PZT layers in opposite directions for series connection during operation. The sample had high yield (~ 80%) for the >1 cm^2 electrodes after using the resurrection treatment as described in Chapter 5.[9,13,]

Figure 7-15(d) shows trapezoidal beams with permanent magnets attached at the end

mounted on the hexagonal frame to clamp the beams. The photo was taken after hot poling each of the beams. Based on the magnet configuration calculated by Tiancheng Xue of the Roundy group, neodymium magnets (2 mm^3) were attached to the weighted eccentric rotor by super glue. In order to attach 6 beams on the hexagonal frame, each beam had to be bent up by hand to reduce undesirable strong magnet coupling between the beams. Then, the hexagonal frame with the petal-shaped beams was placed on the casing and fixed via six screws at the corners. Two wires connecting the top electrodes of each beam were soldered on to customized PCB boards attached on the side of case. Figure 7-15 (e) shows an assembled device on a wrist-worn location.

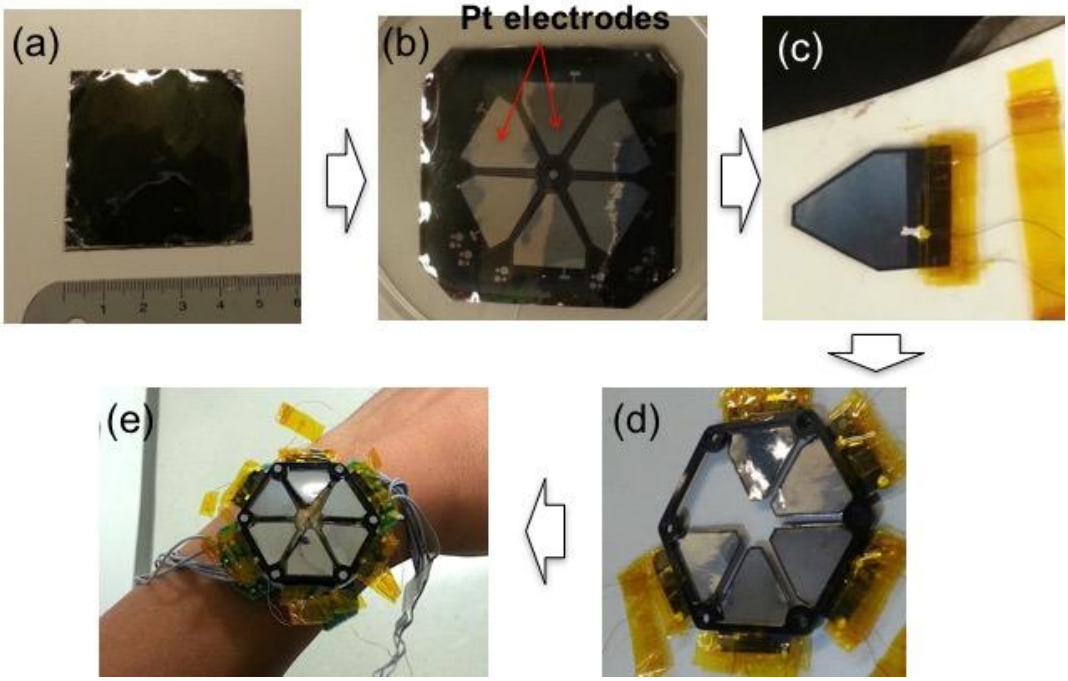

Figure 7-15. Photos describing the fabrication flow for Gen III using bimorph PZT films on Ni foil. (a) Continuous bimorph PZT films sputtered on Ni foil. (b) Pt top coated on PZT layers. (c) Released trapezoid shaped beam after hand-wiring (d) Five PZT beams clamped on the plastic frame by super-glue. (e) Images of complete device being worn on a wrist.

7.3 Results and discussion

7.3.1 Characterization of Bimorph PZT Films for Gen-I

Using a piece of the bimorph PZT film on Ni foil, the microstructure, crystallinity, and orientation were investigated using FESEM and XRD. Images of the surface and cross section view of both PZT layers show no micro-cracking. The grains are columnar across the 3 μm thickness, without a Pb-deficient pyrochlore phase on the surface.

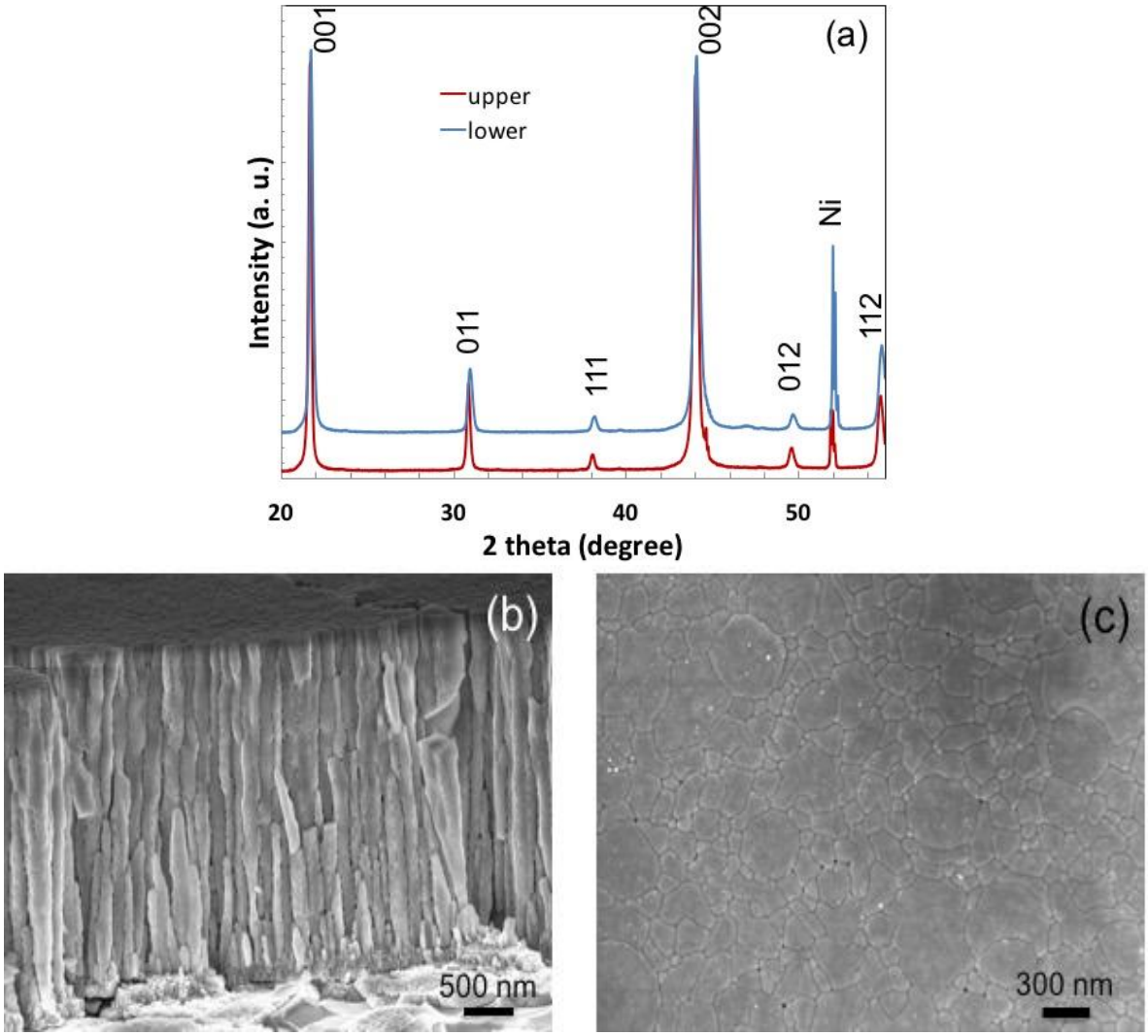

Figure 7-16. (a) XRD θ-2θ scans of sputtered upper and lower PZT layer. (b) Cross-sectional and (c) surface FESEM micrographs of the sputtered PZT films on Ni foil.

Highly {001} textured perovskite phase without any second phase is seen in the XRD pattern, which is consistent with the work shown in Chapter 4.

The electrical properties of both films were investigated to assess the dielectric properties and P-E hysteresis. The remanent polarization and coercive field of both PZT layers are around 37 μC/cm^2 and 41kV/cm at 10 Hz, respectively, with a square shaped loop. Low dielectric constants (ε_r of upper and lower layers = 328 and 346, respectively) and loss (tanδ = 0.01) at 1 kHz were revealed in Figure 7-17(a).

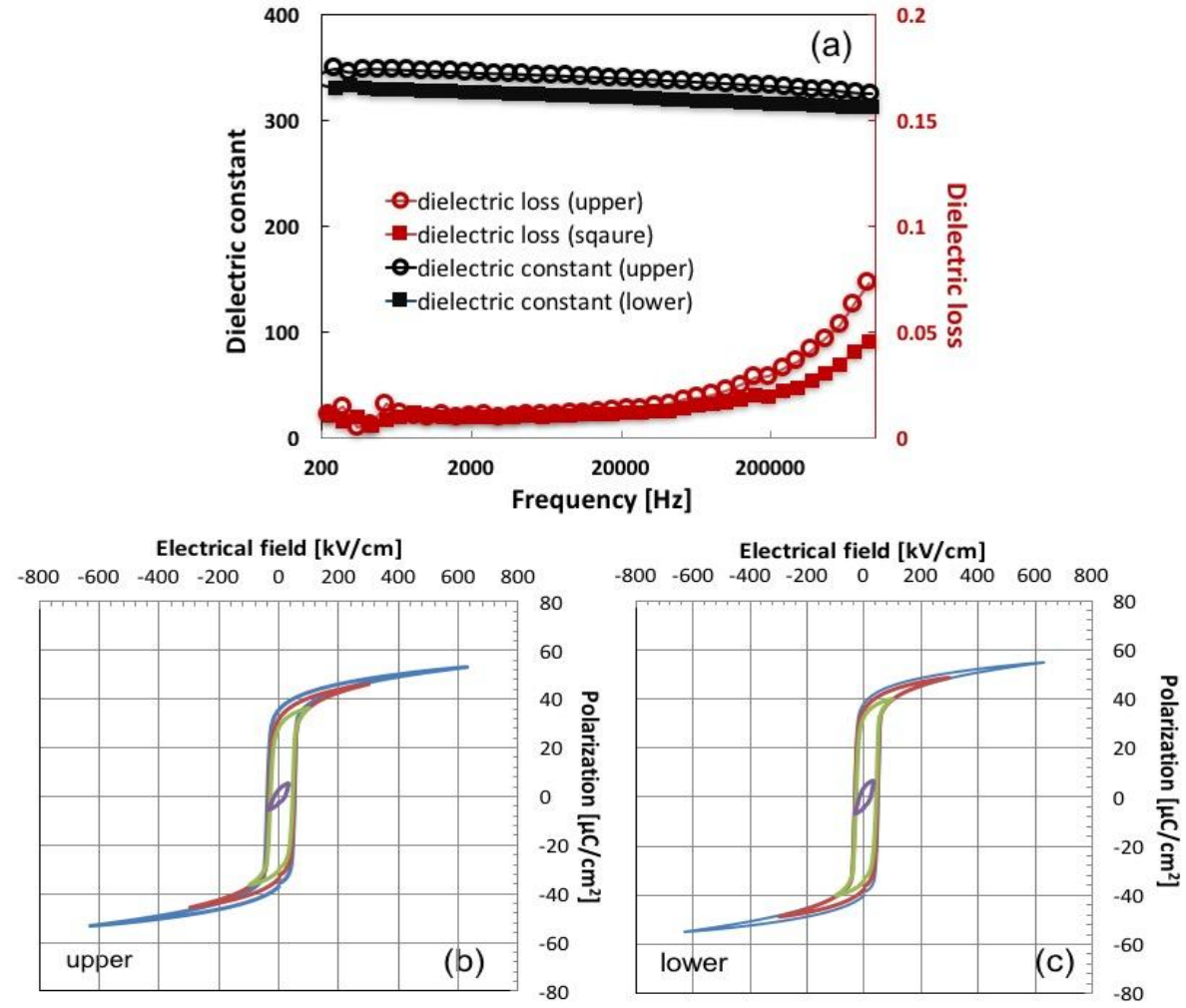

Figure 7-17. Electrical property measurements of both sputtered PZT layer on Ni foil. (a) Dielectric constant and loss tangent of upper and lower PZT layers measured using a 30 mV oscillation voltage. Polarization-electric field hysteresis of (b) upper and (c) lower of PZT layer.

The piezoelectric response was investigated using the wafer flexure technique.[16,17] Following hot poling under high electric field ($3 \times E_c \approx 40$ V) at 150 °C for 15 min, the transverse piezoelectric constants ($e_{31,f}$) of the upper and low PZT layers were -12.1±1.3 and -13.1±1.0 C/m^2 respectively. Thus, the FoM for sputtered bimorph PZT films was around 0.47 C^2/m^4.

7.3.2 Performance of Gen-I

To analyze the rotational energy harvesters based on an eccentric rotor, Xue and Roundy set up a tester to provide a sine wave arm swing motion as a pseudo walking input; this is illustrated in Figure 7-18.[7] The Gen-I energy harvester including two threaded holes on the case was screwed on the swing arm. The arm angle and speed was controlled using a microcontroller and hobby RC motor providing a motion profile called "vigorous pseudo walking". The excitation is a sine wave (0 to peak amplitude: 60 degree, period: 1 second). It was found that one unimorph beam can generate peak to peak output voltages from 1 to 5 volts with 47 kΩ external load resistance, as shown in Figure 7-18 (b).

The Gen-I device had 2 to 5 functioning unimorph beams due to shorts produced during the device fabrication as mentioned earlier. Especially, mechanical shock (such as those due to the pull-in effect in which opposing magnets stick together) during assembly and the weak strength of hand-wiring using silver epoxy could cause either short circuit or loss of functionality of the PZT beams. Thus, it is necessary to improve the assembly in future work.

The working beams generated 0.5 ~ 3.5 μW of output power via swing motion on the bench (pseudo walking). Assuming the ideal case, in which the measured value of 3.5 μW per unimorph could be achieved in all beam segments, it is predicted that a total power of 42 μW

could be generated by 6 bimorph beams; this is in reasonable agreement with a prediction of 50 μW simulation conducted in MATLAB estimated by the Roundy group.[18]

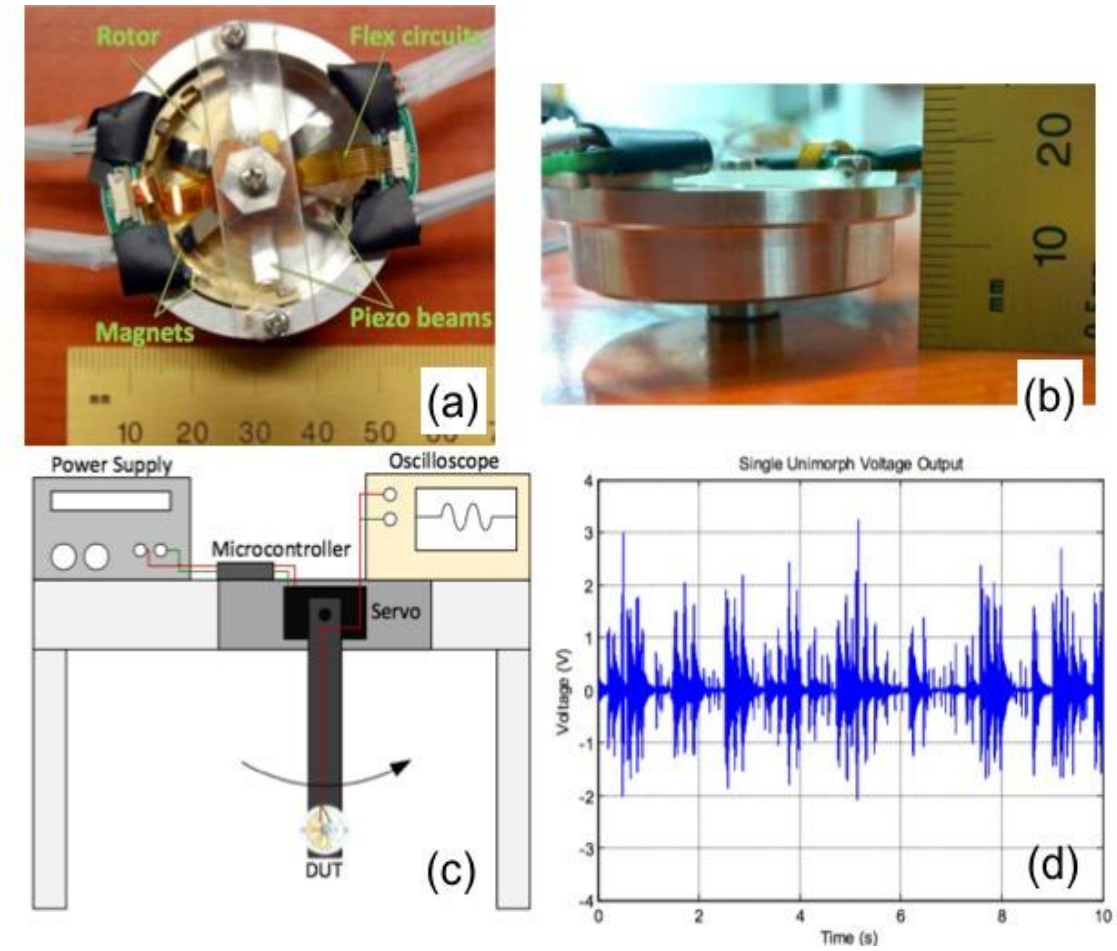

Figure 7-18. Photo of (a) top view and (b) side view of the Gen-I harvester (c) Test set-up for pseudo walking on bench. (d) Voltage output from one unimorph beam during pseudo-walking. (figure from Tiancheng Xue)

The simulation is based on a model for the entire system including the magnet interaction, nonlinear rotor dynamics and the distributed parameter piezoelectric beam model. While the Gen-I prototype device showed the potential to supply power from walking and running for low power wearable systems, improvements are needed for the processing to achieve

fully functioning Gen-I devices. In terms of the piezoelectric material, suboptimal poling is suspected to have degraded the performance of the device. While high field poling at high temperatures facilitates domain alignment, it also increases the possibility of electrical breakdown. With the bimorph PZT samples for the Gen-I device, star shaped bimorph PZT beams could not be sustain high electric field (i.e., ~ $3\times E_C$), which was the electric field used for poling small electrodes (3.14×10^{-8} m^2). In this experiment, some of beams were short circuited during poling at ~ 120 °C.[15] Thus, the piezoelectric response of PZT beams with large electrodes did not function as well as that of small electrodes on the same film. Supplementary studies of modified poling procedure for large electrodes are needed.

In the Gen-I design, multiple variables strongly influence the performance of the harvester, including the gap between rotor and beams, magnetic spacing, and orientation. In particular, the gap and the offset between two magnets is critical to control the magnetic force to deflect the PZT beams. However, in the experiment, it is challenging to place and glue precisely the permanent magnet location to match the modeled 2 mm gap and 0.8 mm offset.[18]

The Gen-I harvester can be improved by increasing the PZT film thickness, which would not significantly change the design of the wrist worn energy harvester. Improving design of device could yield better power levels. Changing the beam shape could improve space utilization. It would also be interesting to utilize a PCM configuration to apply a uniform strain along the beam.[13]

7.3.3 Characterization of Bimorph PZT films for Gen-II.

Bimorph PZT films were prepared via high temperature sputtering in the same way as described in Table 6-2 in Chapter 6. Before fabrication of the Gen-II energy harvester, the films were characterized using XRD and FESEM to determine the orientation, phase purity and assess the existence of microcracks. Strong (001) orientation with pure perovskite phase after post annealing was determined by XRD (not shown here).

The surface images of 5.5 μm thick PZT layers for Gen-II show micro-cracking (red arrows in Figure 6-31 (a) and (b)). It is believed that the cracking in the film developed on post annealing in an RTA at 650 °C. As described in Chapter 6, each sputtered PZT layer was post annealed in an attempt to eliminate the possibility of any pyrochlore phase. It was found that most of the volume of as-sputtered PZT films grown under the same conditions described in Table 6-2 were well crystallized (provided the substrate set temperature was below 585 °C). Thus, post deposition annealing at 650 °C did not induce much pyrochlore-to-perovskite transformation. Thus, it is believe that during heating to the post annealing temperature (650 °C, which exceeded the substrate setting temperature during sputtering), the as sputtered PZT film experienced large thermal tension in-plane resulting from the thermal expansion mismatch between the PZT films and nickel substrate.[19] This thermal stress may be the origin of cracks in the film. Even though the tensile stress switches to compressive stress during cooling, the crack cannot be eliminated. As a result, cracking is clearly observed on the surface of PZT capping layer after post annealing for crystallization in Figure 7-19(b).

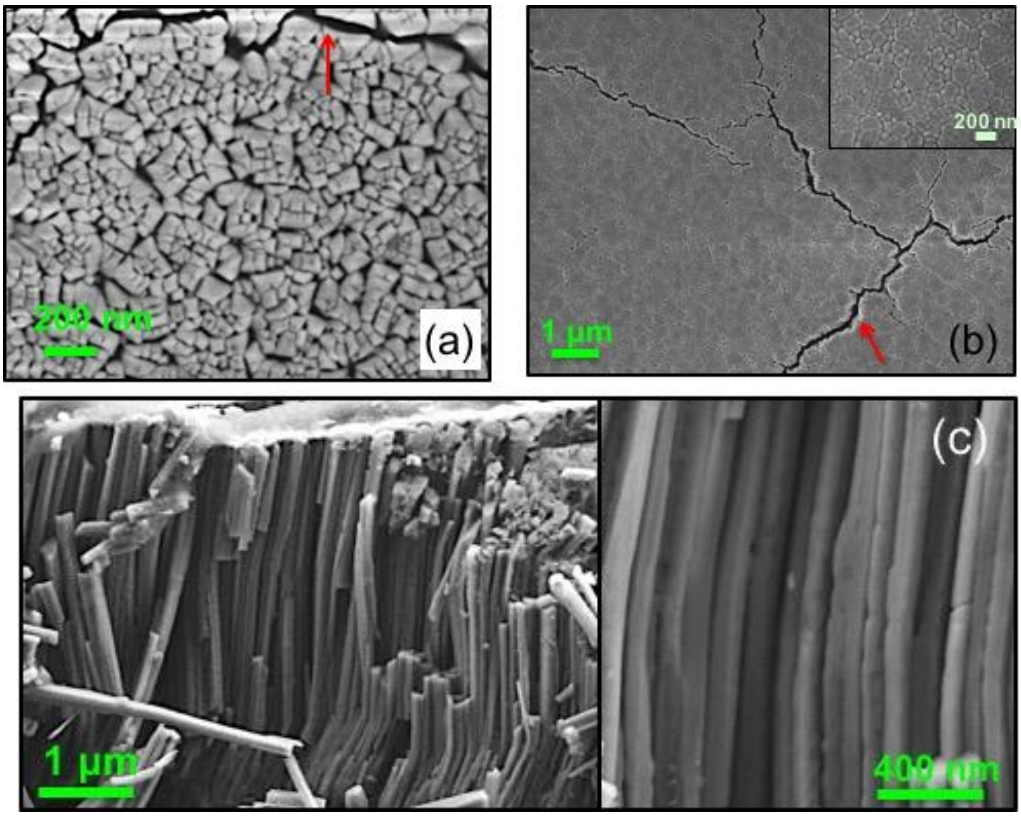

Figure 7-19. (a) Surface FESEM images of 5.4 µm layers of PZT sputtered with in-situ crystallization (530 ~ 555°C) under condtions described in Table 6-2. (b) Top down and (c) cross sectional microstructure images of films after CSD PZT capping layer.

The electrical properties of the sputtered PZT/Ni/PZT bimorphs are shown in Figure 28. A dielectric constant of 580 ($\tan\delta$ = 0.03) and remanent polarization of 37 μC/cm^2 (E_C = 45 kV/cm) was measured at 1 kHz with a 30 mV ac signal and 100 Hz respectively. These low permittivity and high relative polarization are a consequence of a significant *c*-domain population as described in Chapter 3.[16]

However, near the operation frequency, the high loss tangents <200 Hz are likely to degrade charge generation by mechanical excitation.

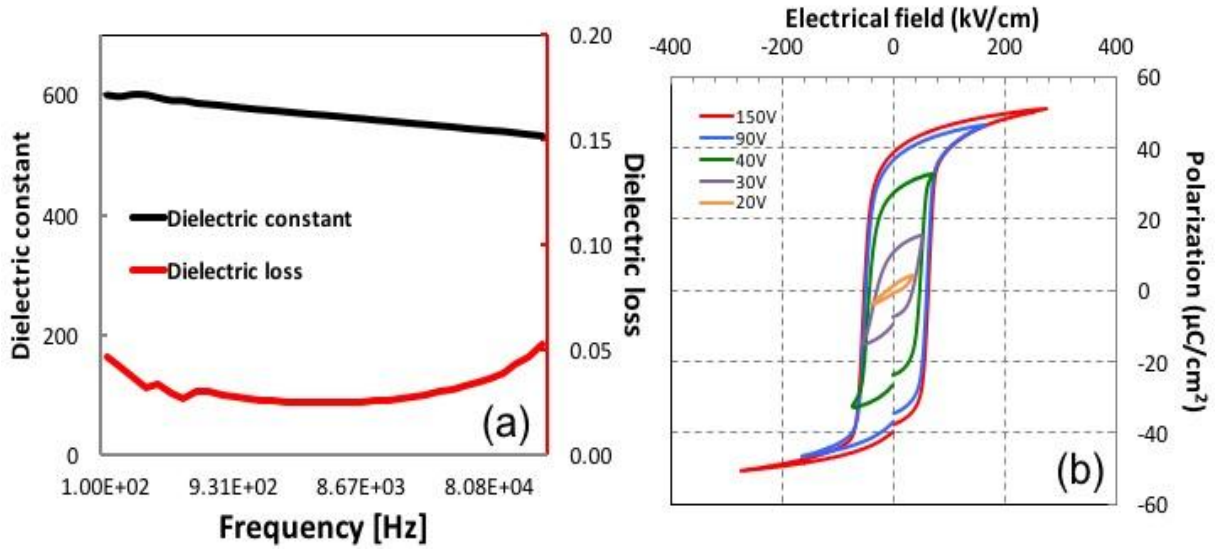

Figure 7-20. Electrical properties of PZT layers on Ni foil grown by high temperature sputtering and used in the Gen-II devices. (a) Dielectric constant and loss tangent of PZT layer. (b) Polarization-electric field hysteresis of PZT layers.

7.3.4 Performance of Gen-II and Gen-III Harvesters

The Gen II and III devices were tested to characterize the energy harvester performance. While the Gen II model was designed with 6 fixed-fixed beams: 4 on the front side and 2 on the back side, initially, the prototype Gen-II device was fabricated with 2 fixed-fixed beams only on the front side, and with magnets at the center of beam. Based on an FEA study of the fixed-fixed beam subject to a load at the center (modeling conducted by T. Xue), a 2 mm cube magnet with a 1 mm gap can produce a 0.08 N load and 0.52 mm maximum displacement with 0.18% strain along the beam direction for a 3 μm thick bimorph PZT film on 50 μm thick Ni foil.

It is noted that the fixed-fixed beam configuration experiences lower strains than a fixed-free beam under the same external force. To achieve the same strains, stronger magnet coupling could be achieved with in-plane magnetic plucking and/or by adding magnets. However, if the magnetic coupling is too strong, and the gap between magnets is limited, sticking is likely to

occur.

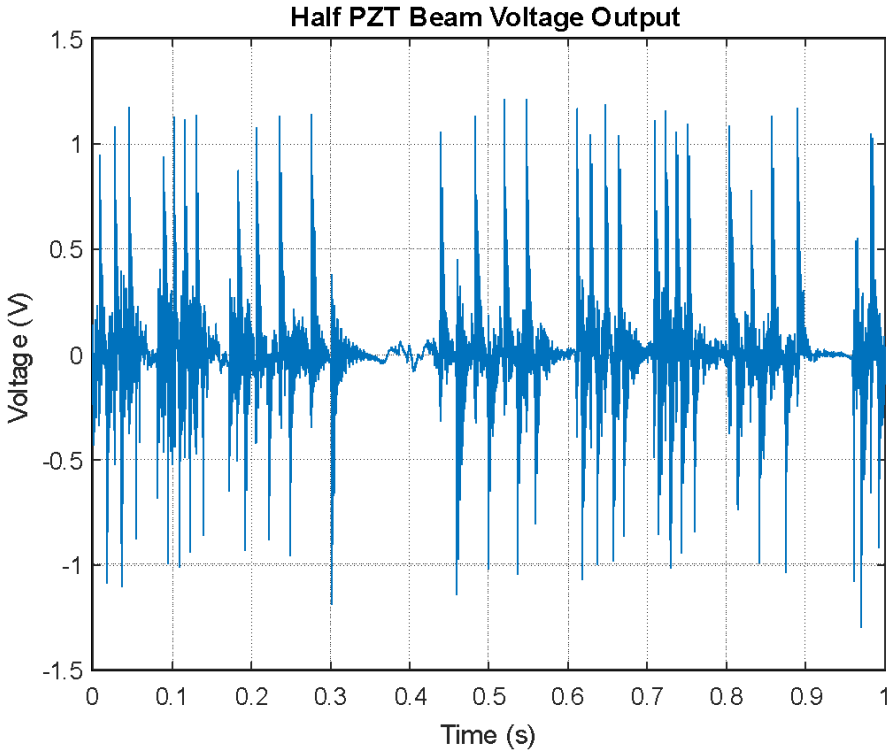

Figure 7-21. V_{OC} signal measured by hand shaking for one of clamped-clamped PZT beam. (from Tiancheng Xue)

Figure 7-21 shows that one pair of electrodes in a beam generated 1 V peak to peak in open circuit conditions by shaking the device in hand to make the rotor swing at high speed continuously. Due to the detent torque problem, it was found that the rotor cannot swing freely at lower speed under the swing arm excitation in the same manner as the Gen-I device). The load resistance is 47k. Note that the only one unimorph was measured, and the power output is 0.5 μW.

There are two key areas that were identified for improvement based on the Gen-II design. First, modification of the high temperature sputtering condition is needed to grow thick crack-free PZT films. Secondly, the design needs to be altered to insure an appropriate distance

between magnets to avoid pull-in.

Before characterizing the rotational energy harvester for a Gen-III device with six trapezoidal beams, each trapezoidal cantilever PZT beam was characterized using a shaker table excited at the beam resonance frequency to validate its functionality. Using a customized plastic clamp, each trapezoidal piezoelectric beam (shown in the green box) was placed on the shaker vertically as seen in Figure 7-22(a). Without proof mass (the neodymium magnet), the resonance frequency of the trapezoid beam is 250 Hz. In Figure 7-22(b), it was observed that the open circuit voltage (blue line) is up to 6.6 $V_{peak\ to\ peak}$ through both PZT layers for a series connection at 0.15 G [G=9.8 ms^{-2}] excitation (yellow line).

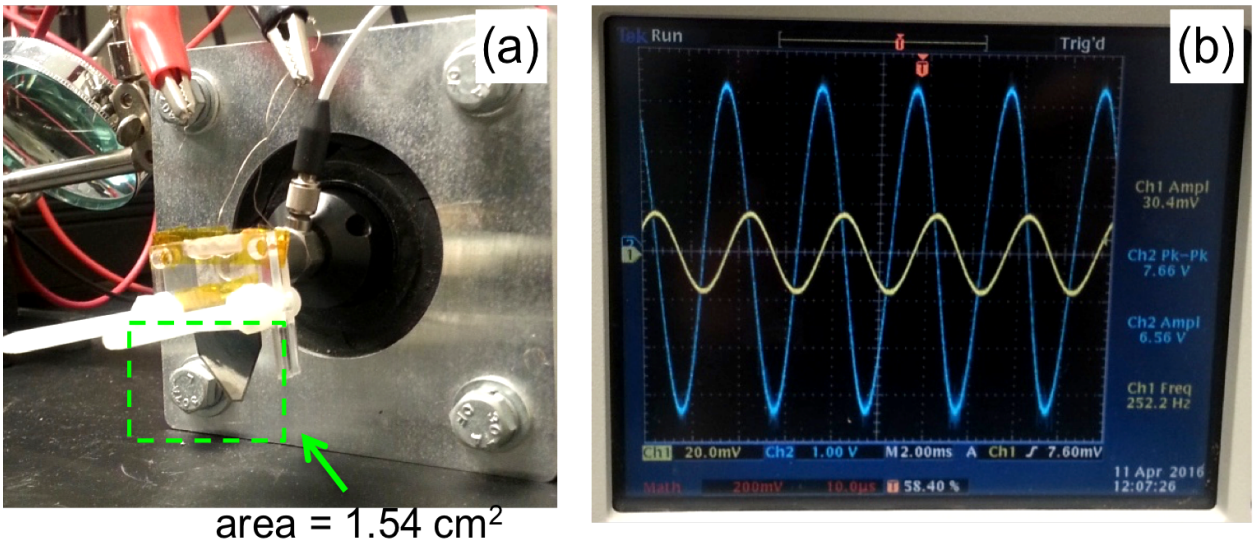

Figure 7-22. (an) Experimental set-up to measure response against vibration at the resonance frequency with one trapezoidal bimorph PZT beam (green box) for Gen III (b) V_{OC} (Ch2; blue) and acceleration waveform (Ch1; yellow) read out by an oscilloscope. (TDS3054C, Tektronix)

To measure the maximum output, the external load resistance was varied (as in Chapter 4) at the resonance frequency (250 Hz) and an excitation level of 0.15 G. Figure 7-22 exhibits

the maximum output power as a function of the external load resistance (for a parallel connection of the load). A maximum generated power ($P_{max}=V_{max}^2/R$) of 201 μW with maximum voltage ($V_{max} = V_{pk-pk}/2$) of 1.85V was obtained at a load resistance of 17 kΩ for series connection.

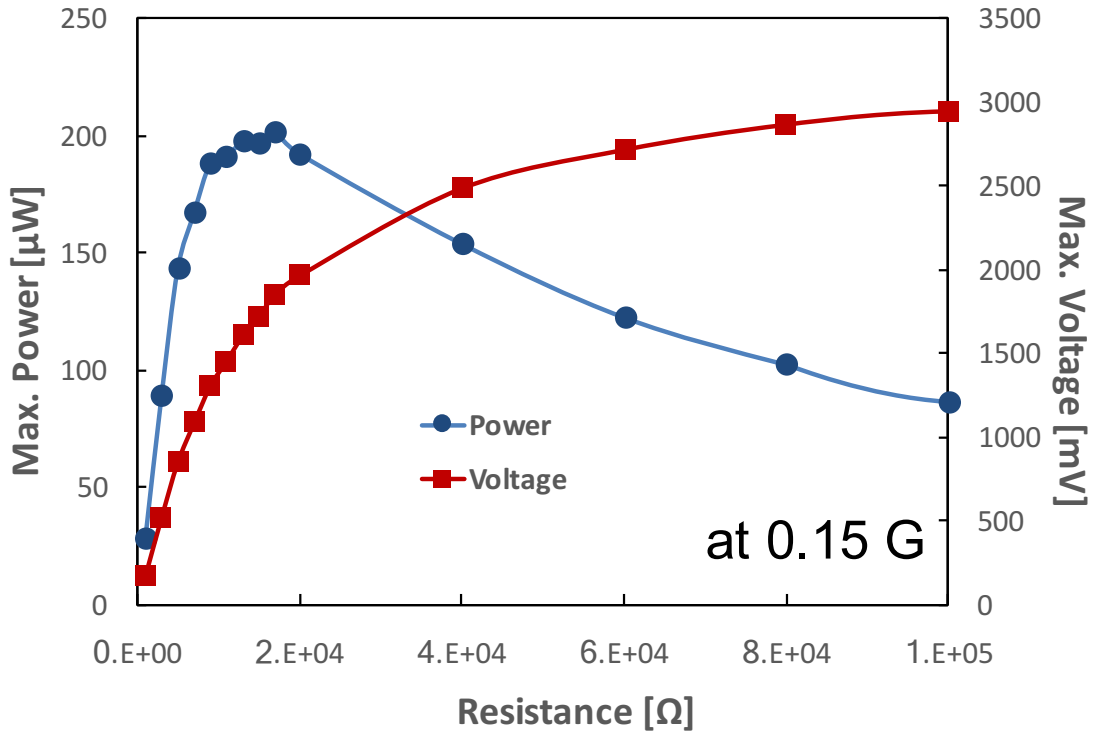

Figure 7-23. Relationship between maximum power and the external load resistance for the bimorph trapezoidal PZT beam.

Table 7-1 shows a comparison of the trapezoidal bimorph and a cantilever unimorph PZT beam fabricated by Yeo at PSU, with their active area, resonant frequency, generated power and area power density. The power density of the trapezoidal bimorph PZT (5.5 μm thick) beam is three time higher than that of 3 μm thick PZT layer sputtered on the rectangular cantilever. The enhancement of power density might be caused mainly by a combination of the increase of PZT volume and improvement in the strain distribution using the trapezoidal beam shape.[12]

Following the experimental validation of the performance of a trapezoidal beam at

resonance, a Gen-III harvester was fabricated based on the design suggested Tiancheng et al., including the magnet configuration.

Table 7-1. Comparison of performance of wo piezoelectric energy harvesters: rectangular cantilever unimorph beam with 3 μm of PZT and bimorph trapezoidal beam with 5.5 μm thick bimorph PZT.

Reference	Active Material, mode	Device area [cm^2]	Acceleration [G]	Frequency [Hz]	$Power_{rms}$ [µW]	Power Density ([$\mu W/cm^2*G^2$]
PSU cant.	3 µm PZT film by sputtering on Ni d_{31}	**0.385**	**0.15**	**72**	**9**	**1036**
PSU Trapezoid	5.5 μm bimorph PZT, d_{31}	**1.54**	**0.15**	**250**	**100**	**2886**

Figure 7-24(a) depicts the magnet configuration for the Gen III harvester. There is a 1 mm gap and 1.3 mm offset between magnets. This should enable 1mm of tip displacement and an average strain on surface 2.82×10^{-4}. 2 mm^3 neodymium magnets were attached on the end of 5.5 μm thick bimorph PZT film on Ni (green arrow) and rotor (red arrow) based on the simulation results for the Gen-III harvester.

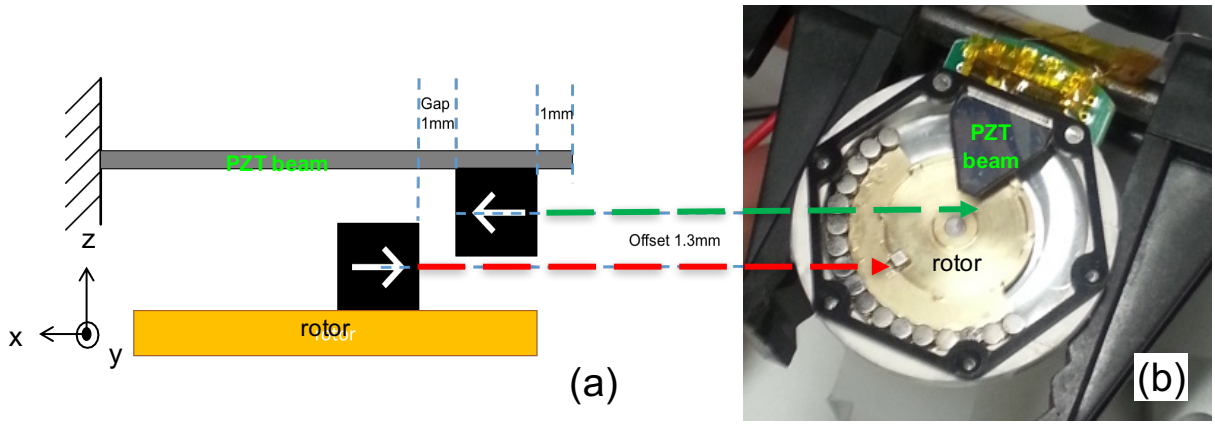

Figure 7-24. (a) Configuration of magnets and (b) photograph of one trapezoidal beam assembled with one pair of magnets placed at the end of beam and on rotor.

Before assembling all of the trapezoidal beams, a single beam with an attached

permanent magnet, as seen in Figure 7-24(b), was tested to understand the static behavior and to compare the results to simulation. This allowed the mechanics to be understood without complications introduced by magnetic coupling between adjacent beams. Based on the results of ringing down one excited beam, the resonance frequency was around 130 Hz without magnetic stiffening force, which is very close to the 129.2 Hz predicated by magnetic dipole model (calculations by Xiaokun Ma).

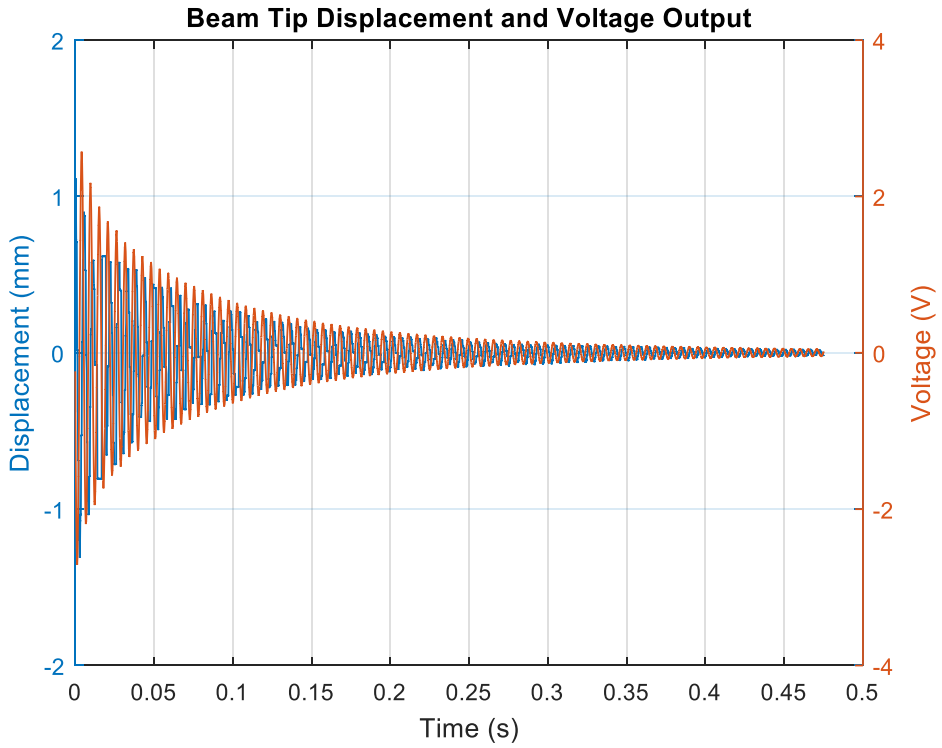

Figure 7-25. Displacement (blue line) and produced voltage (red line) resulting from manually rotating the rotor to 90 degrees and letting it go). This excitation produced magnetic plucking of the trapezoidal beam.

Figure 7-25 reveals the beam tip displacement and voltage output (through an 18 kΩ resistor) from one bimorph PZT beam in a fully assembled device. The test was conducted by rotating the rotor by 90° to pluck the beam under test, and then allowing the device to ring down. However, when all of the beams were assembled, it was found that there was an unexpected

magnetic stiffening force arising from strong magnetic interaction between beams that resulted in the beams curling. Thus, it was necessary to reduce the active length of the beam to increase the distance between magnets on the beam so that they have weaker coupling. However, practically, some beams were found to bend up or down a little bit at rest due to the magnetic force from adjacent beams. The data in Fig. 7-25 correspond to one of the bent beams. The resonance frequency and mechanical quality factor (Q) are around 180 Hz and 28, respectively.

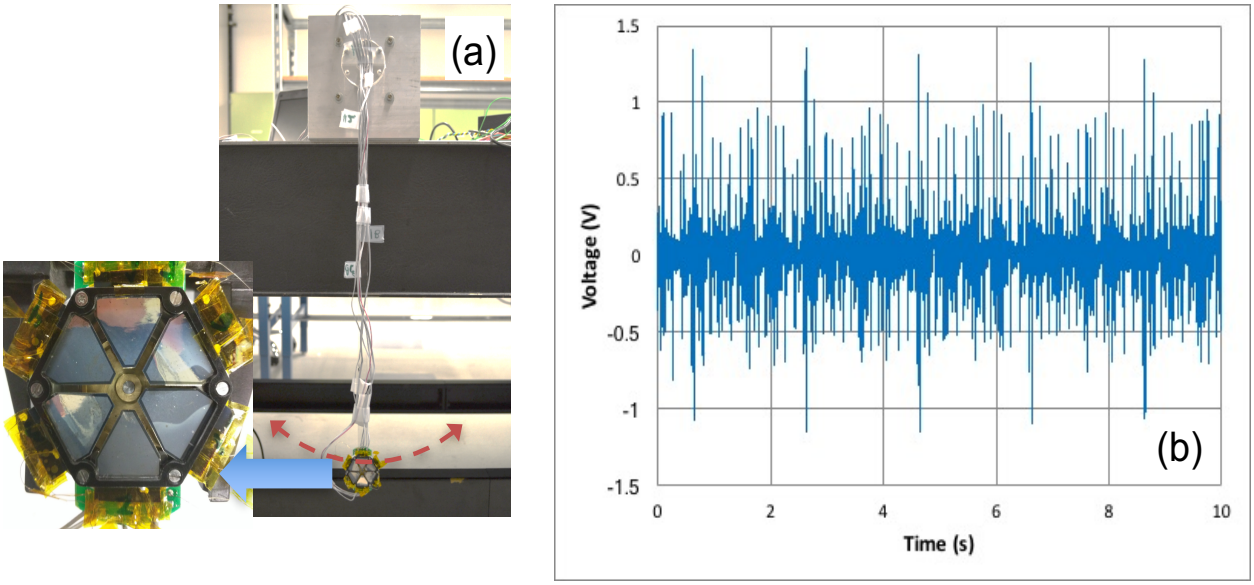

Figure 7-26. (a) Experimental set-up for swing arm test attached with Gen III device on the arm (b) Output voltage from one unimorph beam across 18 kΩ resistor during the pseudo walking on bench (angular rotation speed T=1s from -30 to +30 degree).

The assembled Gen-III device with six trapezoidal PZT beams was characterized using a mechanical device designed to simulate a pseudo wrist-worn situation. In the pseudo walking test, the PZT beams were plucked by the swinging motion (red arrow) or a steel arm that was controlled by a servomotor (Figure 7-26(a)) that provided various swing angles and speeds in a sine wave.

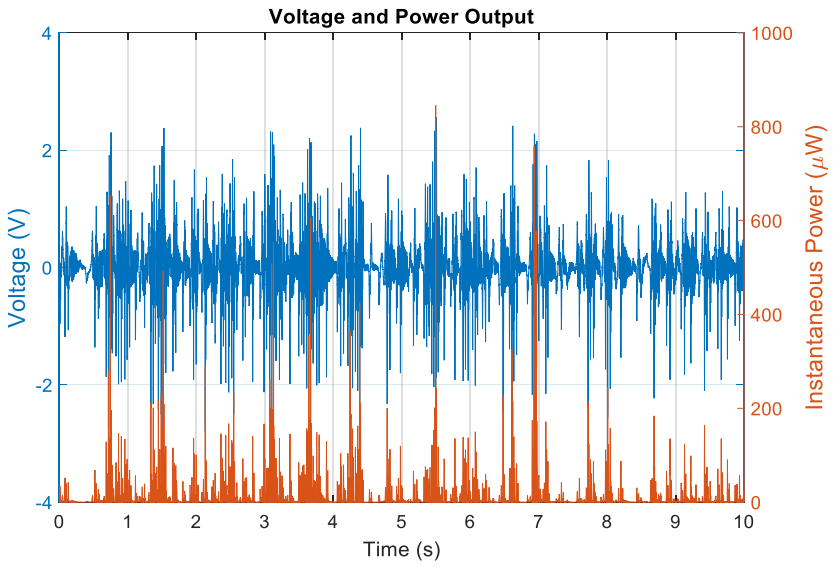

Figure 7-27. Output from one unimorph beam across 27 kΩ resistor during jogging in place on wrist.

Figure 7-27 shows the output voltage and power of one unimorph beam produced by the subject jogging in place with the device located on the wrist. Based on the output power from the best performing unimorph beam in Figure 7-27, the optimal power of 156.6 µW is predicted under a jogging-in-place excitation. The amount of power is similar to the power produced simply by holding the prototype in hand and shaking.

Table 7-2. Summary of performance of Gen-III device.

Input		Total Power from 6 beams [µW]	Total Power [µW] (best unimorph X12)
Pseudo walking on bench $30\sin\frac{2\pi t}{T}$	T=4s	0.9	3
	T=2s	1.7	6.4
	T=1s	10.3	**41.8**
	T=0.5s	19.5	48.2
On Wrist	Jogging in place	38.3	**156.6**
	Rotating the wrist from -90 to +90 (arm hold horizontal)	25.1	**91.4**
Shaking in hand	Rotor in continuous rotation	37.8	**158.8**

Table 7-2 shows the RMS output power from the swing arm test for different sinusoidal swing motions (measured across 33 kΩ/18 kΩ resistor for bimorphs and unimorphs, respectively) and on body (across 56 kΩ/27 kΩ for bimorph and unimorph) test. The optimal load resistance can be predicted by the model ($Load\ resistance \approx {}^{1}/_{2\pi \times natural\ frequency \times\ capacitance}$). Since it is not a standard base excitation, the optimal load may dependent on the excitation intensity. The experimental output power of the Gen-III device increased with increasing angular rotation speed from -30 to +30 degree using the swing arm bench (Table 7-2). However, all 6 beams (3×bimorph, 3×unimorph) in the full harvester assembly did not perform equally well, as expected from simulation. It is believed that the other beams were mechanically damaged during handling and assembly. Moreover, strong magnetic coupling between beams required alternate beams to be bent up to reduce the magnetic repulsive force. Good power output was obtained from one unimorph beam during on body tests such as jogging and rotating on wrist without vertical movement. One of the beams in a fully assembled Gen-III device was able to instantaneously flash a light-emitting diode (LED) when shaken by hand, as shown in Figure 7-28.

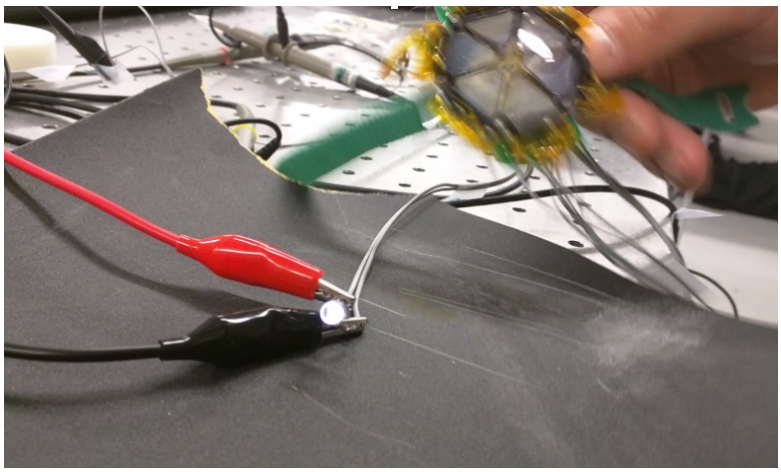

Figure 7-28. Capture of a video showing flashing of an LED through one unimorph beam by hand shaking the harvester.

7.4 Conclusions on Non-Resonant Harvesters

A series of wrist-worn energy harvesters designed by collaborators at the University of Utah were fabricated, which used magnetic plucking to achieve frequency up-conversion. All piezoelectric layers were formed by *rf*-sputtering {001} oriented PZT 52/48 films on both sides of a Ni foil (50 μm of thickness). The continuous bimorph PZT films (5cm × 5cm × 50μm) were customized for 3 different types of eccentric-rotor based on wrist-worn energy harvesters (e.g. Gen-I, -II, and -III).

For the out-of-plane plucking configuration, Gen-I was integrated with six cantilever beams arranged in a star shape and fabricated from a single substrate. Permanent magnets were attached on the rotor and on the tip of each of six beams. Assuming all beams are functional, the assembled Gen-I prototype can generate a 42 μW power from a sine wave swing arm motion driven by motor on bench, based on the unimorph output of 3.5 μW.

Six trapezoidal shaped cantilever beams for Gen-III harvester utilize space better and have a more uniform strain compared to a cantilever beam in Gen-I. To validate the functionality, one trapezoidal piezoelectric beam without a proof mass was tested using a vibration shaker at resonance frequency (~250 Hz) and a fixed acceleration level (0.15 G). A power density of 2886 $\mu W/cm^2g^2$ was obtained at a load resistance of 17 kΩ for series connection. After assembly of the Gen-III device, of the 12 PZT layers (6 bimorph PZT beams), 9 functional PZT layers were obtained. Based on the best unimorph output power, the total output power of device is demonstrated approximately 90 μW from a 90° rotating on-wrist.

The obtained results indicate that these wrist-worn harvesters are able to generate power from real-world multidimensional human motion inputs.

7.5 References

[1] M. Lee, C.-Y. Chen, S. Wang, S. N. Cha, Y. J. Park, J. M. Kim, L-J. Chou, and Z. L. Wang "A hybrid piezoelectric structure for wearable nanogenerators," *Advanced Materials* **24**, 13 (2012) 1759.

[2] D. Han, K.-S. Yun, "Piezoelectric energy harvester using mechanical frequency up conversion for operation at low-level accelerations and low-frequency vibration," *Microsystem Technologies*, **21**, 8 (2015) 1669.

[3] V. Misra, A. Bozkurt, B. Calhoun, T. Jackson, J. S. Jur, J. Lach, B. Lee, J. Muth, O. Oralman, M. Ozturk, S. Trolier-McKinstry, D. Vashaee, D. Wentzloff, and Y. Zhu, "Flexible Technologies for Self-Powered Wearable Health and Environmental Sensing," *Proceeding of the IEEE*, **103**, 4 (2015) 665.

[4] M. Pozzi, M.S.H. Aung, M. Zhu, R.K. Jones, and J.Y. Goulermas, "The pizzicato knee-joint energy harvester: characterization with biomechanical data and the effect of backpack load," *Smart Materials and Structures* **21**, 7 (2012) 075023.

[5] Pillatsch, E. M. Yeatman, and A. S. Holmes, "Real world testing of a piezoelectric rotational energy harvester for human motion," *Journal of Physics: Conference Series*, **476** (2013) 012010.

[6] K. Fan, J. Chang, F. Chao, and W. Pedrycz, "Design and development of a multipurpose piezoelectric energy harvester," *Energy Conversion and Management* **96** (2015) 430.

[7] T. Xue, X. Ma, C. Rahn, and S. Roundy, "Analysis of upper bound power output for wrist-worn rotational energy harvester from real-world measured inputs," *Journal of Physics: Conference Series* **557** (2014) 012090.

[8] T, Xue, S. Roundy, "On magnetic plucking configurations for frequency up-converting mechanical energy harvesters," *Sensors and Actuators A: Physical* **253** (2017) 101.

[9] A. Hajati, "Ultra wide-bandwidth micro energy harvester," Ph. D thesis Massachusetts Institute

of Technology (2011).

[10] Private communication Tiancheng Xue in the Shad Roundy group at the University of Utah

[11] A. Hajati, and S.-G. Kim. "Ultra-wide bandwidth piezoelectric energy harvesting." *Applied Physics Letters* **99**, 8 (2011) 083105.

[12] S. Roundy, E. S. Leland, J. Baker, E. Carleton, E. Reilly, E. Lai, B. Otis, J. M. Rabaey, P.K. Wright, V. Sundararajan, "Improving power output for vibration-based energy scavengers," *IEEE Pervasive Computing* **4**, 1 (2005) 28.

[13] H. G. Yeo, X. Ma, C. Rahn, and S. Trolier-McKinstry, "Efficient piezoelectric energy harvesters utilizing (001) textured bimorph PZT films on flexible metal foils," *Advanced Functional Materials*, **26** (2016) 5940.

[14] A. Erturk, and D. J. Inman, "An experimentally validated bimorph cantilever model for piezoelectric energy harvesting from base excitations," *Smart Materials and Structures* **18**, 2 (2009) 025009.

[15] R. L. Johnson-Wilke, R. H. Wilke, V. Cotroneo, W. N. Davis, P. B. Reid, D. A. Schwartz, S. Trolier-McKinstry, "Improving yield of PZT piezoelectric devices on glass substrates," *In SPIE Optical Engineering+Application. International Society for Optics and Photonics* (2012) 85030A.

[16] H. G. Yeo, and S. Trolier-McKinstry "{001} Oriented piezoelectric films prepared by chemical solution deposition on Ni foils," *Journal of Applied Physics*, **116**, 1 (2014) 014105.

[17] R. H. Wilke, P. J. Moses, P. Jousse, C. Yeager, and S. Trolier-McKinstry, "Wafer mapping of the transverse piezoelectric coefficient $e_{31,f}$, using the wafer flexure technique with sputter deposited Pt strain gauges," *Sensors and Actuators A: Physical* **173**, 1 (2012) 152.

[18] T. Xue, S. Roundy, Analysis of magnetic plucking configurations for frequency up-converting

harvesters, *Journal of Physics: Conference Series* **660**, 1 (2015) 012098.

[19] S. Corkovic, Q. Zhang, and R. W. Whatmore, "The investigation of key processing parameters in fabrication of $Pb(Zr_xTi_{1-x})O_3$ thick films for MEMS applications," *Journal of Electroceramics* **19**, 4 (2007) 295.

Chapter 8

Conclusions and Future Work

8.1 Conclusions

This study pursued the development of high figure of merit PZT thin films on flexible metal foils as well as integration of these films into various types of piezoelectric energy harvester designs. The results gained from the performance of these piezoelectric energy harvesters prove the feasibility of self-powering under a wide range of vibration sources (from human activity to machining tools).[1,2]

Deposition of highly {001} oriented $Pb(Zr_{0.52},Ti_{0.48})O_3$ thin films on Ni foil using chemical solution deposition and *rf*-sputtering was optimized with a buffer layer (HfO_2) to overcome thermodynamic incompatibility between the oxide film and metal substrate. Pretreatments of Ni foil (25 μm ~ 50 μm) such as polishing and pre-annealing in low oxygen partial pressure reduced the surface roughness and played an important role in obtaining preferred orientation of the $LaNiO_3$ template layer.

{001} oriented PZT films on (100)$LaNiO_3$/HfO_2/Ni, grown by CSD, exhibited a low dielectric permittivity (ε_r ~ 530) and a large piezoelectric constant ($|e_{31,f}|$ ~ 10.6 C/m^2), showing promise for improvement of the figure of merit (FoM) for energy harvester. It is noted that PZT films on thin metal substrate are thin, flexible, and can be machined easily for low-cost fabrication of a variety of energy harvesters.[3,4] Additionally, the (001)-orientation provides large remanent polarizations with low coercive electric field, which is of potential interest for ferroelectric random access memory (FeRAM).

Based on these results and the fabrication processing described in Chapter 3, resonant energy harvesters with a simple cantilever configuration were fabricated using undoped and Mn

doped PZT films (thickness: 1 μm ~ 3 μm) on Ni foil (25 μm). Characteristics of the microstructure and crystallinity of those films are similar to the PZT films on Ni described in Chapter 3. In the case of Mn doped 1 μm thick (001) oriented PZT (52/48) films on Ni foil, the dielectric constant and $|e_{31,f}|$ of that film are 390 at 10 kHz and 11.3 C/m^2, respectively, after hot poling. This film achieves superior FoM ($\frac{e_{31,f}^2}{\varepsilon_r}$), around 0.4 C^2/m^4, for piezoelectric energy harvesting, which is comparable with (001) oriented 1% Mn doped PZT films on MgO substrate reported by Yeager et al.[5]

Unimorph cantilever beams were easily fabricated from PZT films on Ni foil using simple mechanical cutting. It was found that the power performance of harvesters strongly depends on the thickness of the film. The maximum power increases from 12 to 60 μW as the thickness of PZT film increases from 1 to 3 μm at resonance frequency (~70 Hz) at 0.5 G. The optimum poling condition (150 ºC, 3E$_C$ for 15 min) enhanced the voltage and power output of the cantilever harvester prepared using (1 μm) PZT films on Ni foil.

For self-powering a wearable device from human motion, MEMS harvesters should resonate at a frequency of less than 10 Hz. To meet this need, a compliant mechanism harvester was successfully fabricated with superior FoM PZT films on flexible nickel foil. The device generated a maximum voltage and power of 7 V and 149 μW, respectively, with a 0.1% strain limit at 0.1 G acceleration level when excited at its resonant frequency. Large power densities (3.9 mW/cm^{2}g^2) exceed those of other microelectromechanical systems by more than a factor of 50; this is in part because the devices have higher mode shape efficiencies (65%). Furthermore, the device has a low resonant frequency ~ 6 Hz that matches the ambient mechanical energy spectrum well. Figure 8-1 exhibits the power density and resonance frequency of the MEMS energy harvesters for a variety materials reported in the literature.[6~21] The performance of the

device investigated in the study is indicated with a red circle. As seen in Figure 8-1, the harvester developed in this work possesses some of the highest power density with lower resonance frequency reported in the literature.[22]

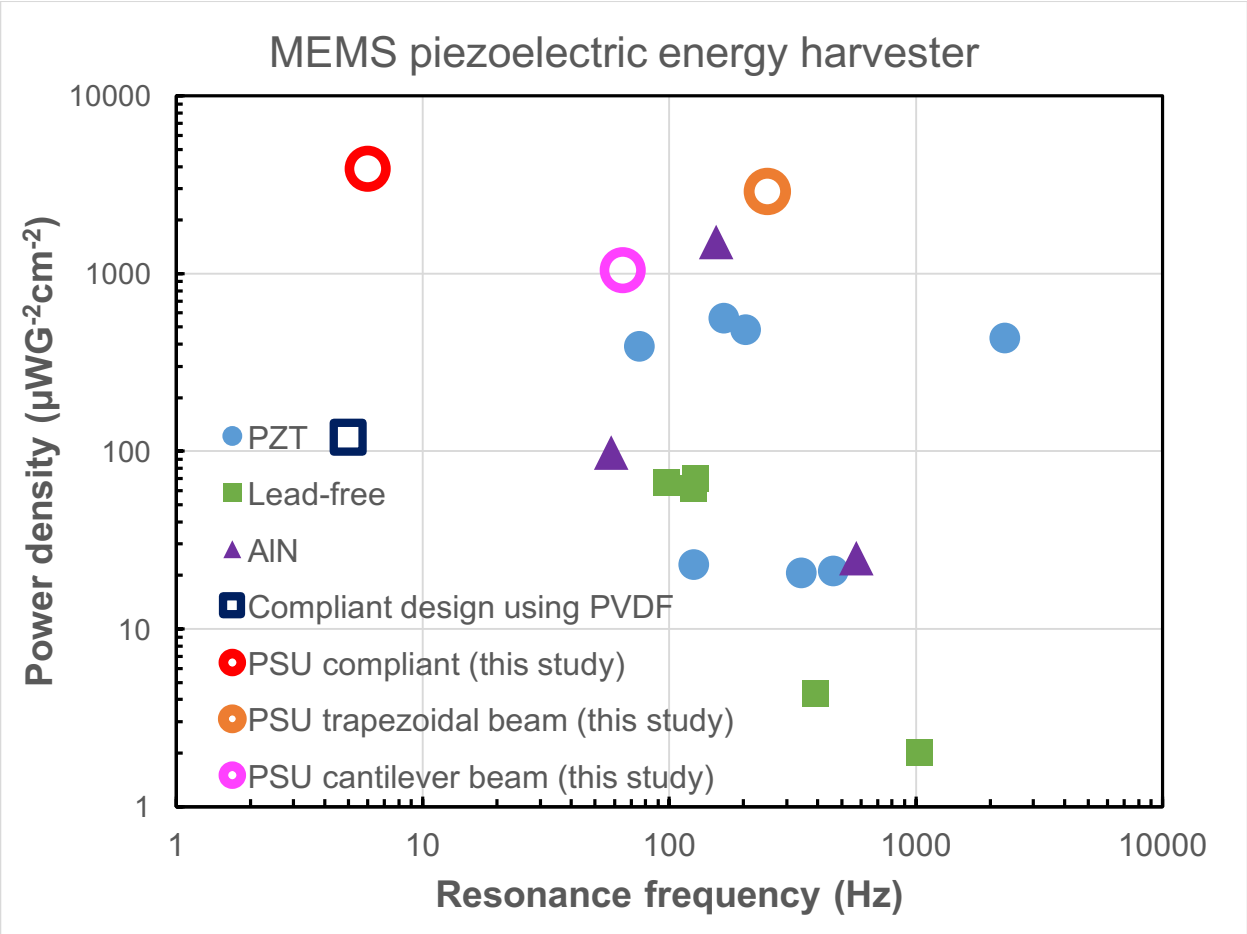

Figure 8-1. Power density and resonance frequency of MEMS piezoelectric energy harvesters for a variety of piezoelectric materials reported; PZT,[6~12], Lead-free (KNN,[13~16] and $BiFeO_3$[17]), AlN,[18~20] Compliant design using PVDF,[21] PSU compliant,[22] and trapezoidal beam.

In Chapter 6, {001} oriented polycrystalline PZT films grown by high temperature sputtering on a PZT (52/48) seeded nickel substrate were reported. The high temperature sputtered process reported provides significant improvements relative to room temperature

sputtering with a post-deposition anneal, including high density and strong orientation. It was also demonstrated that high temperature sputtering is a promising method to grow thick (~5.5 μm) dense PZT films on both sides of a metal substrate. High temperature sputtered PZT films on metal foils were applied to a variety of frequency up conversion designs for non-resonant based energy harvesting. Basically, those harvesters were fabricated with several bimorph PZT beams, permanent magnets and a rotor. For Gen-I, a complex star shape with six piezoelectric elements was machined from high FoM (0.47 C^2/m^4) bimorph PZT films on Ni foil using a laser ablation tool.[15] The performance of these devices was investigated with a pseudo walking set up. It is noted that the first prototype (Gen-I) of wrist-worn piezoelectric energy harvester is able to generate 42 μW from a pseudo walking motion.

The Gen-III wrist worn harvesters utilized an eccentric rotor and six trapezoidal PZT beams that provided better space utilization and thicker PZT films relative to Gen-I. Six trapezoidal beams were fabricated with high temperature sputtered 5.5 μm thick PZT layers on both sides of a 50 μm thick Ni foil. A large remanent polarization (P_r ~ 45 kV/cm) and low dielectric coefficient (ε_r ~ 450 at 1kHz) were shown for the strongly {001} oriented PZT layers fabricated by high temperature sputtering.

One of the trapezoidal cantilever beams (area =1.54 cm^2) without a proof mass was explored experimentally to compare to the performance at resonance with other resonant–driven MEMS energy harvesters. The trapezoidal PZT beam produced an average power of 100 μW at 0.15 G acceleration level. Additionally, the area power density reached 2886 $\mu W/cm^2g^2$.

The device was successfully assembled with six trapezoidal PZT beams and the output power was measured using a pseudo walking motion to simulate a device being worn on the wrist. For jogging in place, the average power of 13 μW per unimorph beam was extrapolated to

be 156 μW of total power with ideal functionality of 6 bimorph beams. Additionally, the device (with only one unimorph beam) was used to flash a commercial LED bulb by hand motion. The energy harvesters should enable operation of wearable devices from real-world multidimensional human motion inputs.

8.2. Future Work

8.2.1. Determining the Limitation of Strain Level in PZT films

To apply a variety of designs for piezoelectric energy harvesting, the mechanical characteristics of PZT films of various thickness need to be further clarified. In particular, the bounds for the allowed strain level needs to be investigated in order to determine the maximum strain that can be reliably and repeatedly experienced without mechanical failure. Higher strains enable higher harvesting levels.

As an initial screen, PZT films on Ni foils were bent around variety of metal rod diameters, as shown in Figure 8-2. Induced strain on the top surface of the PZT should be given by Eq (8.1)[23]

$$\text{Strain } (\epsilon) = \delta / r \qquad (8.1)$$

where δ is the distance between the neutral plane and the top surface of the PZT film and r is the bending radius. Based on equation 8.1, Table 8-1 listed the induced strain levels explored.

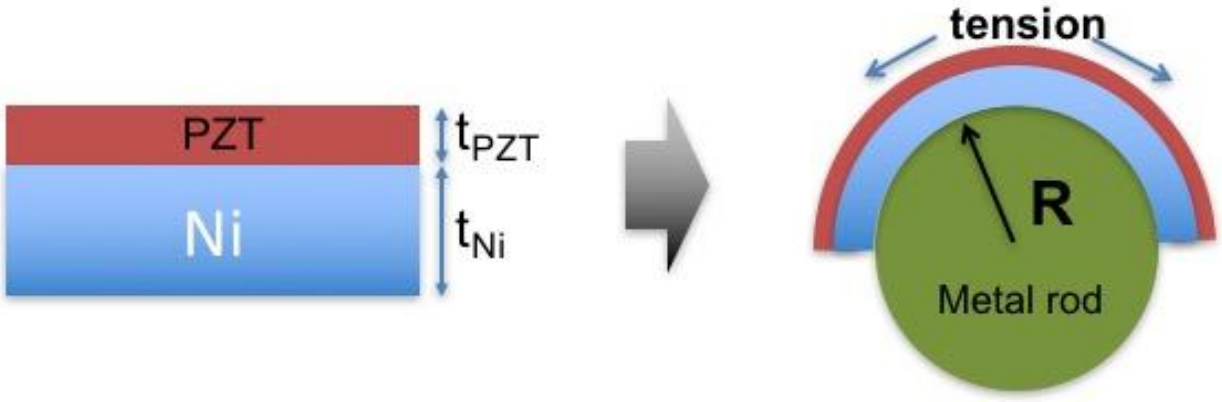

Figure 8-2. Schematic of cross-section of PZT film bent around a metal rod.

Table 8-1. Degree of strain in PZT films on Ni substrate controlled by various rod radii.

Radius of rod (R) [mm]	**3μm thick PZT on 25 μm Ni (δ=10.14 μm)**	**6μm thick PZT on 25μm Ni (δ=9.93μm)**
2.4	0.42%	0.41%
3.05	0.33%	0.325%
3.48	0.29%	0.285%
5.29	0.19%	0.19%

Prior to the bending test, the film surfaces were inspected by field emission scanning electron microscopy (FESEM) to check for cracks and delamination. FESEM surface images of the PZT films on Ni do not exhibited any indication of cracks or delamination and show a smooth surface and fine columnar grains in Figure 8-3(a) and (b). Following this microstructural observation, a tensile stress was applied to the films by bending around a metal rod. 10.6 mm and 7 mm diameter rods produced 0.19% and 0.29% strain levels in the films. The bending was repeated for 10 cycles each. Through re-inspection of the surface microstructure, it was found that strain levels (<0.29%) do not produce any micro-cracking or other structural degradation confirmed by FESEM images (Figure 8-3(c) and (d)).

To determine the precise strain limits for the films, it is necessary to further investigate an increase in strain level until cracks or structural failure are observed in FESEM images.

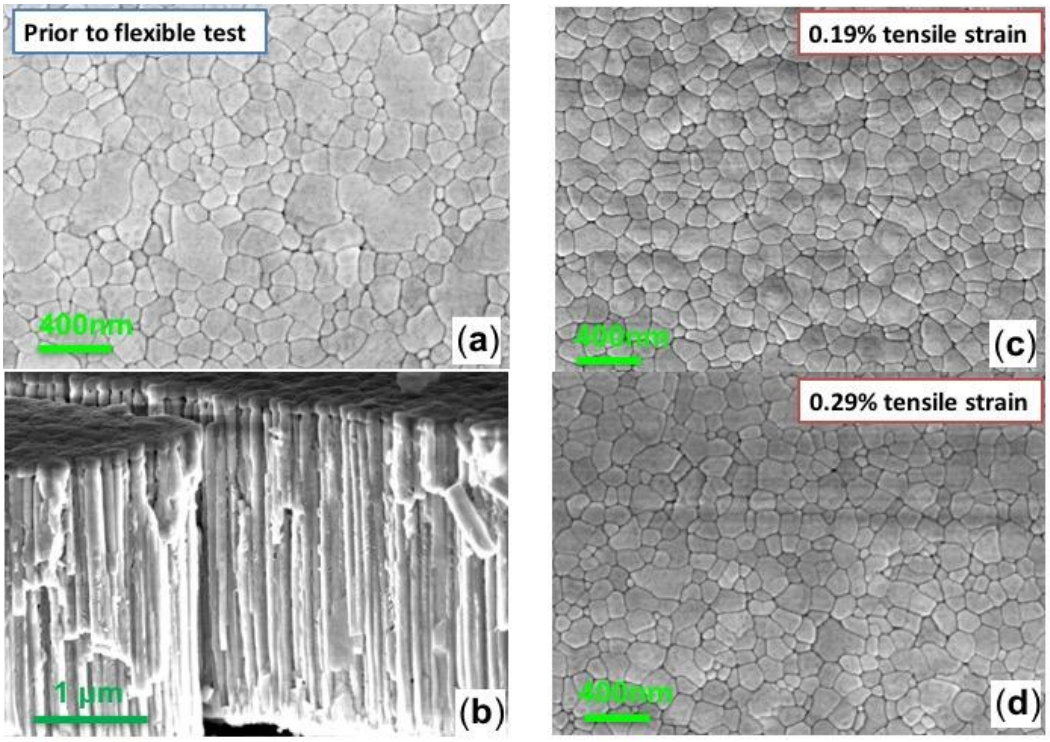

Figure 8-3. (a) Surface and (b) cross-sectional microstructural images of the PZT films before the bending test. Surface micrograph of PZT film after the bending test for (c) 0.19% and (d) 0.29% tensile strain.

8.2.2 Reliability Dependence of Mechanical Stress Cycles

Piezoelectric energy harvesters are exposed to oscillating stress states to scavenge energy from the ambient. As such, the lifetime and reliability of the piezoelectric films should be investigated under repetitive mechanical loading. However, little is known about the reliability of the ferroelectric and piezoelectric properties of PZT films on Ni foil during mechanical cycling. Future work should be directed towards assessing the durability and reliability of the piezoelectric energy harvester under continuous bending. The bending test results can be used to determine the limiting strain levels, the aging behavior of the output power and the electrical

properties as a function of mechanical stress/strain cycling. This could be investigated by using an air slide table which can adjust cycle speed and strain levels. In particular, it is suggested that a study be undertaken regarding whether or not the repetitive excitation influences the domain state (and hence the dielectric permittivity and piezoelectric response), in domain-controlled PZT films. It is noted that a domain state with the *c*-axis *out-of-plane* has the lowest energy for compressive *in-plane* stress. In contrast, *in-plane* tensile stress favors the *a*-domain state. However, energy harvesting systems are exposed to repeated compressive and/or tensile stress to generate power. Therefore, there is a possibility of degrading the properties due to stress cycling. An investigation should be undertaken as to whether mechanical depoling occurs and whether the domain state changes as a function of cycling, type of cycling and level of strain.[33]

For this experiment, a cantilever structure with an {001} textured PZT film on Ni foil should be investigated. The dielectric, ferroelectric and piezoelectric properties should be monitored as a function of the number and amplitude (the radius of curvature of the sample) of bending cycles. The air slide table could be used to perform the mechanical bending and straightening of the device. The effects of the stress types and the number of cycles on the material properties of the PZT films should be investigated to evaluate the piezoelectric and structural degradation related to domain switching.

8.2.3 Strain-based Energy Harvester for Wearable Device

Aperiodic movement and random vibration from body deteriorate the utility of resonant structures for self-powering wearable systems. Thus, it is also interesting to investigate flexible strain-based energy harvesters. Flexibility of the PZT films on metal foil can provide an opportunity to harvest power wherever movement is available.[34]

Ideally, a flexible strain based energy harvester could overcome the limitation of frequency and movement for wearable and implantable devices. An example of this is shown in Figure 8-4, where a piezoelectric PZT film on a nickel (Ni) foil was used to scavenge energy from the motion of a human finger.

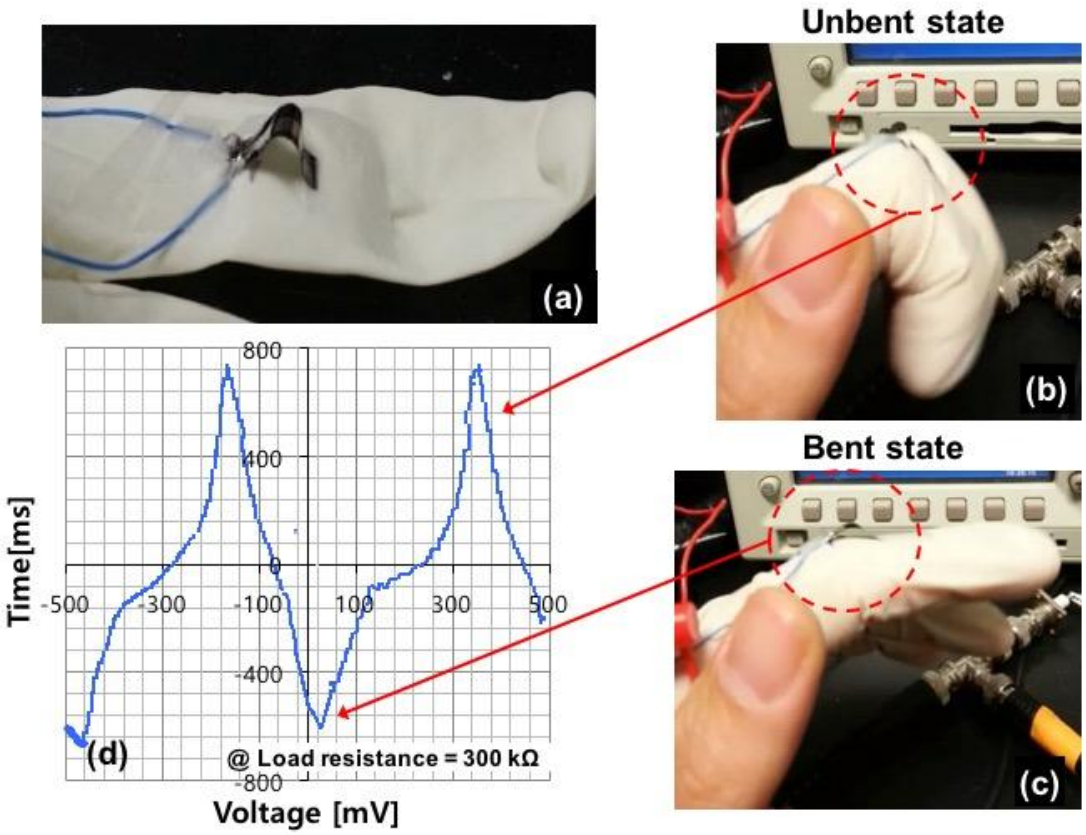

Figure 8-4. (a) Photograph of strain based harvester using PZT/Ni(25 μm) clamped in a bent state on a lab glove. Photographs of device are captured in (b) unbent state (at the knuckle) and (c) bent state (original). (d) The measured output voltage at load resistance (300 kΩ) generated by bending the knuckle.

In Figure 8-4(a), both ends of the unimorph strip with an electrode size of 2 mm × 12 mm were glued onto a lab glove. In this set up, the film is under an initial pre-strain, and is free to move parallel to finger movement. When the index finger is bent, the beam is stretched along the knuckle, and when the finger is straightened, the distance between the clamp points is

reduced. As a result, the harvester buckles away from the knuckle when the finger is straightened. The harvester extracts electrical energy from the finger motion with low resistance as shown in Figure 8-4 (b) and (c). The larger output signals by the straightening motions may be due to the discrepancy in the strain rate between the bending and unbending motions. From this initial harvester, maximum power range from 0.09 μW to 1.7 μW are strongly dependent on the amplitude of forcing movement and strain rate (frequency).

However, it is still feasible to improve power generation from human motion through increasing the volume of PZT in the structure. Bimorph thick PZT films encapsulated with a flexible polymer could be pursued for good power performance with enhanced electrical and mechanical stability.[35,36]

8.2.4 Magnetoelectric Energy Harvesting

The fundamental layered structure of piezoelectric (e.g. PZT) film on a magnetostrictive (e.g. Ni) substrate is a good candidate for magnetoelectric (ME) harvester. In this ME composite, an energy harvester could generate electrical charge across the piezoelectric layer (mechano-electric coupling), when stressed by elongation or contraction of the magnetostrictive layer under an AC magnetic field.[37] Thus, the performance of such a harvester mainly depends on the ME coupling (α_{ME}), which represents the ability to transduce energy between electric and magnetic domains.

Strongly {001} oriented PZT(52/48) film on flexible Ni foil (thickness: 25 μm) is promising for magnetic field sensor and energy harvester as a result of high ME performance below 60 Hz.[37] Figure 8-5 shows the measured magnetoelectric coupling of {001}PZT(1.5 μm)/Ni(25 μm) off resonance (1 kHz) as measured by J. Ryu of the Korea Institute of Materials

Science. The maximum α_{ME} of ~3.2 V/cm·Oe was obtained after corona poling at 12 kV and 130 °C for 20 min and indicates excellent ME performance of PZT based ME system.

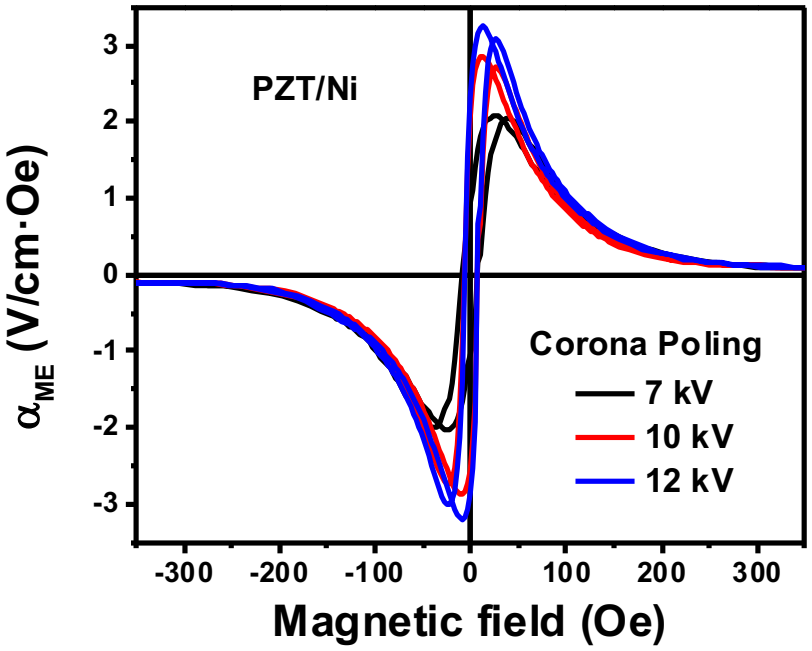

Figure 8-5. Magnetoelectric coupling of PZT/Ni stack as a function of applied magnetic field off resonance frequency (f = 1kHz) [from J. Ryu].

In theoretical model for intrinsic ME coupling coefficient off-resonance, on increasing the thickness of PZT film up to 33 μm, the ME voltage coefficient should continuously increase; this thickness represents the optimized volume fraction of the PZT (f_{PZT} = 0.56) layer when interfacial bonding (k) is strong (k ~1).[38] Thus, theoretically it is predicted that thicker (> 10 μm) PZT film with PZT layers on both sides of Ni foil could produce extraordinary high off-resonance direct ME output.

Additionally, the ferromagnetic nickel substrate, which possesses randomly oriented

magnetic domain, could be magnetized along the direction of external magnetic field. Based on these magnetic properties, strongly magnetized nickel substrate itself can be applied to non-resonant energy harvester in magnetic plucking without an additional permanent magnet.

8.3 References

[1] S.-G. Kim, S. Priya, and I. Kanno, "Piezoelectric MEMS for energy harvesting," *MRS Bulletin*, **37** (2012) 1039.

[2] S. Roundy, P. K. Wright, and J. Rabaey, "A study of low level vibrations as a power source for wireless sensor nodes," *Computer Communications*, **26** (2003) 1131.

[3] Y. Tsujiura, E. Suwa, H. Hida, K. Suenaga, K. Shibata, and I. Kanno, "Lead-free piezoelectric MEMS energy harvesters of stainless steel cantilevers," *in Proc. 17th Transducers*, Barcelona, Spain, Jun. (2013) 474.

[4] Y. Minemura, Y. Kondoh, H. Funakubo, and H. Uchia, "One-axis-oriented crystal growth of lead zirconate titanate thin films on metal substrates using perovskite-type oxide nanosheet layer," *Key Engineering Materials*, **582** (2014) 15.

[5] C. B. Yeager and S. Trolier-McKinstry, "Epitaxial $Pb(Zr_x,Ti_{1-x})O_3$ ($0.3<x<0.63$) films on (100)MgO substrates for energy harvesting applications," *Journal of Applied Physics*, **112** (2012) 074107.

[6] D. Isarakorn, D. Briand, P. Janphuang, A. Sambri, S. Gariglio, J.-M. Triscone, F. Guy, J. W. Reiner, C. H. Ahn, N. F. de Rooij, "Energy harvesting MEMS device based on an epitaxial PZT thin film: fabrication and characterization," *Power MEMS Tech. Dig*, (2010) 203.

[7] E. E. Aktakka, R. L. Rebecca, and N. Khalil, "Thinned-PZT on SOI process and design optimization for piezoelectric inertial energy harvesting," *16th International Conference on Solid-State Sensors, Actuators, and Microsystems, Transducers*, (2011) 1649.

[8] T. Zawada, K. Hansen, R. Lou-Moeller, E. Ringgaard, T. Pedersen, E. V. Thomsen, "High-performance piezoelectric thick film based energy harvesting micro-generators for MEMS," *Procedia Engineering*, **5** (2010) 1164.

[9] R. Xu, A. Lei, C. Dahl-Petersen, K. Hansen, M. Guizzetti, K. Birkelund, and O. Hansen, "Screen printed PZT/PZT thick film bimorph MEMS cantilever device for vibration energy harvesting," *Sensors and Actuators A: Physical*, **188** (2012) 383.

[10] H. Durou, G. A. Ardilla-Rodriguez, A. Ramond, X. Dollat, C. Rossi, D. Esteve, "Micromachined bulk PZT piezoelectric vibration harvester to improve effectiveness over low amplitude and low frequency vibrations," *PowerMEMS 2010*, Leuven, Belgium, (2010) 27.

[11] K. Morimoto, I. Kanno, K. Wasa, and H. Kotera, "High-efficiency piezoelectric energy harvesters of c-axis-oriented epitaxial PZT films transferred onto stainless steel cantilevers," *Sens. Actuators A*, 163,(2010) 428.

[12] D. Shen, J.-H. Park, J. Ajitsaria, S.-Y. Choe, H.C. Wikle, and D.-J. Kim, "The design, fabrication and evaluation of a MEMS PZT cantilever with an integrated Si proof mass for vibration energy harvesting," *J. Micromech. Microeng. 18*, (2008) 055017.

[13] I. Kanno, T. Ichida, K. Adachi, H. Kotera, K. Shibata, and T. Mishima, "Power-generation performance of lead-free (K,Na)NbO_3 piezoelectric thin-film energy harvesters," *Sensors and Actuators A: Physical*, **179** (2012) 132.

[14] Y. Tsujiura, E. Suwa, F. Kurokawa, H. Hida, K. Suenaga, K. Shibata, and I. Kanno, "Lead-free piezoelectric mems energy harvesters of (K, Na)NbO_3 thin films on stainless steel cantilevers," Japanese Journal of Applied Physics 52, 9S1 (2013) 09KD13.

[15] T. Shiraishi, N. Kaneko, M. Kurosawa, H. Uchida, Y. Suzuki, T. Kobayashi, and H. Funakubo, "Vibration-energy-harvesting properties of hydrothermally synthesized (K,Na)NbO_3

films deposited on flexible metal foil substrates," *Japanese Journal of Applied Physics* **54**, (2015) 10ND06.

[16] S.-H Kim, H. Seo, S. Glinsek, Y. Kim and A I. Kingon, "Lead-free piezoelectric thin film-based energy harvesters for self-powered implantable medical devices, " *in 16th US-Japan Seminar on Dielectric and Piezoelectric Materials*, (2013) D13.

[17] T. Yoshimura, S. Murakami, K. Wakazono, K. Kariya, and N. Fujimura, "Piezoelectric vibrational energy harvester using lead-free ferroelectric $BiFeO_3$ films," *Applied Physics Express*, **6** (2013) 051501.

[18] T. Ricart, P. P. Lassagne, S. Boisseau, G. Despesse, A. Lefervre, C. Billard, and E. Defay, "Macro energy harvester based on aluminium nitride thin films," *2011 IEEE International Ultrasonics Symposium. IEEE*, (2011) 1928.

[19] R. Andosca, T. McDonald, V. Genova, S. Rosenberg, J. Keating, C. Benedixen, and J. Wu, "Experimental and theoretical studies on MEMS piezoelectric vibrational energy harvesters with mass loading," *Sensors and Actuators A*, **178** (2012) 76.

[20] R. Elfrink, T. M. Kamel, M. Goedbloed, S. Matova, D. Hohlfeld, Y. Van Andel, and R. Van Schaijk, "Vibration energy harvesting with aluminum nitride-based piezoelectric devices," *Journal of Micromechanics and Microengineering*, **19**, 9 (2009) 094005.

[21] X. Ma, A. Wilson, C.D. Rahn, S. Trolier-McKinstry, "Efficient energy harvesting using piezoelectric compliant mechanisms: Theory and experiment," *Journal of Vibration and Acoustics,* **138**, 2 (2016) 021005.

[22] H. G. Yeo, X. Ma, C. Rahn, and S. Trolier-McKinstry, "Efficient piezoelectric energy harvesters utilizing (001) textured bimorph PZT films on flexible metal foils," *Advanced Functional Materials*, **26** (2016) 5940.

[23] G.-T. Hwang, J. Yang, S. H. Yang, H.-Y. Lee, M. Lee, D. Y. Park, J. H. Han, S. J. Lee, C. K. Jeong, J. Kim, K.-I. Park and K. J. Lee, "A reconfigurable rectified flexible energy harvester via solid-state single crystal grown PMN–PZT," *Advanced Energy Materials*, **5** (2015) 1500051.

33 R. F. Brown, "Effect of two-dimensional mechanical stress on the dielectric properties of poled ceramic barium titanate and lead zirconate titanate," *Canadian Journal of Physics*, **39**, 5 (1961) 741.

[34] S. Lee, S, H, Bae, L. Lin, Y. Yang, C. Park, S. W. Kim, and Z. L. Wang, "Super-Flexible Nanogenerator for Energy Harvesting from Gentle Wind and as an Active Deformation Sensor," *Advanced Energy Materials*, **23** (2013) 2445.

[35] Y. Qu, N. T. Jafferis, K. Lyonas, Jr., C. M. Lee, H. Ahmad, and M. C. McAlpine, "Enhanced piezoelectricity and stretchability in energy harvesting devices fabricated from buckled PZT ribbons," *Nano letters*, **10** (2010) 524.

[36] K.-I. Park, J. H. Son, G.-T. Hwang, C. K. Jeong, J. Ryu, M. Koo, I. Choi, S. H. Lee, M. Byun, Z. L. Wang, and K. J. Lee, "Highly-efficient, flexible piezoelectric PZT thin film nanogenerator on plastic substrates," Advanced Materials, 26, 16 (2014) 2514.

[37] J. Ryu, J.-E. Kang, Y. Zhou, S.-Y. Choi, W.-H. Yoon, D.-S. Park, J.-J. Choi, B.-D. Han, C.-W. Ahn, J.-W. Kim, Y.-D. Kim, S. Priya, S. Y. Lee, S. Jeong, and D.-Y. Jeong "Ubiquitous magneto-mechano-electric generator." *Energy & Environmental Science* **8**, 8 (2015) 2402.

[38] H. Palneedi, D. Maurya, G.-Y. Kim, V. Annapureddy, M-S. Noh, C.-Y. Kang, J.-W. Kim, J.-J. Choi, S.-Y. Choi, S.-Y. Chung, S.-J. L. Kang, S. Priya, and J. Ryu "Unleashing the Full Potential of Magnetoelectric Coupling in Film Heterostructures." Advanced Materials 29 (2017) 1605688.

Appendix A : Supplemental Materials for Chapter 5

Figure A-1 shows pictures of typical unimorph and bimorph PZT films on Ni foil. The bimorph beams are seen to be much flatter due to balancing of the stresses on both sides of the metal.

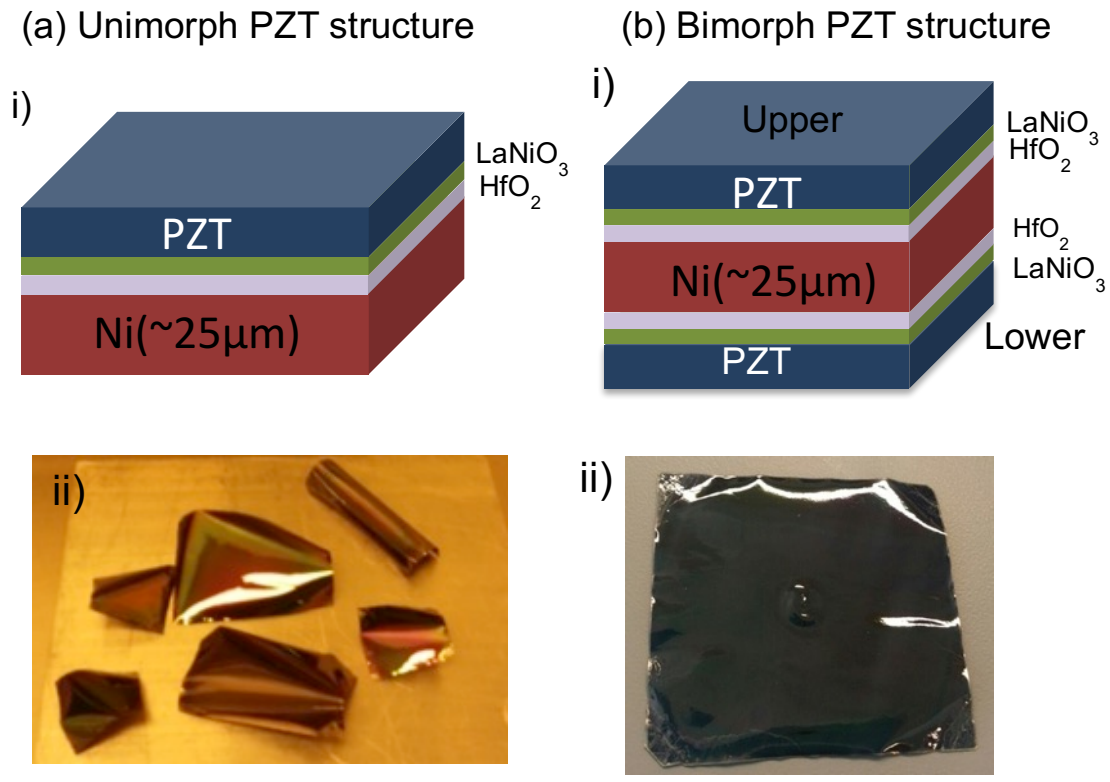

Figure A-1. Schematic configuration of (a-i) unimorph PZT/$LaNiO_3$/HfO_2/Ni and (b-i) bimorph PZT/$LaNiO_3$/HfO_2/Ni/HfO_2/$LaNiO_3$/PZT stacks. Pictures of top view (a-ii) unimorph PZT film showing severe transverse curvature and (b-ii) bimorph flat PZT films on Ni foil with some curvature near the foil edges after crystallization.

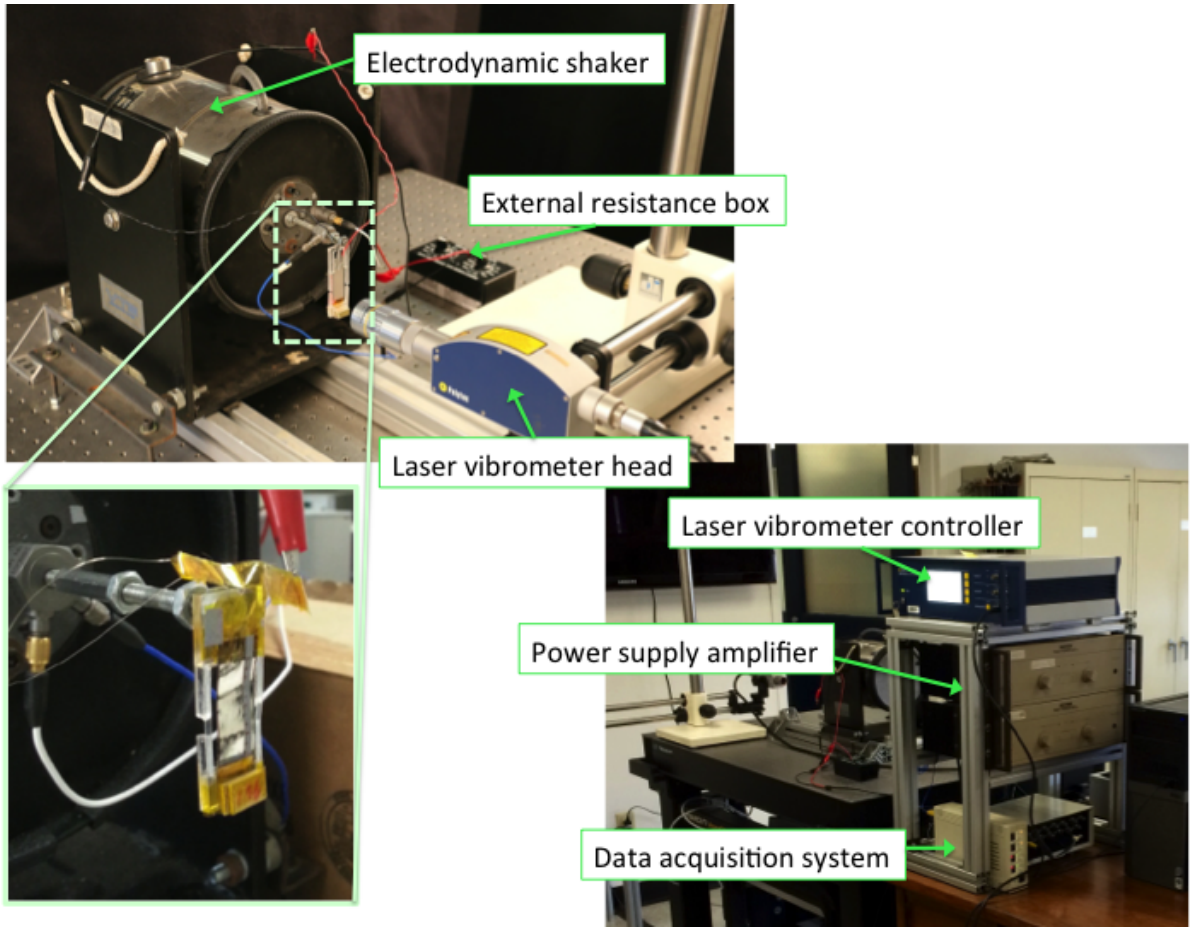

Figure A-2. (a), (b) Experimental setup to measure vibration response by data acquisition system for (c) the PCM device vertically mounted to electrodynamic shaker.

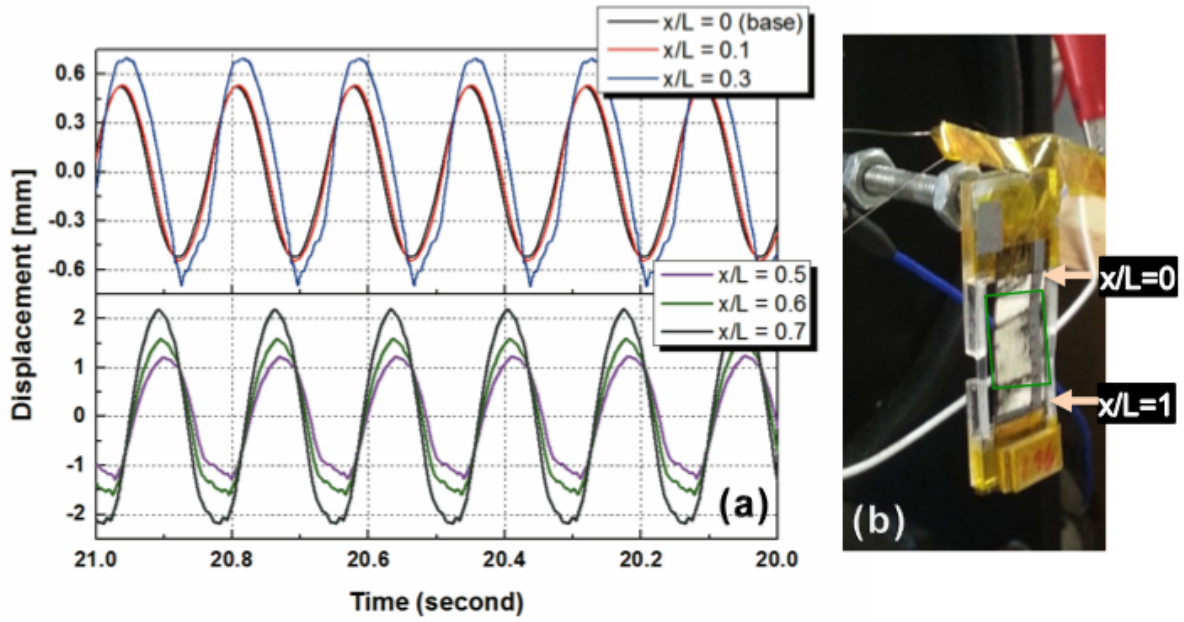

Figure A-3. (a) Sinusoidal base excitation response at different positions along PZT beam and (b) photograph of the device vertically mounted to the shaker with arrows indicates relation positions (x/L = 0 and 1).

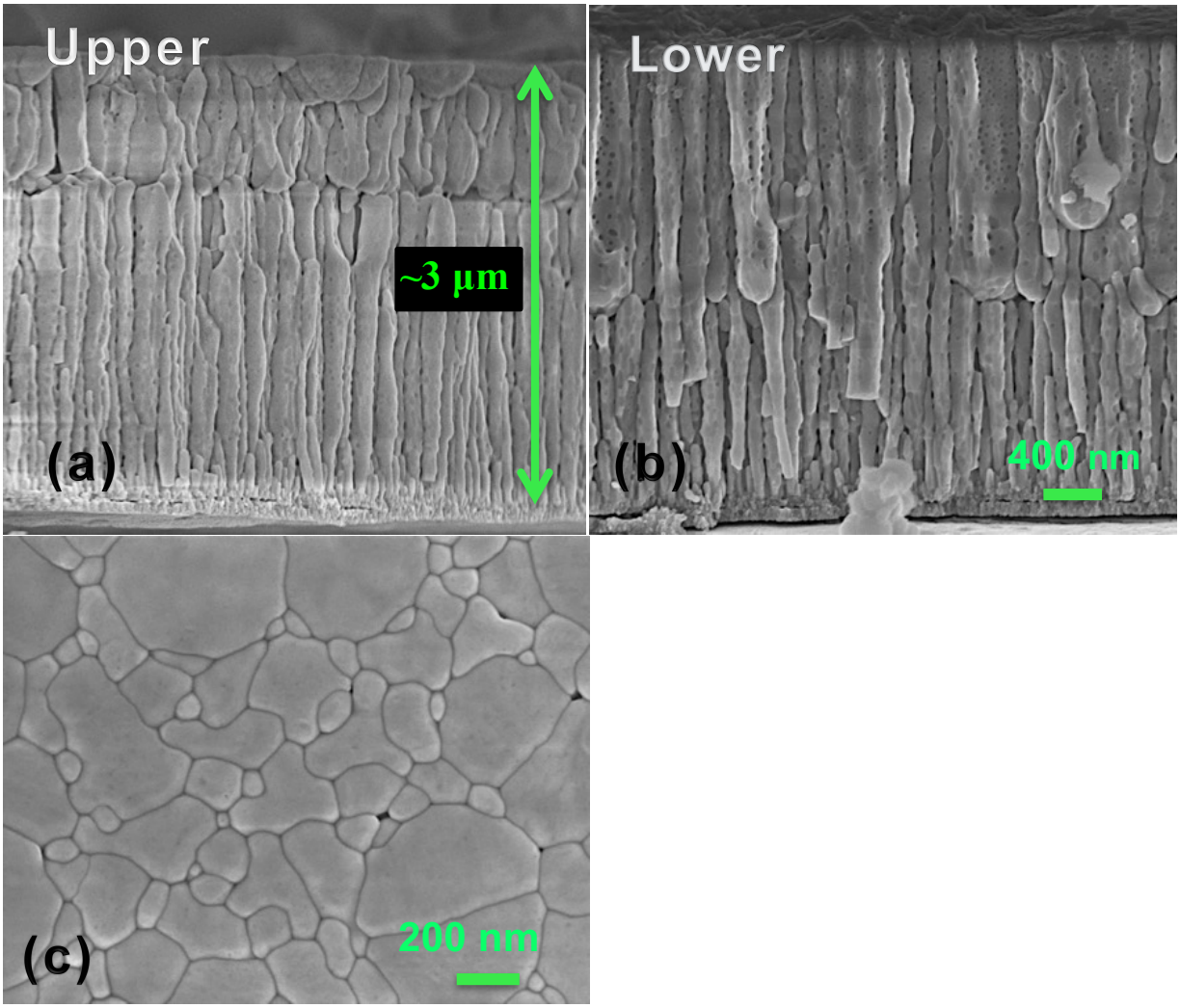

Figure A-4. Cross-sectional images of (a) upper PZT layer and (b) lower PZT layer. (c) Surface microstructure image of PZT film.

Microstructure images of both PZT layers utilizing field emission scanning electron microscopy (FE-SEM, Leo 1530) are shown in Figures A-4. Figures A4a and A-4b illustrate the cross section microstructure of upper and lower PZT films on Ni; both show 150~250 nm columnar perovskite grains with pores at the grain boundaries. Some granular grains, which are expected to be randomly oriented are also seen in Figure A-4a. No pyrochlore phases were observed (Figure A-4c).

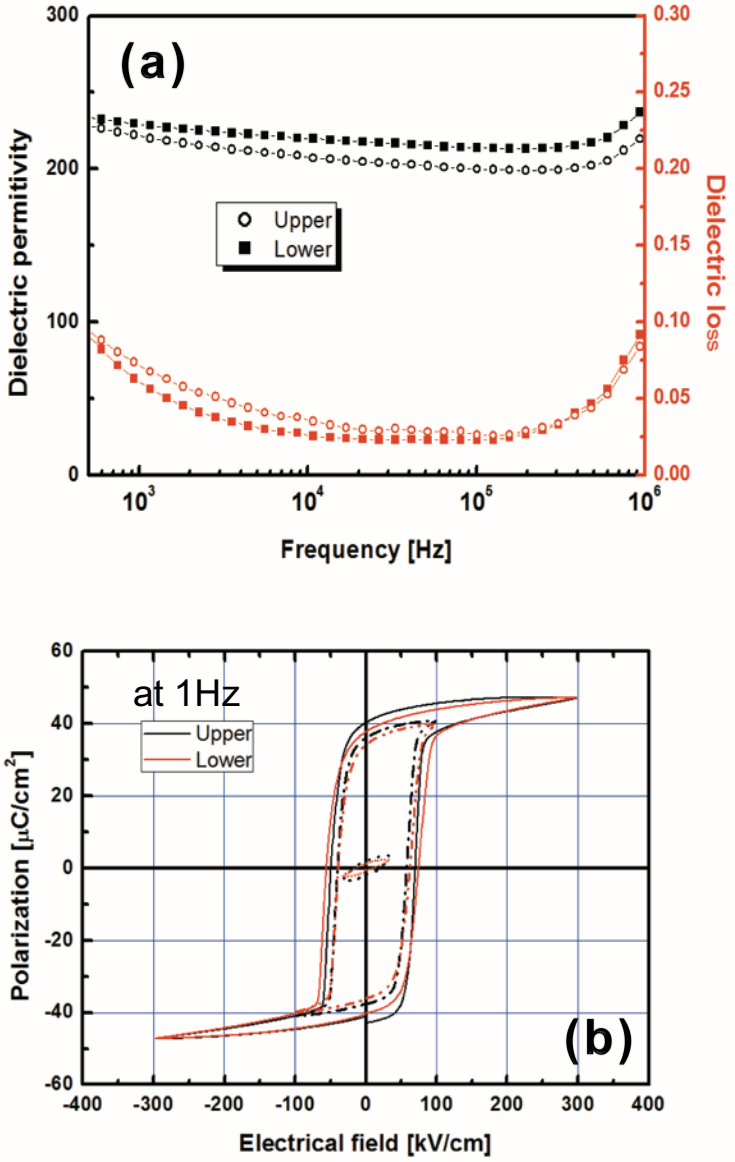

Figure A-5. (a) The dielectric properties as a function of frequency (500 Hz ~ 1 MHz, 30 mV) with low dielectric constant (ε_r ~ 210) and the loss tangent (~ 3%) at 10 kHz, (b) polarization-electric field hysteresis loops of upper and lower PZT films on Ni foil respectively. Polarization-electric field hysteresis loops display well-saturated square hysteresis loops with a remanent polarization ~ 40 μC/cm^2 and a coercive field ~ 65 kV/cm of coercive field (E_c = (-E_c + E_c)/2) at 1 Hz.

Table A-1. Component parameters of PCM model.

Parameter	PCM	Units
Beam length [L]	20	mm
Width of the beam [b_w]	11.5	mm
Thickness of Ni [h_s]	25	μm
Thickness of PZT [h_p]	3	μm
Young's modulus of Ni [Y_s]	200	GPa
Young's modulus of PZT [Y_p]	70	GPa
Mass density of Ni [ρ_s]	8900	kg/m^3
Mass density of PZT [ρ_p]	7500	kg/m^3
Piezoelectric constant [d_{31}]	-90	pm/V
Permittivity [ε_{33}]	3.5	nF/m
Length of brass [L_m]	6	mm
Width of brass [b_m]	8	mm
Thickness of brass [h_m]	4	mm
Density of brass [ρ_m]	8600	kg/m^3
Length of the base link [l_1]	10	mm
Length of the proof mass hinge [l_2]	1.88	mm
Torsional spring constant of tip hinge [K_1]	0.0728	N·m/rad

Table A-2. Performance of the piezoelectric compliant mechanism model (theory) and device at various excitation levels.

Acceleration [g] @ 6.1~ 6.3 Hz	Output voltage [V] (R_{opt} = 330kΩ)	Max. Power [μW]	P_{rms} [μW]	Power Density (Power/area×g^2) [μW/cm^2×g^2]
0.16	9.67	284	142	1065
0.15	8.51	220	110	937
0.125	7.32	190	95	1132
0.105	7.02	149	75	1303
0.088	6.83	141	71	1754
0.05	5.78	101	51	3887
0.05 (Theory)	5.86 (R_{opt} = 239.6 kΩ)	143	72	5500

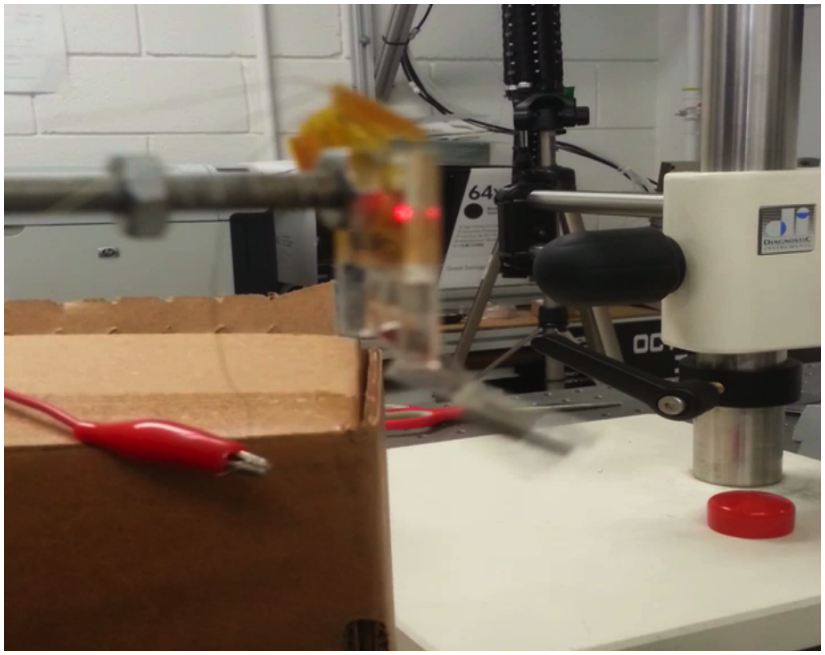

Video A-1. Bending motion of PCM device response to vibration by shaker under resonance frequency (~ 6Hz)

_[1] H.G. Yeo, S. Trolier-McKinstry, *J. Appl. Phys.* **2014**, *116*, 014105.

Appendix B: Optimization for high temperature sputtering with XRD and FESEM images

Table B-1. RF sputter deposition conditions used for PZT on $Pt/TiO_x/SiO_2/Si$

Parameter	Sputtering parameter
Target	PZT (52/48) + 5% PbO excess
Distance between target and substrate	6 inch
RF power	88 Watts (Power density : 2.0 W/cm^2)
Chamber Pressure	6 mTorr
Gas	Ar
Deposition time	12500 s (~0.5 μm)
Setting Temperature of Substrate	25 °C
Post annealing conditions	1 min at 700 °C in O_2

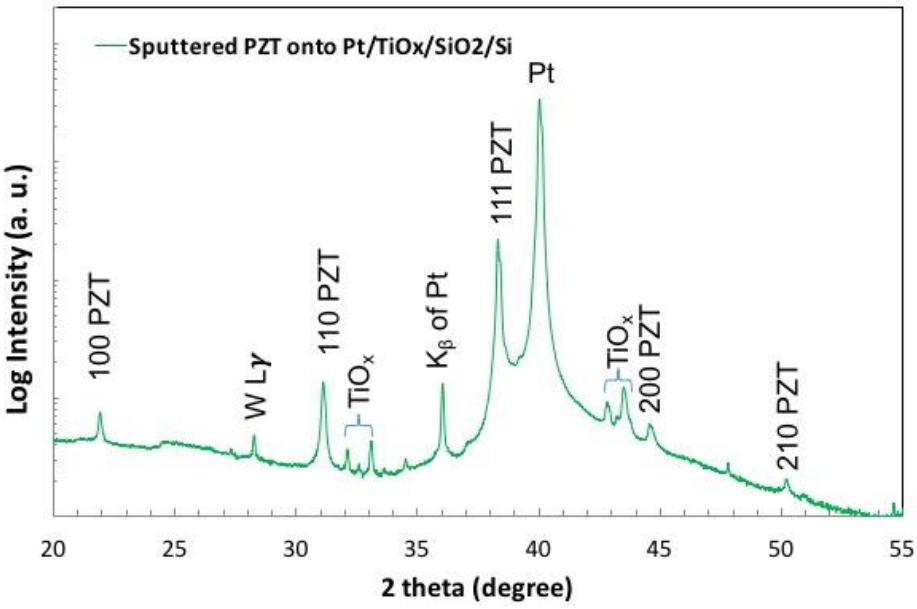

Figure B-1. XRD pattern of PZT seed layer on a $Pt/TiO_x/SiO_2/Si$ substrate using *rf* sputtering with post annealing under the conditions listed in Table B-1.

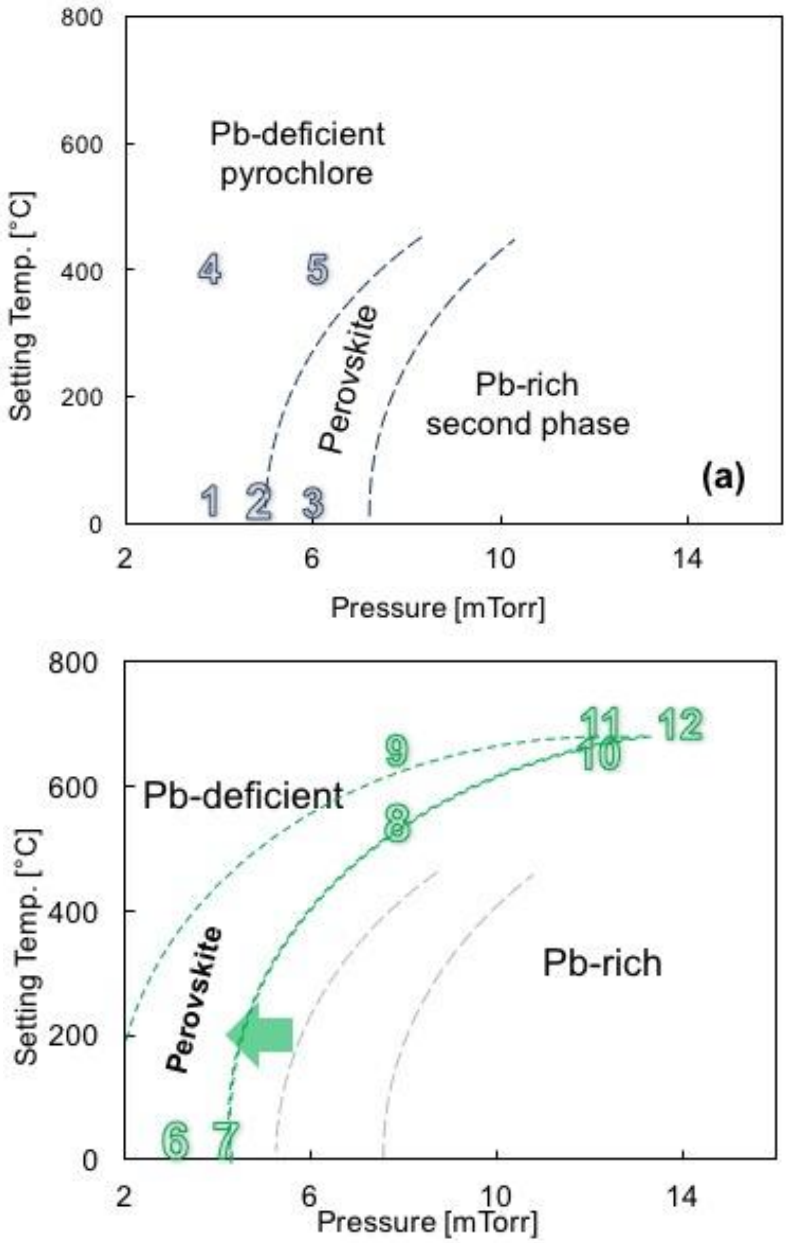

Figure B-2. Schematic phase diagram of sputtered PZT films (following a post-growth heat treatment step: crystallization at 650 °C for 1min in O_2 by RTA) as a function of Ar sputtering pressure and substrate set temperature. Data were acquired with the old sample holder using (a) 5% Pb excess target and (b) 10% Pb excess target. [Samples #1~12 deposited in an argon ambient with an RF power of 88 watt under the conditions described in Figure B-3~14].

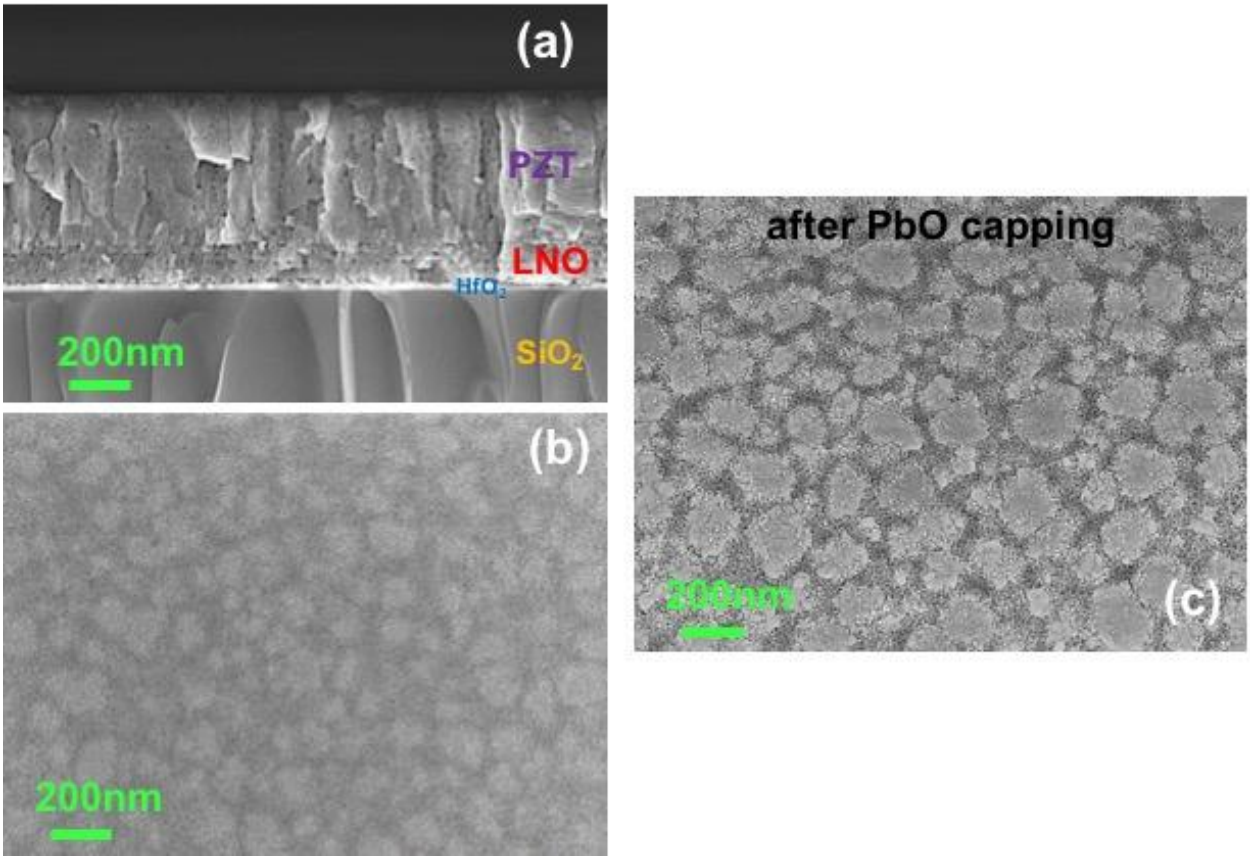

Figure B-3. (a) Cross sectional and (b) surface microstructure of Sample #1 after RTA annealing at 650°C for 1min (c) surface microstructure after PbO capping. There is a large volume of the pyrochlore phase present after the PbO capping.

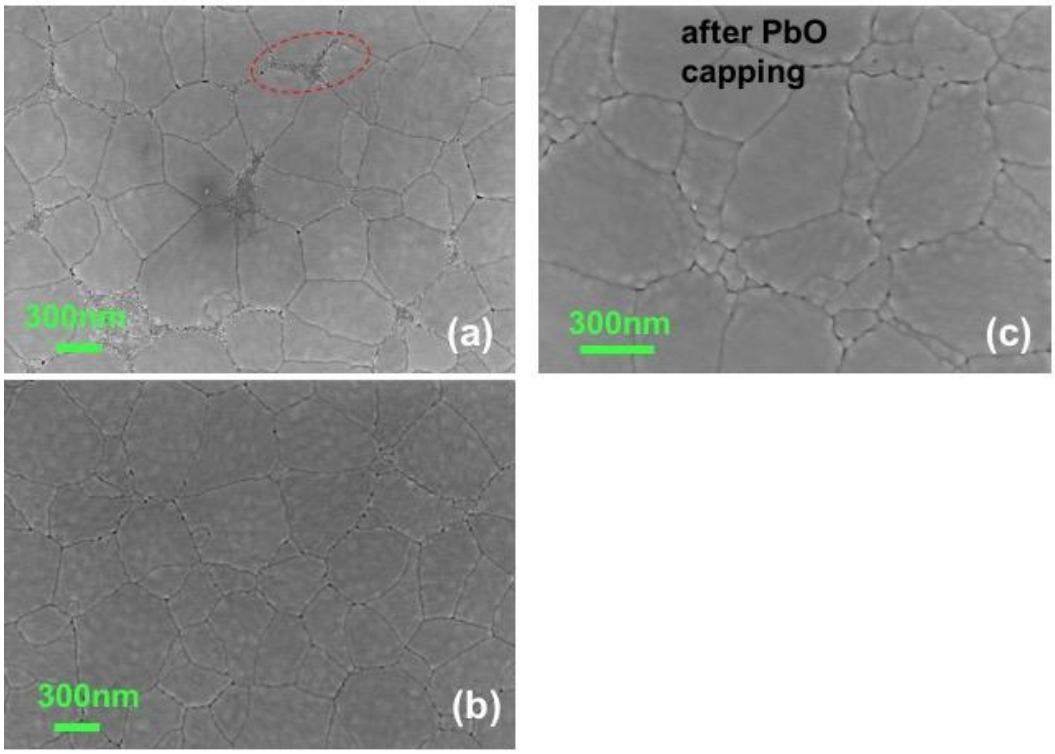

Figure B-4. Surface microstructure of (a) sample #2-i (PZT on $Pt/TiO_x/SiO_2/Si$), (b) sample #2-ii (PZT on $LNO/HfO_2/SiO_2/Si$) [red circle: pyrochlore phase], and (c) sample #2-i after PbO capping.

Sample #2-i on a platinized silicon substrate shows surface pyrochlore phase at the grain boundaries. This surface pyrochlore phase was converted to the perovskite phase by using the PbO cover coat method described by Tani and Payne.[1]. When a PZT film was deposited on an LNO seeded substrate (sample #2-ii) under the same sputtering conditions as that of sample #2-i, there is no visible surface pyrochlore.

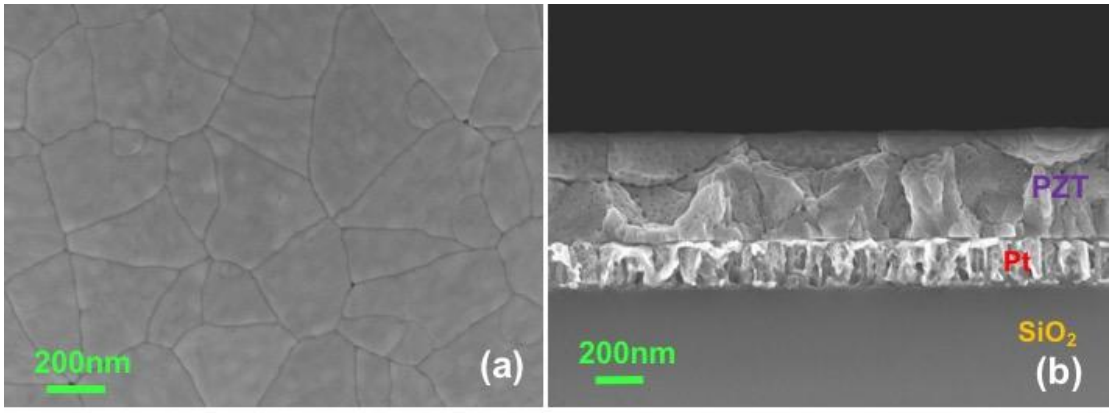

Figure B-5. (a) Surface and (b) cross sectional images of sample #3. The surface pyrochlore phases is not present in surface micrograph images of sample #3.

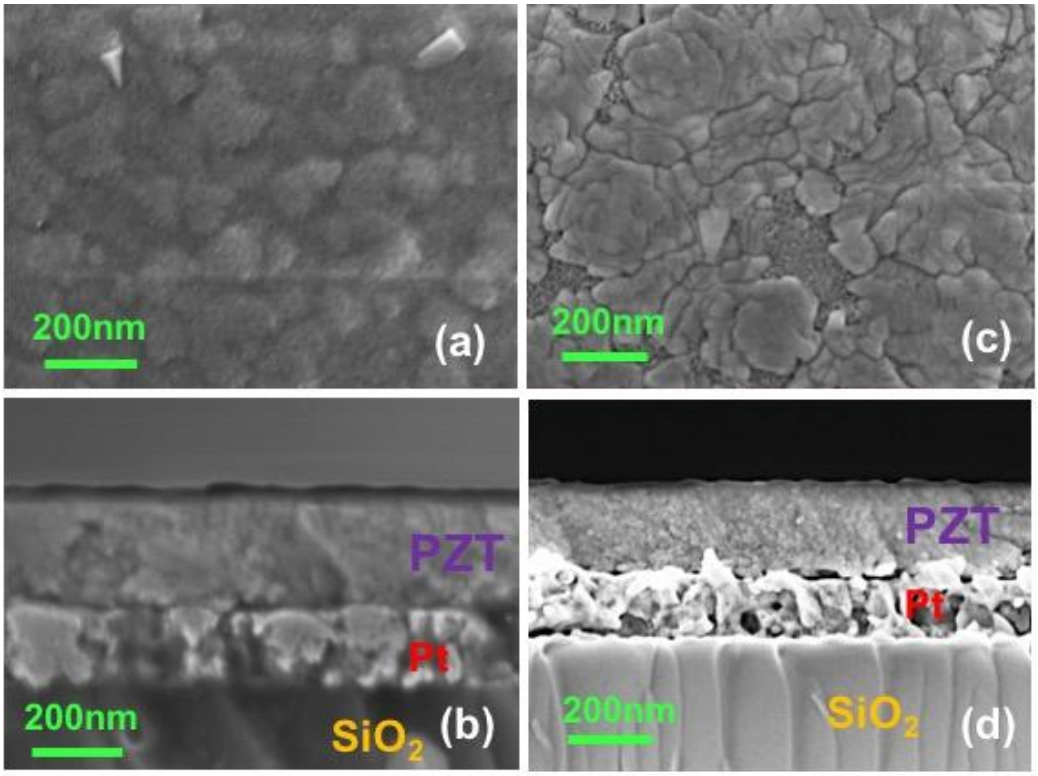

Figure B-6. (a) Surface, (b) cross section images of sample #4 before PbO capping treatment and (c),(d) micrograph of sample #4 after PbO capping. There is a large volume of the pyrochlore phase after PbO capping.

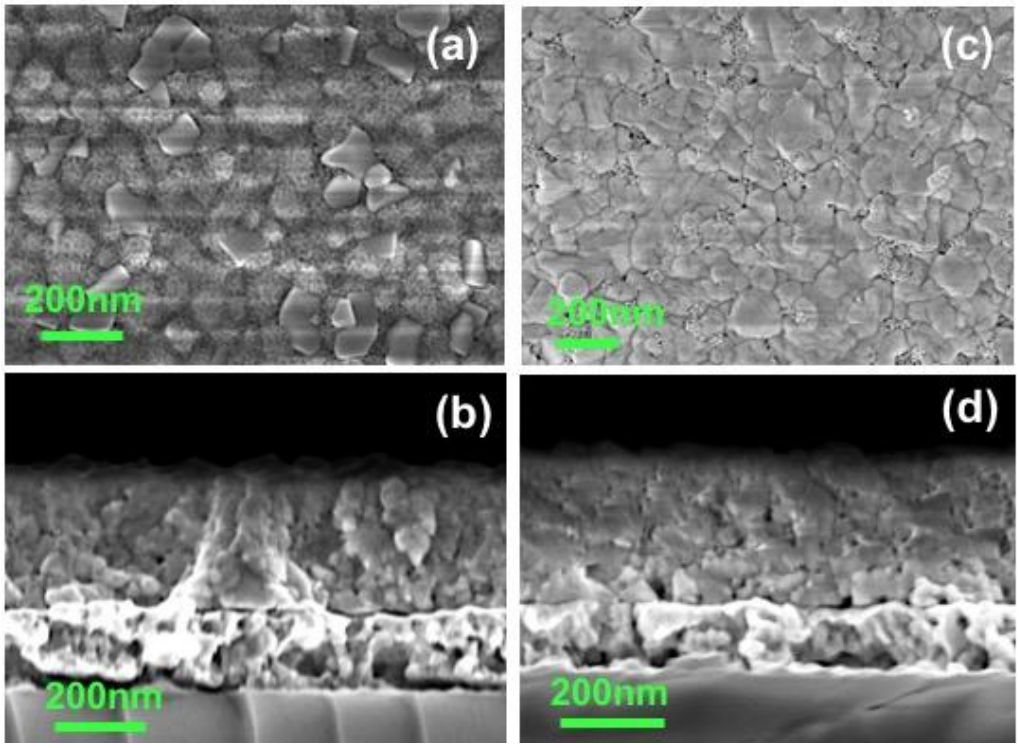

Figure B-7. (a) Surface, (b) cross section micrographs of sample #5 before PbO capping treatment and (c),(d) micrograph of sample #5 after PbO capping. There is a large volume of the pyrochlore phase after PbO capping.

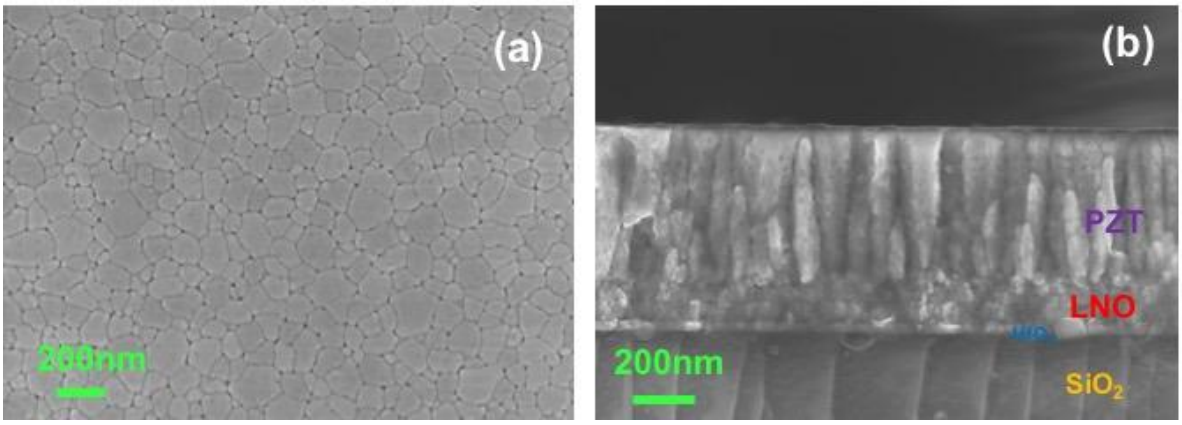

Figure B-8. (a) Surface, and (b) cross section micrographs of sample #6. No surface pyrochlore phases are present in surface micrograph images of sample #6.

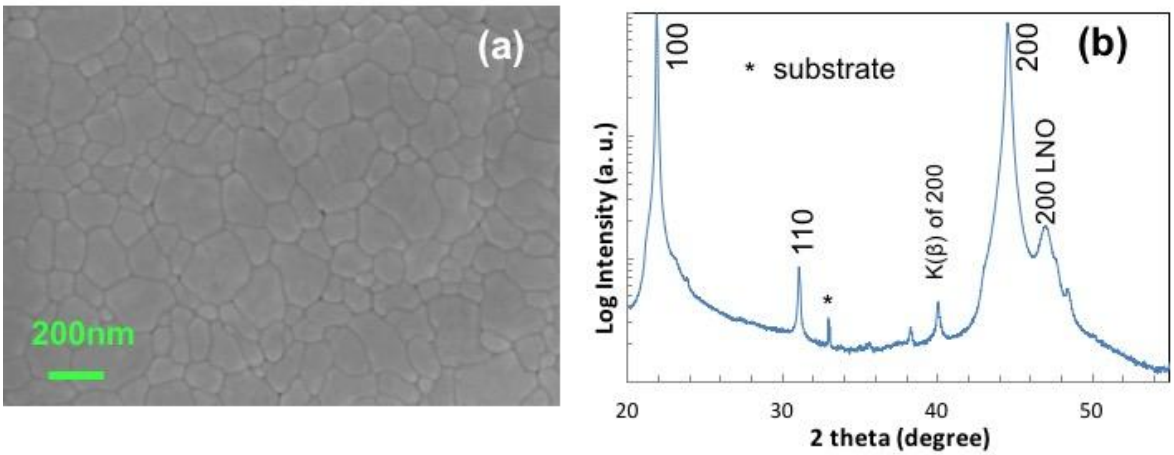

Figure B-9. (a) Surface, micrographs images and (b) XRD patterns of sample #7. The pyrochlore phases were not detected by SEM images and XRD patterns.

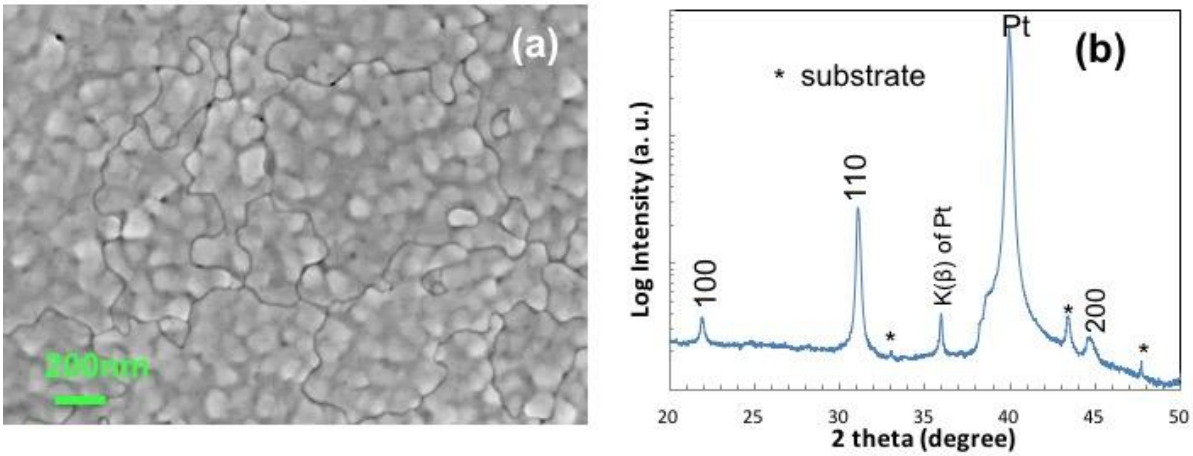

Figure B-10. (a) Surface, micrographs images and (b) XRD patterns of sample #8. No pyrochlore phases were detected by SEM images and XRD patterns.

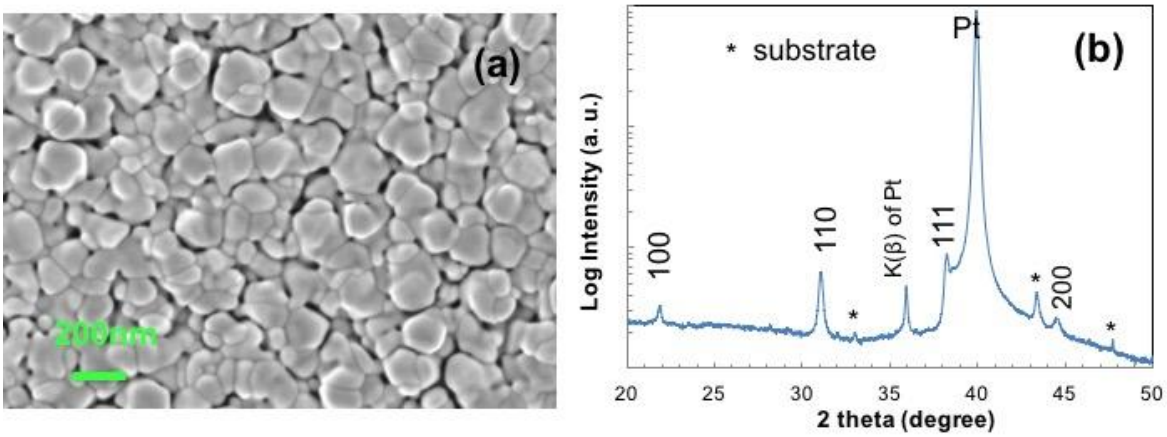

Figure B-11. (a) Surface, micrographs images and (b) XRD patterns of sample #9. No pyrochlore phases were detected by SEM images and XRD patterns. The sample has visible porosity or grooving on the surface.

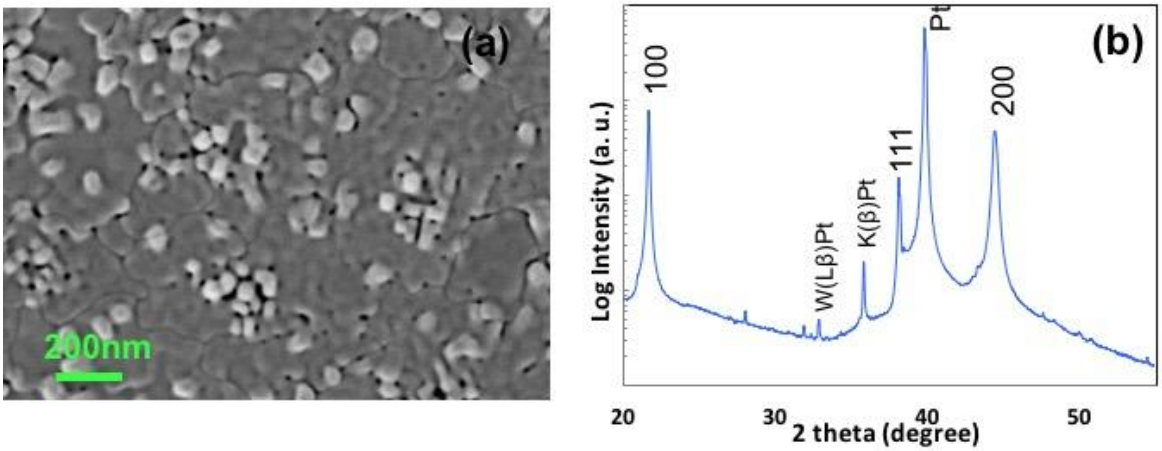

Figure B-12. (a) Surface micrograph and (b) XRD patterns of sample #10. No pyrochlore phases were detected by SEM images and XRD patterns.

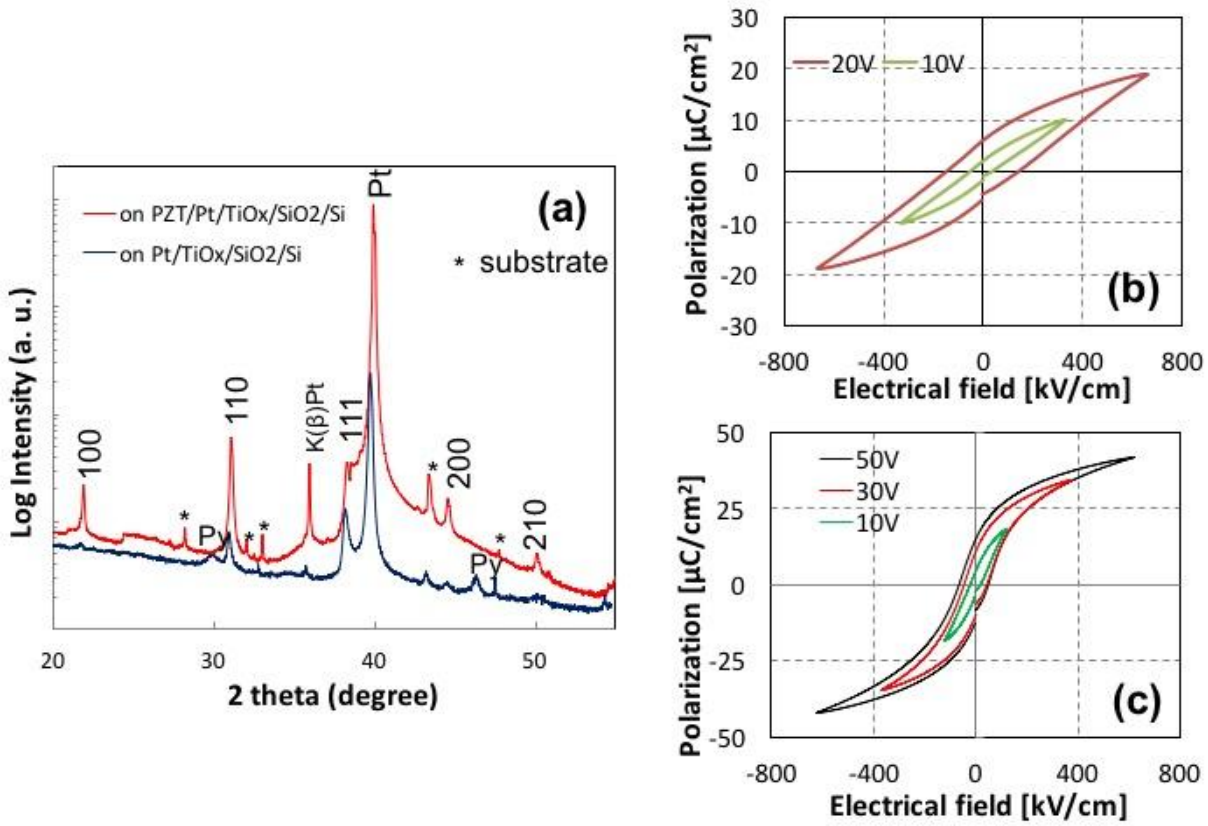

Figure B-13. XRD data of sample #11 and P-E hysteresis loops of (b) on $Pt/TiO_x/SiO_2/Si$ [sample #11-i] and (c) on PZT seeded $Pt/TiO_x/SiO_2/Si$ [sample #11-ii].

The non-ferroelectric pyrochlore phase in sample #11 film on $Pt/TiO_x/SiO_2/Si$ substrate was detected by XRD and leads to an increase in the coercive field and reduces the polarization while producing a significantly less well-saturated hysteresis loop.[2] Sample #11-ii has the perovskite phase as determined by XRD and shows a typical saturated P-E hysteresis loop.

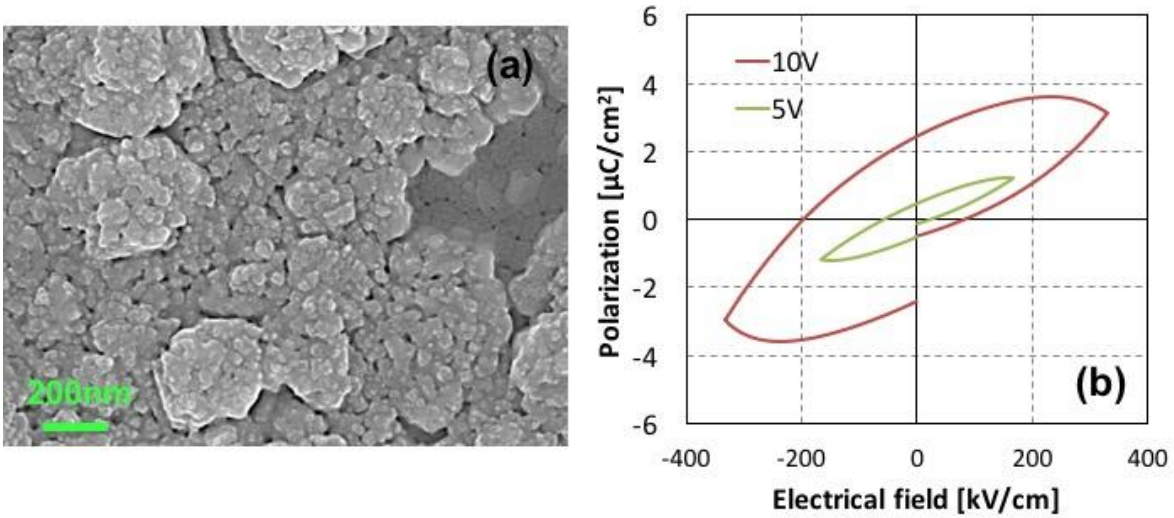

Figure B-14. (a) Surface micrograph image and (b) P-E hysteresis loops of sample #12.

Sample #12 shows fatter P-E hysteresis loops with high loss tangents which might be caused by a Pb rich phase.

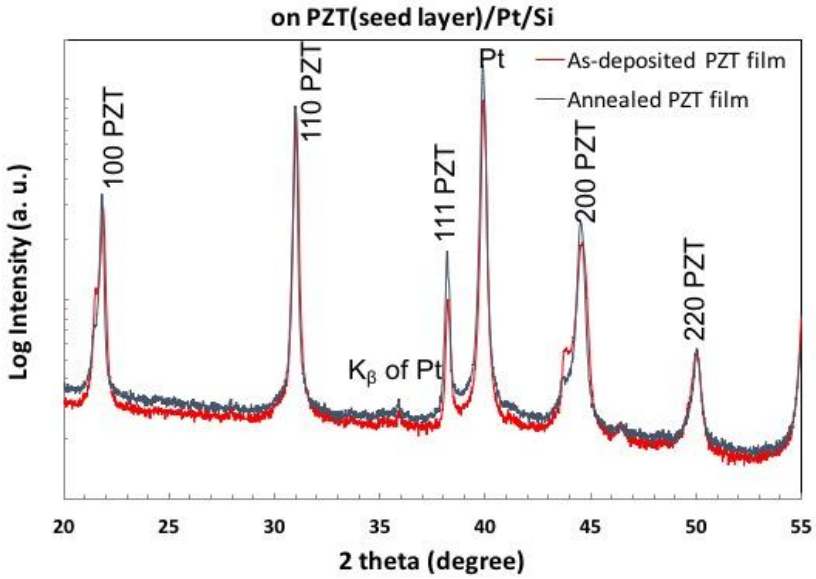

Figure B-15. XRD pattern of sputtered PZT film on PZT(0.5μm)/Pt/TiO_x/SiO_2/Si substrate at a 700 °C substrate setting temperature with the old holder. The sputter time was 16 hr 35 min. The rest of the sputtering conditions are the same as those described in Table B-2.

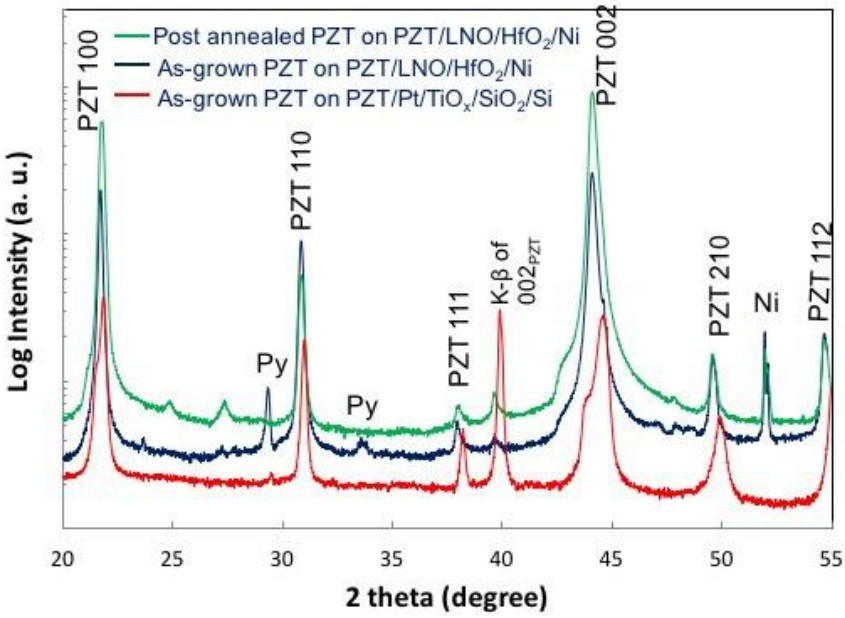

Figure B-16. X-ray diffraction patterns of PZT film were sputtered on PZT seeded Ni and Si substrates at a 700 °C substrate setting temperature with the old holder. The growth time was for 16 hr and 35 min. The other sputtering condition are the same as those described in Table 6-2.

Table B-2. High temperature sputtering parameters of PZT film on large size PZT seeded Ni foil using the old substrate holder.

Target	PZT (52/48) + 10% PbO excess
Substrate	PZT/LNO/Ni
RF power	88 Watts
Chamber Pressure	7.5 mtorr
Gas	97% Ar +3% mixture gas (10% O_2+ 90% Ar)
Deposition Rate	0.11 μm/hr
Set Temperature of Substrate	750 °C (dwell time prior to deposition: 100min)

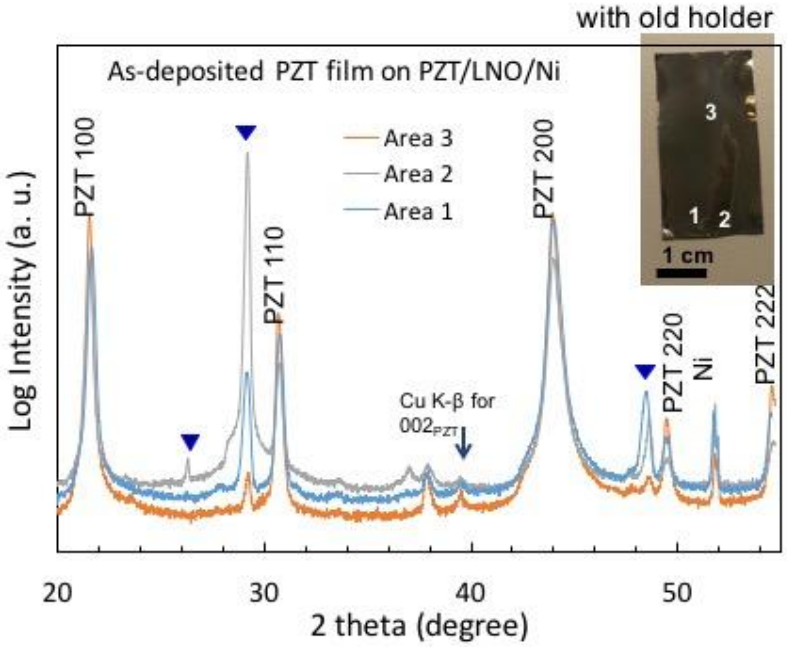

Figure B-17. X-ray diffraction patterns of sputtered PZT film on PZT seeded Ni under the conditions listed in Table B-2.

Table B-3. High temperature sputtering parameters of PZT film on large size PZT seeded Ni foils using the new substrate holder.

Target	PZT (52/48) + 10% PbO excess
Substrate	PZT/LNO/Ni
RF power	88 Watts
Chamber Pressure	8 mtorr
Gas	97% Ar +3% mixture gas (10% O_2+ 90% Ar)
Deposition Rate	0.11 μm/hr
Set Temperature of Substrate	530 °C (dwell time prior to deposition: 100min)

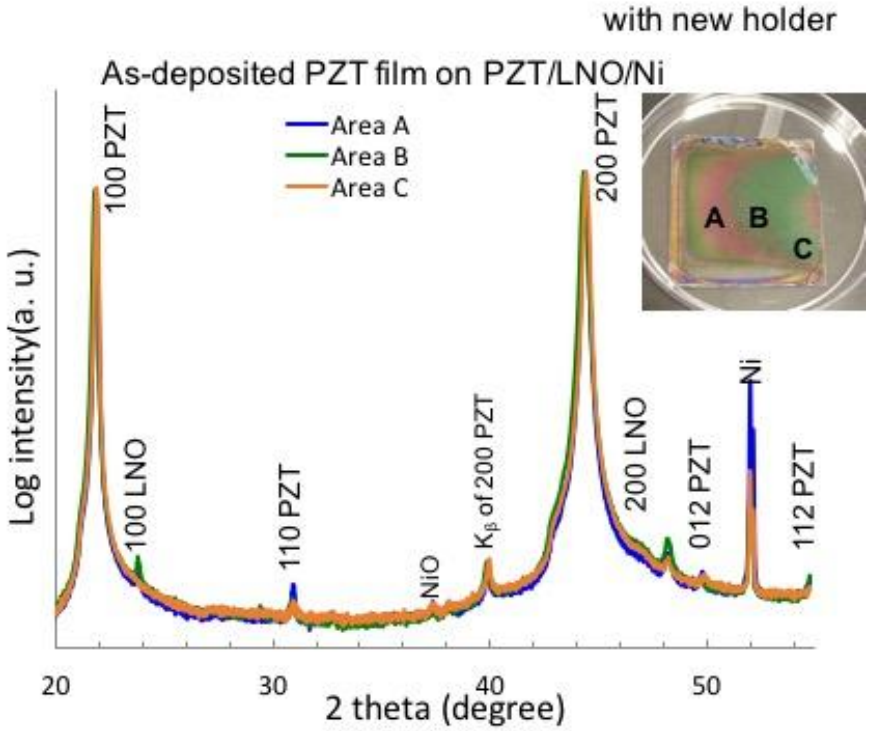

Figure B-18. X-ray diffraction patterns of sputtered PZT film on PZT seeded Ni under the conditions listed in Table B-3.

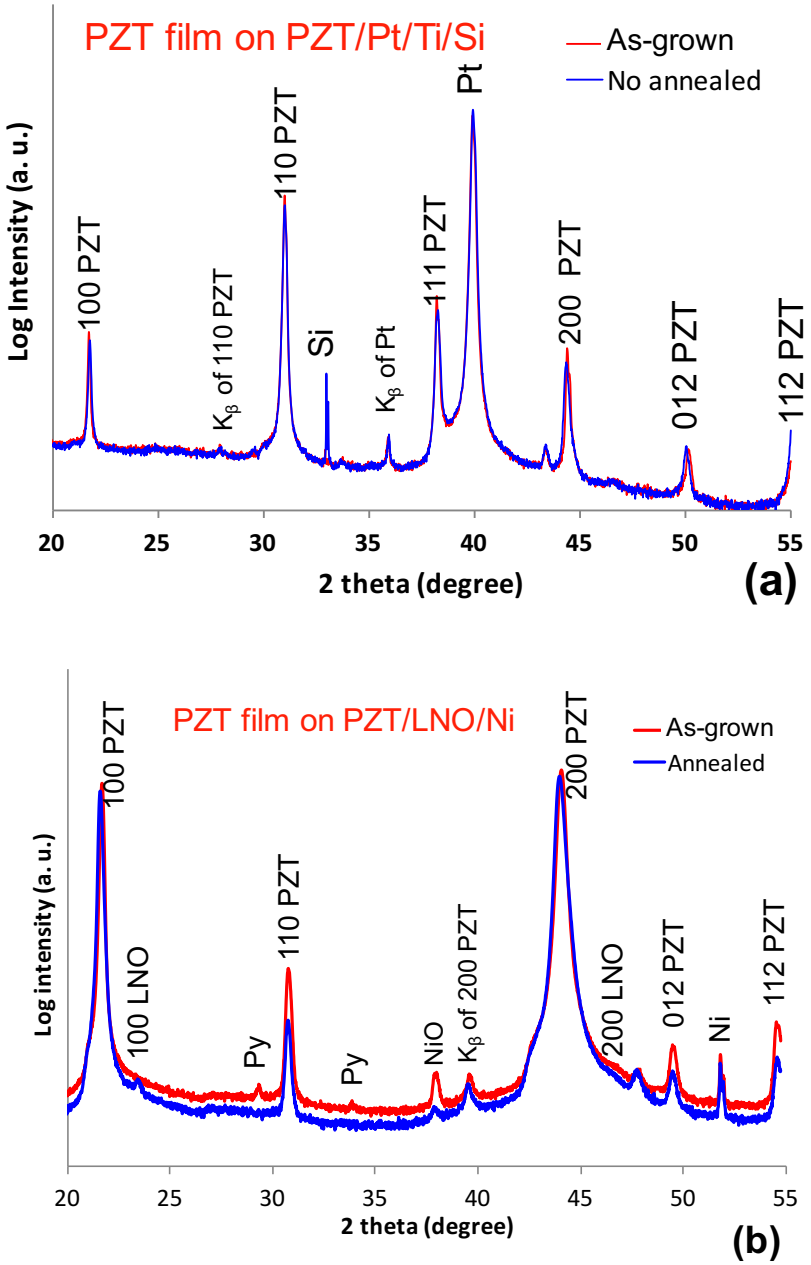

Figure B-19. XRD pattern of sputtered PZT film on (a) PZT/Pt/TiO_x/SiO_2/Si substrate and (b) PZT/LNO/HfO_2/Ni at a 500 °C substrate setting temperature with the new holder. The sputter time was 8 hr 20 min. The rest of the sputtering conditions are the same as those described Table B-3.

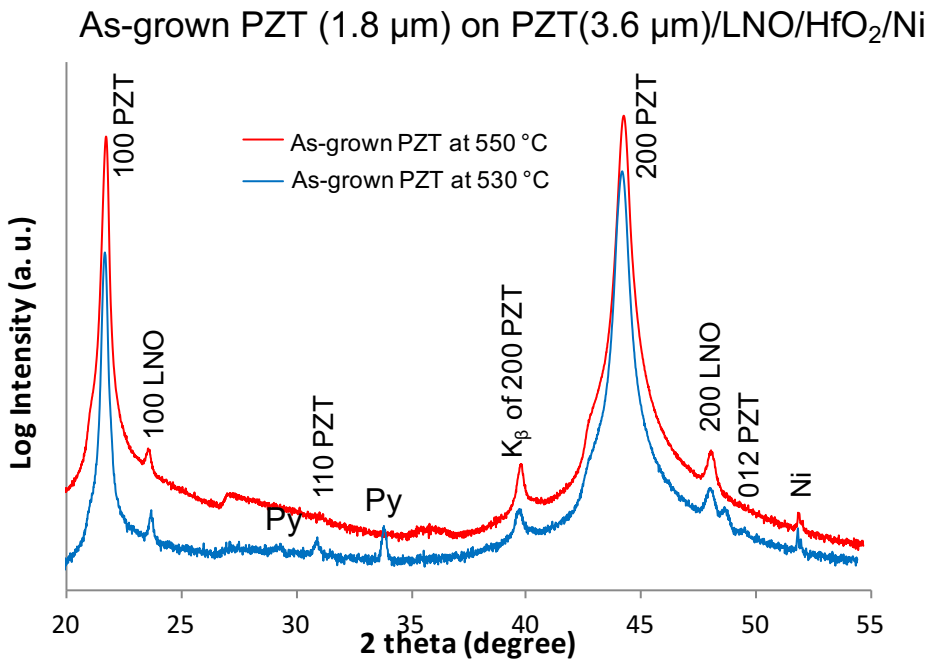

Figure B-20. XRD pattern of sputtered PZT film on PZT(3.6 µm)/LNO(100 nm)/HfO_2(30 nm)/Ni(25 µm) substrate at 530 and 550 ºC setting temperature with the new holder.

References

[1] T. Tani, and D. A. Payne, "Lead Oxide Coatings on Sol–Gel-Derived Lead Lanthanum Zirconium Titanate Thin Layers for Enhanced Crystallization into the Perovskite Structure," *Journal of the American Ceramic Society* **77** (1994) 1242.

[2] G. L. Brennecka, C. M. Parish, B. A. Tuttle, L. N. Brewer, and M. A. Rodriguez, "Reversibility of the perovskite-to-fluorite phase transformation in lead-based thin and ultrathin films," Advanced Materials, 20 (2008) 1407.

VITA

Hong Goo Yeo was born in Busan, South Korea on April 29, 1978. In 1997, he attended Changwon National University, and obtained his B.S degree in Ceramic Science and Engineering in 2001. In 2005, he received his M.S degree in Materials Science and Engineering at Changwon National University.

He got a chance to work in Prof. Trolier-McKinstry group, MRI as a visiting researcher 2009. One year later he began his doctorate degree in Materials Science and Engineering at the Pennsylvania State University under the guidance of Professor Susan Trolier-McKinstry. His research resulted in a dissertation.